SCHOOL OF MINERAL RESOURCES ENGINEERING
ΠΟΛΥΤΕΧΝΕΙΟ ΚΡΗΤΗΣ
TECHNICAL UNIVERSITY OF CRETE

FORTH
INSTITUTE OF GEOENERGY

Modelling and kinetic analysis of the thermal maturity of kerogen in Western Greece and its correlation to the prevailing palaeoenvironmental conditions

Vagia Ioanna Makri

A Dissertation for the degree of Doctor of Philosophy

School of Mineral Resources Engineering, Technical University of Crete
Institute of GeoEnergy, Foundation for Research and Technology – Hellas (FORTH/IG)

October 2025

Modelling and kinetic analysis of the thermal maturity of kerogen in Western Greece and its correlation to the prevailing palaeoenvironmental conditions

Μοντελοποίηση και ανάλυση της κινητικής της θερμικής ωρίμανσης του κηρογόνου στην Δυτική Ελλάδα και η συσχέτιση της με τις επικρατούσες παλαιοπεριβαλλοντικές συνθήκες

Βάγια Ιωάννα Μακρή

Διδακτορική διατριβή

Σχολή Μηχανικών Ορυκτών Πόρων, Πολυτεχνείο Κρήτης
Ινστιτούτο ΓεωΕνέργειας, Ίδρυμα Τεχνολογίας και Έρευνας (ΙΤΕ/ΙΓ)

"This research was supported by Helleniq Energy S.A., within a sponsorship to the Institute of GeoEnergy (FORTH/IG), Foundation for Research and Technology – Hellas"

In Science we don't prove, we gather evidence.

Karl Popper

Thesis committee

Professor Nikolaos Pasadakis (Supervisor)
School of Mineral Resources Engineering
Technical University of Crete

Principal Researcher Dr. Spyridon Bellas
Institute of GeoEnergy (FORTH/IG), Foundation for Research and Technology – Hellas

Professor David Muirhead
Department of Geology and Geophysics, School of Geosciences
University of Aberdeen

Professor Avraam Zelilidis
Department of Geology
University of Patras

Professor Emmanouil Manoutsoglou
School of Mineral Resources Engineering
Technical University of Crete

Professor Nikolaos Kallithrakas-Kontos
School of Mineral Resources Engineering
Technical University of Crete

Professor Despoina Vamvouka
School of Mineral Resources Engineering
Technical University of Crete

ACKNOWLEDGMENTS

First and foremost, I would like to express my deepest gratitude to my supervisor, Professor Nikolaos Pasadakis, for his trust and for giving me the opportunity to undertake this research. Although the journey was at times challenging, his constant availability, insightful discussions, and guidance were invaluable. It has truly been an honour to work under his supervision.

I am also sincerely thankful to Dr. Spyridon Bellas for our in-depth discussions and his valuable feedback and advice on geology-related topics. His readiness to engage and share his expertise has been greatly appreciated.

Special thanks are extended to Professor David Muirhead for his support since my initial visit to the University of Aberdeen as a trainee. His assistance with analyses, constructive feedback, and encouragement throughout my work have been of great importance.

I owe particular gratitude to Dr. Ioannis Oikonomopoulos, who was far more than an external supervisor. I am deeply thankful for his trust and for providing me with the opportunity to work on samples from Helleniq Energy. His thorough discussions, continuous guidance, patience, and unwavering support throughout these years have been crucial. Without his contribution, this PhD thesis would not have been possible.

I would also like to thank the members of my thesis examination committee, Professors Avraam Zelilidis, Emmanouil Manoutsoglou, Despoina Vamvouka, and Nikolaos Kallithrakas-Kontos, for kindly accepting the invitation to evaluate my dissertation.

In addition, I am grateful to Professors Nikolaos Kallithrakas-Kontos and Stavros Kalaitzidis for their assistance with the laboratory analyses undertaken at the Technical University of Crete and the University of Patras.

I extend my appreciation to my colleagues Eleni Chamilaki, Konstantina Selekou and Iona Copley for their help in laboratory analyses, and to Dr. Andrea Schito for his support during analyses at the University of Aberdeen and for contributing to the advancement of my research goals.

I gratefully acknowledge Helleniq Energy for their financial support to the Institute of GeoEnergy, which in turn enabled the completion of my research.

Finally, I wish to express my heartfelt thanks to my family and friends for their support in every possible way during these years, and myself for the dedication. A PhD journey is demanding in many ways, I am profoundly grateful for their constant encouragement, understanding, and efforts to make this path easier for me.

ABSTRACT

The fold-and-thrust belt of Western Greece preserves a succession of Mesozoic organic-rich intervals that vary in depositional environment, geochemical character, and hydrocarbon generation potential. This thesis investigates the mineralogical, geochemical, and kinetic properties of these intervals through the integration of XRD, XRF, Rock-Eval, biomarker, and palynofacies data, combined with 1D thermal modelling.

Mineralogical analysis indicates a predominantly carbonate-rich character throughout the stratigraphy, with dolomite prevailing in Late Triassic – Early Jurassic samples and calcite dominating the younger units. Elemental geochemistry and redox-sensitive trace elements reveal evolving depositional conditions through time. Arid settings and euxinic conditions dominated the Late Triassic – Early Jurassic intervals, transitioning to more variable redox regimes with enhanced anoxia during the Jurassic and Early Cretaceous.

Organic geochemical and palynological data indicate a range of kerogen types, mainly from Type II to II(S). Total organic carbon (TOC) reaches 35.56 wt% and Hydrogen Index (HI) values up to 728 mgHC/gTOC, while most samples remain thermally immature to early mature. Amorphous organic matter dominates, whereas increased sporomorph and phytoclast input in some units reflects terrestrial influence, affecting both preservation and kerogen reactivity. These variations are stratigraphically coherent and control kinetic behavior and generation profiles.

Kinetic modelling demonstrates that activation energy (Ea) distributions vary with age and facies. Late Triassic – Early Jurassic and Early – Middle Jurassic samples show broad Ea-distributions with two to three principal peaks, covering 58–94% of the total generation potential, indicating chemically heterogeneous kerogens and gradual transformation profiles. In contrast, Mid – Late Jurassic and Early Cretaceous samples display narrower Ea-distributions, with up to 95% of potential concentrated in one or two peaks, consistent with more homogeneous kerogen and sharper generation windows. Organic sulfur content reduces Ea values and enhances reactivity, whereas calcite-rich matrices may moderate it.

1D thermal modelling of the AY-3 and PxGa-1x wells underscores the critical influence of kinetic model selection on hydrocarbon generation predictions. Differences in TR10 values between custom and library kinetics result in depth shifts exceeding 1 km under a uniform geothermal gradient. Custom kinetics yield lower TRmax and delayed hydrocarbon generation, whereas library kinetics often overestimate maturity, particularly in shallow or structurally complex

intervals. Burial and thermal history calibration using vitrinite reflectance and biomarker ratios provide additional constraints on uplift, erosion, and structural evolution, suggesting eroded intervals exceeding 1 km of thickness.

This study highlights the mineralogical and kinetic complexity of Mesozoic source rocks in Western Greece and the necessity of custom kinetic models for accurate simulations. These findings improve our understanding of organic matter reactivity in carbonate-rich fold-and-thrust belts and enhance hydrocarbon system prediction in analogous geological settings.

ΠΕΡΙΛΗΨΗ

Η πτυχοεφιππευτική ζώνη της Δυτικής Ελλάδας διατηρεί μια ακολουθία Μεσοζωικών οργανικά πλούσιων στρωμάτων, τα οποία παρουσιάζουν ποικιλία ως προς το περιβάλλον απόθεσης, τον γεωχημικό τους χαρακτήρα και το δυναμικό γένεσης υδρογονανθράκων. Η παρούσα διατριβή διερευνά τα ορυκτολογικά, γεωχημικά και κινητικά χαρακτηριστικά αυτών των στρωμάτων, μέσω ολοκληρωμένης ανάλυσης δεδομένων XRD, XRF, Rock-Eval, βιοδεικτών και παλυνολογίας, σε συνδυασμό με θερμική μοντελοποίηση 1D.

Η ορυκτολογική ανάλυση καταδεικνύει κυρίως ανθρακικό χαρακτήρα σε όλη τη στρωματογραφία, με τον δολομίτη να επικρατεί στις Ύστερες Τριαδικές – Πρώιμες Ιουρασικές αποθέσεις και τον ασβεστίτη να κυριαρχεί στις νεότερες. Η στοιχειακή γεωχημεία και τα ίχνη στοιχείων ευαίσθητων σε οξειδοαναγωγικές συνθήκες αποτυπώνουν την εξέλιξη των συνθηκών απόθεσης με την πάροδο του χρόνου. Ξηρά περιβάλλοντα και ευξινικές συνθήκες επικρατούν στην Ύστερη Τριαδική – Πρώιμη Ιουρασική, ενώ κατά την Ιουρασική και Πρώιμη Κρητιδική περίοδο εμφανίζονται μεταβαλλόμενες συνθήκες με επεισόδια ενισχυμένης ανοξίας.

Τα οργανικογεωχημικά και παλυνολογικά δεδομένα υποδεικνύουν ποικιλία τύπων κηρογόνου, κυρίως τύπου II έως II(S). Η περιεκτικότητα σε ολικό οργανικό άνθρακα (TOC) φτάνει έως 35.56 wt% και οι τιμές του δείκτη υδρογόνου (HI) έως 728 mgHC/gTOC, ενώ τα περισσότερα δείγματα είναι θερμικά ανώριμα έως πρώιμα ώριμα. Η άμορφη οργανική ύλη κυριαρχεί, ενώ αυξημένες αναλογίες σπορομόρφων και φυτοκλαστών σε ορισμένους σχηματισμούς μαρτυρούν χερσαία συνεισφορά, η οποία επηρεάζει τόσο τη διατήρηση όσο και την αντιδραστικότητα του κηρογόνου. Οι διαφοροποιήσεις αυτές παρουσιάζουν στρωματογραφική συνοχή και καθορίζουν τη κινητική συμπεριφορά και το προφίλ γένεσης υδρογονανθράκων.

Η κινητική ανάλυση δείχνει ότι οι κατανομές ενέργειας ενεργοποίησης (Ea) μεταβάλλονται ανάλογα με την ηλικία και τη λιθοφάση. Οι Ύστερες Τριαδικές – Πρώιμες Ιουρασικές και Πρώιμες – Μέσες Ιουρασικές αποθέσεις παρουσιάζουν ευρείες κατανομές Ea με δύο έως τρεις κύριες κορυφές, που καλύπτουν 58–94% του συνολικού δυναμικού, υποδηλώνοντας χημικά ετερογενή κηρογόνα και σταδιακό μετασχηματισμό. Αντιθέτως, οι Μεσο – Ύστερες Ιουρασικές και Πρώιμες Κρητιδικές αποθέσεις εμφανίζουν στενότερες κατανομές, με έως 95% του δυναμικού συγκεντρωμένο σε μία ή δύο κορυφές, ενδεικτικές πιο ομοιογενούς οργανικής ύλης και πιο μικρού παραθύρου γένεσης. Η παρουσία οργανικού θείου μειώνει τις τιμές Ea και αυξάνει την αντιδραστικότητα, ενώ οι ασβεστιτικές μήτρες φαίνεται να την περιορίζουν.

Η θερμική μοντελοποίηση των γεωτρήσεων AY-3 και PxGa-1x αναδεικνύει τον καθοριστικό ρόλο της επιλογής κινητικού μοντέλου στις προβλέψεις γένεσης υδρογονανθράκων. Οι διαφορές στις τιμές TR10 μεταξύ εξατομικευμένων και βιβλιογραφικών κινητικών μοντέλων οδηγούν σε μετατοπίσεις του βάθους έναρξης γένεσης που υπερβαίνουν το 1 χλμ υπό σταθερή γεωθερμική βαθμίδα. Τα εξατομικευμένα κινητικά μοντέλα δίνουν χαμηλότερες τιμές TRmax και καθυστερημένη γένεση, ενώ τα βιβλιογραφικά τείνουν να υπερεκτιμούν την ωριμότητα, ιδίως σε ρηχά ή τεκτονικά πολύπλοκα περιβάλλοντα. Η βαθμονόμηση της ταφής και της θερμικής ιστορίας μέσω της ανακλαστικότητας του βιτρινίτη και των λόγων βιοδεικτών προσφέρει πρόσθετους περιορισμούς στην ανύψωση, τη διάβρωση και την τεκτονική εξέλιξη, υποδεικνύοντας διαβρωμένα πάχη που υπερβαίνουν το 1 χλμ.

Η διατριβή αυτή αναδεικνύει την ορυκτολογική και κινητική πολυπλοκότητα των Μεσοζωικών μητρικών πετρωμάτων της Δυτικής Ελλάδας και υπογραμμίζει την ανάγκη χρήσης εξατομικευμένων κινητικών παραμέτρων για ακριβέστερη μοντελοποίηση. Τα αποτελέσματα συμβάλλουν στην κατανόηση της αντιδραστικότητας της οργανικής ύλης σε ανθρακικά πλούσια πτυχοεφιππευτικά περιβάλλοντα και στη βελτίωση των προβλέψεων συστημάτων υδρογονανθράκων σε ανάλογες γεωλογικές περιοχές.

CONTENTS

LIST OF FIGURES

LIST OF TABLES

ABBREVIATIONS

A	Frequency factor	**VPDB**	Vienna Pee Dee Belemnite Standard
FTB	Fold-and-thrust belt	VR	Vitrinite reflectance
CPI	Carbon Preference Index	XRD	X-ray diffraction analysis
Ea	Activation Energy	XRF	X-ray fluorescence
GC-MS	Gas Chromatography–Mass Spectrometry	Minerals	
GU	Gavrovo Unit	Anh	Anhydrite
HBI	Highly Branched Isoprenoids	Bar	Barite
HF	Heat Flow	Bas	Bassanite
HFTB	Hellenides Fold-and-thrust belt	Cal	Calcite
HI	Hydrogen Index	Chl	Chlorite
IU	Ionian Unit	Dol	Dolomite
MAS	Monoaromatic steroids	Gy	Gypsum
OI	Oxygen Index	Hem	Hematite
OM	Organic matter	Hl	Halite
Ph	Phytane	Ill	Illite
Pr	Pristane	Kfs	K-Feldspar
PU	Pre-Apulian (Paxi) Unit	Py	Pyrite
RE/RE6	Rock-Eval/ Rock-Eval 6	Qz	Quartz
TAS	Triaromatic steroids	Sulph	Sulfides
TR	Transformation ratio		

CHAPTER 1.
INTRODUCTION

1.1. Research questions and goal

This study examines the characteristics, quality, and thermal maturity of Mesozoic organic-rich layers of Western Greece, linking them to palaeoenvironmental conditions. Also, it evaluates the impact of custom versus standard library kinetics in thermal maturity modelling, demonstrating how variations within the same organic-rich interval influence kinetic parameters and kerogen transformation.

To achieve this, this thesis integrates geochemical analysis, generation kinetic modelling, and palaeoenvironmental insights to investigate the factors influencing hydrocarbon generation, source rock heterogeneity, and burial histories. Key research questions include:

- Which are the differences of the Mesozoic (Late Triassic – Early Cretaceous) organic-rich intervals in the Hellenides fold-and-thrust belt?
- How do variations in depositional conditions affect kerogen kinetics?
- What impact do these variations have on kerogen maturation and thermal evolution of the organic-rich layers?
- Are custom kinetic models necessary for understanding kerogen transformation, or are global models sufficient?

By addressing these questions, this research seeks not only to characterize the Mesozoic source rocks of Western Greece, but also to refine our broader understanding of how depositional environment, mineralogy, and organic composition interact to control thermal reactivity and hydrocarbon generation.

1.2. Petroleum Systems

A petroleum system encompasses the interconnected geological elements and processes necessary for hydrocarbon generation, migration, and accumulation [1]. It comprises a pod of mature source rock and all the migration paths, a reservoir rock, caprock, and a trap that can be charged by that source rock [1]. The critical elements of a petroleum system include the source rock, reservoir

rock, seal rock, and overburden, while key processes involve hydrocarbon generation, migration, entrapment, and preservation [1].

Among these elements, the source rock is arguably the most critical, as it forms the foundation of any petroleum system. The effectiveness of a source rock depends on the presence of organic matter, its quality, and the thermal history that drives hydrocarbon generation [1]. However, source rock development is contingent on suitable biological productivity, depositional environments, and preservation conditions [2]. Timing is equally essential, as the processes of hydrocarbon generation and migration must coincide with the formation of effective traps to ensure hydrocarbon accumulation [1].

1.3. Organic matter in sediments

The organic matter (OM) in sediments serves as the primary precursor to hydrocarbons, influencing the quality and potential of source rocks. Derived from algae, plants, and microorganisms, OM undergoes preservation, transformation, and degradation in depositional environments, forming the foundation for petroleum generation [2]. The organic matter in sediments originates from three primary sources:

- Autochthonous OM, produced in situ by photosynthetic organisms such as algae and phytoplankton in the photic zone, in the upper water column [3].
- Allochthonous OM, transported from terrestrial environments, primarily from higher plants via fluvial or aeolian processes [4]. A portion may also be delivered to aqueous depositional systems by aeolian processes.
- Reworked OM, derived from erosion and redeposition of older sediments, though its hydrocarbon-generating potential is usually negligible due to degradation [3].

The accumulation of sufficient OM to form source rocks requires high primary biological productivity in or near the depositional environment [5] (Figure 1). This productivity is influenced by solar radiance, nutrient supply, and water availability [2]. While terrestrial productivity is concentrated in equatorial regions due to abundant solar energy and water, marine productivity is highest along nutrient-rich continental margins and polar upwelling zones. In contrast, open oceans, depleted in nutrients, exhibit limited productivity [2].

Another critical factor is the preservation of OM which depends on several factors:

- Anoxic Conditions: The position of the oxic/anoxic boundary is vital. When the boundary lies above the sediment-water interface, anoxic bottom waters protect the OM from oxidative degradation and bioturbation, promoting preservation [2,6].
- Sediment Grain Size: Fine-grained sediments, limit oxygen circulation below the sediment-water interface, fostering localized anoxia, while coarser sediments enhance it, encouraging degradation [7].
- Sedimentation Rate: Optimal rates (~1 mm/year) [5,8,9] ensure OM burial is swift enough to minimize degradation but not so rapid as to dilute its concentration [8].

Once buried, OM characteristics (determined by its origin) dictate its hydrocarbon potential [7]. Marine OM, rich in lipids, is hydrogen-rich and yields both oil and gas upon maturation. Terrestrial OM, dominated by lignin and cellulose, is oxygen-rich and gas-prone. Lacustrine OM, derived from freshwater algae, is highly hydrogen-rich and predominantly oil-prone [7].

1.4. From kerogen to hydrocarbons

Kerogen, the insoluble in organic solvents OM formed during early sediment burial, serves as the intermediate step between the latter, and hydrocarbons [10]. Its composition and transformation through diagenesis, catagenesis, and metagenesis is key to hydrocarbon (HC) generation [11]. This transformation is called thermal maturation and represents the chemical changes in OM under the influence of pressure and temperature due to burial over geological time.

During the stage of diagenesis (< 60 °C) (Figure 1), the OM undergoes microbial decay and biochemical transformation under shallow burial conditions. This process leads to water expulsion and the conversion of proteins and carbohydrates into kerogen and bitumen. Under reducing conditions, hydrogen-rich compounds, essential for the formation of oil-prone kerogen are preserved [12].

As burial depth and temperature increase, kerogen enters the mature catagenesis (60–175 °C), often referred to as the "cracking" stage. Within this range, HC are released. The "oil window" marks the peak generation of liquid hydrocarbons, followed by thermal cracking into to lighter hydrocarbons in the "wet gas zone" [12]. At the stage of metagenesis (> 175 °C), kerogen yields dry gas before becoming inert carbon or graphite [12].

Thermal maturation alters the structure and composition of kerogen. Immature OM is hydrogen-rich with abundant aliphatic structures, which progressively transform into dominant aromatic structures as hydrogen is lost. By the overmature stage, nearly all OM is aromatic. These changes are reflected in elemental composition, particularly hydrogen depletion, which is mapped in the Van Krevelen diagram [13]. As kerogen thermally evolves, Type I and Type II kerogens converge, documenting hydrogen and oxygen loss while carbon content increases. In the gas generation zone, all kerogen types become nearly indistinguishable.

Maturity-related compositional shifts are also evident in chromatographic profiles of generated oil and bitumen. Immature sediments predominantly contain C16 to C22 hydrocarbons and odd-numbered C25 to C35 n-alkanes. As maturity increases, odd-number predominance diminishes, while C15 to C18 isoprenoids and C20 to C30 n-alkanes increase, marking significant HC generation. With continued maturation, chromatographic profiles smooth out.

These systematic changes serve as key maturity indicators, offering insights into the thermal history of sediments, OM transformation, and HC generation, while aiding reconstructions of paleodepositional environments and paleo-erosion processes.

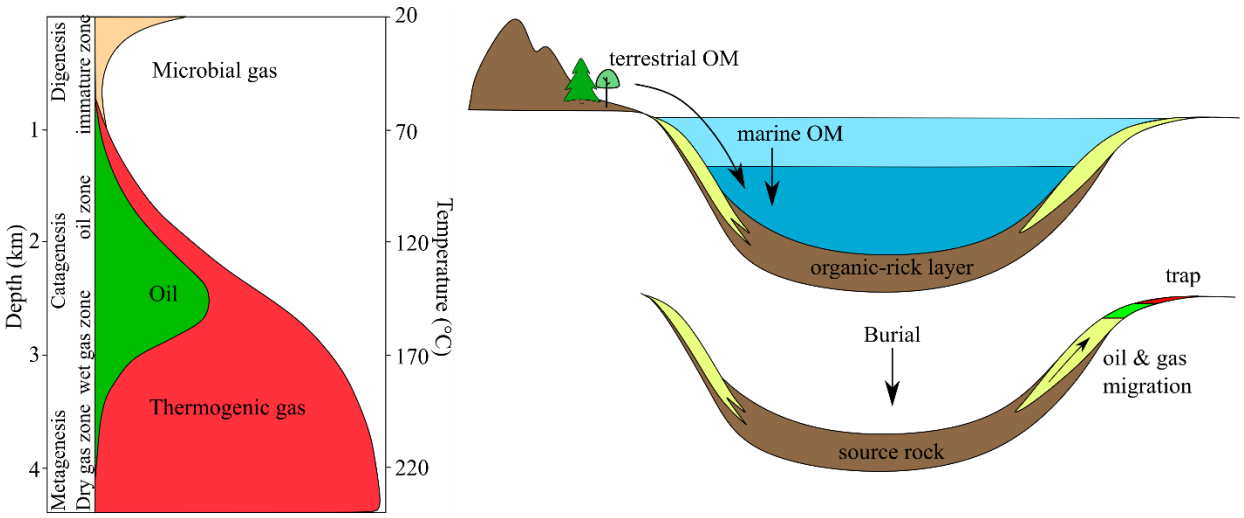

Figure 1. Generalized evolution of OM after deposition, modified after Tissot and Welte (1984).

1.5. Kerogen types and hydrocarbon potential

Kerogen composition varies significantly, determining its hydrocarbon-generating potential (Table 1):

- Type I kerogen, hydrogen-rich and derived from algal material, generates waxy oil and is typically associated with lacustrine environments.
- Type II kerogen, moderately hydrogen-rich, produces a mix of oil and gas and is linked to marine settings with reducing conditions.
- Type III kerogen, oxygen-rich, primarily generates gas and is dominated by terrestrial plant material.
- Type IV kerogen, severely altered and hydrogen-poor, is inert and lacks hydrocarbon-generating potential [13,15].

The preservation of OM during deposition significantly influences kerogen quality. Hydrogen-rich OM, such as lipids, waxes, and fats, produces oil-prone kerogen, while poor preservation or oxic conditions reduce hydrogen content, yielding gas-prone or inert kerogen [2]. Seasonal variations and depositional heterogeneity often result in mixed kerogen types within a single source rock.

Table 1. Geochemical parameters describing the level of thermal maturity, organic matter quality and potential, modified after Peters (1994).

Potential (quantity)	TOC (wt.%)	Rock-Eval	(mg/grock)	Bitumen (ppm)	Hydrocarbons (ppm)
		S1	S2		
Poor	<0.5	<0.5	<2.5	<500	<300
Fair	0.5–1	0.5–1	2.5–5	500–1000	300–600
Good	1–2	1–2	5–10	1000–2000	600–1200
Very good	2–4	2–4	10–20	2000–4000	1200–1400
Excellent	>4	>4	>20	>4000	>2400

Kerogen (quality)	(mgHC/gTOC)	S2/S3	Atomic H/C	Main product at peak maturity
	HI			
I	>600	>15	>1.5	Oil
II	300–600	10–15	1.2–1.5	Oil
II/III	200–300	5–10	1–1.2	Oil/Gas
III	50–200	1–5	0.7–1	Gas
IV	<50	<1	<0.7	None

Maturity	Ro (%)	Maturation	TAI	Bitumen/TOC	Generation (mg/grock)	S1/(S1+S2)
		Tmax (°C)			Bitumen	PI
Immature	0.2–0.6	<435	1.5–2.6	<0.05	<50	<0.1
Mature						
Early	0.6–0.65	435–445	2.6–2.7	0.05–0.1	50–100	0.1–0.15
Peak	0.65–0.9	445–450	2.6–2.7	0.15–0.25	150–250	0.25–0.4
Late	0.9–1.35	450–470	2.9–3.3			>0.4
Postmature	>1.35	>470		>3.3		

Table 1 continued.

1.6. Transformation processes and the need for custom generation kinetics

The transformation of kerogen into hydrocarbons is a function of burial depth, temperature, and time, governed by chemical reactions that vary with kerogen type and structure [16]. The transformation follows a series of thermal decomposition reactions, largely controlled by the cross-linking of chemical moieties within kerogen, such as carbon-carbon (C=C) and carbon-oxygen (C=O) bonds, which determine the energy required for hydrocarbon generation.

Hydrocarbon generation is commonly modelled using first-order Arrhenius kinetics, which describe temperature-dependent reaction rates of kerogen transformation [15]. These models assume uniform reaction behavior across the same kerogen types, yet of different depositional and geographical settings [16]. However, such generalizations may oversimplify OM heterogeneity, potentially leading to inaccurate predictions of hydrocarbon generation timing and potential.

To address this, custom generation kinetics are applied in this study to organic-rich samples from Western Greece. Given the complex palaeoenvironmental conditions and tectonic history of the region, a custom kinetic approach offers a more accurate representation of kerogen transformation pathways. This enhances thermal modelling and geotectonic interpretations.

1.7. Study area

The study area is in Western Greece, covering approximately 7000 km² (Figure 2), and forms part of the Hellenides fold-and-thrust belt (FTB), a southern extension of the Albanides. From a geological perspective, it is associated with the Ionian (IU) and Pre-Apulian Units (PU), which have undergone a complex geotectonic history. Although with proven indications, the area is still frontier in terms of hydrocarbon exploration, due to its complex structure, and thus increased risk.

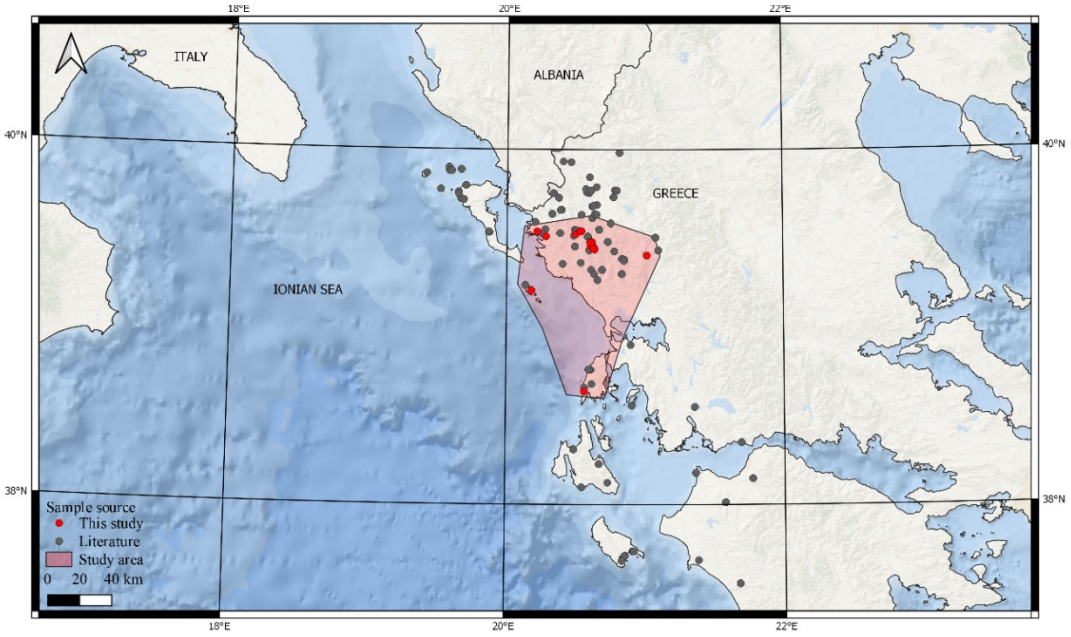

Figure 2. Map showing the distribution of the data points. The red polygon delineates the study area, the red points represent the data points of this study, and the grey points represent the literature data.

The presence of Mesozoic organic-rich intervals in these units suggests a potential for hydrocarbon generation. Evidence of active petroleum systems has been documented both within the study area and in adjacent FTB settings. Previous research includes organic geochemical studies, some burial history reconstructions, and a single kerogen kinetics study, highlighting the need for a more comprehensive investigation.

This study investigates the characteristics, quality, and thermal maturity evolution of kerogen in the Mesozoic organic-rich layers of Western Greece, focusing on the relationship with the palaeoenvironmental conditions and hydrocarbon generation. By integrating geochemical analyses and generation kinetic modelling, this research refines our understanding of the organic-rich intervals in the region, burial histories, kerogen evolution, and hydrocarbon generation potential. It also highlights the importance of custom generation kinetics in refining thermal maturity modelling, addressing the impact of source rock heterogeneity on kerogen transformation.

CHAPTER 2.
REGIONAL GEOLOGICAL & GEOCHEMICAL FRAMEWORK

2.1. Database

A comprehensive database was developed by integrating available literature data and data from Helleniq Energy related to potential organic-rich intervals in Western Greece, covering a geological age range from Triassic to Oligocene. The total number of literature data entries accounts to 1704 with 578 entries from Helleniq Energies.

The following pie chart (Figure 3) illustrates the distribution of samples within the dataset, while Figure 4 shows the amount of data per analysis. This dataset highlighted a gap in the data for the Mesozoic sequences, leading to the selection of a target set of samples from wells and outcrops.

These samples were initially analyzed using Rock-Eval 6 to assess the organic content, and the most organic-rich samples were further analyzed using additional geochemical techniques, including biomarker analysis, XRF, XRD, and palynology (Figure 4).

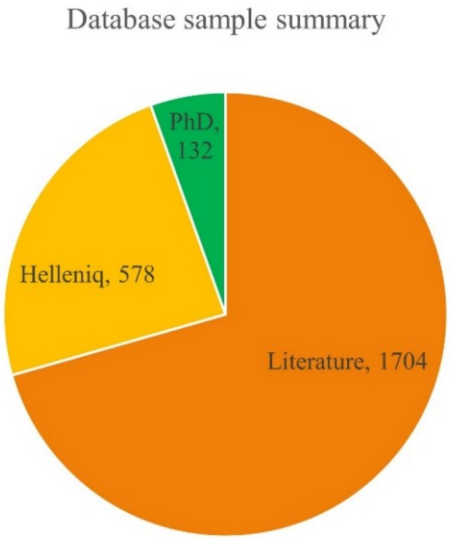

Figure 3. Pie chart summarizing the database sample distribution, representing the number of literature samples, Helleniq Energy samples, and samples analyzed in this thesis.

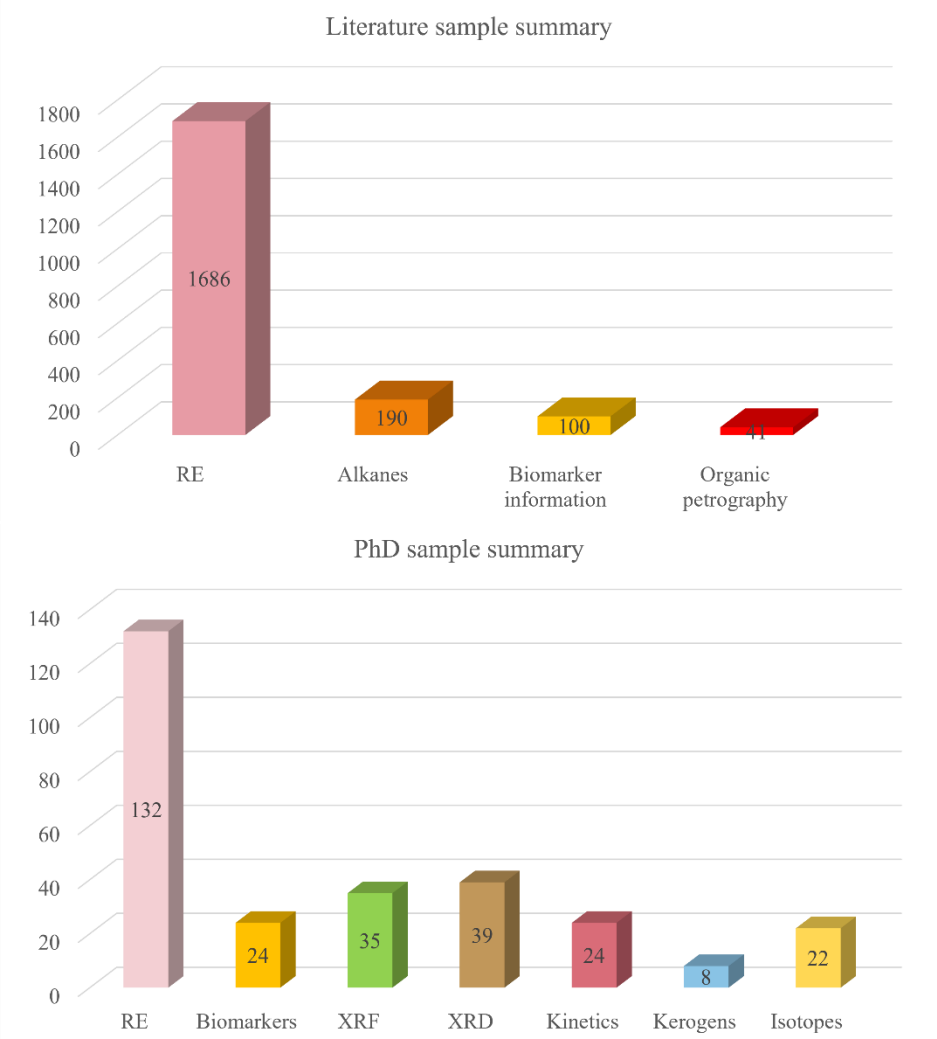

Figure 4. Bar charts of (Top): Literature samples showing the number of data available per analysis, and (Bottom): PhD samples showing the number of samples analyzed per method.

2.2. Geotectonic background

The study area is situated at the External Hellenides region, Western Greece. From Triassic to Late Cretaceous, this region was part of the Apulian continental block along the southern margin of the Tethys Ocean [17]. The Hellenides fold-and-thrust belt (HFTB), a segment of the Alpine orogenic belt, formed due to the collision of the Adriatic plate with elements of the Eurasian plate [18]. This collision led to the closure and obduction of the Mesozoic Tethyan Ocean, which had previously

separated these plates [18–21]. The HFTB extends from the Alps and Carpathians through the eastern Adriatic coast to Greece and Crete [18].

During the Alpine orogeny, sub-basins of the Tethyan margin were inverted [22], with thrusting directed westward over external Paleogene-Neogene flysch sequences [18–20,23]. While extensional faults were often reactivated, some were also thrust due to basal evaporite movement [17,24]. The External Hellenides consist of NW-SE trending structural units, from east to west: the Gavrovo Unit (equivalent to Kruja in Albania), the Ionian Unit (IU; equivalent to Ionian in Albania), and the Pre-Apulian (Paxi) Unit (PU; equivalent to Sazani in Albania) [18,25].

Prior to the Alpine Orogeny, when Western Greece was part of the Apulian continental block in the southern passive margin of Tethys, Mesozoic rifting led to the formation of horsts and grabens [26]. One such graben is the Ionian (IU), bound by normal faults and situated between the Gavrovo platform to the east and the Apulian platform to the west (Figure 5), with the PU representing its slope. These sub-basins were later inverted, forming the Hellenic thrust sheets, which progressively propagated westward from the Inner (eastern) to the External (western) Units [25,27–30]. On a broader scale, the Alpine orogenic belt represents the margin of the Tethyan Ocean, shaped by the collision of Apulia with Eurasia [31].

The Ionian Unit, the most hydrocarbon-prospective unit in Western Greece, is bounded by the Gavrovo thrust to the east and the Ionian thrust to the west. It comprises Triassic evaporites, Triassic – Eocene carbonates, Eocene – Oligocene flysch, and Neogene marine to continental clastics. The pre-evaporitic basement does not outcrop, and halokinetic movements have resulted in structural complexity [18,22,25,32–34]. The IU extends across the western Greek mainland, parts of the Ionian Islands, Peloponnese, and southwestern Albania.

The orogenic front of the IU consists of a thrust system, beneath which on the west lays the carbonate-rich PU [18,25,33]. Offshore, the IU forms a thrust stack over the PU, both resting atop the eastward-dipping Apulian platform, influenced by the HFTB load [18]. The IU is further divided into internal, central, and external sub-basins, from east to west. The orogenic front lies within a region of thinned continental crust in the present-day Adriatic Sea [18,25].

The PU belongs to the Adria microplate margins and consists of Late Triassic – Early Jurassic anhydrites interbedded with carbonates [17]. Stratigraphic completeness and faunal/floral content vary within the unit. Following the Lias rifting of the IU, evaporite deposition ceased, giving way to limestones intercalated with cherts and marls [18,25]. Late Cretaceous – Oligocene

sedimentation was dominated by shallow platform and slope deposits, followed by Miocene marls, sands, and clays. Unlike other units, no flysch has been identified within the PU [18,25].

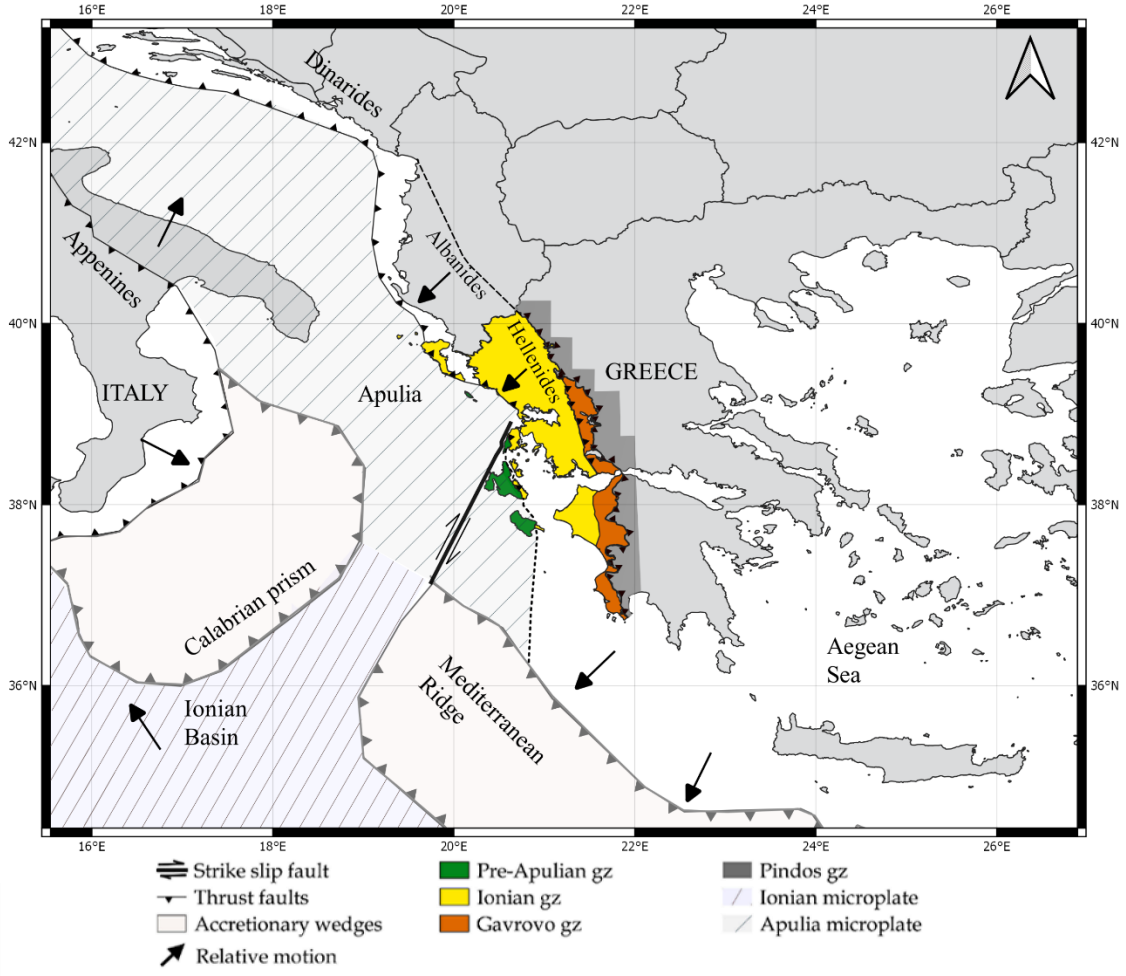

Figure 5. Simplified tectonic map of the area of interest, modified from multiple sources, i.e. [18,25]. Gz; Unit.

Both the PU and IU are separated by thrusts, with additional thrusts further subdividing each unit. The present geological features of these subunits are closely tied to pre-existing tectonic and stratigraphic elements, such as sub-basin-bounding faults, synclines, and anticlines [18,22,25,35]. The HFTB which formed between Middle Miocene to Late Miocene, dominates Western Greece with a NNW-SSE trend. It encompasses the Mesozoic carbonate successions of the IU and PU, which are the primary focus of this study (Figures 5 and 6, and Table 2).

Extensive geological research has examined the tectonostratigraphy and hydrocarbon potential of the IU and PU, particularly their Mesozoic and Cenozoic evolution. Key organic-rich intervals within the IU have been identified by multiple studies [27–29,36–41]. The tectonostratigraphic evolution of the IU is characterized by three major depositional sequences, each reflecting distinct tectonic regimes and conditions [24,42] (Table 2):

(1) Pre-rift sequence (Late Triassic – Early Jurassic): Characterized by platform carbonates, including the Pantokrator Limestones, which overlie Triassic evaporites via the Foustapidima Limestones of Ladinian-Rhaetian age [24,42]. Van Hinsbergen et al. (2020) suggested the presence of a rifting stage of the Ionian Unit between 235–200 Ma, supported by the presence of organic-rich layers found by Alexandridis et al. (2022).

(2) Syn-rift sequence (Pliensbachian – Tithonian): Deposited during extensional faulting and halokinesis of Triassic evaporites and carbonates, leading to the formation of the IB. This phase initiated internal smaller sub-basins with asymmetric half-graben geometries and varying carbonate thickness accumulations [24,42].

(3) Post-rift sequence (Early Cretaceous – Eocene): Formed after the extensional faulting ceased, marked by a synchronous Early Berriasian break-up event and an unconformity at the base of the pelagic Vigla Limestones [24,42]. However, a recent study by Bourli et al. (2019) interpret this phase as part of the syn-rift sequence.

This Mesozoic carbonate succession transitions into synorogenic siliciclastic turbidite and flysch deposits, which began accumulating during the Eocene-Oligocene in the IU [24,42]. Until Early Miocene the Ionian basin was filled with submarine fan deposits in response to the movement of Pindos thrust on the east, compressional structures, and deformation of the External Hellenides which migrated westwards, and uplift of the HFTB, with a foreland basin developed at the edge of the Apulian microcontinent [24,42,44–47].

Karakitsios (1995) identified four organic-rich rift-related intervals within the Ionian Unit, corresponding to distinct Mesozoic rifting phases: Late Triassic – Early Jurassic, Early – Mid Jurassic, Mid – Late Jurassic, and Early Cretaceous.

Table 2. Summarizing chronostratigraphic table of the main Units; Sazani, Pre-Apulia (PU), and Ionian (IU) units. "H" represents the HFTB and "A" the Albanides FTB.

	Time/Tectonic event	Sazani (A)	Pre-Apulia (H)	Ionian (H/A)
	Late Pliocene – Pleistocene	Erosion [25,48]	Initial activity of Pre-Apulian thrusts [27,33,49]	Post-Alpine sediments (H), Erosion (A) [25]
	Pliocene	Erosion [25]	**Marine** marlstones and sands [27]	**Deltaic – continental** clastcs (Pebbles, Cobbles, conglomerates) (H) [28,50]
	Early Pliocene	Turbidites [25]		Initial activity of the Ionian thrust [27]
	Messinian	Calcareous sandstones & turbidites [25]	Parts of evaporites [27]	Evaporites (H) [28,50], molasse and local emersion (A) [25,48]
Tectonic uplift and instability [17,25]	Burdigalian - Serravalian	Shortening, inversion of the Ionian Basin [25,27]		
	Miocene	Calcareous sandstones [25]	Deepening - **Marine** marlstones and marly limestones [27]	**Deltaic – shallow marine** successions of sandstone marlstone/shale with benthic fauna (H) [50] Local emersion (A) [48]
	Aquitanian	Compression (A, H) [50] and emersion (A) [48]		
	Oligocene	**Shallow marine** carbonates [25]	**Slope** limestones with breccias, often marly + hiatuses and emergent areas – general tectonic instability [27,32]	Deep water fan system deposits of sandstone/siltstone/mudstone alternations (flysch) (A and H) [26,50–52] with Late Cretaceous – Eocene limestone clasts, and local emersion (A) [48] & organic-rich layers (H) [50]
	Paleocene - Eocene	Platform carbonates and emersion [25]	Pelagic carbonates [25]	**Slope to deep marine** carbonates [25,42]
	Late Cretaceous – Early Eocene	Apulia microplate - Eurasia plate collision [25,53]		
	Late Cretaceous	**Mainly platform** carbonates [25]	**Pelagic** homoclinal ramp limestones and breccias limestones [25,27,32,42]	Micritic, clastic and bioclastic slope - deep **marine** limestones with chert nodules and debris flows (H) [26,42,50,51] deep marine micritic and detrital limestone (A) [48]
	Early Cretaceous (post-rift)	**Mainly platform** carbonates [25]	**Rimmed platform** limestones with cherts, brecciated upwards, + hiatuses [27]	**Deep marine** carbonates (cherts, shales, siliceous limestone, marlstones, dolomites, clays) (H) [26,51]/ Deep water carbonate deposition with bituminous clays (A)[48,52,54]
	Berriassian			Syn-rift cessation, post-rift deposition [25,27,42,50]
	Mid - Late Jurassic (syn-rift)			Deep water carbonates and shales [25]
	Early Jurassic (syn-rift)	Limestones and dolomites [55]	Limestones, marly limestones, cherts, anhydrites, shales [27,50]	**Deep wate**r cherts, diatomites, siliceous marlstone and limestone, clay (H) [26,51] (marls with some pyrite) (A) [24,50–52]
	Pliensbachian			Syn-rift extension [24,25,27,50,51]
	Late Triassic – Early Jurassic	Dolomites [25]	Shallow restricted conditions [42]	**Shallow marine** sedimentary rocks (A) [56] and evaporitic lagoonal settings [54]/ shallow marine to peri-tidal lagoonal settings(H) and organic-rich layers [28,42]
	Triassic		Evaporites, dolomites, shales [27]	

2.3. Geological overview of the Mesozoic organic rich intervals

2.3.1. Late Triassic – Early Jurassic

During the Triassic, the IU was dominated by evaporite deposits, up to 2000 m thick, with alternations of anhydrites and shales evident in the PU [24]. The Late Triassic – Early Jurassic organic-rich interval, part of the Pantokrator formation, forms the pre-rift sequence of the IU and is described as a set of carbonate platforms of various sizes and shapes [50].

This interval has been previously characterized as carbonate-rich hosting calcareous algae and benthic foraminifera in tidal and restricted environments as inferred from the presence of algal stromatolites, codiacean algae, and pellets [24,28,42,57]. Alexandridis (2022, 2023) identified Rhaetian-Sinemurian Pantokrator neritic carbonate depositional facies within the Souli Basin, encompassing black bituminous limestones in deeper water settings and shale intervals in coastal lagoon environments. These organic-rich intervals are linked to a worldwide Oceanic Anoxic Event (OAE), attributed to volcanic activity in the Central Atlantic Magmatic Province (CAMP), which caused water column stratification and anoxic conditions [28] with a uniform organic-rich layer extending from Greece to Albania and Italy [28].

Reducing, silled environments are particularly prominent during the Triassic – Jurassic transition, as observed by Zappaterra (1994) and Alexandridis et al. (2022). The organic-rich interval was classified as Type IIS kerogen, indicative of deposition in an anoxic, lagoonal setting [28]. The carbonate platform extended from the PU to the GU, with the Pre-Apulian Unit dominated by evaporites, dolomites, black shales, and limestones [24], as observed in the well Paxi-Gaios-1x (PxGa-1x) well.

2.3.2. Early – Mid Jurassic

The Pliensbachian marks the likely rift initiation and the formation of the Ionian basin (IU), with the Pliensbachian – Toarcian interval representing the rift climax phase [59]. This structural differentiation led to smaller paleogeographic units with half-graben geometries, evident by varying syn-rift formation thicknesses [17,51]. This interval includes the Lower Posidonia beds (Toarcian – Aalenian) and is linked to the Toarcian OAE (T-OAE), which has been correlated with the syn-rift sequence [24,60]. Posidonia shales or beds have been widely used to describe shaly/cherty formations of Early – Mid Jurassic age in the IU. They are characteristic of this Early

– Mid Jurassic interval and are the most extensive siliciclastic, clay-rich layer within the Late Triassic – Eocene carbonate succession, reaching over 150 m in thickness [28,50].

This organic-rich interval is mainly composed of fissile black shale, typically laminated and organic-rich, laminated mudstone with thin limestone beds, black chert beds, Posidonia shells, ammonites and nannofossil assemblages [17,28,50]. The restricted subbasins promoted euxinic conditions and water stagnation, favouring the deposition of organic-rich intervals with planktonic or nektonic organisms [17,24,27]. Kafousia et al. (2014) geographically linked neighbouring intervals of the same age to the T-OAE.

Existence of mass transport complexes and coarse-grained carbonate cherts are found within organic-rich intervals of the IU, suggesting proximity to subaerially exposed blocks [50]. Posidonia shells potentially indicate alternating oxygenated and anoxic conditions, contributing to the preservation of OM [50]. Alexandridis (2022, 2023) has supported that this formation was deposited in distinct, tectonically controlled sub-basins, under oxygen-deficient and occasionally iron-lean conditions.

This interval is often characterized by black, grey, blue and brown shales, often carbonaceous, transitioning upwards into black bedded chert, limestone and shale. Kafousia et al. (2014) proved fluctuating $CaCO_3$ between 4–42 wt% in the Toka section (Internal IU). In the central IU, Petousi and Chionistra sections, $CaCO_3$ range between 2.6–55 wt% and 20–70 wt% respectively.

The wedge-shaped geometry of these beds is consistent with half-graben basin dynamics, supporting continuous sedimentation and organic matter preservation [22,24,28,42,57,60,61]. However, global climate perturbations leading to sea level changes, erosion, sea water salinity and stratification might also have affected the deposition of this interval. During this period, the PU was dominated by limestones, alternating with anhydrites and shales [24].

2.3.3. Mid – Late Jurassic

The Mid – Late Jurassic interval includes the Upper Posidonia beds of the IU, considered part of the syn-rift sequence [17,29,51], though Alexandridis (2023) suggested these beds were deposited in a late syn-rift to post-rift setting. The Upper Posidonia beds are often indistinguishable from the Lower Posidonia beds [17,29] and are primarily composed of bedded chert containing radiolaria, silicified shale, pelagic limestone, and clay beds, along with Posidonia shells [28,51].

In the IU, the absence of detectable OM has been attributed to lithological composition, with the oxidation of OM due to meteoric water circulation [50]. In the PU, the interval is marked by white chalky limestones, dolomite intercalations, and rare cherts, with organic-rich black shales. Planktonic species, benthic foraminifera, and algal species indicate a depositional environment ranging from pelagic to slope and neritic respectively [24]. Subsidence during the Late Jurassic led to the deposition of organic-rich intervals in the PU [22,51,57].

2.3.4. Early Cretaceous

The Early Cretaceous Vigla organic-rich intervals are part of the post-rift sequence and correlate with the Paquier OAE (OAE1b) of Early Aptian and Bonarelli OAE (OAE2) of Cenomanian – Turonian age [17,42,51,62,63]. These deposits mark the cessation of extensional faulting [24,50] and are believed to have been deposited synchronously throughout the Ionian basin, with differential subsidence during deposition likely due to continued halokinesis of the basal evaporites.

Within the IU, the Early Cretaceous holds similar lithological composition to the Upper Posidonia beds [50], consisting of limestone, chert, clay, and shale, and is deposited under pelagic carbonate conditions [17,28,29,51,57]. This interval is rich in planktonic organisms like calpionellids, radiolarians, and globotruncanes [42]. The organic-rich interval varies in thickness from a few meters to 60 m, as seen in the Elataria section (Aptian – Turonian) [50], dating between Aptian – Turonian as suggested by radiolaria and globotruncanids. Thickness variations are likely caused by continued halokinesis of the basal evaporites [51,64].

In the PU, Early Cretaceous deposits are composed of limestones and dolomites. The facies are described as less pelagic compared to the IU [24] according to algal species found (Thaumatoporella sp.), cropping out only in Kefalonia island [17,24]. In the younger layers, planktonic foraminifera and rudist fragments suggest intra-platform basins characterizing the slope between Apulian platform and Ionian basin [17,24].

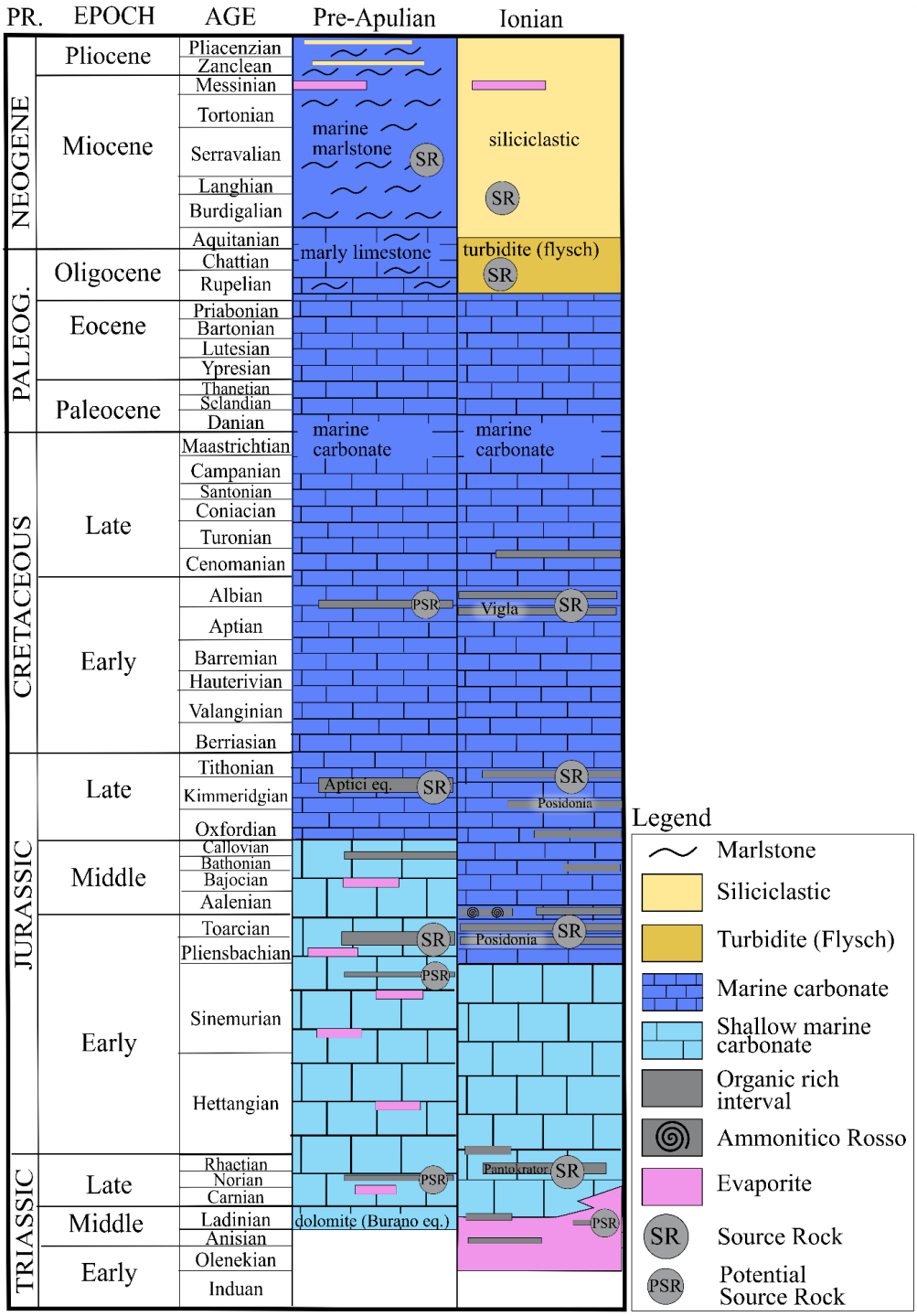

Figure 6. Simplified time-proportional stratigraphic column of the PU and IU in Western Greece as presented by Makri et al. (2024). The PU section is primarily based on the PxGa-1x well from Paxi island, the only source of Jurassic data for this Unit. Equivalent intervals in Italy are marked as "eq". The columns synthesize information from relevant literature, i.e. [18,27,28,66–70].

2.4. Geochemical overview of the Mesozoic organic rich intervals

Several source rock intervals have been identified as organic-rich with proven hydrocarbon generation potential [24,27–29,37,50,51,71,72]. The key Rock-Eval parameters of the literature data are presented in Table 3 and Figure 7. The former, also includes the maximum TOC for the equivalent source rocks in the Albanides.

Figure 7 shows that the thermal maturity of these intervals (Triassic – Oligocene) ranges from immature to oil window. The following chapters focus on the four Mesozoic organic-rich intervals, detailed in the next table.

Table 3. Table of the main Mesozoic organic-rich intervals in Western Greece from the IU and PU, highlighting their key RE characteristics. "No"; the number of samples considered, "avg"; average value. A minimum HI of 50 mgHC/gTOC and a maximum OI of 200 mg CO_2/gTOC were applied to exclude weathered samples.

Age	No	S1 (mgHC/ grock)		S2 (mgHC/ grock)		Tmax (°C)		TOC (wt%)		HI (mgHC/ gTOC)		Ker. type	Lithologies	Ref.	TOC max (wt%)
		max	avg	max	avg	max	avg	max	avg	max	avg				IU Albanides
Early Cret.	458	18.7	0.7	174.1	11.08	541	432	26	2.4	1186	347	II	Shale, chert, marlstone & siltstone	[50,51,73–75]	27 [48]
Mid-L. Jurassic	38	21	3.7	170.3	32.7	481	427	38.2	11.7	445	242	II - III	Shale, chert, marlstone & siltstone	[50,51]	9.4 [48]
Early Jurassic	376	29.2	0.96	207.8	17.55	460	422	42.6	3.7	1160	434	I-II	Shale, marlstone & mudstone	[29,50,51,73,76]	3.7 [48]
Late Tr.-E. Jur.	61	5.1	0.88	265.6	54.45	460	424	38.7	8	790	482	I-II/IIS	bituminous shales & marlstones	[28,50,51,76,77]	52 [25,48,52]

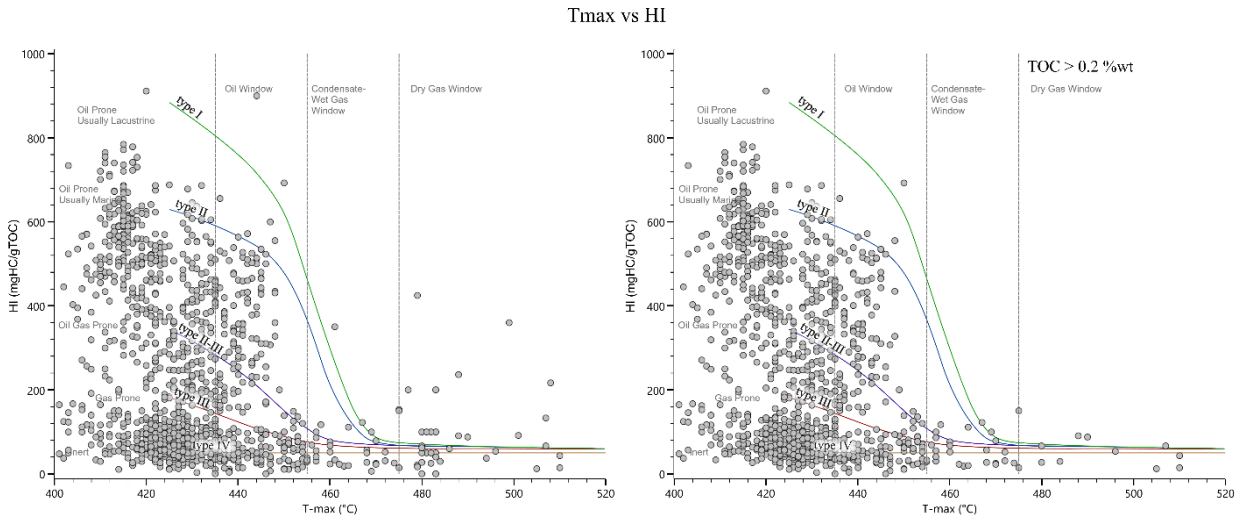

Figure 7. HI vs. Tmax for literature Triassic – Pliocene samples, modified from Hackley and Lünsdorf (2018). Left: All samples. Right: Samples with a minimum TOC threshold of 0.2 wt%.

2.4.1. Late Triassic – Early Jurassic

Organic petrography of the Late Triassic – Early Jurassic Pantokrator shales from Souli Mountain shows liptinite dominance, mainly as bituminite and alginite, with solid migrabitumens, rare primary and recycled vitrinite, and common framboidal pyrite [28,50]. Frequent migrabitumens suggest organic matter maturation, with kerogen types primarily I and II/IIS [28,50].

GC-MS analysis by Alexandridis (2023) indicates a carbonate/evaporite-rich, clay-poor, and saline depositional environment with strong reducing and euxinic conditions, likely a stratified, not spatially-restricted lagoon, a conclusion also supported by Curi (1993). Abundance of aromatic steroids and hopanoids indicates that the initial oil/bitumen mostly originated by eukaryotic algae and was not generated solely from prokaryotic microbial biomass [50], analogous to formations in Albania and Italy [28,50].

As shown in Table 3, TOC values reach nearly 39 wt%, with elevated sulfur content [50]. Tmax distribution (Figures 8 and 9), peaks in the internal IU at greater depths, while in central Ionian outcrops the values (415–431 °C) indicate thermal immaturity. Bitumen reflectance data [50] further support this, with a mean reflectance of 0.55 %VRE aligning with Tmax (approx. 417 °C) for the mainly immature central IU samples.

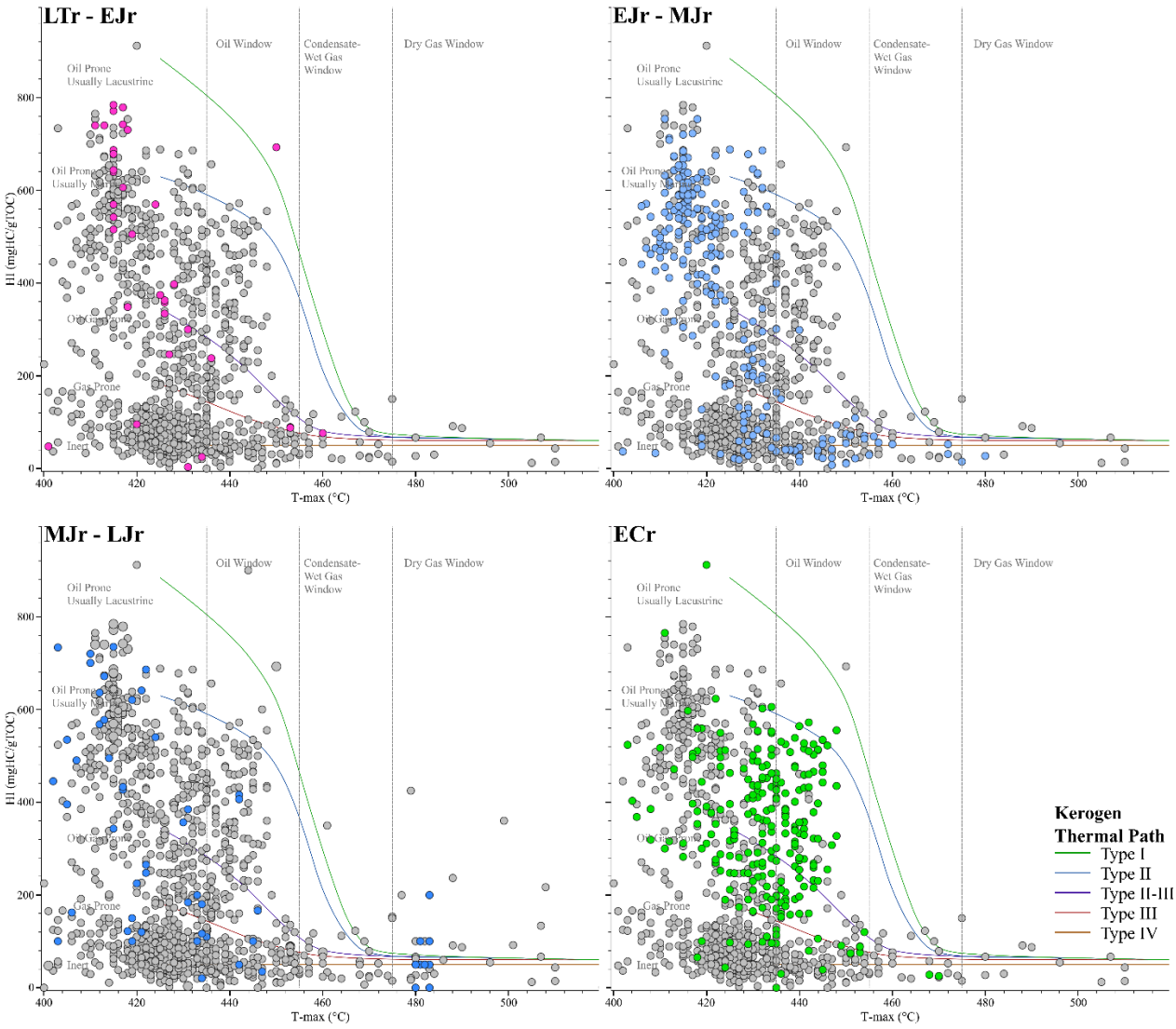

Figure 8. HI (mgHC/gTOC) vs. Tmax (ºC) for all literature samples. LTr – Elr; Late Triassic – Early Jurassic, EJr – MJr; Early – Mid Jurassic, MJr – LJr; Mid – Late Jurassic, ECr; Early Cretaceous. A minimum TOC threshold of 0.2 wt% is applied. Legend applies to all the subplots.

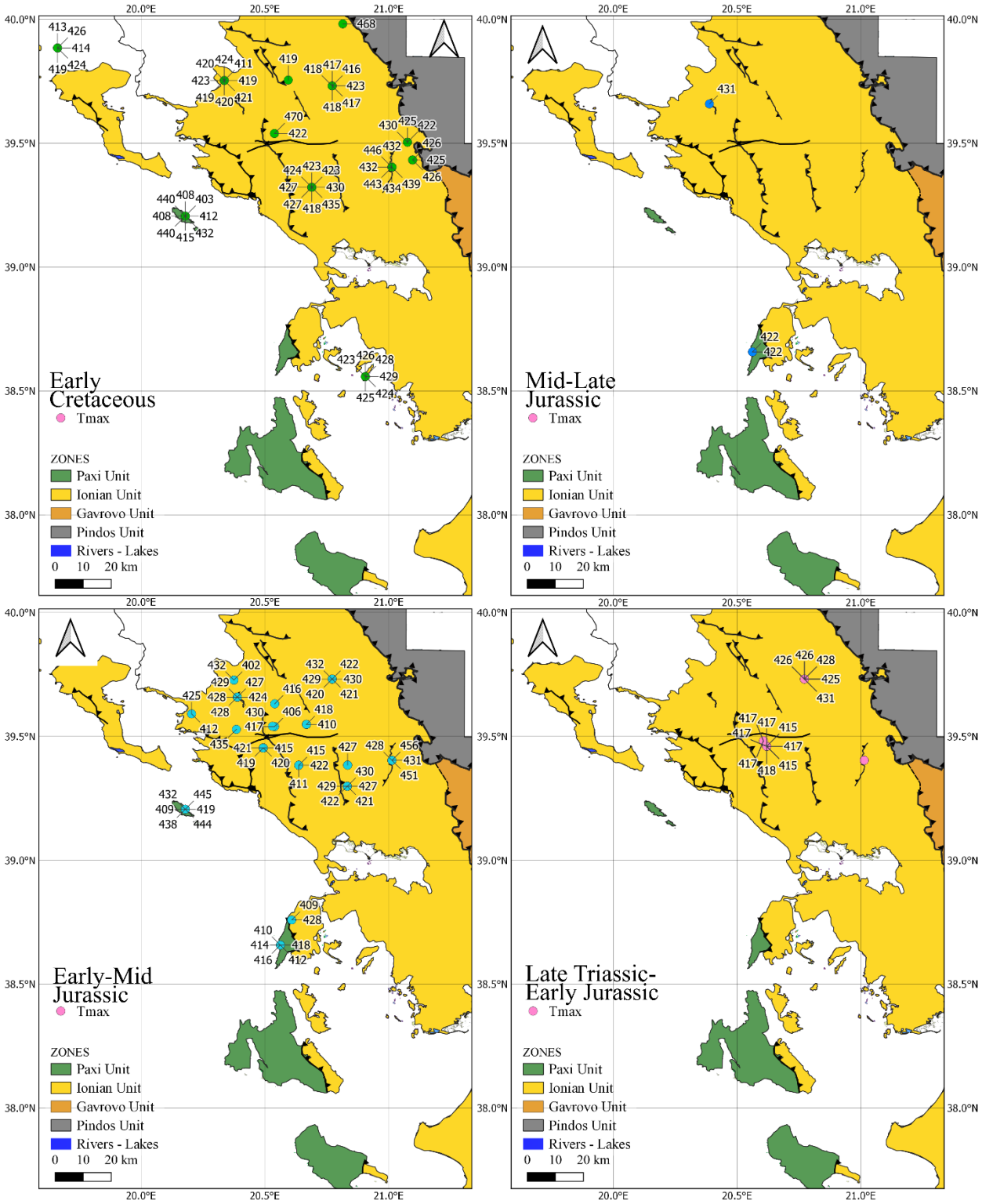

Figure 9. Tmax (°C) distribution of (Bottom right): Late Triassic – Early Jurassic, (Bottom left): Early – Mid Jurassic, (Top right): Mid – Late Jurassic, (Top left): Early Cretaceous samples from the literature.

2.4.2. Early – Mid Jurassic

The Lower Posidonia (Lower – Mid Jurassic) organic-rich intervals of the IU are considered the most significant source rocks in Western Greece [17,24,27,29,51,60], with thicknesses varying from 10 to 150 m [17,24].

Organic petrography [50] of the Elataria organic-rich samples (central IU) reveals abundance of sporinite, alginite, liptodetrinite, and large resinite particles, with common framboidal pyrite, indicating mainly Type II and I kerogens. Several studies [51,73,79] also report abundant amorphous organic matter (AOM) in both the PU and IU, with the latter showing liptinite macerals, traces of vitrinite, and inertinite; typical of Type I and II kerogens.

TOC values range between 0.21 and 42.60 wt% in the IU, while in the PU (PxGa-1x well), TOC varies from 0.21 to 23.08 wt%, with kerogen types mainly II-III [17]. In Italy, TOC values reach 8 wt% [80,81].

GC-MS analyses show Pr/Ph ratios in the IU peaking at 2.6, with organic-rich samples from the AY-3 well peaking at approximately 1 and the IO-1 well at approximately 1.7 [27,29,51], indicating predominantly anoxic conditions under normal salinity [50]. The PU (PxGa-1x well) exhibits Pr/Ph values of 0.54–1.20, while the maximum CPI is nearly 6, averaging 1.67 [27,29,51]. C27/C29 sterane ratios (0.35–5.10) in the IU (Figure 10) suggest a predominantly open marine environment. Most samples show low pregnanes, characteristic of carbonate hypersaline, clastic-starved settings [82–84]. The C21/C29 steranes range from 0.03–0.72, with higher values (> 0.5) in Dragopsa-1 and AY-3 wells [29,51]. Geological, biomarker, and petrographic data indicate marine depositional settings with minimal terrestrial input for the IU and likely the PU [50,51,73]. Thermal maturity varies widely, with Tmax values of 402–457 °C for the IU and 403–480 °C for the PU (Figure 9).

Bitumen reflectance (approx. 0.55 %VRE) aligns with immature Tmax readings in the IU [50]. Additionally, the C20+C28)TAS/((C20+C28)TAS+C29MAS) ratio ranges from 0.14–0.87 [29,51] with IO-1 and Dragopsa-1 samples showing lower values, while AY-3 peaks at 0.87. The C20/(C20+C28) TAS ratio varies from 0.13–0.88, with values above 0.64 in AY-3 and Dragopsa-1 (indicating peak maturity) and below 0.24 in IO-1 (indicating immaturity) [29,51,85].

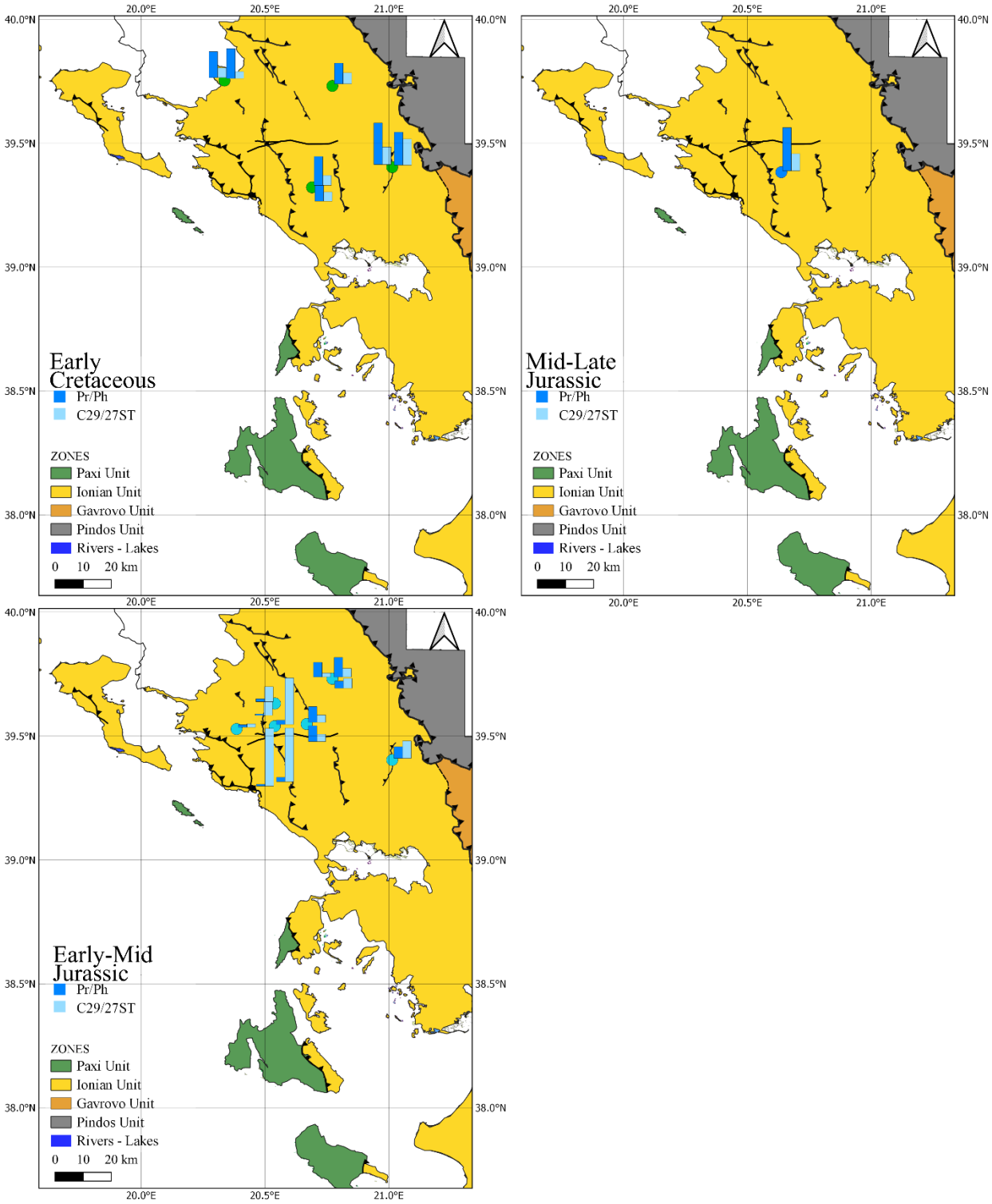

Figure 10. Distribution of Pr/Ph and C29/C27 Sterane of (Bottom left): Early – Mid Jurassic, (Top right): Mid – Late Jurassic, and (Top left): Early Cretaceous literature samples [51].

2.4.3. Mid – Late Jurassic

Organic petrography of Mid – Late Jurassic organic-rich samples, conducted by Oikonomopoulos et al. (2023) reveals mix of vitrinite (Type III kerogen) with a slightly grainy texture, solid bitumen, migrabitumen, spherical hydrocarbons, matrix bituminite, and faunal inertinite (Type IV kerogen). Vitrinite reflectance (0.59 %Ro) indicates early maturity at the onset of the oil window (approx. 0.60 %Ro). UV excitation highlights alginite and hydrocarbon spheres with greenish-yellow fluorescence, olive-green fluorescing bitumen, and dull-yellow, fracture-filling migrabitumen [86], consistent with Alexandridis (2023) who identified Type II-III kerogens.

TOC content ranges from 1 to 3.3 wt% in the IU and 0.6 to 11.2 wt% in the PU [17], comprising one of the best source rocks in the IU [17]. Thermal maturity data suggest the IU is thermally immature (Figure 9), with low MAS, TAS ratios [29,51,85], and Tmax values up to 431 °C [17,29]. Biomarker data, available only for the IU, show Pr/Ph ratios ranging from 0.2 to 1.5 (Figure 9), with the lowest values recorded in northernmost samples [76]. Higher Pr/Ph samples exhibit low C27/C29 sterane ratios, indicating a transitional environment (Figure 10).

2.4.4. Early Cretaceous

Organic petrography studies on Early Cretaceous organic-rich intervals in the IU (AY-3 well) by Foscolos (1989) and Rigakis (1999) identified abundant liptinite, including tasmanales marine algae, dinoflagellate cyst traces, and amorphous fluorescing matrix, with minor vitrinite and inertinite. In the PU (PxGa-1x well), Rigakis (1999) reported AOM reaching 55%, with exinite and vitrinite comprising up to 60% of samples.

Alexandridis (2023) analyzed IU outcrop samples (Epirus region), finding alginite, alginate colonies, and migrabitumen, with AOM dominating, and algae and exinite as main components [29,51]. Similarly, outcrops in Sistrouni and Gotzikas contained up to 99% AOM with traces of vitrinite and inertinite [51]. These studies confirm Type II kerogen, derived from marine organisms (phytoplankton, zooplankton, and bacteria) in a reducing, low-terrestrial-input environment. A recent study [86] also identified Type III gas-prone kerogen, two types of solid bitumen, oil-prone liptinite (Type II), and Type IV inertinite, with UV excitation revealing highly oil-prone marine telalginite (golden-yellow fluorescence), liptodetrinite, and weakly fluorescing amorphous matrix. TOC values reach 26 wt% [17,29] similar to age-equivalent Albanian intervals.

GC-MS analysis [29,51,88] indicates Pr/Ph values of 0.13-2.89 in IU samples (Figure 10), averaging 1.17, with AY-3 well samples exceeding 2. The IU gammacerane ratio remains below 0.15 [37,51]. C21 steranes are low in both PU and IU samples. C27/C29 sterane ratios suggest a carbonate to mixed marine setting under low salinity, dysoxic conditions [89].

Tzortzaki et al. (2013) identified isorenieratane derivatives (PSB biomarkers) in Aptian – Albian IU outcrop samples near the Greece-Albania border, indicating coexisting chemoautotrophic archaea and photoautotrophic bacteria in a euxinic ocean during the Paquier Event. Isotopically enriched monocyclic isoprenoids of putative archaeal origin [63,90] suggest anoxic conditions during OAE1b [91] and d intermittent photic zone euxinia (PZE) due to restricted basin connectivity. This supports a mixed autochthonous and allochthonous organic matter origin [92].

Thermal maturity ranges from immature to late mature, with Tmax values reaching 468 °C. Alexandridis (2023) reported abundant bb steranes and equilibrated C22-isomerization, while C20+C28)TAS/((C20+C28)TAS+C29MAS) values range from 0.03 to 0.79, with < 0.10 in Sistrouni and PxGa-1x [29,51]. Similarly, C20/(C20+C28) TAS ranges from 0.14 to 0.65, with Sistrouni and PxGa-1x below 0.15 [29,51]. These findings suggest thermal immaturity for the PU samples, with only two early mature samples, while IU samples show a broader maturity range, with AY-3 reaching 440 °C Tmax at depths higher than 2860 m [51].

Across Western Greece, internal IU wells (AY-3, EER-1) show higher maturity, while IU outcrops and PU well samples (PxGa-1x) remain thermally immature (Tmax < 435°C). Notably, this interval exhibits significant petroleum potential, reaching S2 of 183 mgHC/grock in Gotzikas, with an overall average of 11.5 mgHC/grock.

CHAPTER 3.

GENERATION KINETICS

Kerogen-specific kinetics are increasingly used to predict organic matter transformation under thermal stress, aiding in the understanding of paleodynamic settings and thermal evolution modelling [93–98]. This is essential for describing reaction rates and the time-temperature dependence of OM transformation [99,100].

Oil and gas transformation volumes in petroleum system and basin modelling rely on kinetic data from laboratory pyrolysis experiments [99–101], typically conducted on unweathered, thermally immature samples [100]. Pyrolysis kinetics are generally measured in open systems, though closed-system experiments have also provided valuable insights [102–106].

Hydrocarbon generation from kerogen follows first-order parallel reaction kinetics [107], where kerogen consists of components with varying thermal stabilities, reflected in different activation energies (Ea) and pre-exponential factors (A) [108–110]. Global kinetics, employing a fixed number of first-order reactions, are commonly used for modelling.

The transformation of kerogen involves overcoming an energy barrier, with reactions either absorbing heat and form weaker bonds (endothermic) or releasing heat and form stronger bonds (exothermic). The difference between the energy required for the forward and reverse reactions (heat absorbed or released) is known as enthalpy. OM transformation depends on time and temperature, with the reaction rate increasing exponentially with temperature, as described by the Arrhenius equation [111].

$$k = Ae^{\frac{-Ea}{RT}} \quad \text{(Equation 1)}$$

Where k is the reaction rate, A is the frequency factor in s^{-1}, Ea is the activation energy in kcal/mol, T is the temperature in Kelvin, and R is the universal gas constant in kcal/mol [111]. Kerogen breakdown occurs via multiple first-order reactions which are proportional to the decay products during open-system pyrolysis [112,113].

Due to the large number of individual reactions, bulk kinetic concepts are used to describe the transformation of kerogen into hydrocarbons. Non-isothermal heating rates (r = dT/dt) are used for pyrolysis, more accurately reflecting geological temperature increases compared to isothermal

heating [112]. All kinetic calculations are based on the discrete model [13,112,114] and consider the rate of bulk petroleum generation (dm/dT) (Equation 2).

$\frac{dm}{dT} = \sum_{i=1}^{n} k_i \times (M_i - m_i)$ (Equation 2)

Where ki is the overall reaction rate (Equation 1), Mi is the gross hydrocarbon potential and mi is the mass of generated petroleum [115]. Following the approach of Jüntgen and Klein [107] and Schaefer et al [110], which considers the integrated form of Equation 2 and the heating rate, the temperature-dependent rate of bulk petroleum generation (Equation 3) is given by:

$\frac{dm}{dT} = \sum_{i=1}^{n} M_i \times \frac{A}{r} e^{(-\frac{E}{RT} - \frac{A}{r} \times J_i)}$ (Equation 3)

$J_i = \int_0^T e^{-(\frac{Ea}{RT})dT}$ (Equation 4)

Where Ji is the integral of Ea over temperature [95].

The kinetic modelling in this study was performed using the Kinetics2015 software, which applies the discrete distribution model. This approach represents kerogen transformation as a set of parallel first-order reactions, each characterized by a specific activation energy (Ea) and fractional contribution to the total hydrocarbon yield.

Kinetics2015 optimizes the frequency factor (A) and the distribution of Ea values using a two-step regression process. An outer nonlinear regression loop adjusts the frequency factor, while an inner linear regression estimates the best-fit Ea fractions. The optimization proceeds until the sum of squared differences between measured and modelled pyrolysis curves is minimized.

However, this process can yield multiple local minima, or in other combinations of Ea and A that equally fit experimental data but diverge when extrapolated to geological heating rates. This is largely due to the compensation effect [116], in which variations in Ea are offset by changes in A, producing similar results under laboratory conditions but differing outcomes under natural maturation rates. Consequently, model calibration using multiple heating rates is advised to improve extrapolation robustness [95,107,117].

Two or more heating rate measurements (Figure 11) are essential for the modelling [100,102,118], though some studies suggest that one heating rate may suffice [119–122]. Peters et al. (2015) recommend evaluating the organic richness before selecting heating rates.

The type of OM is considered the primary factor influencing kinetic parameters. Ea-distributions indicate the breakdown of various bond types. With increasing temperature, kerogen converts to hydrocarbons based on activation energies, with lower Ea-groups converting to hydrocarbons at lower temperatures [98,123–126]. According to Petersen et al. (2010), a unique Ea-A pair cannot illustrate a specific kerogen type, age, or depositional environment.

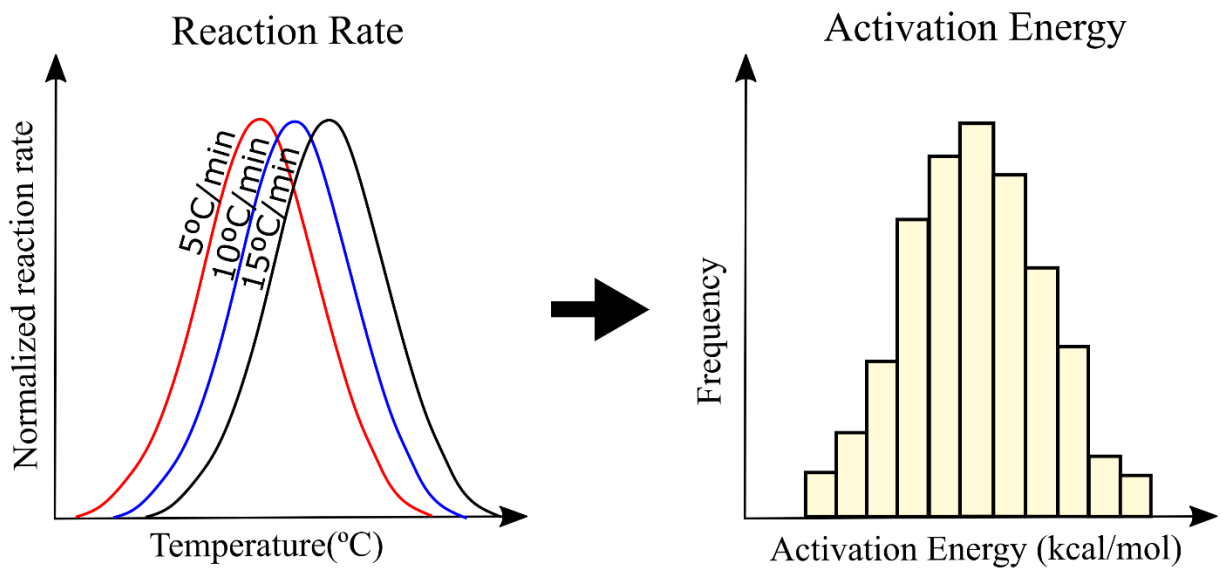

Figure 11. Pyrolysis curves for a single kerogen type at three heating rates (5, 10, and 15 °C/min) showing peak shift with increasing heating ramp rate (left), and the corresponding activation energy distribution (right) derived from kinetic analysis. This illustrates the transformation of experimental thermal data into a kerogen-specific kinetic model.

The type of OM influences kinetic parameters, with broad Ea-distributions indicating diverse OM sources, while narrow Ea-distributions suggest chemically homogeneous kerogen [94,95,98,106,115,127]. Kerogen with narrow Ea-distribution kerogen and one principal Ea decomposes more rapidly, over a narrow temperature range [98,128]. Most hydrocarbon generation occurs within narrow oil windows [98], with brackish and marine oils decomposing faster than freshwater oil shales [98].

Dembicki (1992) supported that OM type, mineral matrix, and organic content influence kinetic parameters. Sulfur-rich kerogens decompose at lower temperatures than sulfur-poor kerogens due to sulfur bonds cleaving more easily than carbon (C-C) bonds, leading to faster decomposition and lower Ea [98,105,113,124–126,129–131]. A 2 wt% TOC threshold is recommended for selecting representative samples to minimize mineral matrix effects [99,132]. Under natural thermal maturation (10 °C/Ma), Type IIS kerogen expels liquid hydrocarbons at 110–130 °C, while Type II kerogen (e.g., Woodford Shale) requires temperatures higher than 135°C [28,133].

The mineral matrix can also affect kerogen kinetics, with certain minerals catalysing thermal decomposition and decreasing Ea [93,105,127,134]. Clay minerals, such as kaolinite, montmorillonite, and illite [127,135–138], and iron-bearing minerals like pyrite and siderite, catalyse the hydrocarbon generation [139,140], while carbonate minerals have debating catalytic effects [135,137,138,141–143].

Kerogen isolation is sometimes omitted in kinetic experiments due to potential adsorption effects, which may distort results by influencing the behavior of generated compounds on the kerogen surface [144,145].

Alexandridis et al. (2022) analyzed kerogen kinetics in Late Triassic – Early Jurassic samples from Western Greece, identifying Type II and Type IIS kerogens. The S-rich Type IIS kerogens exhibited wide Ea-distributions of 39–62 kcal/mol, with a dominant peak at 52–53 kcal/mol, accounting for 80% of hydrocarbon generation. A low Ea tail suggests thermally reactive sulfur-bound kerogen [105,124]. The S-poor Type II kerogens displayed a broader Ea range (41-61 kcal/mol) with three principal Ea values contributing 72% of their generation potential [28].

In southern Italy, a study by Lehne and Dieckmann (2007) has focused on the generation kinetics of S-rich kerogens of carbonate source rocks, of the same age as the ones in Greece [28]. These samples according to Di Primio and Horsfield (1996) indicate hypersaline depositional environments with alternating subtidal and intertidal environments. Their findings align with the heterogenous OM and thermally reactive characteristics of sulfur-rich kerogens found in Greece, having an Ea-distribution between 40–60 kcal/mol and dominant Ea around 50–52 kcal/mol accounting for around 40% of the generation potential [146].

Understanding these kinetic behaviours is critical for interpreting the thermal evolution and petroleum potential of tectonically complex, redox-sensitive basins like those in Western Greece.

CHAPTER 4.
MATERIALS AND METHODS

4.1. X-ray fluorescence spectrometry (XRF)

Fifty samples underwent x-ray fluorescence to determine their elemental composition. Exemplary photos of samples that underwent these analyses can be found in Appendix I (Figures S1 and S2). The analyses followed a standard procedure. The samples were ground, and 1–4 g of the powdered sample was packed to a flat surface within a sample cup holder.

Measurements were performed with a Spectro Xepos bench-top XRF Spectrometer using X-Lab Pro 4.0 software and the Turbo Quant screening method. Excitation was achieved via a palladium (Pd) anode X-ray tube, operating under either helium gas flushing or ambient air atmosphere, as described in Hatzistavros et al. (2014) and Makri et al. (2024). The instrument featured three excitation modes and a silicon drift detector (SDD) [148]. Each sample was irradiated of 15 minutes.

Quantification was conducted using X-Lab Pro software (AMETEK) with glass tablet recalibration (FLX-S AMETEK). The results were refined through recalibration against standards from the International Atomic Energy (IAEA) and National Institute of Standards and Technology (NIST) [148]. The XRF measurements yielded elemental concentrations expressed in wt%.

4.2. X-ray diffraction mineralogy (XRD)

Mineralogical analyses were performed at the Department of Geology, University of Patras, using X-ray diffraction (XRD) on dry powder samples (–50 μm), as described by Makri et al. (2024). The measurements were conducted with a Bruker D8 X-ray diffractometer equipped with a LynxEye® detector. Qualitative and quantitative mineral phase identifications were caried out using EVA® and Topas® software, respectively.

4.3. Elemental analysis (CHNS)

Elemental analyses for carbon (C), hydrogen (H), nitrogen (N), and sulfur (S) were conducted on dry samples using a ThermoFisher Scientific FLASH 2000 Elemental Analyzer. Carbonate-bound carbon was removed prior to combustion through HCl treatment, and aliquots of 0.5–10 mg of

powdered material were analyzed. Combustion was carried out at 1100 °C, with system calibration performed using BBOT, sulfanilamide, and cystine quantitative standards. Elemental concentrations are reported on a dry, ash-free basis (d.a.f.).

4.4. Programmed open system pyrolysis - Rock-Eval 6

Rock-Eval analyses were performed using a Rock-Eval 6® (RE6) open-system pyrolizer (Vinci Technologies) [149,150]. Representative portions of finely ground (< 250 μm) bulk rock samples were analyzed following the bulk-rock method [151]. Sample quantities ranged from 2–5 mg for isolated kerogens and 50–70 mg for bulk rock analyses.

Pyrolysis was carried out under isothermal conditions, starting at 300 °C and increasing by 25 °C increments up to 650 °C. Oxidation followed at 300–850 °C at a heating rate of 20 °C/min. The analytical workflow is summarized in the workflow diagram in Appendix I (Figure S3).

The analysis determined key parameters: S1 and S2 (mgHC/grock) representing free hydrocarbons and hydrocarbons released from kerogen cracking, respectively; S3 ($mgCO_2$/grock) indicating CO_2 production; Tmax (°C) the temperature of maximum hydrocarbon generation; and TOC (wt%.) for total organic carbon content [15,150,152,153]. Hydrogen and oxygen indices (HI = 100 × S2/TOC and OI = 100 × S3/TOC) were calculated to evaluate organic content, kerogen type, and hydrocarbon potential (Tables 4 and 5).

In addition to the bulk-rock method, all samples were analyzed using RE6 under 3–4 heating rates for pyrolysis between 300–650°C.

Table 4. Rock-Eval 6 pyrolysis acquisition parameters.

Acquisition Parameters	Unit	Name
S1	mgHC/grock	Free hydrocarbons
S2	mgHC/grock	Oil potential
TpKS2	°C	Temperature of maximum S2 peak
S3	$mgCO_2$/grock	CO2 organic source
S3'	$mgCO_2$/grock	CO2 mineral source
S3CO	mgCO/grock	CO2 organic source
S3'CO	mgCO/grock	CO organic and mineral source

Table 5. Rock-Eval 6 calculated parameters.

Calculated parameters	Unit	Formula	Full Name
Tmax	°C	TpS2 – δTmax	Tmax
PI		$\frac{S1}{S1+S2}$	Production Index
PC	wt%	$\frac{\left((S1+S2)\times 0.83\right)+(S3\times 0.27)+((S3CO+\frac{S3'CO}{2})\times 0.43))}{10}$	Pyrolysable organic carbon content
RC CO		$\frac{S4CO\times 0.43}{10}$	Residual organic carbon (CO)
RC CO_2		$\frac{S4CO2\times 0.27}{10}$	Residual organic carbon (CO_2)
RC	wt%	RC CO + RC CO2	Residual organic carbon content
TOC	wt%	PC + RC	Total organic carbon content
HI	mgHC/gTOC	$\frac{S1\times 100}{TOC}$	Hydrogen Index
OI	mgCOs/gTOC	$\frac{S2\times 100}{TOC}$	Oxygen Index
PyroMINC	wt%	$\frac{(S3'\times 0.27)+(\frac{S3'CO}{2}\times 0.43)}{10}$	Pyrolysis mineral carbon content
OxiMINC	wt%	$\frac{S5\times 0.27}{10}$	Oxydation mineral carbon content
MinC	wt%	PyroMinC + OxiMinC	Mineral carbon content

4.5. Gas Chromatography-Mass Spectrometry (GC-MS)

Ground samples were extracted for 24 h using a Soxhlet apparatus with dichloromethane:methanol (DCM:MeOH, 90:10 v/v). The extract was de-asphalted using n-pentane (n-C_5), and the isolated maltenes were separated into saturated, aromatic, and polar (NSO) fractions via open-column chromatography. Separation employed 5 mL serological pipets packed with a mixture (5:2 w/w) of SiO_2 (100–200 mesh, 30 Å, Davisil type 923) and Al_2O_3 (70–230 mesh), using a 60:40 v/v toluene–methanol mixture for NSO compounds.

GC-MS analysis of saturated fractions was conducted on an Agilent 7890A GC coupled to a 5975E MS with an automatic liquid sampler. The GC was fitted with an Agilent HP-5MS UI capillary column (60 m x 250 µm x 0.25 µm). Saturated fractions were dissolved in n-hexane (0.5 mL) and

spiked with 15 µL of an internal standard mixture (Chiron S-4121-ASS-IO), containing n-Dodecane-d_{26}, Fluoronaphthalene, 3-Fluorophenanthrene, n-Hexadecane-d_{34}, 2-Fluorochrysene, and 5b(H)-Cholane.

The oven temperature program began at 40 °C (2 min), followed by a 20 °C/min ramp to 300 °C, and a final isothermal hold of 30 min for the saturate fraction. For the aromatic fraction, the final ramp reached 320 °C with a 20 min isothermal hold. The transfer line was set at 280 °C, and the MS source at 230 °C. The analytical procedure is summarized in Appendix I (Figure S4).

Normal alkanes, isoprenoids, steranes, and terpanes were identified based on selected ions, relative retention times, and mass spectra following literature [89,154–157]. The monitored ions included m/z 85 (normal alkanes and isoprenoids), m/z 217–218 (steranes), m/z 191 (terpanes), m/z 253 (monoaromatic steroids; MAS), and m/z 231 (triaromatic steroids; TAS) (Tables 6 and 7).

Table 6: List of recognized biomarkers of the saturated (aliphatic) fraction.

Acronym	Ion	Biomarker compound
n-C10	85	n-Decane
n-C11	85	n-Undecane
n-C12	85	n-Dodecane
n-C13	85	n-Tridecane
n-C14	85	n-Tetradecame
n-C15	85	n-Pentadecane
n-C16	85	n-Hexadecane
n-C17	85	n-Heptadecane
Pr	85	Pristane
n-C18	85	n-Octadecane
Ph	85	Phytane
n-C19	85	n-Nonadecane
n-C20	85	n-Eicosane
n-C21	85	n-Heneicosane
n-C22	85	n-Docosane
n-C23	85	n-Tricosane
n-C24	85	n-Tetracosane
n-C25	85	n-Pentacosane
n-C26	85	n-Hexacosane
n-C27	85	n-Heptacosane
n-C28	85	n-Octacosane
n-C29	85	n-Nonacosane
n-C30	85	n-Triacontane
n-C31	85	n-Hentriacontane

n-C32	85	n-Dotriacontane
n-C33	85	n-Tritriacontane
n-C34	85	n-Tetratriacontane
n-C35	85	n-Pentatriacontane
21Preg5a	217	C21 5a(H), 14b(H), 17a(H)-pregnane
21Preg5b	217	C21 5a(H), 14b(H), 17b(H)-pregnane
22Homopreg	217	C21 5a(H), 14b(H), 17b(H), 20-methyl pregnane
27badiaS	217	C27 13b(H), 17a(H)- diacholestane (20S)
27badiaR	217	C27 13b(H), 17a(H)-diacholestane (20R)
21Norchol	217	21 Norcholestane
28badiaSa	217	C28 13b(H), 17a(H), 24-20S methyldiacholestane a
28badiaSb	217	C28 13b(H), 17a(H), 24-20S methyldiacholestane b
28badiaRa	217	C28 13b(H), 17a(H), 24-20R methyldiacholestane a
28badiaRb	217	C28 13b(H), 17a(H), 24-20R methyldiacholestane b
27aaaS	217	C27 5a(H), 13a(H), 17a(H)-cholestane (20S)
27abbR	217	C27 5a(H), 13b(H), 17b(H)-cholestane (20R)
27abbS	217	C27 5a(H), 13b(H), 17b(H)-cholestane (20S)
27aaaR	217	C27 5a(H), 13b(H), 17b(H)-cholestane (20R)
29badiaR	217	C29 13b(H), 17a(H), 24-ethyldiacholestane (20R)
28aaaS	217	C28 5a(H), 14a(H), 17a(H)-methylcholestane (20S)
28abbR	217	C28 5a(H), 14b(H), 17b(H)-methylcholestane (20R)
28abbS	217	C28 5a(H), 14b(H), 17b(H)-methylcholestane (20S)
28aaaR	217	C28 5a(H), 14a(H), 17a(H)-methylcholestane (20R)
29aaaS	217	C29 5a(H), 14a(H), 17a(H)-ethylcholestane (20S)
29abbR	217	C29 5a(H), 14b(H), 17b(H)-ethylcholestane (20R)
29abbS	217	C29 5a(H), 14b(H), 17b(H)-ethylcholestane (20S)
29aaaR	217	C29 5a(H), 14a(H), 17a(H)-ethylcholestane (20R)
19tri	191	C19 tricyclic terpane
20tri	191	C20 tricyclic terpane
21tri	191	C21 tricyclic terpane
22tri	191	C22 tricyclic terpane
23tri	191	C23 tricyclic terpane
24tri	191	C24 tricyclic terpane
25triS	191	C25 tricyclic terpane (S)
25triR	191	C25 tricyclic terpane (R)
24tet	191	C24 17,21 - Secohopane / des-E-Hopane
26triS	191	C26 tricyclic terpane (S)
26triR	191	C26 tricyclic terpane (R)
25tet	191	C25-17,21 - Secohopane
28triS	191	C28 tricyclic terpane (S)
26tet	191	C26-17,21 - Secohopane
28triR	191	C28 tricyclic terpane (R)
29triS	191	C29 tricyclic terpane (S)

27tet	191	17,21 - Secohopane (C27)
29triR	191	C29 tricyclic terpane (R)
Ts	191	C27 18a(H)-22,29,30 Trisnorneohopane
TNH25,28,30	191	C27 17a(H),18a(H), 21β(H)-25,28,30-Trisnorhopane
27TNH1721	191	C27 Trisnorhop17(21)-ene
Tm	191	C27 17a(H)-22,29,30 Trisnorhopane
30triS	191	C30 tricyclic terpane (S)
30triR	191	C30 tricyclic terpane (R)
BNH28,30	191	17a(H), 18a(H), 21β(H)-28, 30-Bisnorhopane
TNH22,29,30,17b	191	17β(H)-22,29,30 Trisnorhopane
30HN1318	191	30-Norneohop13(18)-ene
29H	191	C29 - 17a(H), 21β(H)-30-Norhopane
29Ts	191	18a(H)-30-Norneohopane
30diaHop	191	C30 17a(H)-diahopane
30H1721	191	30 hop17(21)-ene
29Mor	191	17β(H), 21a(H)-30-Normoretane
Ole	191	18a(H)-Oleanane
30H	191	C30 - 17a(H), 21β(H)-Hopane
30NH1318	191	30 Neohop13(18)-ene
30Mor	191	17β(H)-, 21a(H)-Moretane
31SHH1721	191	C31 22S Homohop17(21)-ene
31RHH1721	191	C31 22R Homohop17(21)-ene
31abS	191	C31 17a(H), 21β(H)-30-Homohopane (22S)
31abR	191	C31 17a(H), 21β(H)-30-Homohopane (22R)
32HH1721	191	C32 Homohop17(21)-ene (22R) (coeluting with 31abR)
Gam	191	C30 Gammacerane
31Mor	191	17β(H), 21β(H)-30-Norhopane
32abS	191	C32 17a(H), 21β(H)-30,31-Bishomohopane (22S)
32abR	191	C32 17a(H), 21β(H)-30,31-Bishomohopane (22R)
	191	2-methyl-17b,21b-Bishomohopane
33abS	191	C33 17a(H), 21β(H)-30,31,32-Trishomohopane (22S)
33abR	191	C33 17a(H), 21β(H)-30,31,32-Trishomohopane (22R)
34abS	191	C34 17a(H), 21β(H)-30,31,32,33-Tetrakishomohopane (22S)
34abR	191	C34 17a(H), 21β(H)-30,31,32,33-Tetrakishomohopane (22R)
35abS	191	C35 17a(H), 21β(H)-30,31,32,33,34-Pentakishomohopane (22S)
35abR	191	C35 17a(H), 21β(H)-30,31,32,34-Pentakishomohopane (22R)

Table 6 Continued.

Table 7: List of recognized biomarkers of the aromatic fraction.

Abbreviation	Ion	Biomarker compound
C13AIP	133+134	C13 1-alkyl-2,3,6-trimethyl aryl isoprenoid
C14AIP	133+134	C14 1-alkyl-2,3,6-trimethyl aryl isoprenoid
C15AIP	133+134	C15 1-alkyl-2,3,6-trimethyl aryl isoprenoid
C16AIP	133+134	C16 1-alkyl-2,3,6-trimethyl aryl isoprenoid
C17AIP	133+134	C17 1-alkyl-2,3,6-trimethyl aryl isoprenoid
C18AIP	133+134	C18 1-alkyl-2,3,6-trimethyl aryl isoprenoid
C19AIP	133+134	C19 1-alkyl-2,3,6-trimethyl aryl isoprenoid
C20AIP	133+134	C20 1-alkyl-2,3,6-trimethyl aryl isoprenoid
C21AIP	133+134	C21 1-alkyl-2,3,6-trimethyl aryl isoprenoid
C22AIP	133+134	C22 1-alkyl-2,3,6-trimethyl aryl isoprenoid
C23AIP	133+134	C23 1-alkyl-2,3,6-trimethyl aryl isoprenoid
C24AIP	133+134	C24 1-alkyl-2,3,6-trimethyl aryl isoprenoid
C21 MAS	253	C21 Ring-C Monoaromatic steroid
C22 MAS	253	C22 Monoaromatic steroid
C20 TAS	231	C20 Triaromatic steroid
C21 TAS	231	C21 Triaromatic steroid
C27ßS + C27diaS MAS	253	C27reg 5b(H), 10b(CH3) 20S & C27dia 10b(H), 5b(CH3)20S
C27bR + C27diaR MAS	253	C27reg 5b(H), 10b(CH3) 20R & C27dia 10b(H), 5b(CH3)20R
C27aS + C28ßS MAS	253	C27reg 5a(H), 10b(CH3) 20S & C28reg5a(H), 10b(CH3)20S
C28ßS + C28Sdia MAS	253	C28reg 5a(H), 10b(CH3) 20S & C28dia5a(H), 10b(CH3)20S
C27aR MAS	253	C27reg 5a(H), 10b(CH3) 20R
C28aS MAS	253	C28reg 5a(H), 10b(CH3) 20S
C28ßR + C28diaRMAS	253	C28reg 5b(H), 10b(CH3) 20R & C28dia 10α(H), 5a(CH3) 20R
C29ßS + C29diaS MAS	253	C29reg 5b(H), 10b(CH3) 20S & C29dia 10β(H), 5b(CH3) 20S
C29bS MAS	253	C29reg 5α(H), 10β(CH3) 20S
C29bR MAS	253	C29reg 5a(H), 10β(CH3) 20R
C26S TAS	231	C26 20S Triaromatic steroid
C28aR MAS	253	C28reg 5a(H), 10a(CH3) 20R
C29aR MAS	253	C29reg 5a(H), 10a(CH3) 20R

4.6. Bulk generation kinetics

Bulk kinetic analyses were conducted using open-system pyrolysis to model activation energy (Ea) and frequency factor (A or FF). These parameters were determined using KINETICS2015 software (Lawrence Livermore National Laboratory) by minimizing errors between experimental and synthetic pyrolysis curves [94,95].

The S2 signal from each RE6 run were used as input after baseline subtraction in Matlab R2019b, based on initial and final pyrolysis points (300–650 °C). The discrete energy distribution model was applied with an Ea-spacing of 1 kcal/mol, preventing multiple minima [95,118,145]. The model fitted an average frequency factor, relative fractions, and Ea values for up to 500 parallel first-order reactions [89,90]. The A values ranged from 2e11 to 2e16 s^{-1}, following Pepper and Corvi (1995).

Error minimization between experimental and simulated curves was achieved through iterative linear regression and constrained non-linear regression using the Levenberg-Marquardt algorithm [95,158]. Three (1, 5, and 10 °C/min) to four (1, 5, 10, and 25 °C/min) heating ramps were applied per sample, depending on fitting precision. When S2 was < 1 mgHC/grock, the 1 °C/min rate was replaced with 3 °C/min due to low signal-to-noise ratios. The analytical workflow is illustrated in Appendix I (Figure S5).

4.7. Organic carbon isotope determination

For bulk organic carbon isotope determination, TOC-rich samples were first decarbonated by acidification using dilute HCl at room temperature to remove inorganic carbonates [159]. The residues were then rinsed, centrifuged, and dried. Approximately 0.1–0.3 mg of carbonate-free material was weighed into pre-cleaned tin capsules and analyzed using an elemental analyzer coupled to an isotope ratio mass spectrometer (EA–IRMS; Flash EA interfaced with a Delta Q IRMS system). The $\delta^{13}C$ values were calibrated against a urea working standard with $\delta^{13}C$ value of –35.46‰ VPDB (Vienna Pee Dee Belemnite Standard).

4.8. Kerogen isolation

Kerogen extraction followed established procedures [160,161] at the Palynology laboratory, University of Aberdeen. Samples were treated sequentially with:

- 40% hydrofluoric acid (HF), followed by sieving (10 μm nylon mesh) and pH neutralization.
- 40% hydrochloric acid (HCl) at 150 °C, followed by sieving and pH neutralization.
- 20% nitric acid (HNO_3), followed by final sieving and pH adjustment.

4.9. Palynofacies analysis

The organic residues obtained from chapter 4.8 were mounted on slides, and at least 300 palynomorphs were counted per sample to quantify the relative abundances of amorphous organic matter (AOM), phytoclasts (opaque and translucent), palynomorphs (sporomorphs) and degraded organic matter (semi-amorphous/DOM). Identification and classification of organic components followed the visual categories and terminology of Tyson (1995).

CHAPTER 5.
RESULTS

5.1. Mineralogy

5.1.1. X-ray diffraction (XRD)

XRD analysis (Table 8 and Figure S6) showed a dominance of carbonates. Late Triassic – Early Jurassic samples in the central IU were mainly dolomite-rich (78–93 wt%), except for the northernmost sample, which was silicate-dominated (98 wt%, including 62 wt% illite). Other samples contained 5–21 wt% silicates, with the lowest in the south. Early – Mid Jurassic samples contain 28-58 wt% calcite, with 39–41 wt% silicates and 1–2 wt% pyrite. Early Cretaceous well samples are also calcite-dominated, with 29–96 wt% calcite, in contrast to the silicate-rich outcrop samples.

The PU samples (PxGa-1x well and sample 1-19-LE), are carbonate-dominated, with calcite ranging from 57–99 wt% and minor dolomite ($\leq$ 2 wt%). Silicate content varies, with quartz reaching up to 35 wt% and illite/chlorite up to 26 wt%. Sulphides and sulfates are present in low amounts, with pyrite (< 1–2 wt%) and gypsum (up to 6 wt%), while anhydrite reaches 20 wt% in one sample, indicating evaporitic influence.

Table 8. Mineral content (in wt%) distribution from XRD analysis for the samples studied.

	Carbonates		Silicates			Sulph	Sulfates				Oxides		Other	
Sam.	Cal	Dol	Qz	Ill/Chl	Kfs	Py	Gy	Bas	Anh	Bar	Hem	Hl	Age	Well/ Outcrop
120KB	92	1	7	<1		<1							E. Cretaceous	AY-3
1KD	82	11	1	5		<1				1			E. Cretaceous	AY-3
2KD	78	4	18	<1		<1							E. Cretaceous	AY-3
4KD	54	21	3	18		3				1			E. Cretaceous	AY-3
5KD	95	5	<1										E. Cretaceous	AY-3
115KB	90	2	8										E. Cretaceous	AY-3
9KD	96	1	2	1		<1							E. Cretaceous	AY-3
10KD	45	2	38	13		1				1			E. Cretaceous	AY-3
11KD	55	4	30	10		1							E. Cretaceous	AY-3
12KD	62	3	29	5		1							E. Cretaceous	AY-3
111KB	79	1	20			<1							E. Cretaceous	AY-3
106KB	57	27	14	2		<1							E. Cretaceous	AY-3
95KB	29	47	20	4									E. Cretaceous	AY-3
3-17-CS			27	62	6	1		4					E. Cretaceous	outcrop
3-16-CS	14		61	24		1							E. Cretaceous	outcrop
30KD	91	1	8	<1		<1							E. Cretaceous	PxGa-1x
1-19-LE	57		10	26			6			1			Late Jurassic	outcrop
38KD	62		35	2		1						<1	Mid-Late Jur.	PxGa-1x
39KD	90		<1			<1			9			1	Mid-Late Jur.	PxGa-1x
44KD	82		16	1								1	Mid-Late Jur.	PxGa-1x
42KD	92	1	6			<1						1	Mid-Late Jur.	PxGa-1x
33KD	99		1			<1							Mid-Late Jur.	PxGa-1x
34KD	99	<1	<1	1									Mid-Late Jur.	PxGa-1x
35KD	98	1										1	Mid-Late Jur.	PxGa-1x
36KD	88		<1						11			1	Mid-Late Jur.	PxGa-1x
16KD	98	2	<1			<1							Early-Mid Jur.	PxGa-1x
20KD	99		1			<1							Early-Mid Jur.	PxGa-1x
22KD	98		1			<1						1	Early-Mid Jur.	PxGa-1x
47KD	79	<1	<1	<1	1				20				Early-Mid Jur.	PxGa-1x
52KD	80	14							5			1	Early-Mid Jur.	PxGa-1x
E38	58	<1	16	10	13	2				1			Early-Mid Jur.	outcrop
E28	56	<1	21	12	8	1	2			<1			Early-Mid Jur.	outcrop
F31	42	<1	13	28	11	2	2			1	1		Early-Mid Jur.	outcrop
B19	28	1	30	19	15	2	3			1	1		Early-Mid Jur.	outcrop
D17	38		19	19	23	1	1						Early-Mid Jur.	outcrop
D23	2	91	3	4									Late Tr.-E. Jur.	outcrop
E4		78	4	9	8		1						Late Tr.-E. Jur.	outcrop
C26	2		15	62	18					3			Late Tr.-E. Jur.	outcrop
7-21-J1	2	93	2		3								Late Tr.-E. Jur.	outcrop

5.1.2. X-ray fluorescence (XRF)

Major oxides and paleo-environmental proxies of Mesozoic formations in Western Greece (Table 9) indicate compositions primarily of CaO, SiO_2, MgO, and SO_3.

- Late Triassic – Early Jurassic: CaO (2.4–22.11 wt%), SiO_2 (4.33–31.18 wt%), MgO (1.22–9.12 wt%), SO_3 (1.6–10.32 wt%).
- Early – Mid Jurassic: CaO (16.96–45.02 wt%), SiO_2 (0.14–1.81 wt% in PU, up to 35.62 wt% in IU), MgO (0.57–2.41 wt%), SO_3 (0.54–8.74 wt%).
- Mid – Late Jurassic: CaO (24.47–44.27 wt%), SiO_2 (0.65–24.21 wt%), MgO (0.39–1.40 wt%), SO_3 (0.79–2.82 wt%).
- Early Cretaceous: CaO (23.70–42.53 wt% in AY-3, 1.90–9.27 wt% in external IU), SiO_2 (reaching 25.81 wt% in the internal IU, approximately 52 wt% in external IU), MgO (maximizing at 7.02 wt%), SO_3 (reaching approximately 4 wt%).

The results emphasize high CaO and SiO_2 contents with significant SO_3 concentrations, particularly in the Late Triassic – Early Jurassic and Mid – Late Jurassic. The Fe_2O_3 content is also notable peaking in the Early Cretaceous. The detailed XRF data can be found in Appendix II (Table S1), while the major oxides are presented in Table 9.

Table 9. Distribution of major oxides (in wt%) from XRF analysis for the studied samples, categorized by geological age.

Sample	Na_2O	MgO	Al_2O_3	SiO_2	P_2O_5	SO_3	K_2O	CaO	TiO_2	Fe_2O_3	LOI	Age
3-17-CS	0.53	1.84	9.28	52.35	0.27	3.98	2.55	1.90	0.69	3.90	12	E. Cretaceous
3-16-CS	0.25	0.50	3.10	52.07	0.23	1.47	0.72	9.27	0.16	1.21	10	E. Cretaceous
120KB	0.44	0.53	0.46	4.49	0.19	0.14	0.14	40.85	0.01	0.24	40	E. Cretaceous
118KB	0.38	0.58	0.56	4.09	0.09	0.11	0.16	40.65	0.02	0.25	41	E. Cretaceous
115KB	0.38	0.60	0.55	4.93	0.08	0.22	0.21	40.18	0.02	0.28	38	E. Cretaceous
1KD	0.68	1.72	1.81	4.71	0.48	0.93	0.82	36.11	0.12	0.70	40	E. Cretaceous
2KD	0.32	0.95	0.39	8.59	0.06	0.37	0.16	38.43	0.01	0.26	65	E. Cretaceous
4KD	0.97	3.08	4.55	11.77	0.80	1.98	1.98	28.94	0.26	1.56	36	E. Cretaceous
5KD	0.38	1.45	0.41	2.42	0.06	0.24	0.20	42.07	0.01	0.15	62	E. Cretaceous
9KD	0.42	0.63	0.95	3.53	0.06	0.30	0.43	42.53	0.04	0.38	61	E. Cretaceous
113KB	0.34	0.89	0.84	9.44	0.08	0.24	0.32	35.99	0.04	0.45	34	E. Cretaceous
10KD	0.37	0.81	2.73	32.24	0.11	0.99	0.89	23.70	0.14	1.14	23	E. Cretaceous
11KD	0.36	1.14	3.16	25.81	0.12	0.88	1.11	27.09	0.17	1.30	74	E. Cretaceous
12KD	0.32	0.91	2.00	23.55	0.09	0.53	0.69	31.06	0.10	0.82	72	E. Cretaceous
111KB	0.48	0.62	0.80	10.46	0.05	0.33	0.24	35.32	0.04	0.48	67	E. Cretaceous
109KB	0.38	1.63	0.89	8.45	0.07	0.24	0.28	36.86	0.04	0.51	36	E. Cretaceous
106KB	0.39	4.57	1.01	8.89	0.07	0.29	0.31	35.43	0.05	0.50	36	E. Cretaceous
104KB	0.37	4.03	1.09	9.71	0.06	0.35	0.39	35.91	0.05	0.63	36	E. Cretaceous
102KB	0.31	6.39	1.18	8.32	0.06	0.31	0.36	33.63	0.06	0.60	37	E. Cretaceous
100KB	0.32	6.35	1.30	8.53	0.05	0.32	0.38	32.96	0.07	0.65	37	E. Cretaceous
98KD	0.28	4.67	0.97	14.65	0.06	0.36	0.31	30.48	0.04	0.45	34	E. Cretaceous
95KD	0.28	7.02	1.08	12.77	0.06	0.40	0.30	27.95	0.04	0.49	35	E. Cretaceous
30KD	0.38	0.43	0.11	4.50	0.02	0.46	0.01	41.88	0.00	0.08	60	E. Cretaceous
1-19-LE	0.83	1.40	4.70	17.61	0.49	2.82	1.22	24.47	0.27	1.67	34	Late Jurassic
38KD	0.62	0.59	1.47	24.21	0.04	2.40	0.49	28.31	0.08	0.85	72	Mid-Late Jurassic
39KD	0.54	0.39	0.33	13.65	0.04	1.46	0.10	38.55	0.01	0.21	64	Mid-Late Jurassic
44KD	0.63	0.46	0.38	9.78	0.02	1.59	0.11	37.43	0.03	0.19	37	Mid-Late Jurassic
42KD	0.68	0.60	0.29	3.82	0.02	1.42	0.10	40.27	0.01	0.16	58	Mid-Late Jurassic
33KD	0.79	0.63	0.37	1.73	0.02	1.67	0.16	40.72	0.03	0.25	43	Mid-Late Jurassic
34KD	0.54	0.53	0.14	0.65	0.02	0.79	0.04	44.27	0.01	0.10	56	Mid-Late Jurassic
35KD	0.61	0.57	0.09	0.43	0.01	0.63	0.01	45.02	0.00	0.07	57	E-M. Jurassic
36KD	1.25	1.04	0.10	0.56	0.00	5.04	0.04	43.49	0.00	0.12	39	E-M. Jurassic
16KD	0.61	0.83	0.61	1.40	0.13	1.47	0.23	42.66	0.05	0.37	57	E-M. Jurassic
20KD	0.42	0.72	0.64	1.81	0.03	0.69	0.23	42.56	0.04	0.23	58	E-M. Jurassic
22KD	0.49	0.70	0.31	0.90	0.04	0.93	0.10	42.95	0.01	0.12	43	E-M. Jurassic
47KD	1.45	1.49	0.14	0.69	0.00	8.74	0.06	41.43	0.02	0.15	33	E-M. Jurassic
52KD	0.75	2.38	0.00	0.14	0.00	2.16	0.00	42.50	0.00	0.01	58	E-M. Jurassic
54KD	0.46	2.41	0.05	1.45	0.01	0.54	0.00	40.49	0.00	0.04	43	E-M. Jurassic
F31	0.36	1.60	6.26	25.83	0.06	2.30	2.25	22.86	0.45	2.85	25	E-M. Jurassic
B19	0.29	1.61	4.93	35.62	0.04	2.24	2.21	16.96	0.34	2.25	19	E-M. Jurassic
E28	0.37	0.93	3.97	24.69	0.05	1.33	1.59	27.50	0.26	1.77	28	E-M. Jurassic
E38	0.37	0.96	4.50	21.55	0.04	2.00	2.16	27.58	0.30	2.23	28	E-M. Jurassic
D17	0.24	1.21	7.53	31.18	0.05	1.60	3.50	17.22	0.52	2.51	80	E-M. Jurassic
D23	1.08	6.77	1.94	5.46	0.01	6.09	0.75	16.16	0.09	1.09	52	Late Tr-E. Jur.
E4	1.15	6.15	2.95	7.98	0.01	8.45	1.02	11.87	0.13	1.18	56	Late Tr-E. Jur.
C29	0.87	8.44	1.61	4.42	0.02	4.65	0.55	18.76	0.07	0.98	-	Late Tr-E. Jur.

C26	1.03	1.22	4.87	13.09	0.04	10.32	1.68	2.40	0.27	1.65	63	Late Tr-E. Jur.
7-21-J1	0.57	9.12	1.57	4.33	0.01	2.87	0.56	22.11	0.06	0.78	47	Late Tr-E. Jur.
57KD	0.45	15.36	0.15	0.52	0.01	1.15	0.02	27.47	0.00	0.06	45	Triassic
62KD	0.27	15.43	0.10	0.51	0.02	0.60	0.00	26.56	0.00	0.32	46	Triassic

Table 9 Continued.

5.2. Organic Geochemistry

5.2.1. Rock-Eval 6 analysis

The dataset includes Late Triassic – Early Cretaceous samples, with TOC levels varying across formations:

- Late Triassic – Early Jurassic: TOC reaches 35.56 wt% in central IU, decreasing to 2.20 wt% in the Early – Mid Jurassic. PU samples range from 0.20–4.60 wt%.
- Mid – Late Jurassic: TOC reaches 6.83 wt%.
- Early Cretaceous: TOC varies from 0.12–6.89 wt% in the Inner IU, 1.67–3.16 wt% in the external IU, and averages 1.10 wt% in the PU.

The S2 values indicate high hydrocarbon potential in the Late Triassic – Early Jurassic (reaching 202 mgHC/grock), declining in the Early – Mid Jurassic (up to 10 mgHC/grock in IU, 21.91 mgHC/grock in PU). Mid – Late Jurassic S2 increases to 24.13 mgHC/grock in PU. Early Cretaceous S2 varies widely (0.14–37.45 mgHC/grock in the IU). Tmax values suggest most samples are thermally immature or in early maturation:

- Late Triassic – Early Jurassic: IU outcrops range between 415–424 °C.
- Early – Mid Jurassic: Tmax ranges between 400 and 464 °C.
- Mid – Late Jurassic: maximum Tmax values are 419 °C in PU and 409 °C in IU.
- Early Cretaceous: Tmax peaks at 443°C in the AY-3 well but remains immature in the external IU.

HI and OI show significant variability:

- Late Triassic – Early Jurassic: maximum HI of 728 mgHC/gTOC and OI of 25 $mgCO_2$/gTOC.
- Early – Mid Jurassic: maximum HI of 455 mgHC/gTOC and OI of 26 $mgCO_2$/gTOC). PU wells range from 38–705 mgHC/gTOC (HI) and 4–317 $mgCO_2$/gTOC (OI).

- Mid – Late Jurassic: IU outcrops: maximum HI of 489 mgHC/gTOC and OI of 55 $mgCO_2$/gTOC. PU wells: HI (502–734 mgHC/gTOC), OI (16–48 $mgCO_2$/gTOC).
- Early Cretaceous: IU wells: HI (up to 544 mgHC/gTOC), OI (up to 482 $mgCO_2$/gTOC). PU wells: HI (up to 514 mgHC/gTOC), OI (up to 107 $mgCO_2$/gTOC).

5.2.2. Biomarker analysis

Saturate, Aromatic, Resin and Asphaltene (SARA) analysis

The solvent-extractable organic matter varies widely, from 590 to 51190 ppm (Table 10). Lower concentrations in the silicate-rich horizons of the Early – Mid and Mid – Late Jurassic suggest reduced OM preservation due to oxygen exposure. In contrast, carbonate-rich horizons of the Late Triassic – Early Jurassic and Early Cretaceous show higher extractable OM, likely due to improved preservation conditions in carbonate environments which can limit oxygen exposure and enhance OM preservation. The following saturate/aromatic ratios indicate early thermal maturity, aligning with Rock-Eval results, while bituminous samples range from mature to highly mature:

- Late Triassic – Early Jurassic: 0.11–0.68.
- Early – Mid Jurassic: 0.58–0.91 (IU outcrops), 0.20 (PU).
- Mid – Late Jurassic: 0.19–0.39 (PU), 0.82–1.04 (central IU outcrops).
- Early Cretaceous: 0.18–1.33, reflecting varied thermal maturity due to lithological and burial differences.

Higher saturate/aromatic ratios in carbonate-rich units and outcrop samples suggest better OM preservation, whereas lower ratios in siliciclastic horizons indicate more advanced degradation, consistent with maturity trends.

Table 10. SARA analysis results of the studied samples (sed.), showing the ppm of extract yield, and the percentage of maltenes (malt.) and asphaltenes (asph.) in the extract, and the percentage of aliphatic (saturated), aromatic, and NSO fractions in the maltene fraction.

Sample	mg/g sed.	Extract ppm	Malt. ppm	Malt. (%)	Asph. (%)	NSO (g)	Rec. (%)	Sat (%)	Arom (%)	NSO (%)
1KD	4.29	4290	1657.20	38.67	61.33	0.01	92	25	42	33
4KD	6.27	6270	1305.37	20.81	79.19	0.01	98	21	44	34
10KD	3.08	3080	1866.09	60.68	39.32	0.01	100	10	57	33
11KD	2.48	2480	1639.93	66.16	33.84	0.01	97	40	30	30
3-16-CS	0.59	590	259.63	44.12	55.88	0.01	93	11	25	64
91KD	6.28	6280	2494.56	39.71	60.29	0.01	90	62	13	25
1-19-LE	2.56	2560	896.89	35.02	64.98	0.01	93	6	18	77
38KD	9.63	9630	2922.72	30.36	69.64	0.00	100	17	44	39
44KD	7.29	7290	2170.62	29.76	70.24	0.01	100	16	54	30
33KD	7.80	7800	1008.96	30.94	69.06	0.01	100	9	48	42
B19	0.47	470	242.12	51.46	48.54	0.00	96	23	28	49
F31	0.68	680	419.39	61.45	38.55	0.00	92	28	27	46
E28	0.29	290	148.31	50.57	49.43	0.00	92	20	22	59
E38	0.80	800	557.39	69.95	30.05	0.01	80	18	31	51
22KD	3.96	3960	458.04	11.55	88.45	0.00	98	11	55	34
20KD	3.74	3740	1040.07	27.82	72.18	0.01	98	11	55	34
7-21-J1	12.18	12180	606.80	26.24	73.76	0.00	92	9	51	39
C26	51.19	51190	964.00	13.40	86.60	0.00	100	25	37	37
E4	45.22	45220	724.06	14.83	85.17	0.00	100	6	54	39
D23	30.93	30930	539.32	9.80	90.20	0.00	100	10	50	40

Aliphatic and Aromatic fractions

Gas chromatography-mass spectrometry identified biomarkers in the Mesozoic samples, providing insights into their biological precursors and paleodepositional environments. These biomarkers, minimally altered during diagenesis, reflect the source of the organic matter [89,163,164]. Representative chromatograms can be found in Figure 12, and related data in Table 11, while all chromatograms can be found in Appendix I (Figures S7 to S12).

Late Triassic – Early Jurassic samples display a bimodal n-alkane distribution (n-C22 and n-C28), transitioning to unimodal at n-C28, and further south peaking at n-C19. Pr/Ph consistently stays below unity, and nC27/nC17 ranges from below unity to 26.5. These samples are rich in C29aaaR sterane relative to C27aaaR, with moderate pregnanes, more 30H than 29H, abundant homohopanes > C31, and traces of gammacerane.

Early – Mid Jurassic IU samples have a unimodal peak at n-C18 (Pr/Ph averaging 1.3, nC27/nC17 averaging 0.2), while PxGa-1x samples peak at n-C22 and n-C24, with Pr/Ph averaging 0.7 and nC27/nC17 averaging 1.8. IU samples are richer in C29aaaR, while PxGa-1x has comparable

C27aaaR and C29aaaR steranes, with increased C30 steranes. Both regions show abundant 29H to 30H, with abundant homohopanes and tricyclic terpanes. Mid – Late Jurassic samples mainly peak at short-chain alkanes (n-C18), apart from the 1-19-LE sample, which peaks at n-C23 with abundant long-chain alkanes. The C29aaaR sterane dominates in the IU, while the PU samples are richer in C27aaaR. All show higher 30H compared to 29H, with abundant homohopanes.

Early Cretaceous samples display a unimodal distribution of n-alkanes, peaking at short-chain alkanes (Pr and n-C19). Internal IU samples are rich in C27aaaR and pregnanes, with more 30H than 29H and increased C31ab homologues. External IU samples show abundant C31ab homologues, 30H, and homohopanes. The biomarker profiles indicate variations in OM sources and depositional environments across different intervals in the study area.

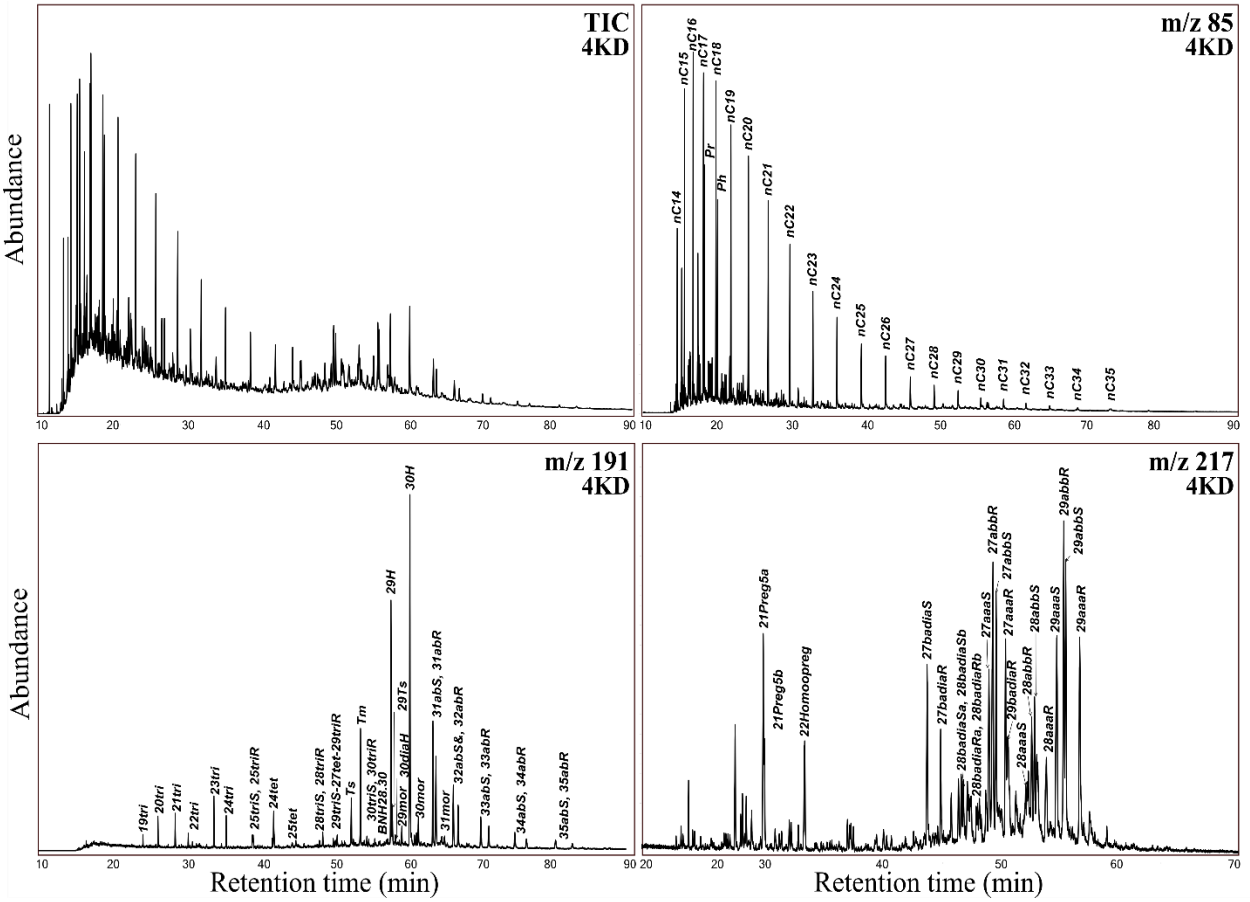

Figure 12. Exemplary mass chromatograms of the saturated fraction, for the 4KD sample of the AY-3 well. Top left; Total Ion Count, top right; ion m/z 85 illustrating the normal alkanes, bottom left; m/z 191 illustrating the hopanes, and bottom right; m/z 217 illustrating the steranes.

Table 11. Data on aliphatic (terpanes, steranes, hopanes) and aromatic biomarkers of different wells and outcrop samples.

		Well AY-3						Well PxGa-1x												
	Early Cretaceous					Late Jurassic		Mid - Late Jurassic			Early – Mid Jurassic						Late Triassic – Early Jurassic			
Terpanes m/z 191	3-16-CS	1KD	4KD	10KD	11KD	91KD	1-19-LE	38KD	33KD	44KD	22KD	20KD	B19	F31	E38	E28	7-21-J1	C26	E4	D23
19tri/20tri	0.31	0.35	0.35	0.37	0.14	0.40	0	0.81	0.49	0.80	0.60	0.77		0.56	0.33	0.38	0.39	0.31	0.32	0.42
22tri/21tri	0	0.19	0.17	0	0	0.69	0	0.85	0.57	0.89	0.94	1.27		0.34	0	0	0	0.27	0	0.18
24tri/23tri	0.64	0.62	0.57	0.63	0.47	0.59	0.66	0.35	0.48	0.31	0.26	0.19	0.69	0.39	0.63	0.49	1.13	1.15	2.16	0.96
24tet/23tri	0.25	0.21	0.16	0.25	0.13	0.41	0.43	0.15	0.08	0.08	0.07	0.05	0.25	0.07	0.55	0.16	0.70	0.94	4.04	0.46
Ts/(Ts+Tm)	0.06	0.28	0.30	0.55	0.58	0.49	0.06	0.12	0.09	0.08	0.22	0.20	0.06	0.06	0.05	0.05	0.03	0.03	0.04	0.02
29H/30H	0.32	0.64	0.68	0.36	1.59	0.62	0.50	0.72	0.81	1.27	1.27	1.37	0.38	0.34	1.44	0.51	0.60	0.62	0.54	0.88
31abR/30H	1.16	0.29	0.28	0.25	0	0.24	1.40	3.01	0.32	0.34	0.36	0.37	1.48	1.33	0.52	1.75	1.52	0.38	0.44	0.40
29Ts/29H	0	0.15	0.16	0.49	0	0.28	0	0	0.03	0.04	0.09	0.07	0	0	0.05	0	0	0.08	0.09	0.04
31abS/S+R	0.14	0.58	0.59	0.58	1.00	0.56	0.07	0.52	0.58	0.56	0.56	0.56	0.12	0.13	0.44	0.11	0.75	0.59	0.58	0.58
32abS/S+R	0.33	0.59	0.60	0.59	0.44	0.57	0.08	0.46	0.58	0.60	0.60	0.60	0.13	0.13	0.57	0.13	0.43	0.60	0.58	0.59
29Mor/30H	0.15	0.07	0.07	0.12	2.70	0.17	0.84	4.18	0.07	0.07	0.08	0.08	0.27	0.27	0.07	0.34	6.58	0.11	0.12	0.10
Gamm/30H	0.07	0.02	0.04	0.01	0	0.03	0.04	0.51	0.05	0.18	0.05	0.07	0.06	0.06	0.29	0.07	0.74	0.11	0.15	0.20
Steranes m/z 217																				
%C27aaaR	29	33	35	30	31	37	0	42	31	38	32	40	25	27	22	24	35	29	23	30
%C28aaaR	17	21	22	23	22	23	0	16	21	17	17	18	14	15	18	12	21	22	17	20
%C29aaaR	54	46	43	47	47	40	100	42	48	45	51	42	61	58	60	64	44	49	60	51
29abb/(aaa+abb)	0	0.25	0.24	0.22	0.24	0.20	0	0.15	0.23	0.22	0.23	0.26	0	0	0.03	0	0	0	0	0
Alkanes m/z 85																				
Pr/Ph	0.88	1.46	1.55	1.78	2.05	0.58	0.38	0.72	0.77	0.59	0.75	0.60	0.85	0.86	1.30	1.31	0.37	0.38	0.48	0.67
Pr/nC17	3.39	1.07	1.07	2.37	2.42	0.95	0.61	0.90	0.95	0.82	0.41	0.44	1.38	0.91	1.74	1.39	0.96	0.91	0.94	0.29
Ph/nC18	3.04	0.69	0.67	1.54	1.23	1.40	0.77	0.89	1.41	1.08	0.45	0.66	2.00	0.75	1.12	0.77	1.77	1.35	1.63	0.46
CPI	1.12	1.00	1.01	1.04	0.99	2.25	2.01	1.08	1.03	1.10	1.02	1.02	1.40	1.67	1.23	1.40	1.03	1.00	0.99	0.97
OEP (1)	1.02	0.95	0.95	0.97	0.95	1.28	1.45	0.94	0.92	0.96	0.99	0.99	0.92	1.19	0.84	0.84	1.03	1.03	1.12	0.98
TAR	0.55	0.28	0.10	0.37	1.14	2.32	3.09	0.18	0.17	0.14	1.88	0.94	1.05	0.79	0.26	0.23	0.25	3.14	0.30	32.84
nC24+/nC24-	0.40	0.30	0.17	0.52	0.91	2.31	0.98	0.19	0.23	0.18	1.08	0.76	0.62	0.58	0.37	0.19	0.25	1.24	0.33	13.12
nC27/nC17	0.67	0.31	0.15	0.34	1.43	1.93	4.12	0.19	0.12	0.14	1.82	0.99	0.62	0.51	0.14	0.14	0.23	6.85	0.47	20.95
Paq	0.73	0.80	0.88	0.63	0.65	0.72	0.51	0.84	0.78	0.81	0.57	0.61	0.62	0.58	0.61	0.79	0.80	0.53	0.74	0.19
Aromatics m/z 133-134																				
AIP								0.17	0.16	0.24	0.31	0.32		0.17			0.07	0.28	0.14	0.32

5.3. Organic carbon isotope composition

Carbon-isotope compositions (δ^{13}Corg) are presented in Table S4 (Appendix II). The organic-rich samples exhibit δ^{13}Corg values ranging from –26.0‰ to –29.8‰, indicating variable isotopic signatures across the stratigraphic succession. Samples from the Late Triassic – Early Jurassic display the most depleted values (reaching –29.8‰), while those from the Early – Middle Jurassic show a broader range (–26.0‰ to –29.3‰). Mid – Late Jurassic samples fall between –26.4‰ and –29.1‰, and Early Cretaceous values range from –26.7‰ to –28.1‰.

5.4. Palynological kerogen classification

Palynological kerogen classification focuses on ten samples from the main organic-rich intervals. The Late Triassic – Early Jurassic samples are broadly similar, with only E4 showing minor sporomorphs; AOM is abundant, and DOM is more prevalent, indicating higher oxidation.

The Early – Mid Jurassic (represented by sample 22KD) in the PxGa-1x well is characterized by a dominance of AOM and secondarily the presence of translucent and opaque phytoclasts, with a moderate proportion of sporomorphs. A similar picture holds for the outcrop Early – Mid Jurassic samples (E38 and E28), yet with increased opaque phytoclasts, illustrating the terrestrial influence. Late Jurassic on the other hand, is very heterogenous, suggesting a mixed setting.

Early Cretaceous samples (4KD; AY-3 well and 3-16-CS) display a slightly more homogenous palynological OM. The latter has slightly opaquer phytoclasts, no sporomorphs, and less DOM, while the former lacks DOM but shows abundant AOM. Detailed classification can be found in Table 12, and related microphotographs in Appendix I (Figure S13).

Table 12. Palynological kerogen classification for ten kerogen residues.

Samples	D23	C26	E4	D17	22KD	E38	E28	1-19-LE	3-16-CS	4KD
Translucent phytoclasts (%)	7	10	11	10	5	8	10	6	4	9
Opaque phytoclasts (%)	12	8	9	33	15	29	31	3	14	14
AOM (%)	52	46	49	55	77	61	57	64	80	63
Sporomorphs (%)	0	0	2	2	1	0	2	4	2	0
DOM (%)	30	36	28	0	3	2	0	22	0	13

5.5. Bulk generation kinetics

The discrete energy distribution model, supported by Burnham [94,165] was used to illustrate Ea-distributions for the sample set (Table 13 and Figure 13). Raw kinetic data can be found in Appendix II (Table S5); principal Ea peaks are summarized in Table 13. A 5 °C/min heating rate gave consistent results across most samples, in line with previous studies [122].

Each bar in the Ea-distribution represents compounds with similar chemical bonds [121]. The Ea-distributions vary both in range and peak position, spanning from 38 to 70 kcal/mol, with the majority focusing between 43 and 70 kcal/mol. The principal Ea peaks typically lie between 46 and 59 kcal/mol, with most clustering between 47 and 58 kcal/mol.

- Late Triassic – Early Jurassic samples exhibit broad Ea-distributions, with principal peaks centred around 49 to 53 kcal/mol.
- Lower – Mid Jurassic samples from the IU and PU show similarly broad distributions, with principal peaks at 50 to 51 kcal/mol for the IU and 50 to 54 kcal/mol for the PU.
- Mid – Late Jurassic samples also generally show broad distributions, with principal Ea peaks at 53 to 57 kcal/mol for the IU and 46 to 52 kcal/mol for the PU.
- Early Cretaceous samples have narrower Ea-distributions, particularly from the IU, peaking at 50 to 56 kcal/mol. The less organic-rich and external IU samples show broader distributions, yet with similar principal Ea values.

This variability in Ea-distributions reflects the complexity and heterogeneity of organic matter across different geological intervals, with frequency factors (A) ranging from 5.5e11 to 1e15 s^{-1}.

Table 13. Frequency factors (A) and principal activation energy (Ea) peaks, along with Tmax, total sulfur (TS) content, age, and depth for each analyzed sample, presented in decreasing Ea-order.

Sample	A	Ea													Total	Tmax	TS	Depth	Age
		46	47	48	49	50	51	52	53	54	55	56	57	58					
	(1/s)	(kcal/mol)													(%)	(°C)	(wt%)	(m MD)	
F31	1.01E+15										16%	14%	**18%**		47	400	2.2	-	M. – L. Jur.
1-19-LE	7.92E+14										12%	11%	**13%**		36	409	2.1	-	L. Jurassic
12KD	5.12E+14											**48%**	13%	27%	88	436		3378.9	E. Cret.
108KB	1.01E+14								12%	25%	**35%**				72	437		3428	E. Cret.
115KB	1.01E+14									22%	**31%**				53	439		3216	E. Cret.
4KD	1.23E+14									**69%**	10%	13%			92	439	4.7	3224.83	E. Cret.
2KD	3.85E+13							17%	18%	**45%**					80	439		3224.7	E. Cret.
10KD	4.24E+13								**60%**	10%	17%				87	438	1.5	3377	E. Cret.
11KD	5.11E+13								**54%**	14%	27%				95	439	1.6	3378	E. Cret.
B19	7.44E+13								**25%**		19%				44	407		-	M. – L. Jur.
20KD	2.96E+13							**69%**	10%	15%					94	436		2085.2	E. – M. Jur.
22KD	2.08E+13							**80%**		13%					93	438		2086.05	E. – M. Jur.
9KD	3.32E+13							**46%**	18%	28%					92	441		3237.8	E. Cret.
C26	4.91E+13							**26%**	22%	9%					58	424	7.3	-	L. Tr - E. Jur.
D23	1.49E+13					21%	**45%**								66	423	9	-	L. Tr - E. Jur.
44KD	2.57E+13						**40%**	15%							55	419		1450	M. – L. Jur.
1KD	4.51E+12					**73%**		20%							94	440		3224.5	E. Cret.
16KD	8.52E+12					**57%**	15%								72	429		2070.4	E. – M. Jur.
E4	9.03E+12			13%	14%	**40%**									67	417	9.5	-	L. Tr - E. Jur.
3-16-CS	1.26E+13					**21%**	17%	19%							57	416	0.8	-	E. Cret.
E28	9.36E+12				21%	22%	**23%**								66	421	1.9	-	E. – M. Jur.
E38	1.24E+13				16%	20%	**24%**								60	418	3.7	-	E. – M. Jur.
7-21-J1	6.13E+12				**40%**	28%									69	421		-	L. Tr - E. Jur.
38KD	1.59E+13				**21%**	22%	17%								61	411		1328	M. – L. Jur.
111KB	2.77E+12			**39%**	21%	23%									83	432		3388	E. Cret.
33KD	5.49E+11	**55%**	13%												68	419		1550	M. – L. Jur.

The table lists samples by their main Ea peak (in bold). Total (%) indicates the combined generation potential. Abbreviations: L. Tr–E. Jur.; Late Triassic – Early Jurassic, E.–M. Jur; Early – Mid Jurassic, M–L. Jur.; Mid – Late Jurassic, E. Cret.; Early Cretaceous.

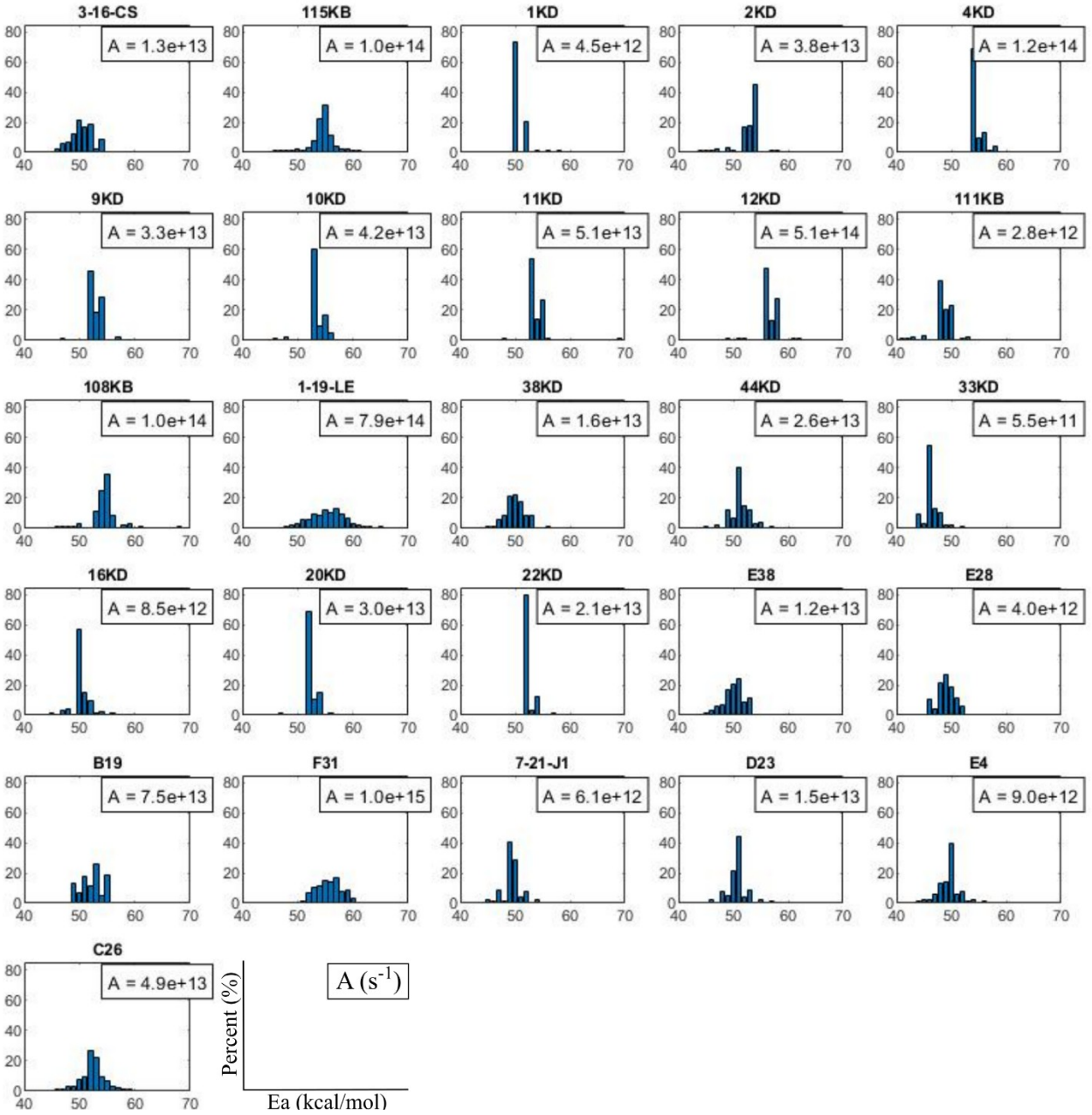

Figure 13. Activation energy distributions for the analyzed samples. The x axis represents Ea in kcal/mol ranging from 40 to 70 kcal/mol and the y axis the percentages (%). "A" refers to the frequency factor (in s^{-1}). The distributions were derived from the software KINETICS2015, using the discrete energy distribution model with 1 kcal/mol spacing.

CHAPTER 6.
DISCUSSION

6.1. Mineralogical and geochemical screening in two wells: Insights into paleoenvironments and generation kinetics

6.1.1. PxGa-1x well

The PxGa-1x well, located on Paxi Island in the Ionian Sea (Figure 14), is the only well penetrating the PU stratigraphic column from Triassic to Eocene, while Mid – Late Jurassic outcrops have been identified on Lefkada island [51,166]. PxGa-1x is a vertical well reaching a 5500m MD through an anticline, penetrating Eocene, Early Cretaceous, Jurassic (Late, Mid, Early), and Late Triassic.

From this well, 42 samples underwent RE6 analysis across all geological formations, along with 17 XRF, 14 XRD, and 7 biomarker analyses, including two bitumen samples. Additionally, multi-ramp kinetic analysis was conducted on six samples from the Early – Mid and Mid – Late Jurassic, while palynofacies analysis was performed on one sample from each Jurassic interval.

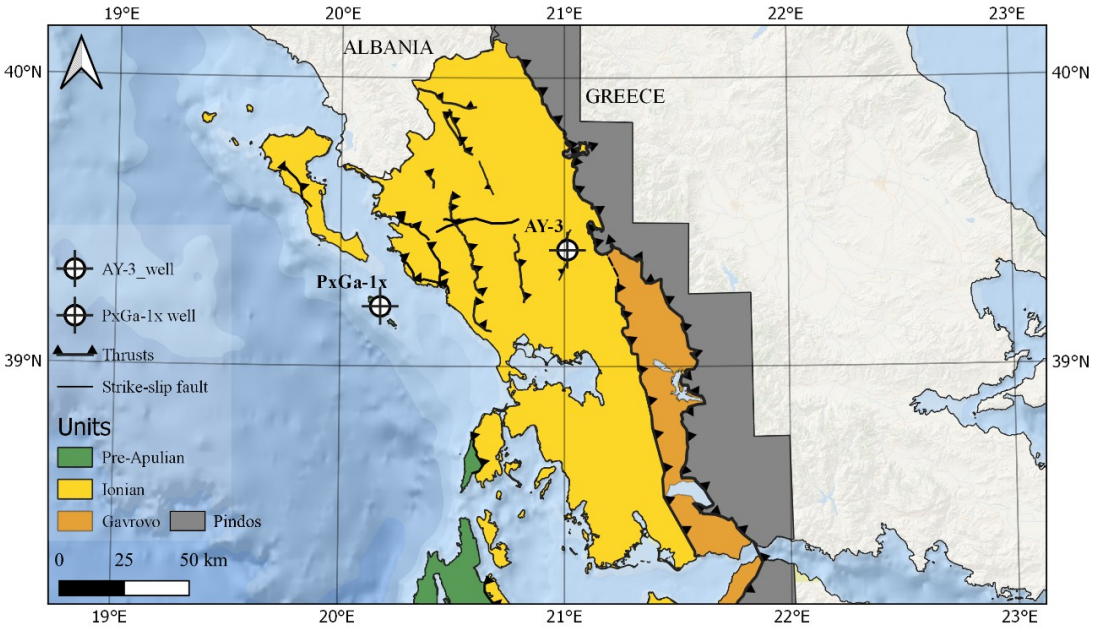

Figure 14. Map of the Units under consideration and the PxGa-1x and AY-3 well locations.

6.1.1.1. Triassic

OM quality

PP and HI assess kerogen quality, while Tmax and HI indicate the kerogen type (Figure 15). In this interval, low PP (< 2) and HI (< 50 mgHC/gTOC) suggest poor-quality, inert Type IV kerogen. Rigakis (1999) reported approx. 60% vitrinite, 20% exinite, and 20% AOM in the Triassic interval. This composition, along with the low HI, suggests a highly oxic, possibly marginal fluvio-deltaic environment, as supported by the literature [162,167,168].

OM maturity

RE6 pyrolysis shows Triassic samples with Tmax values of mainly 412–425 °C, with some exceptions (Figure 15), consistent with literature. The HI vs. Tmax (Figure 15) cross-plot suggests thermal immaturity, though some samples appear overmature. These are around 4100 m MD, while deeper samples show lower maturity; possibly due to localized heating or varying thermal histories from uplift and erosion linked to rift-related faulting during Neotethys opening.

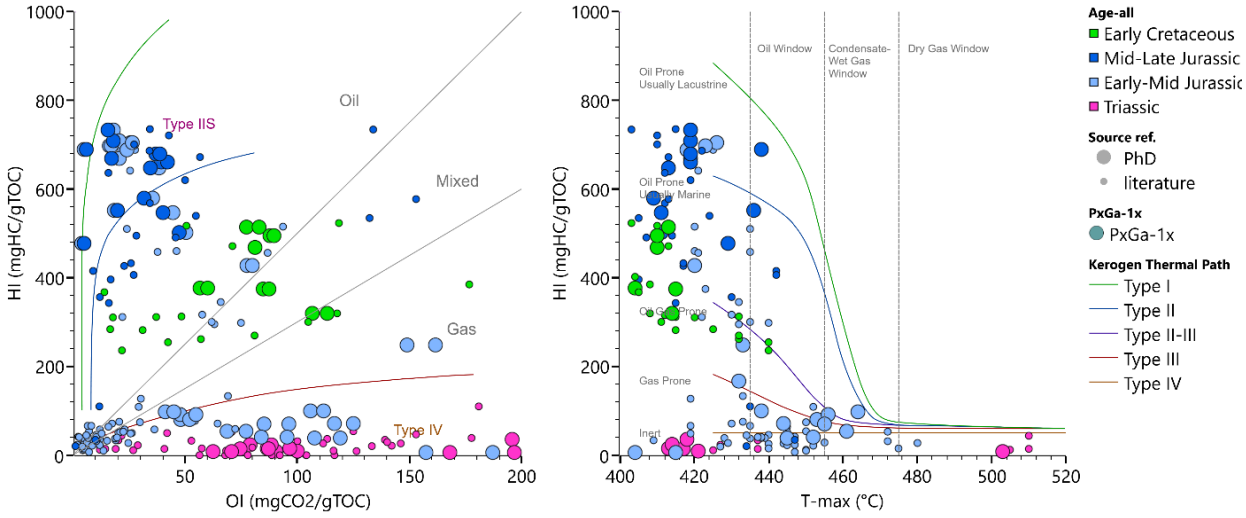

Figure 15. (Left): Pseudo Van Krevelen diagram for PxGa-1x samples from Triassic to Early Cretaceous. Kerogen type lines are based on Dembicki (2009) and Vandenbroucke and Largeau (2007). (Right): HI vs. Tmax for all PxGa-1x samples integrated with literature data, modified after Hackley and Lünsdorf (2018).

General paleodepositional environment

XRF proxies

Rigakis and Karakitsios [27,51] described this interval as consisting of intercalated dolomites, shales, and anhydrites, associated with a tidal flat complex on a platform spanning from the PU to the GU. While GC-MS analysis was not conducted on samples from this interval, Rigakis (1999) presented data on aliphatic hydrocarbons, showing Pr/Ph ratios between 0.43 and 0.93, indicating mainly algae-derived OM under reducing conditions. Organic petrography confirmed the abundance of vitrinite, with equal amounts of AOM and exinite, supporting a marine environment influenced by terrigenous sources.

Elemental analysis of two samples from the Late Triassic suggested a dry climate, indicated by Sr/Cu > 10, and deposition under mainly oxic-dysoxic conditions, supported by Ni/Co < 0.5 and V/(V+Ni) < 0.85. Although U/Th > 1 typically suggests anoxic conditions, the U concentration in carbonates is influenced by its concentration in seawater, leading to a decrease in U/Th in carbonate sediments [170,171]. Additionally, a low Sr/Ba ratio (<1) suggests a more saline depositional setting, consistent with the intercalation of anhydrites and low Pr/Ph. The Al_2O_3 and TiO_2 levels are very low, around 0.1 wt%, decreasing with depth, reaching a minimum in the Late Triassic. Their poor correlation with SiO_2 suggests a more complex source, not dominated by terrestrial debris.

6.1.1.2. Early – Mid Jurassic

Mineralogy

Early – Mid Jurassic is dominated by calcite. Dolomite is present in the lower sample by 14 wt%. Silicate minerals and pyrite are mainly absent, with quartz maximizing at 1 wt% and illite/chlorite at 0.5 wt% (Figure 16). Anhydrite is present in three samples, ranging from 5 to 20 wt%, with halite at 1 wt% in some samples. These data indicate a carbonate-dominated, mainly calcite-rich interval, with intercalations of anhydrite, consistent with the lithology presented by Rigakis (1999).

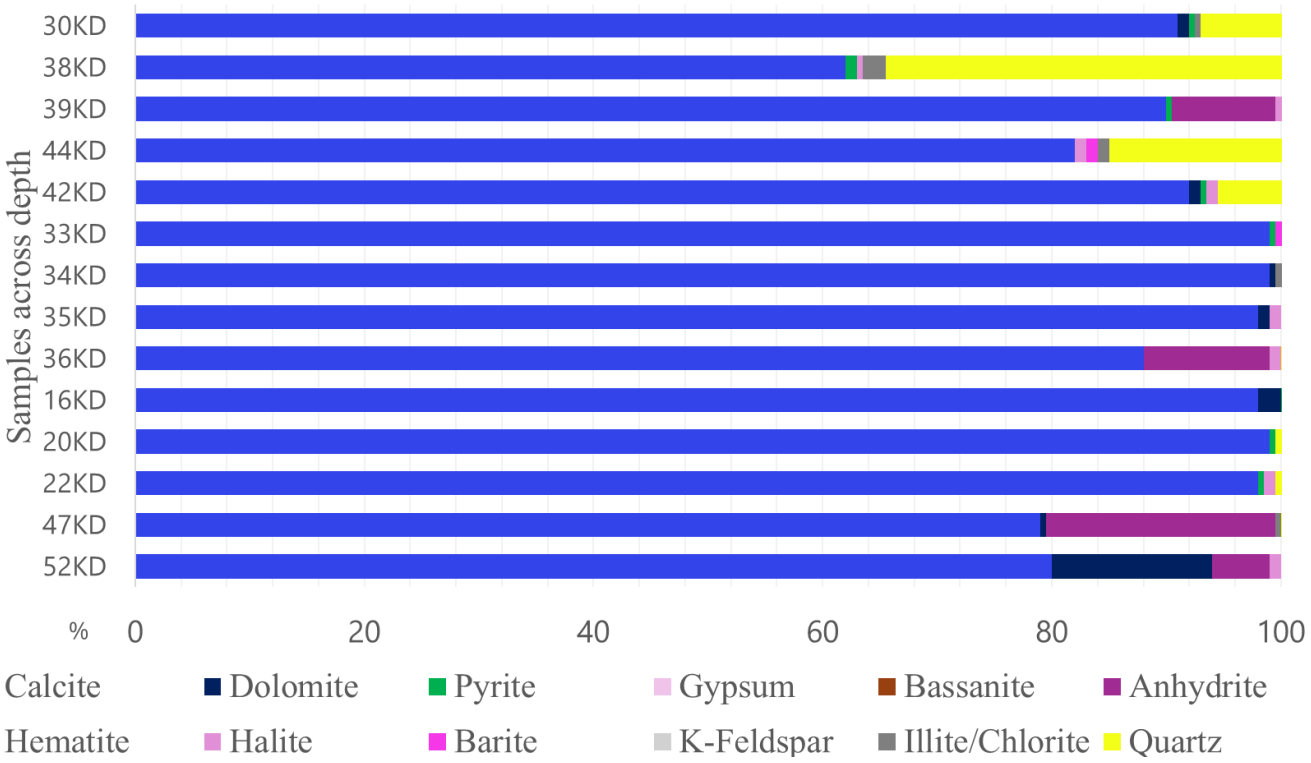

Figure 16. Mineralogy for the PxGa-1x samples across depth.

OM richness

The TOC of the Early – Mid Jurassic samples ranges between 0.2 and 4.6 wt%, showing an upward increase. Free HC (S1) amounts range from 0.1 to 1.1 mgHC/grock, with the highest values found in the upper parts of the formation. Various studies suggest reducing the TOC threshold for identifying effective carbonate source rocks to below 0.5 wt%, even as low as 0.2 wt% [15,172–178]. Additionally, thermally cracked HC (S2) values follow a similar trend, ranging from 0.1 to 21.9 mgHC/grock. Plotting the samples on a logarithmic S2 vs. TOC graph indicates poor to excellent generation potential (Figure 17). This is further confirmed by the related EOM in two samples, ranging from 3738 to 3964 ppm.

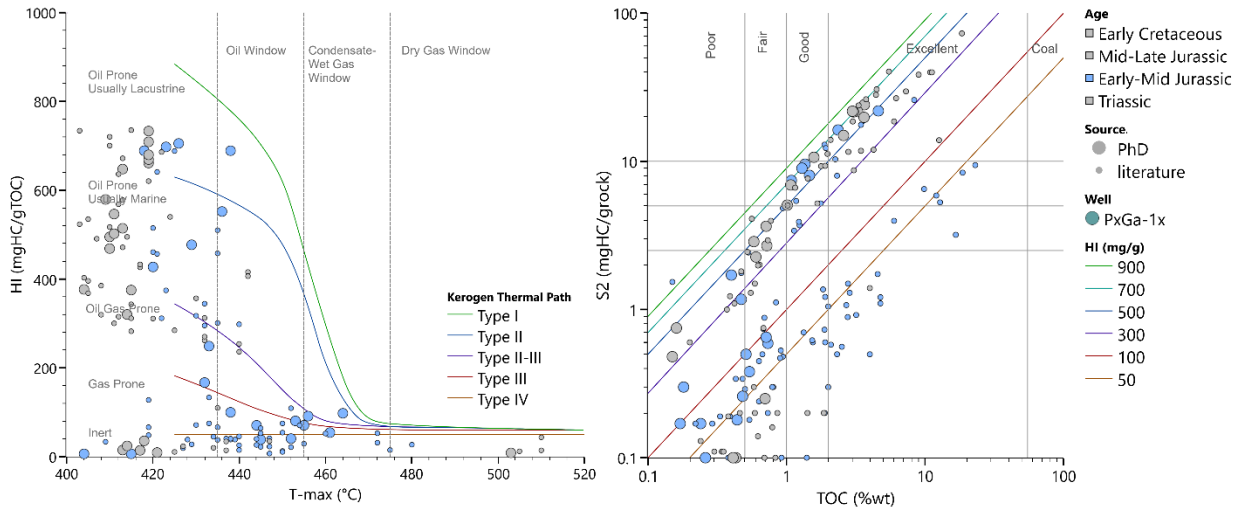

Figure 17. (Left): HI vs. Tmax for the Early – Mid Jurassic samples of the PxGa-1x well, modified after Hackley and Lünsdorf (2018). (Right): S2 vs. TOC for the Early – Mid Jurassic samples of the PxGa-1x well, modified after Langford and Blanc-Valleron (1990). HI in mgHC/gTOC.

OM quality

The HI vs. OI and Tmax analysis suggests that the Early – Mid Jurassic samples are predominantly Type I–II kerogen, with some inert (Type IV) samples. The inert samples have TOC < 1 wt% and S2 < 4 mgHC/grock. This is further supported by the HI vs. TOC diagram, indicating oil-generation potential for Type I–II samples and inert to gas & oil-generation potential for Type III and IV. Although Type I–II or potentially IIS kerogen is identified, no evidence supports a lacustrine organic-rich interval.

The integration of elemental H/C (ranging from 1.05 to 1.21) and S/C (ranging from 0.15 to 0.20) suggests a predominantly oil-prone kerogen of Type II–IIS, based on the literature classifications [180,181].

Palynofacies analysis of sample 22KD indicates a more marine origin, with AOM being the most abundant component accounting for 76%. It also identified 15% opaque phytoclasts and 5% translucent phytoclasts. According to the classifications of Dow and Connor (1982), as well as Tyson (1995), the upper part of this interval, represented by sample 22KD, suggests a dysoxic–anoxic depositional environment, supporting the Type II–IIS kerogen.

The TOC/S ratio for the Early – Mid Jurassic samples ranges from 5.3 to 7.8 in the upper formation, indicating water bottoms with higher oxidation, potentially due to freshwater conditions, even when accounting for potential sulfur quantification errors [183].

The Ea-distributions reveal kerogen heterogeneity. Lower interval samples (20KD and 22KD) show Ea values between 43–63 kcal/mol, with dominant peaks at 52 kcal/mol, contributing 69–80% of the total generation potential. The uppermost 16KD sample has a broader Ea-distribution (41–65 kcal/mol), with a peak at 50 kcal/mol, accounting for 57% of the generation potential.

The narrow Ea-distributions imply a more uniform organic source, with the principal Ea suggesting a Type II marine kerogen [184], though with some terrestrial influence, as indicated by the biomarker analysis. Organic petrology [51], shows increasing AOM (15% to 55%) and exinite (~20%) in the upper part, while vitrinite decreases from 70% to 20% (avg. 40%). Several studies [162,167,168] suggest that these distributions, coupled with the increasing HI, indicate a transition from Type III–IV kerogen in the lower part to Type II in the upper part. This points to a shift in the depositional environment from a proximal shelf with oxic conditions to a more distal, anoxic-dysoxic shelf, likely associated with a restricted basin.

OM maturity

Tmax was used to assess the maturity of the organic matter. The immature diagenesis stage is characterized by a Tmax of 435 ºC or lower [173] (Figure 17). As burial depth and temperature increase, Tmax rises, reaching over 470 °C in the post-mature metagenesis stage. In this well, thermal maturity increases linearly with depth, with a distinct "cut" around 2100 m MD. The Early – Mid Jurassic interval falls within the immature to late oil window (Figure 17), with the uppermost, most organic-rich samples being immature to early mature. The saturate/aromatic ratio shows a slight decrease at shallower depths, from 0.20 to 0.19, supporting lower maturities.

According to Peters et al. (2004) isomerization of the C29 5a,14a,17a(H)-Steranes causes the 20S/(20S+20R) ratio to increase from 0 to 0.5 with rising maturity, reaching equilibrium at around 0.55, corresponding to a vitrinite reflectance of 0.7 %Ro. Within this interval, two samples in the upper part of the formation show values between 0.48 and 0.58, supporting an immature to oil window maturity. The Ts/(Ts+Tm) ratio, used for maturity assessment, falls below 0.2 here, yet carbonate source rocks tend to reduce Ts/(Ts+Tm) values [85] (Table 10).

General paleodepositional environment

XRF proxies

Eight samples in total underwent elemental analysis for this interval. According to the Sr/Cu ratio, they all suggest a dry climate, with some fluctuations around 2085 m. The integration of U/Th, Ni/Co, and V/(V+Ni) indicates that depositional conditions changed from suboxic to anoxic during deposition. Towards the Mid Jurassic, in the upper part of the interval, conditions appear to remain suboxic-anoxic, yet with an increasing trend in Ni and U concentrations. This could be related to a decrease in anoxic sedimentation during this period, as discussed by Brennecka et al. (2011).

Additionally, the Sr/Ba ratio, indicative of water column salinity, is elevated, with values around 10, suggesting a saline water column, based on several studies [185–188]. Notably, Al_2O_3 and TiO_2 show an increase in the interval corresponding to higher concentrations of uranium. However, this increase is not reflected in silicate minerals compared to the deeper parts of the interval. The Al_2O_3 and TiO_2 do not correlate well with SiO_2, indicating more complex sources not dominated by terrigenous material.

Paleoproductivity, which reflects the quantity of OM in sedimentary rocks, was assessed using the P/Ti ratio. Phosphorus (P) is a key component of many organisms and can be used to characterize biological productivity [189]. In this interval, paleoproductivity shows a decrease in the Early Jurassic, followed by an increase towards the upper part of the interval, reaching a value of 2. Additionally, copper (Cu), an important nutrient often indicative of productivity from both terrestrial and primary inputs [190], is used in the Cu/Ti ratio to assess paleoproductivity while eliminating terrigenous influences.

Biomarkers

The aliphatic content of all samples contains n-alkanes ranging from n-C10 to n-C35. Early – Mid Jurassic samples from the Px-Ga-1x well on Paxi Island show a dominance of mid-chain alkanes, peaking at n-C21 in 20KD and n-C24 to n-C26 in 22KD. A Paq value of around 0.6 suggests submerged and emerged aquatic plants, particularly seagrasses, were the main producers of these compounds (Figure 18) according to classifications proposed by several authors [191–194]. Unlike terrestrial plants that produce long-chain alkanes and algae that produce short-chain alkanes, seagrasses are typically found in tidal, lagoonal, and inner platform environments [195,196]. In contrast, GU environments were dominated by inner carbonate platform/lagoonal

sabkha environments with elevated salinity. Similar carbonates of Liassic age are found in other Western Tethys regions, such as Morocco and Italy, deposited in peritidal platform environments [197]. These low-energy environments, indicated by anhydrite intercalations, support such setting consistent with the described geology [17].

The isoprenoids pristane and phytane, mainly derived from the phytol side chain of chlorophyll [198,199], show a Pr/Ph ratio well below 1 across the interval, with a decrease in shallower depths (Table 11). Ten Haven (1987) suggests that a low Pr/Ph ratio (< 1) is typical of hypersaline environments, where halophilic bacteria are influenced by variable salinity. The distribution of Pr/nC17 and Ph/nC18 indicates a marine, reducing depositional environment (Figure 19), a trend also supported by literature [51], showing a consistent pattern across the Early – Mid Jurassic interval. Additionally, m/z 85 shows a unimodal distribution in 20KD and a bimodal distribution in 22KD sample, with key alkanes at n-C18 and n-C18, n-C22, respectively.

The TAR values decrease from approximately 2 to 0.9 (Table 11) with decreasing depth, indicating an increasing aquatic influence over time and a corresponding reduction in terrigenous input, consistent with previous research [89,201]. This trend is evident throughout the Early – Mid Jurassic interval, as supported by literature data [51] and is also reflected by the nC27/nC17 ratio. According to Katz and Lin (2014) lacustrine settings generally show ratios of 2 or higher, while marine environments tend to tave values below 0.8. In this case, a decrease in the nC27/nC17 ratio is observed at shallower depths, ranging from 1.8 to around 1, supporting the interpretation of reduced terrestrial influence and suggesting a transition to more distal marine settings.

This interpretation is consistent with the narrow Ea-distributions observed in the lower parts of the analyzed samples. The principal Ea suggests a predominantly marine origin for the organic matter [118], as higher Ea values are often linked to terrestrial input [106,203]. While lacustrine and marine Ea-distributions can share similarities, pure Type I kerogens typically show a single dominant Ea peak. The presence of refractory organic components requiring higher thermal maturity, indicated by their higher Ea, points toward a more Type II kerogen. The deeper 22KD shows similarities to lacustrine samples discussed by Petersen et al. (2010), while the upper 20KD is more comparable to brackish water environments and Type II marine kerogens.

Furthermore, C21, C25, and C30 highly branched isoprenoids (HBI) were identified. While not quantified, their relative abundance to longer neighbouring alkanes appears to increase at

shallower depths. According to Grice et al. (1998) C21+ isoprenoidal components are likely derived from lipids of organisms tolerant to extreme salt concentrations.

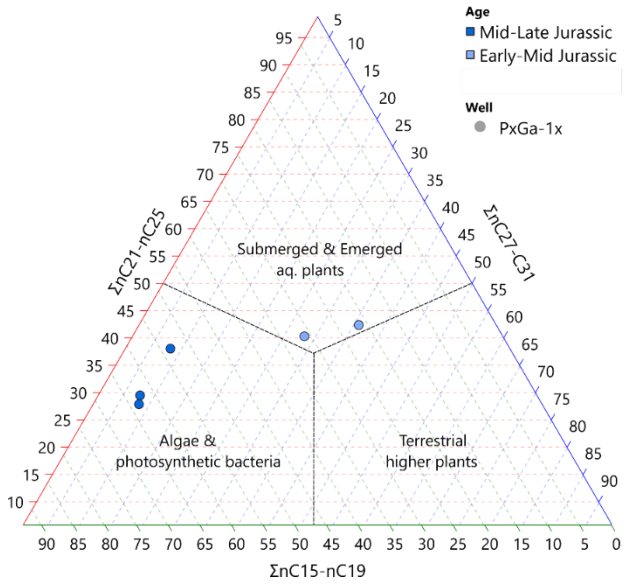

Figure 18. Ternary diagram of short-, mid- and long-chain normal alkanes to essential categories of OM for the Jurassic studied samples of the PxGa-1x well, modified after Basu et al.(2017) and Moghazy et al. (2023).

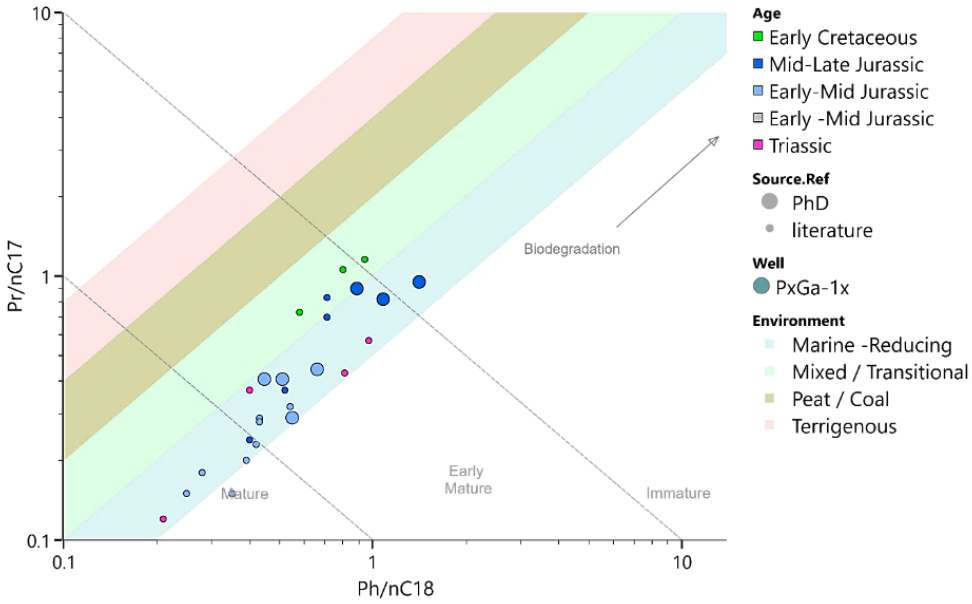

Figure 19. Pr/nC17 vs. Ph/nC18 plot for all studied samples of the PxGa-1x well, integrated with literature data, following Shanmugam (1985) and oxidizing zones following Peters et al. (1999).

Wang et al. (2015) suggested that 5a,14b,17b-pregnane and homopregnane are geological products derived from steroids bound to the kerogen by a sulfurized side chain. Pregnane and its homologues are typically associated with restricted, clastic-starved carbonate marine or saline depositional settings, such as those found in lagoons with a stratified water column, low dissolved oxygen, and minimal terrigenous organic matter influx [206,207]. Previous studies have linked high pregnane and homopregnane contents to hypersaline sulfur-rich environments [82] and marine carbonate source rocks [208]. Yet, low pregnane and homopregnane levels can indicate less saline conditions or different depositional environments [83].

In the upper part of the Early – Mid Jurassic, the abundance of pregnane and homopregnane is particularly evident in sample 20KD, suggesting a more restricted, clastic-starved marine or saline depositional setting. Both samples exhibit higher (C21–22)/(C27–29) sterane ratios relative to the dia/reg C27 sterane ratios, supporting a restricted water column origin with significant carbonate mineral deposition, as proposed in the literature [206,209].

The relative distribution of regular steranes (C27, C28, and C29) is commonly used to identify the source of organic material and to characterize the depositional environment [210], based on studies of steranes in both marine and terrigenous settings [89,211–213]. Within just 1 meter of depth difference, the sterane distribution shifts, with C27aaaR becoming more abundant than C29aaaR at shallower depths. This could indicate a change in depositional conditions, transitioning from shallow to deeper marine environments (Figure 20).

These samples are also characterized by a medium abundance of C30 steranes. The origin of these steranes are 24-n-propylcholestanes [214], although it seems possible that they arise from the marine sterols, as identified through the research of Djerassi et al. (1981). C30 steranes are typically absent in lacustrine and terrestrial plants [89,216], abundant in marine carbonate and siliciclastic settings, and moderate in marine evaporitic and calcareous environments. Their low abundance and decrease in shallower depths, along with high C34 homohopanes, suggests a restricted marine, evaporitic depositional environment, consistent with literature interpretations [217].

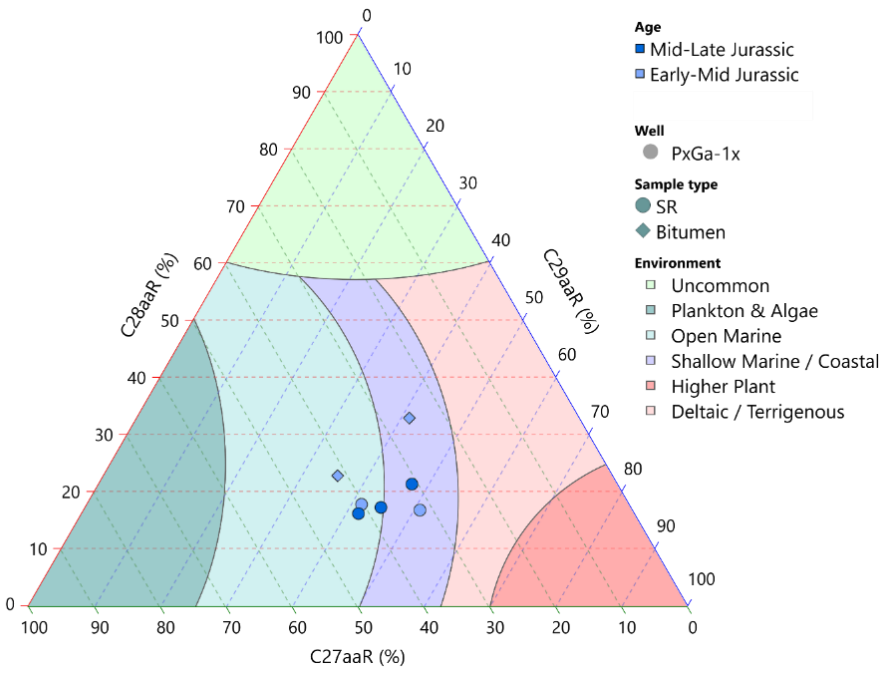

Figure 20. Ternary diagram of normal sterane distribution of the analyzed Jurassic samples of the PxGa-1x well, modified after several sources [89,210,218].

Gammacerane, a diagenetic product of tetrahymanol [219], known to be generated by ciliated protozoans living in oxic-anoxic water interfaces, is considered an indicator of water column stratification and saline waters [213,220–223]. In this interval the Gammacerane/30H ratio is lower than 0.5 indicating low abundance, ruling out hypersaline or alkaline lake conditions [218,221,224]. The 35HHI abundance is around 12%, suggesting reducing conditions [224], which could preserve the alkyl side chain of C35 hopanepolyol. The HHI, combined with Pr/Ph, further support a reducing depositional environment, while the less abundant tricyclic terpanes compared to hopanes suggest fresh water presence [89]. No re-arranged hopanes (m/z 367) were identified, even though they are commonly associated with thermally immature samples [225,226], and also reported in shelf sediments and terrestrial clays worldwide [227,228]. Also, while Ts/(Ts+Tm) cannot be used for thermal assessment, this ratio, along with diasteranes and regular steranes, points to an anoxic carbonate depositional setting [89,229].

Aryl isoprenoids, present at low, yet detectable levels in the Early – Mid Jurassic samples, suggest anoxic and occasionally euxinic conditions in the photic zone [230–233]. The two organic-rich Early – Mid Jurassic samples reveal low levels of 2,3,6 aryl isoprenoids, primarily in the C15 to C22 range (Appendix I; Figure S11). In contrast, only trace amounts were found in the younger

samples (38KD and 44KD). These are typically biomarkers for Green Sulfur Bacteria (GSB), from the Chlorobiaceae family [231]. However, precursors like b-carotene and isorenieratene [230,231,234–236] were not detected, potentially remaining within the kerogen structure due to the low maturity of the organic material.

Aryl isoprenoids yield characteristic fragment ions at m/z 133 and 134. Their mass spectra are characterized by a base peak at m/z 133 and 134, along with a molecular ion peak (M+) following the general formula C_nH_{2n-6} corresponding to the trimethylbenzene series where n ranges from 13 to 24. Where aryl isoprenoids were identified, the aryl isoprenoid ratio (AIR), based on peak abundance, is significantly below 1. According to Schwark and Frimmel (2004), the low AIR, with low Pr/Ph ratio, suggests persistent photic zone anoxia (PZA) or euxinia under sulfidic conditions, ruling out sea ventilation [233].

Two isotopically analyzed samples, 20KD and 22KD, show δ^{13}Corg values ranging from –27.41‰ to –27.70 ‰. They are more depleted than Mid – Late Jurassic, indicating a marine environment with moderate terrigenous influence, particularly from C3 plants [237], consistent with their biomarker signatures. The presence of pregnane, homopregnane, and AIP, along with the narrow δ^{13}Corg range, suggests consistent depositional conditions with restricted water circulation and periodic anoxia in a marine carbonate platform.

6.1.1.3. Mid – Late Jurassic

Mineralogy

Moving to shallower depths, within the Mid – Late Jurassic, the mineralogy is still carbonate-dominated. Within this interval, anhydrite is almost absent apart from one sample at approximately 1370 m depth. Besides this sample, there is a decrease trend in the calcite content towards shallower depths, with dolomite reaching absence. Halite holds a small percentage of 1 wt% on the shallower samples while silicate minerals are increasing in shallower depths, suggesting a change towards more silica-rich carbonate rocks towards the upper part of the interval.

OM richness

TOC within the Mid – Late Jurassic ranges between 1 to 3.7 wt%. The amount of free HC maximizes at 0.8 mgHC/grock, and the thermally cracked HC range between 5.1 to 24.1

mgHC/grock. The S2 vs. TOC plot (Figure 21) reflects a good to excellent generation potential for this interval. Their EOM, as estimated in three samples underpin this, also following several studies [15,238,239].

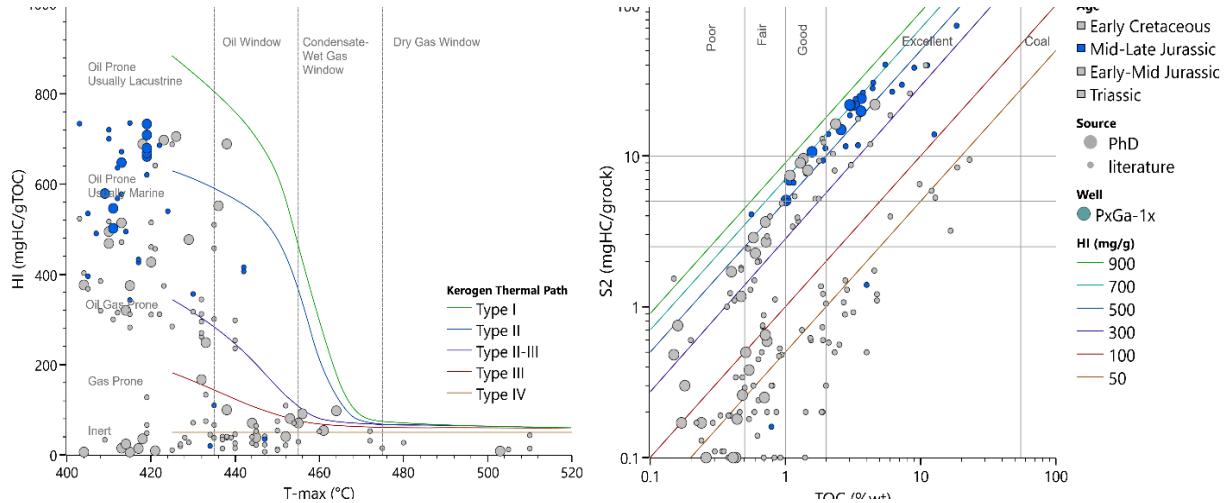

Figure 21. (Left): HI vs. Tmax for the Mid – Late Jurassic samples of the PxGa-1x well, modified after Hackley and Lünsdorf (2018). (Right): S2 vs. TOC for the Mid – Late Jurassic samples of the PxGa-1x well, modified after Langford and Blanc-Valleron (1990). HI in mgHC/gTOC. Other sample ages and literature data from this well are represented by grey color in the background.

6.1.1.4. OM quality

The pseudo-Van Krevelen diagram suggests a mainly Type I–II kerogen, supporting the available literature data [51]. HI vs. Tmax suggests mainly oil prone, Type II kerogens for the under-evaluation samples. However, the relative to the organic carbon sulfur content, points towards a more Type IIS–(II) kerogen rather than Type II, potentially related to marine carbonate depositional environment according to established classifications [180,181]. The S2 vs. TOC plot suggests a mainly oil with fair to very good generation potential (Figure 21).

The TOC/S ratio for this interval is decreased and ranges between 3.8 and 5.4, lower than the Early – Mid Jurassic. This, indicates a less oxygenated environment, potentially of periodic anoxia, and more marine conditions [183].

The Ea-distributions of this interval change towards the upper part (Figures 13 and 24). The deepest sample, 33KD, has a principal Ea at 46 kcal/mol, accounting for 55% of its generation

potential, which is the lowest focal point in this well. The 44KD sample has a principal Ea at 51 kcal/mol, representing 40% of its generation potential. The shallowest 38KD sample does not exhibit a single principal Ea but rather two peaks at 49 and 50 kcal/mol, accounting together for 43% of its generation potential.

These broader Ea-distributions suggest a more complex organic source compared to the Early – Mid Jurassic samples, yet mostly within the suggested Type II kerogen range [118]. Rigakis (1999) observed a slight decrease AOM, averaging 60%, with exinite at 25% and vitrinite at 15%. This trend, along with increasing HI 547–669 mgHC/gTOC [162,167,168], supports the presence of kerogen Type I–II kerogen and a middle shelf environment with anoxic-dysoxic conditions followed by a more heterogenous organic matter source as evidenced by the broad Ea-distributions. It is interesting that although samples 33KD and 44KD hold similar HI values, their Ea focal points change, suggesting potential differences in the hydrocarbon generation timing, considering differences in their frequency factors.

6.1.1.5. OM maturity

This interval, following the trend of the Early – Mid Jurassic, appears to be immature with Tmax maximizing at 419 °C (Figure 21, Table S2), increasing linearly with depth. This is also supported by the relative abundance of 29Ts over 29H and 27Ts over 27Tm as well as the relative abundance of saturates over aromatics.

However, saturate/aromatic shows an increase towards shallower depths from 0.29 to 1.2, which is controversial with thermal maturity, yet these fractions are also affected by organofacies [239]. Interesting is that the principal Ea of the two Jurassic intervals illustrate a fade tendency of increasing principal Ea with Tmax (Figure S14). Although there is no linear relationship derived, the tendency cannot be disregarded, potentially influencing the focal point of the distribution.

General paleodepositional environment

XRF proxies

Five samples in total have undergone elemental analysis for this interval from 1328 to 1550m depth. According to the Sr/Cu ratio, there seems to be a change in the upper part of the formation, from dry climate to humid and warm. The integration of U/Th, Ni/Co and V/(V+Ni) suggests that

the depositional environment was mainly dysoxic, with silicate mineral input. An increased uranium content is evident in the upper part of the formation which is characterised as more silicate-rich supporting more anoxic conditions, according to published interpretations [170,171]. On top of that, Sr/Ba shows a decreasing trend towards the upper part of the interval indicative of decreasing salinity [185–188], yet this ratio has been characterised by Wang et al. (2021) as unsuitable for characterizing whole rock samples.

The Al_2O_3 and TiO_2 show an increasing trend (Figure 24), supporting the silicate mineral content of these samples. Al_2O_3 and TiO_2 with SiO_2 show a better correlation (R^2 ~0.5–0.6) suggesting the relation to terrigenous sources. The increase in silicate mineral input along with indicators of dysoxic and anoxic conditions suggest that this interval saw more stratified column conditions and possibly greater nutrient availability, promoting marine productivity compared to the Early – Mid Jurassic.

Biomarkers

The Mid – Late Jurassic samples of this well, have a predominance of short-chain alkanes, in contrast to the Early – Mid Jurassic samples. The three studied samples of this interval named 33KD, 44KD and 38KD show a prominence of n-C18, having a unimodal distribution, indicative of algae and photosynthetic bacteria precursors [7,196,241]. The Pr/Ph hold values between approximately 0.6–0.77 (Figure 22), having high similarity to the Early – Mid Jurassic samples, supporting the continuation of marine depositional environment with algal/bacterial input. Even predominance in alkanes is also evident yet with terrigenous input [7,241]. The TAR decreases abruptly to values close to 0 (Table 11), pinpointing the decrease of terrigenous input and the increased aquatic influence [242] with geological time.

In contrast to the Early – Mid Jurassic samples, solely the C21 isoprenoid has been identified within this interval, probably supporting the decrease in salt concentrations during this period [83]. A decrease in the abundance of pregnane and homopregnane is also evident, with the sample 44KD being only exception.

As seen in Figure 20, this interval is characterized by increasing C27 sterane relative to C29 in younger intervals. This, reflects a change in depositional conditions, changing from shallower to more open marine conditions, according to literature interpretations [89,211–213]. Additionally,

the C30 steranes are less abundant compared to the older, Early – Mid Jurassic samples, which might indicate a marine evaporitic and restricted setting [218].

Interesting is the increase on the abundance of gammacerane, which along with its relation to 30H relative to the Pr/Ph (Figure 22), showcases stratification in the water column during sediment deposition, under reducing conditions [89]. On top of that, the decreasing trend in δ^{13}Corg from the Lower – Mid to Mid – Late Jurassic that reaches –28.63‰ to –28.78‰ reflects a shift towards deeper marine conditions dominated by algal and bacterial productivity and stratified water columns with reduced terrigenous input [237,243]. This is also illustrated by biomarker analysis, as well as the broader Ea-distributions (Figure 13).

The observed Ea-distributions indicate a transition in the depositional environment. In the Early – Mid Jurassic, the setting was marine, yet potentially more restricted or deep marine, leading to a narrow range of chemical bonds in OM from a uniform algal source. By the Mid – Late Jurassic, the environment shifted to a marine setting with some terrigenous influence. This resulted in broader Ea-distributions, reflecting increased diversity in the OM chemical bonds. Overall, these changes highlight shifts in OM composition and environmental factors throughout the Jurassic period.

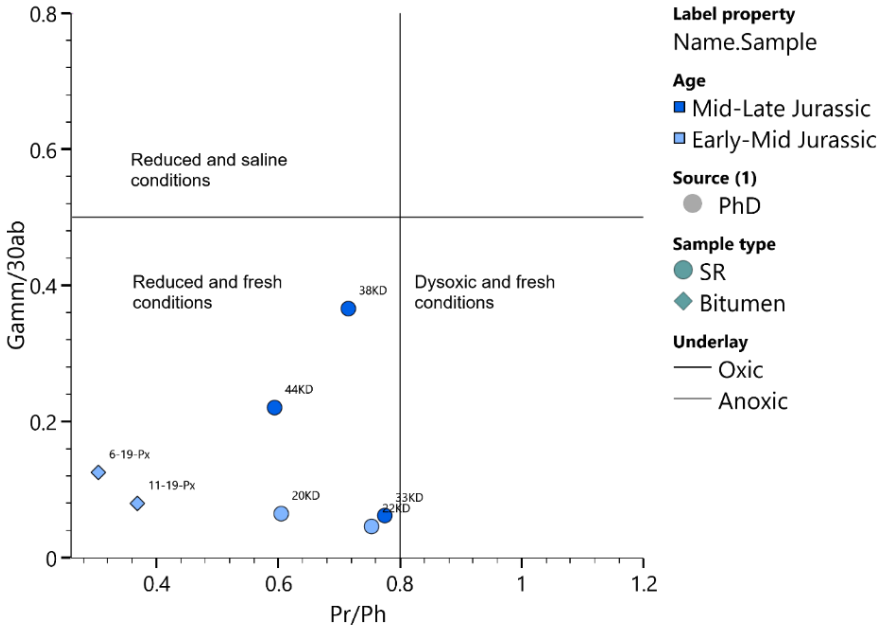

Figure 22. Gammacerane/30H vs. Pr/Ph revealing depositional environment variations of the Jurassic PxGa-1x well samples. Modified after Moldowan et al.(1985) and Peters et al. (2004).

6.1.1.6. Early Cretaceous

Mineralogy

In this well the Early Cretaceous is represented by six samples. This sample is dominated by calcite with 91 wt%, with silicate minerals, mainly quartz representing the rest of the mineral phase (Table 8 and Table S1). Studies of Rigakis and Karakitsios [27,51] have described this formation dominated by limestone with cherts, rudist fragments, benthic foraminifera and algal species with less pelagic than the age-equivalent Ionian facies, suggesting an intra-platform basins.

OM richness

The TOC of Early Cretaceous reaches a maximum of 0.7 wt%, with relevant literature having samples reaching 10 wt% [51]. The S2 of these samples range between 0.5 to 3.7 mgHC/grock. Plotting the analyzed samples, on the logarithmic plot of S2 vs. TOC (Figure 23) shows that all Early Cretaceous samples have mainly poor to fair hydrocarbon generation potential, with some literature data reaching excellent potential according to their higher TOC (Figure 23).

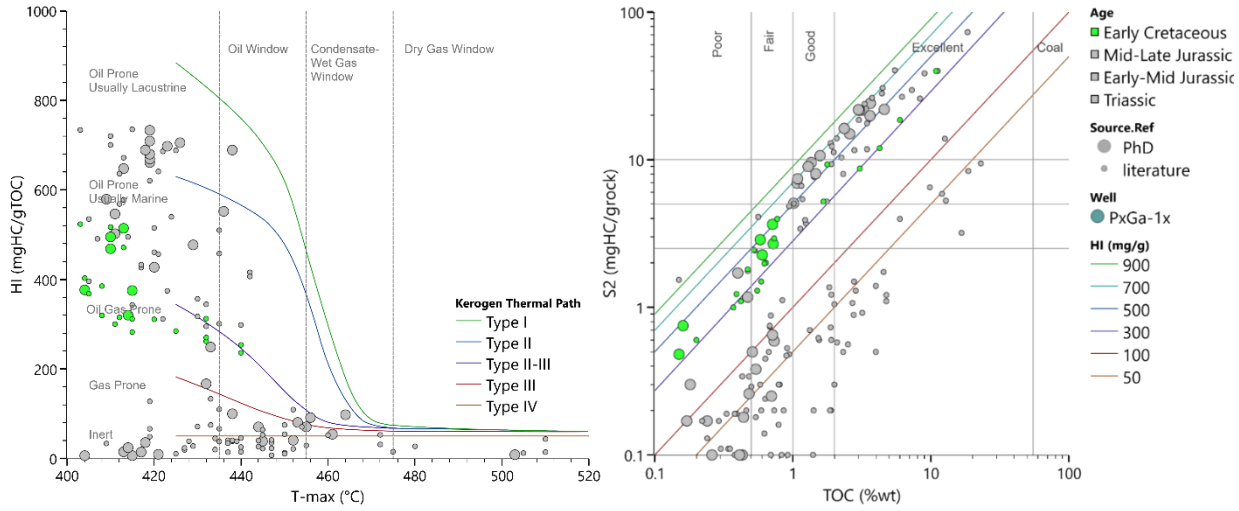

Figure 23. (Left): HI vs. Tmax for all the PxGa-1x samples, modified after Hackley and Lünsdorf (2018). (Right): S2 vs. TOC for the Early Cretaceous samples of the PxGa-1x well. Early Cretaceous is represented by the green points, while literature data and other age intervals by the grey points. Modified after Langford and Blanc-Valleron (1990). HI in mgHC/gTOC.

OM quality

The kerogen quality seems to be poor to fair with PP < 5, while the HI is less than 514 mgHC/grock, suggesting a Type II–III interval. The same trend is evident when incorporating literature samples of this age interval from this well.

Rigakis (1999) observed an increase in AOM, averaging 60%, with exinite at 25% and vitrinite at 15%. This trend, along with increasing hydrogen index (HI) values, as noted in literature [162,167,168], supports the presence of kerogen Type I–II and a more distal shelf environment with anoxic-dysoxic conditions followed by a more heterogenous source.

OM maturity

RE6 analysis shows that all Cretaceous samples have a Tmax ranging mainly from 404 to 415 °C. The thermal immaturity window is also evident by the literature data with most samples having values below 435 °C. A cross-plot of HI vs. Tmax (Figure 23) reveals that the studied formation of the PxGa-1x has not entered the oil window yet.

It is noteworthy that the principal Ea of the studied samples shows a trend of increasing values with decreasing Tmax. Additionally, Ea tends to rise with increasing A, suggesting a complex interplay. Although no linear relationship has been established, these tendencies highlight the importance of the OM composition in maturity and generation potential.

In lower maturity samples, higher principal Ea values may indicate a predominance of more resistant OM, such as Type III kerogen, which requires greater energy to break down for hydrocarbon generation. Conversely, more mature samples likely consist of Type II kerogen, characterized by narrower Ea-distributions and lower Ea (Figure 13), reflecting the presence of simpler or previously cracked organic compounds that generate hydrocarbons more readily.

This trend suggests that in less mature, organic-rich environments, complex OM preservation requires more energy to initiate hydrocarbon generation. As maturity increases, OM degradation facilitates the breakdown and enhances hydrocarbon generation potential.

General paleodepositional environment

XRF proxies

Some aliphatic biomarker data from relevant literature from Rigakis and Karakitsios [27,51] show Pr/Ph between 0.8–1.2, suggesting higher terrigenous input compared to the Jurassic intervals (Figure 24). Elemental analysis was performed on two samples of the mid-upper part of the Late Triassic. They suggest a dry climate originating from Sr/Cu > 10, and deposition under mainly oxic-dysoxic conditions, supported by Ni/Co < 0.5, V/(V+Ni) < 0.85. Although U/Th > 1, which would normally suggest anoxic conditions, the U concentration of carbonates is related to the U concentration of the seawater they were deposited, which under anoxic conditions result in a decrease of U/Th of carbonate sediments [170,171], leading to the influence of U/Th both from the anoxic levels and the mineralogy of the organic-rich rock.

On top of that, an increased Sr/Ba < 1 suggests a potentially more saline depositional environment, which is also supported by the intercalations of anhydrites and the low Pr/Ph. The Al_2O_3 and TiO_2 are very low, close to 0.1wt%, and they seem to decrease with depth, reaching a minimum in Late Triassic. Their correlation with SiO_2 at this interval is very poor, suggesting that their sources are more complex and not dominated by terrestrial debris sources.

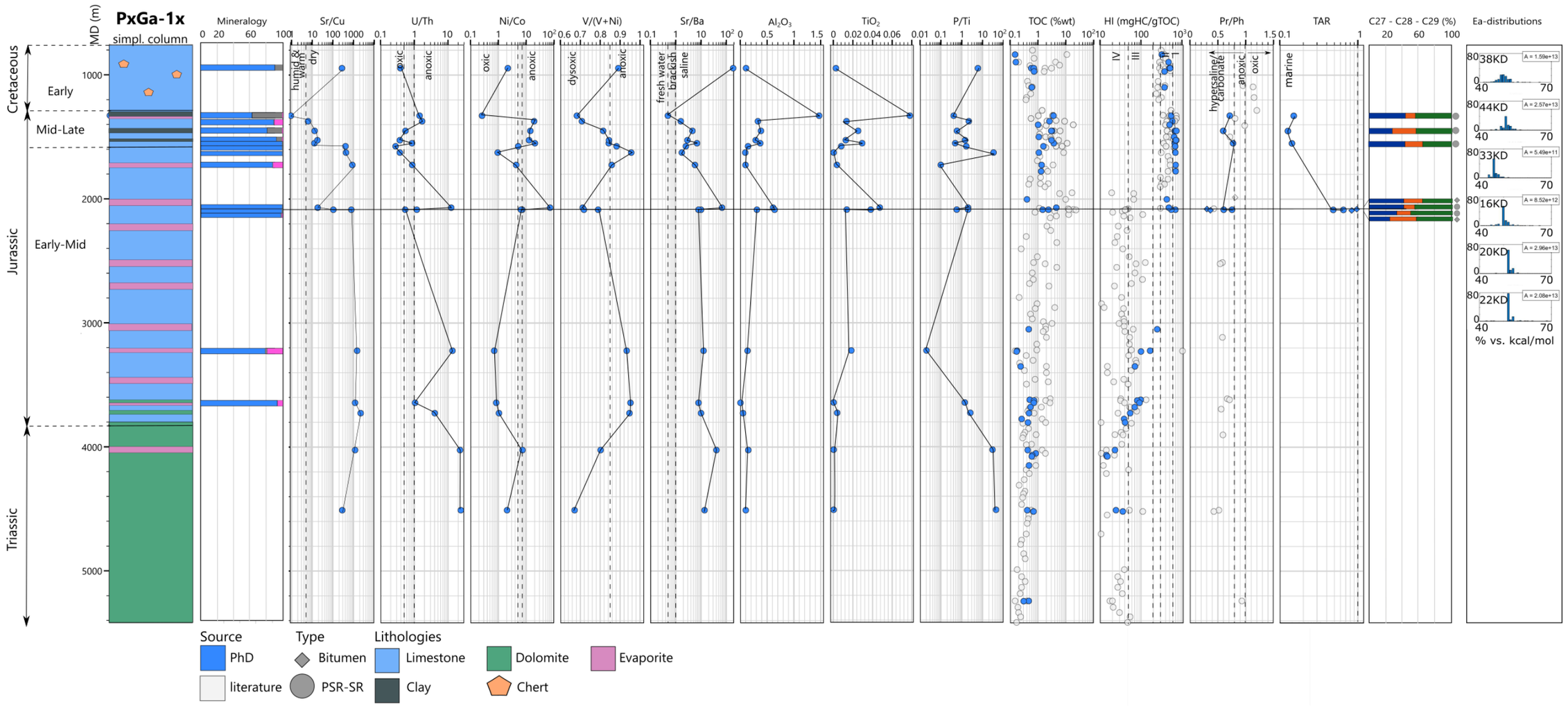

Figure 24. Multi depth plot of PxGa-1x well including XRF proxies, RE6 parameters, biomarker ratios and Ea-distributions from the analyzed samples.

6.1.2. AY-3 well

The AY-3 well is located in Epirus, SE of Ioannina city, and is in the Inner IU. It has reached high depths, 4288 m TD, penetrating Oligocene, Eocene, Late to Early Cretaceous and Jurassic strata [51]. Within the Early Cretaceous, two organic rich layers have been identified.

From this well, 49 samples in total have been analyzed with RE6 distributed across the Early Cretaceous and some within Jurassic. From the most organic-rich Early Cretaceous interval, twenty samples have undergone XRF analysis, thirteen XRD, five GC-MS analysis, while two samples have undergone palynofacies analysis and six bulk kinetic analysis.

6.1.2.1. Early Cretaceous

Mineralogy

Within the Early Cretaceous interval, the mineralogy was studied through XRD in thirteen samples (Figure 25). This interval has been described by Rigakis and Karakitsios as dolomitic limestones to dolomites in the lower part, deeper than 3220 m MD, which change to intercalated limestones with radiolarians, cherts and marly limestones in the upper part.

XRD analysis has proved the abundance of carbonate minerals with calcite reaching 96 wt%, and dolomite 47 wt%. It is evident from Figure 25 that quartz content has an increasing upwards trend up at the deepest organic-rich layer, which then decreases in the top-most organic-rich layer. Clay minerals follow this trend, increasing to 18 wt% at around 3225 m MD and then rapidly decrease below 1 wt%. The high carbonate content often implies that the depositional environment was at least partially oxygenated. However, the presence of organic-rich material suggests that there were periods or localized conditions where reducing environments were prevalent. This mix can indicate a dynamic depositional environment with variations in redox conditions.

As described by Rigakis (1999), the lower parts of the formation are dolomite rich, while the upper parts are more calcite rich. These differentiations are justified using XRD analysis in a detailed content and are illustrated in Figure 25 and Figure 26. This mineral composition aligns with various descriptions from other authors, i.e. [28,42,57,90], who described these organic-rich intervals as marly or in parts shaly limestones and shales with chert intercalations. In addition, layers have been linked to the Paquier OAE [27,63,90].

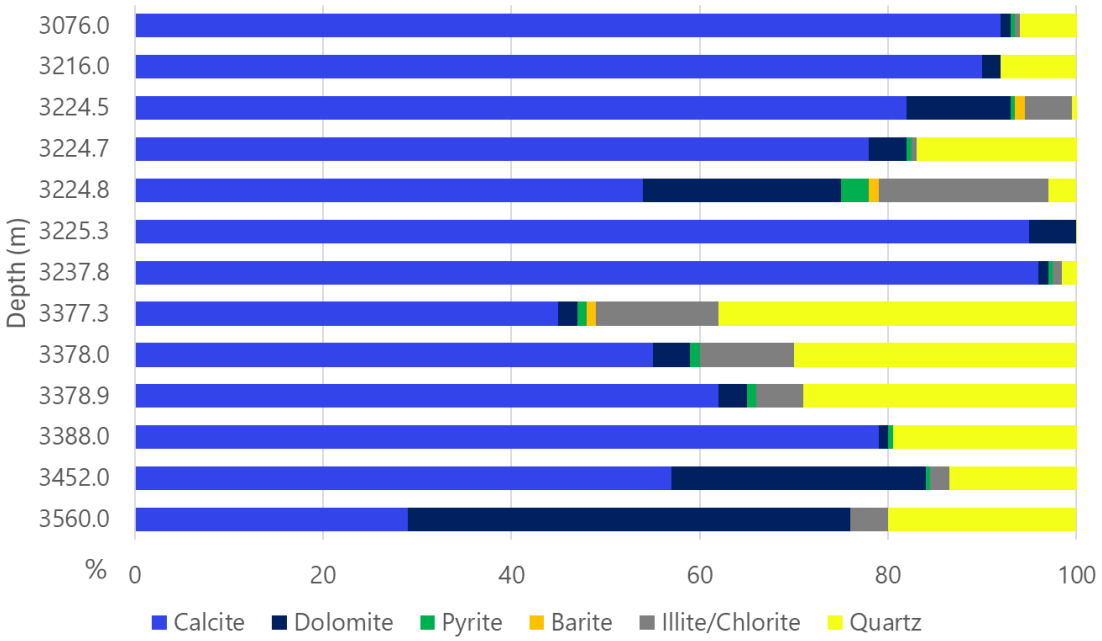

Figure 25. Mineral composition of the Early Cretaceous interval of the AY-3 well with depth.

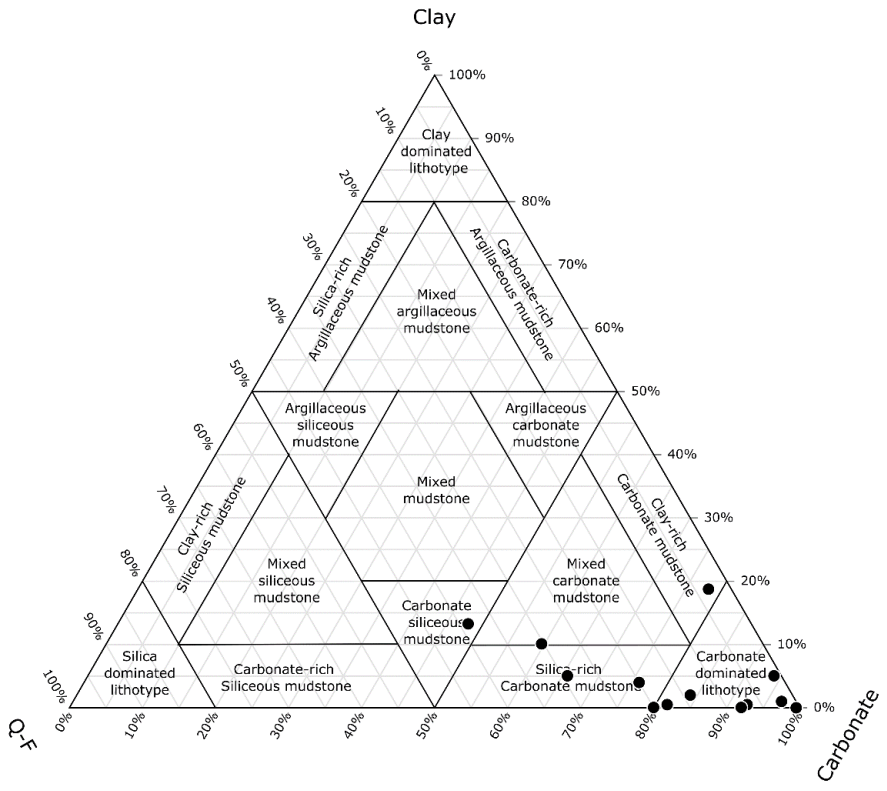

Figure 26. Ternary mineralogy diagram for the Early Cretaceous samples of the AY-3 well.

OM richness

The TOC of Early Cretaceous ranges between 0.1–6.9 wt%, while literature has shown maximum values at around 20 wt%. The S2 of these samples range between 0.1 to 37.5 mgHC/grock. Plotting the samples in the S2 vs. TOC logarithmic plot (Figure 27) shows a wide trend, with the hydrocarbon generating potential ranging between poor to excellent. The same trend is observed in the analyzed samples, with a few showing good to excellent potential. The latter are core samples of the two most organic-rich layers penetrated by the AY-3, at depths between 3224–3225 and 3377–3378m MD.

This generation potential range is also illustrated in the four representative samples that have undergone organic matter extraction. Their EOM to TOC suggests that the generation potential is good to excellent, according to Le Tran and Philippe (1993).

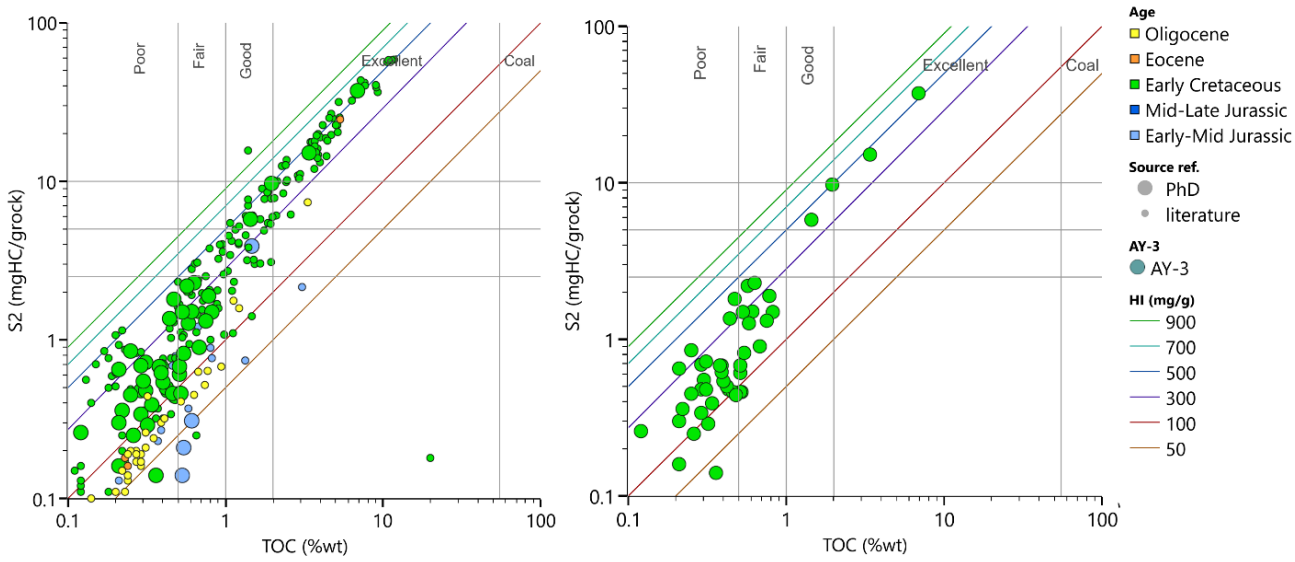

Figure 27. S2 vs. TOC for (Left): all the analyzed samples of the AY-3 well and (Right): all the Early Cretaceous samples analyzed in this study. Legend applies for both plots.

OM quality

PP and HI indicate Early Cretaceous kerogen quality ranging from poor to excellent. PP varies between 0.2–38 mgHC/grock, and HI spans 76–543 mgHC/gTOC, suggesting a range between inert Type IV and oil-prone Type II kerogen (Figure 28). Core samples show lower OI and higher HI, leading to their selection for further organic geochemical analysis.

Across depth, samples show similar Ea-distribution patterns, with Ea ranging from 48 to 61 kcal/mol. Principal Ea in organic-poor samples (S2 < 2.5 mgHC/gTOC) accounts for 31.2–45.7% of generation potential (Table 13), while in organic-rich samples it represents 49.4–73.5%. Organic-rich samples show two main Ea values contributing 75.1–94% of the generation potential, suggesting better kerogen quality and higher hydrocarbon potential, likely dominated by Type II kerogen. In contrast, broader Ea-distributions in low-organic samples may reflect more oxidized or mixed kerogen types with lower potential.

Organic-rich samples show consistent focal points around 50–53 kcal/mol and frequency factors between 4.5e12 and 1.2e14 s^{-1}, suggesting stable and concentrated hydrocarbon potential. In contrast, lower-organic-content samples show broader focal points (48–56 kcal/mol) and wider range of frequency factors (2.8e12 to 1e14 s^{-1}) (Figure 13), which could reflect a more heterogeneous organic composition and reduced hydrocarbon yield.

The concentration of organic-rich samples within the 3224–3379 m MD range suggests favourable conditions for the preservation of high-quality kerogen. Further geochemical analysis may clarify kerogen types and their thermal history, solidifying the relationship between depth, organic richness, and hydrocarbon potential.

The intervals represented by samples 1KD, 2KD, 4KD, 10KD, 11KD, and 12KD, as noted by Foscolos (1989) and Rigakis (1999) contain abundant liptinite (Tasmanales marine algae, dinoflagellate cysts, liptodetrinite) and an amorphous fluorescing matrix, with minimal vitrinite and inertinite. These findings indicate a Type II marine kerogen, formed under low or no terrigenous influence. In addition, Oikonomopoulos et al. (2023) analyzed the sample 4KD and found a mix of oil-prone liptinite (Type II), gas-prone vitrinite (Type III), two types of solid bitumen, and inertinite (Type IV). The UV fluorescence also confirmed highly oil-prone marine telalginite and bitumen, consistent with a marine depositional environment and oil-generation potential.

These align with the narrower Ea-distributions and higher organic content seen in the samples, further supporting the presence of high-quality Type II kerogen, predominantly marine, with low terrigenous input and strong hydrocarbon generation potential.

OM maturity

The immature to early mature diagenesis stage, as depicted by Hunt (1995), is distinguished in this interval by a Tmax ranging between 429 to 443 ºC in the analyzed samples with a wider range, mainly between 416–460 ºC (Figures 27 and 28) presented on the literature. In this well, thermal maturity does not show a linear trend with depth. In contrast, considering the Tmax values of the younger and older formations, the Tmax mostly fits within the early mature to early mature window, while Early Cretaceous samples range between similar Tmax values across depth.

This abnormality could reflect a uniform thermal maturity resulting from inconsistent burial due to tectonic processes, and subsequent erosion that preserved these maturity levels across the interval. This is studied by Makri et al. (2023), who discussed the scenario of stabilization of post-erosional thermal maturity before significant uplift and erosion, resulting in such Tmax across the remaining stratigraphy.

An inconsistent effect is also illustrated in the EOM/TOC ratio which seems to increase towards shallower depths, instead of decreasing. However, EOM is partly affected by organofacies [239]. On top of that, the 4KD sample, as studied by Oikonomopoulos et al. (2023) found vitrinite reflectance of 0.68 %Ro and Tmax up to 440 °C indicating early maturity.

The isomerization of the C29 5a,14a,17a(H)-sterane for the analyzed samples showed values between 0.45 and 0.5 for the 3224–3225 m depth, and 0.51 to 0.54 for the deeper 3377–3378m interval (Figure 29). Therefore, a slightly increasing isomerization with depth. This increase according to Peters et al. (2004) suggests an early mature window stage, and a slightly maturity increase with depth.

Moreover, although carbonate source rocks typically exhibit a lower Ts/(Ts+Tm) ratio [85], the data in this case reveal an increasing trend with depth. Specifically, samples from the 1KD–9KD interval show Ts/(Ts+Tm) values around 0.2, while those from the 10KD–12KD m interval exhibit nearly double this value. When considering the 29Ts/29H ratio (Figure 29), this trend further supports the interpretation of an early mature stage for the deeper samples and an immature stage for the shallower ones. This suggests a variance in thermal maturity that is not fully captured by the Tmax values from Rock-Eval pyrolysis.

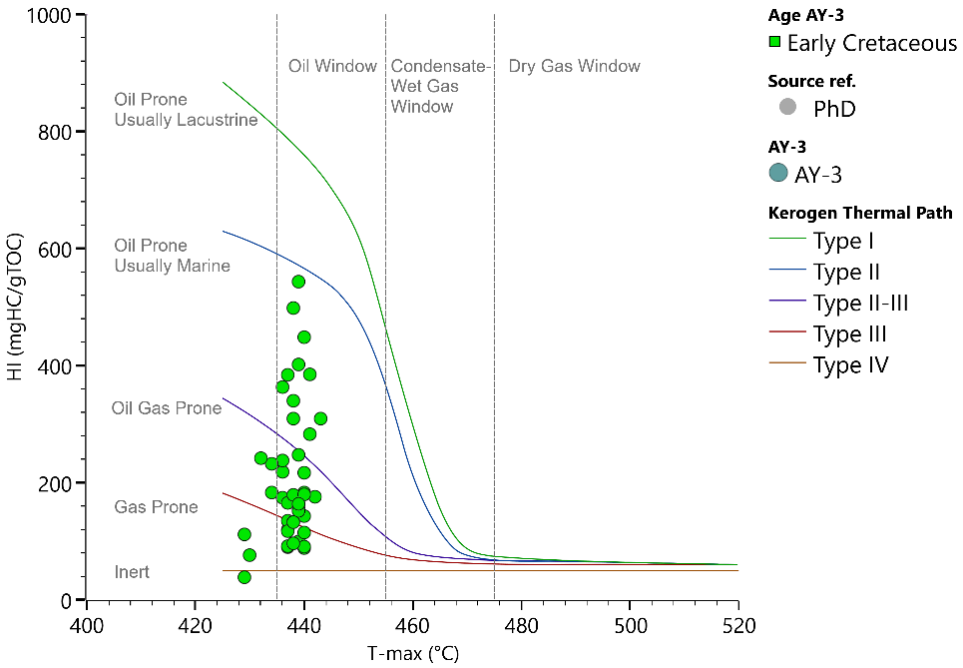

Figure 28. HI vs. Tmax for the Early Cretaceous of the AY-3 well.

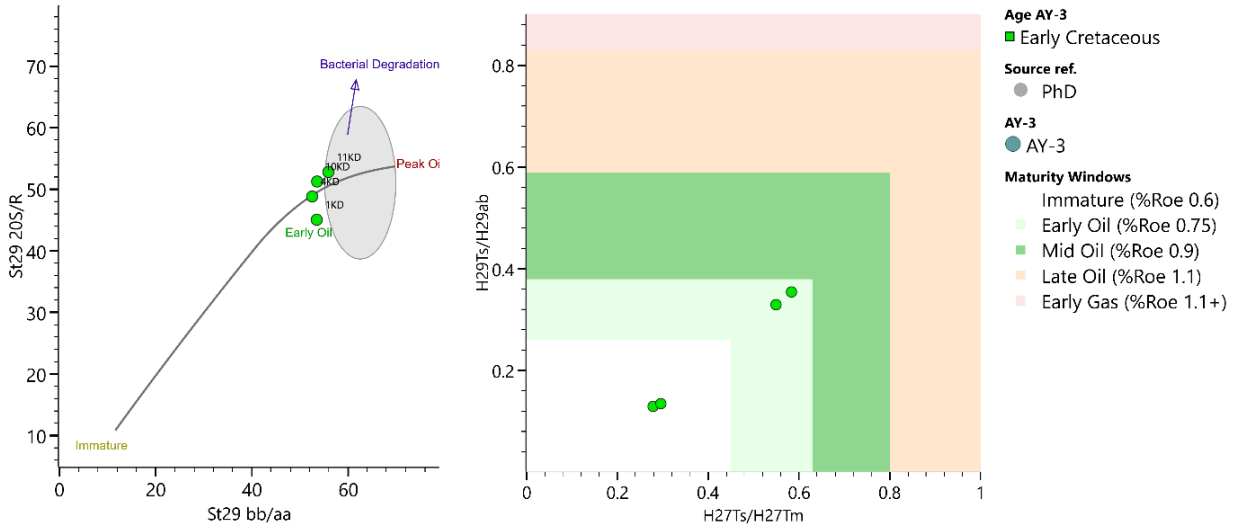

Figure 29. (Left): Isomerization of the C29 sterane, and (Right): H29Ts/H29ab vs. H27Ts/H27Tm, illustrating the thermal maturity of the Early Cretaceous samples of the AY-3 well.

General paleodepositional environment

XRF proxies

A total of twenty samples from 3150 to 3575m depth interval were subjected to elemental analysis. The Sr/Cu ratio fluctuates between 10 and 100 from bottom to top, with some organic-rich samples showing even lower values. Most of these samples suggest a predominantly dry climate, though some fluctuations in the more organic-rich intervals, where the ratio drops below 10, may indicate brief periods of increased humidity.

Analysis of U/Th, Ni/Co, and V/(V+Ni) ratios reveals a shift from oxic to dysoxic-anoxic conditions in the more organic-rich layers, as evidenced by higher levels of uranium, nickel, and vanadium [170]. The U/Th values are mainly lower than 1, Ni/Co between 1 and 10, and V/(V+Ni) mainly around 0.8. The most organic-rich layers around 3220–3400m show higher values for all three proxies.

Considering the increased TOC in the upper organic-rich layer, less efficient uranium sequestration into the organic-rich sediments could be inferred, leaving U in the seawater to be incorporated into carbonates. Alternatively, the anoxic conditions may not have been intense enough to fully deplete the seawater with U. This could be plausible under suboxic or fluctuating redox conditions, with OM preservation linked to potentially higher productivity. Paleoproductivity, indicated by the P/Ti ratio [189], increases towards the upper sections of the column, rising from 0.6 in the lower, organic-rich, and least carbonate-rich interval to 3.4 in the upper organic- and most carbonate-rich interval. These results imply that higher productivity in the upper section and more oxygenated (dysoxic to suboxic) conditions in the lower organic-rich layer may have contributed to lower U concentration in the sediments.

The Sr/Ba ratio, reflecting water column salinity, is generally low, mostly remaining below 1 throughout the interval, except for depths between 3076–3144 m MD where it reaches 1.4, suggesting low salinity waters [185–188]. Additionally, Al_2O_3 and TiO_2 show a linear increasing trend with SiO_2, though the correlation is not strong, indicating a complex source composition not solely dominated by terrigenous input. Additionally, the Cu/Ti productivity proxy, remains consistent across samples, averaging 0.09.

Biomarkers

Four Early Cretaceous samples underwent biomarker analysis. Two from the lower, and two from the upper organic-rich interval. All samples show a prominence of short-chain alkanes with a unimodal distribution, peaking at n-C17, and decreasing towards the mid- and long-chain alkanes. The Paq values [191] are around 0.6 for the lower organic rich interval, and around 0.8 for the upper interval (Figure 30), suggesting the presence of submerged and emerged aquatic plants [191–194]. The general n-alkane abundance indicates a marine algae and cyanobacterial origin based on published frameworks [245] (Figure 33).

Short-chain alkanes are associated with algae and photosynthetic bacteria [191,196] and they have been seen to live in marine and lacustrine environments [246,247], with a marine depositional environment being supported by palynological and geochemical data by several studies [37,51,90]. Tzortzaki et al. (2013) suggested photic zone euxinia for an organic-rich Early Cretaceous interval in a neighbouring region.

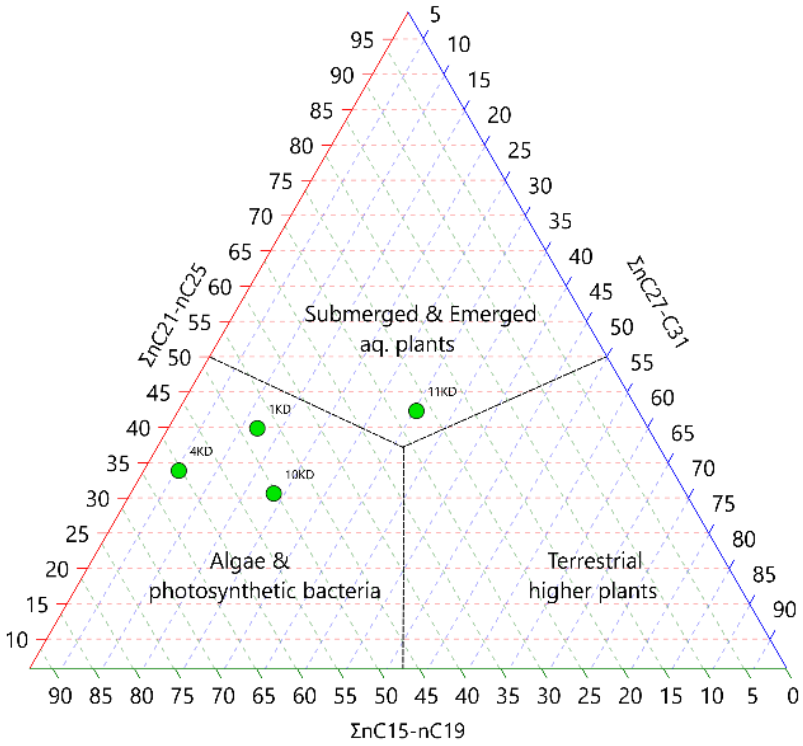

Figure 30. Triplot of short-,mid- and long-chain normal alkanes to essential categories of OM from the Early Cretaceous samples of the AY-3 well. Plot modified after El-Moghazy et al. (2023).

The isoprenoid Pr/Ph ratio, believed to derive mainly from the phytol side chain of chlorophyll [198,199], decreases from around 2 to 1 towards the upper parts of the formation. While this ratio is commonly used as a palaeoenvironmental proxy, it may also be influenced by geological variability, and maturation as evidenced by Ten Haven (1987), requiring cautious interpretation. The relative distribution of Pr/nC17 and Ph/nC18 suggests a transitional depositional environment [89] (Figure 31), with higher pristane concentration indicating terrigenous influence.

TAR values, which is another ratio that should be used with caution as different non-marine algae may contribute to long-chain alkanes it is useful to understand differences across depth[242]. Here TAR values decrease from approximately 1 to 0.1 with decreasing depth, illustrating an increase in aquatic flora over geological time and a decrease in terrigenous input according to several authors [89,201]. This aligns with stronger anoxic conditions suggested by XRF analysis. Similarly, the nC27/nC17 ratio, which has been used by Katz and Lin (2014) to differentiate between marine and lacustrine sources, varies from 1.4 in the deepest Early Cretaceous to values between 0.2 and 0.3 in shallower parts, reflecting a shift from terrigenous to marine OM origin.

Isotopic $\delta^{13}C$ values of 1KD, 4KD, and 10KD range between –26.69‰ to –27.06‰. While such values in modern environments would typically suggest a terrigenous OM source [243,248], during Early Cretaceous elevated atmospheric CO_2 levels likely influenced marine primary productivity and carbon isotope fractionation. This lead to marine plankton with lighter $\delta^{13}C$ values compared to their modern counterparts [243,249], and a more depleted $\delta^{13}Corg$ signal.

Kinetic analysis shows narrow Ea-distributions in the organic-rich Early Cretaceous samples, with one principal Ea accounting for 60 to 78% of the total generation potential (Table 13), narrowing the main stage of hydrocarbon generation [115]. Narrow Ea-distributions coincide with lacustrine source rocks from the literature [98,113,118,202,250]. These distributions imply a more uniform OM source, potentially associated with freshwater algae [98] or marine Type II kerogen [118,251]. Elevated Tmax values (437–444 ºC) suggest sufficient burial eliminating thermally reactive kerogen fractions, reducing generation potential and increasing Ea. The variation of Ea-distributions throughout the well could be linked to the OM variation during diagenesis.

Pregnane and homopregnane content, evident in the Early Cretaceous samples, supports carbonate-rich, mixed OM source rocks deposited under restricted water column conditions [206,208]. The 10KD sample indicates open conditions with higher clay minerals and broader Ea-distributions with three Ea accounting for 86% of its generation potential. The upper organic-rich interval (1KD,

4KD) shows higher pregnane and homopregnane levels, narrower Ea-distributions and one principal Ea accounting for more than 70% of the generation potential supporting a more restricted water column.

The relative sterane abundance reveals a prevalence of C29 compared to C27 and C28, plotting within a shallow marine transitional setting (Figure 32). However, all four analyzed samples show a somewhat similar trend, which is also evident through the narrow Ea-distribution and their n-alkane distributions. Low C30 sterane abundance (Appendix I, Figure S9) supports a restricted marine calcareous depositional environment [215,218], potentially reflected also in the narrow Ea-distribution. Low gammacerane abundance (Table 11) indicates low salinity or unstratified waters [221,224]. The low 35HHI further supports a more restricted depositional environment with anoxic conditions where the enhanced preservation of higher hopane homologues does not occur [224]. Combined with the abundance of pregnane and homopregnane and the narrow Ea-distribution, this may point to a stable, low-salinity marine setting with possible anoxia and consistent organic matter deposition.

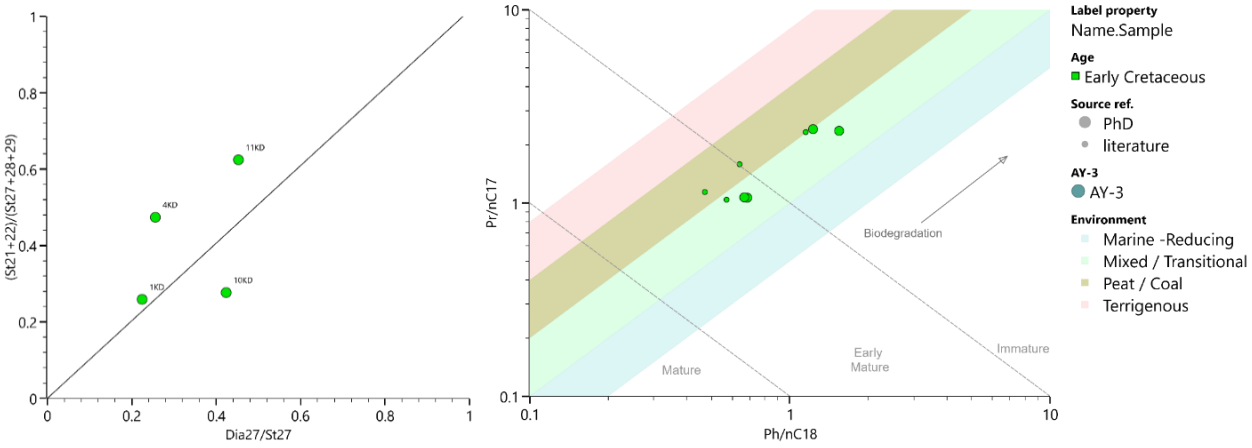

Figure 31. (Left): (C21–22)/(C27–29) sterane vs. dia/reg C27 sterane ratio. (Right): Pr/nC17 vs. Ph/nC18. Both plots are used to assess the depositional environments of the studied Early Cretaceous samples from the AY-3 well.

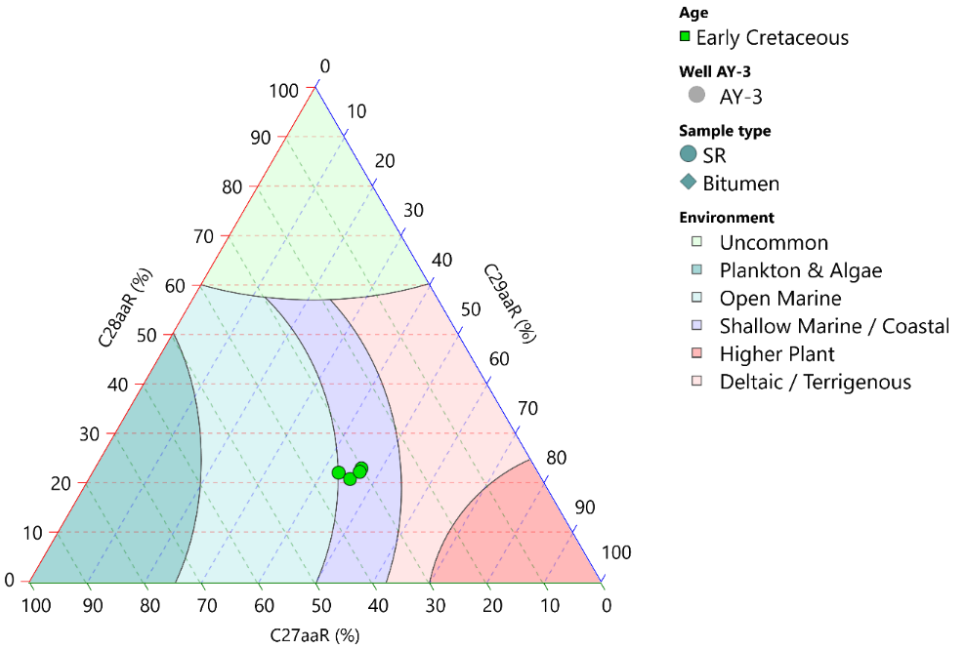

Figure 32. Ternary diagram of normal sterane distribution for the analyzed Early Cretaceous samples from the AY-3 well.

Aromatic biomarkers from all four Early Cretaceous samples show an abundance of lighter components, indicating a freshwater origin [252]. However, the presence of TAS in the upper organic-rich layer points to more marine conditions. The absence of 2,3,6 AIP, typically associated with photic zone anoxia and euxinia [230–232], suggests less reducing conditions or a mixed water column with lower stratification.

Moldowan et al. (1985) notes that MAS and sterane distributions help to assess the relative contributions of organic matter from land plants versus aquatic organisms. Several authors [89,218,253], suggest that non-marine algae may contain higher C29 sterols and MAS. Lower C29MAS relative to C27MAS in the silicate-rich 10KD sample implies a more marine environment, while the higher C29MAS in the carbonate-rich 4KD sample suggests a more restricted, algal-dominated setting with reduced terrigenous input [89] indicated by a C29/(C28 + C29) ratio lower than 0.5, compared to the higher than 0.5 ratio in the 4KD sample. This setting is further supported by the XRF data and narrower Ea-distributions in the upper organic-rich layer. TAS ratios (C20 and C21 nearly equal to C26+) and low C26TAS relative to 28S and 27RTAS support low salinity for this interval [259] while heavier TAS components observed in m/z 231 suggest a marine depositional environment.

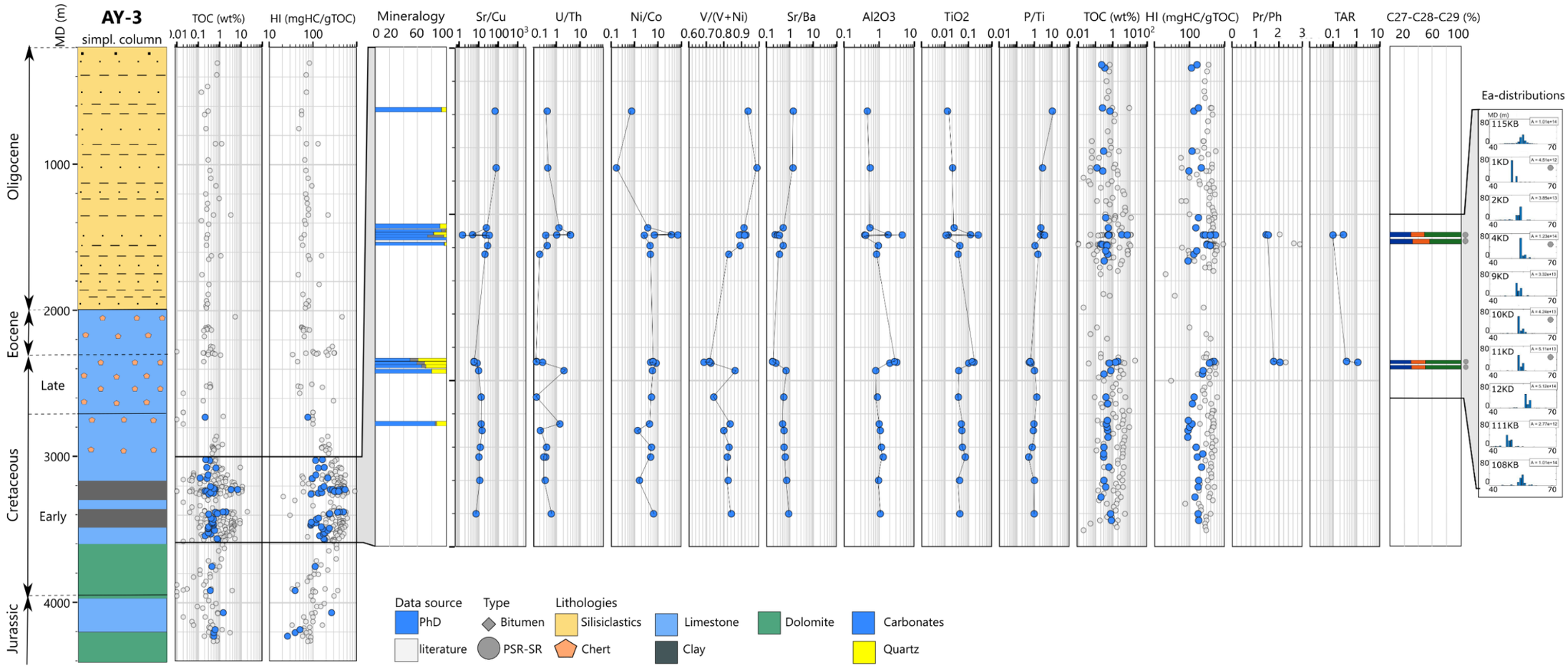

Figure 33.Multi depth plot of the AY-3x well including XRF proxies, RE6 parameters, biomarker ratios and Ea-distributions from the analyzed samples. The grey-shaded area indicates the interval of studied samples, corresponding to the Early Cretaceous and encompassing the two organic-rich layers.

6.2. Comparative distribution of generation kinetics, geochemical and mineralogical characteristics in wells and outcrops of Western Greece

6.2.1. Late Triassic – Early Jurassic

6.2.1.1. Organic content

Organic carbon content reaches 35.56 wt%, with S2 values up to 202.04 mgHC/grock, indicating excellent hydrocarbon potential (Figure 34, Figure 35). Rock-Eval 6 analysis shows thermal immaturity, with most Tmax values below 435°C. In TOC-rich samples (> 0.5 wt%), HI values reach at least 334 mgHC/gTOC. HI vs. OI and Tmax plots (Figure 34) mostly follow the Type I–II kerogen trend, however Type IIS kerogen can overlap with Type I due to high hydrogen content and sulfur substitution for oxygen [132,254].

Alexandridis et al. (2022) also classified this organic-rich interval as Type IIS kerogen based on Rock-Eval 7S results, suggesting deposition in a strongly anoxic, restricted -likely lagoonal- basin, further supported by elevated sulfur content, illustrated also in this study (Table 13).

Petrographic analysis by Alexandridis et al. (2022), confirms this classification, showing a dominance of liptinite (mainly bituminite and alginite), solid migrabitumens, inertinite fragments, and minor primary/recycled vitrinite; all characteristic of Type IIS kerogen in a reducing, restricted basin. The presence of solid migrabitumens indicates significant maturation and hydrocarbon generation.

Ea-distributions for this interval show low activation energies (45–57 kcal/mol), consistent with thermally labile sulfur-bound kerogen in this interval [105,124].

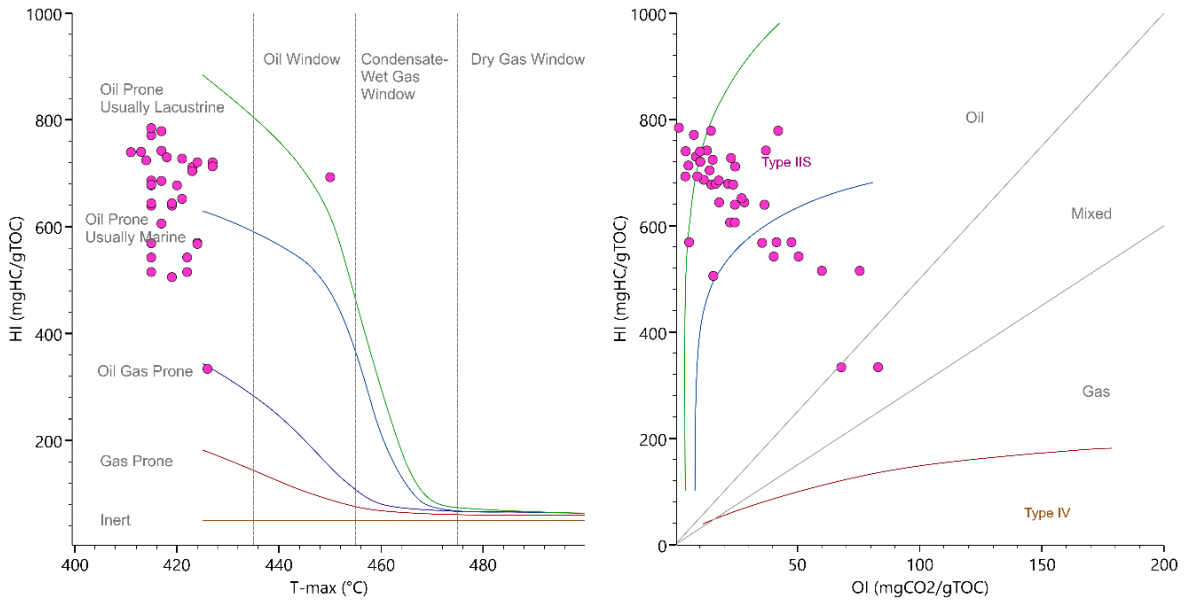

Figure 34: (Left): HI vs. Tmax plot, modified from Hackley & Lünsdorf (2018). (Right) Pseudo-Van Krevelen diagram for Late Triassic – Early Jurassic samples (TOC > 0.5 wt%). Kerogen type lines from Dembicki (2009).

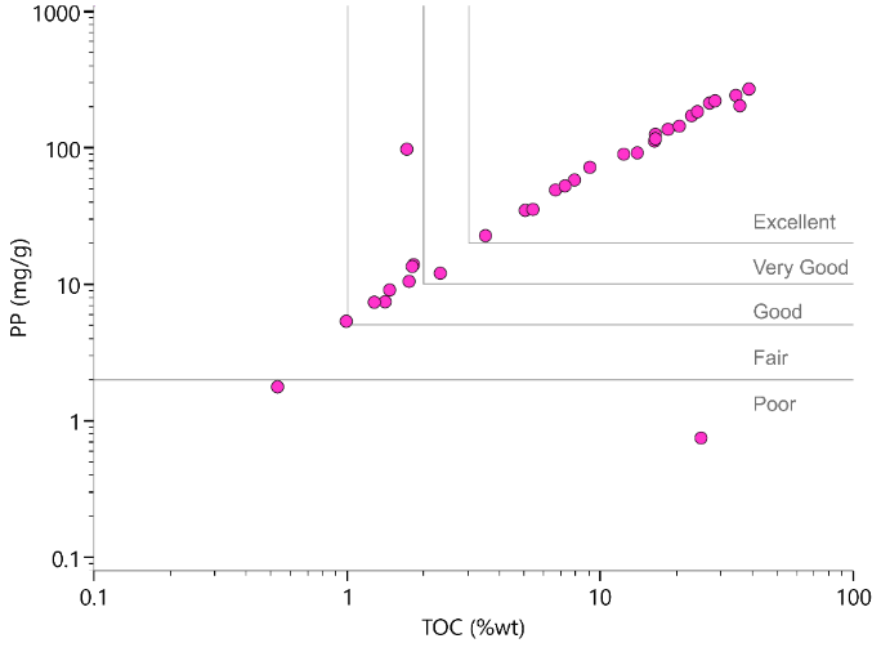

Figure 35. PP (mgHC/gTOC) vs. TOC (wt%) plot representing the kerogen generation potential of the Late Triassic – Early Jurassic samples with TOC > 0.5wt%.

6.2.1.2. Geochemical signatures

Mineralogical analysis of four organic-rich samples reveals calcite up to 2 wt% and dolomite up to 93 wt% (Figure 36). Silicate minerals reach 7 wt% in D23, E4, and 7-21-J1, while C26 (the northernmost sample) contains 21 wt%, with illite/chlorite making up 62 wt% of its 95 wt% silicate fractions.

The Ca content; Ca/(Fe+Ca) > 0.6 and wide range of Sr/Ba proxy values suggest fresh to brackish depositional environments according to the literature [185,240], apart from D23 and E4, where higher values and gypsum content indicate saline waters. However, as whole-rock samples, interpretations require caution. Paleoclimate Sr/Cu proxy suggests humid and warm conditions for samples below 10, while ratios above 10 indicate a dry, hot climate [255]. Most samples fall below 10, except 7-21-J1 and D23.

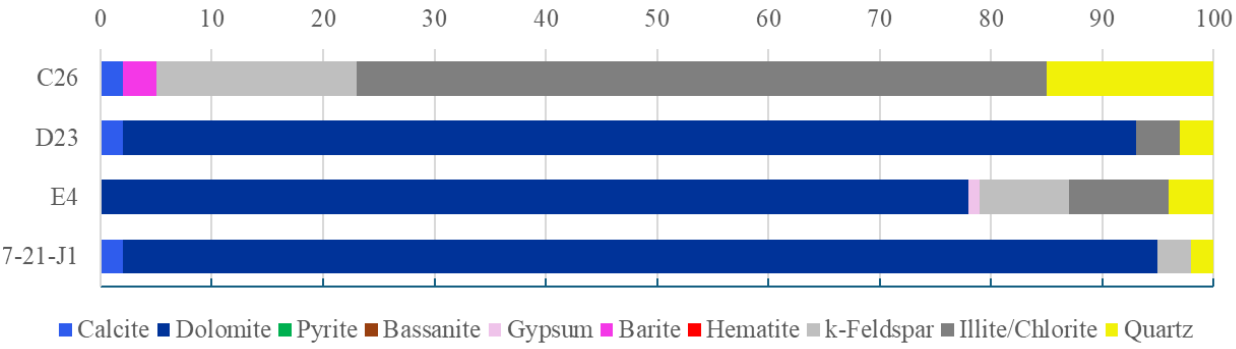

Figure 36. Mineralogy of the Late Triassic - Early Jurassic.

The V/(V+Ni) proxy averages 0.8, indicating moderately to strongly stratified, reducing conditions [255–257]. In contrast, Cr, typically detrital [261], found in the V/Cr ratio, which exceeds 5, confirms an anoxic depositional environment [163,256–258]. Nickelium, enriched under marine sulfate-reducing conditions [259,260], reaches 340 ppm, the highest in these samples. CHNS analysis shows total sulfur content between 9–9.51 wt%, aligning with literature findings [124,125,261]. Given the TOC/TS ratios (Figure 37) (5–1.5 for dysoxic/suboxic, < 1.5 for anoxic conditions) [183,262], these values suggest a suboxic to dysoxic environment, with periodic anoxia.

XRF analysis shows Fe content between 2.44 and 4.13 wt%, with no detectable siderite or pyrite, implying Fe incorporation into clay minerals or organic complexes. This supports a coastal setting

with fluctuating redox conditions. The presence of OM and sulfur suggests significant microbial activity, particularly sulfate-reducing bacteria, potentially influencing dolomitization and organic sulfur formation.

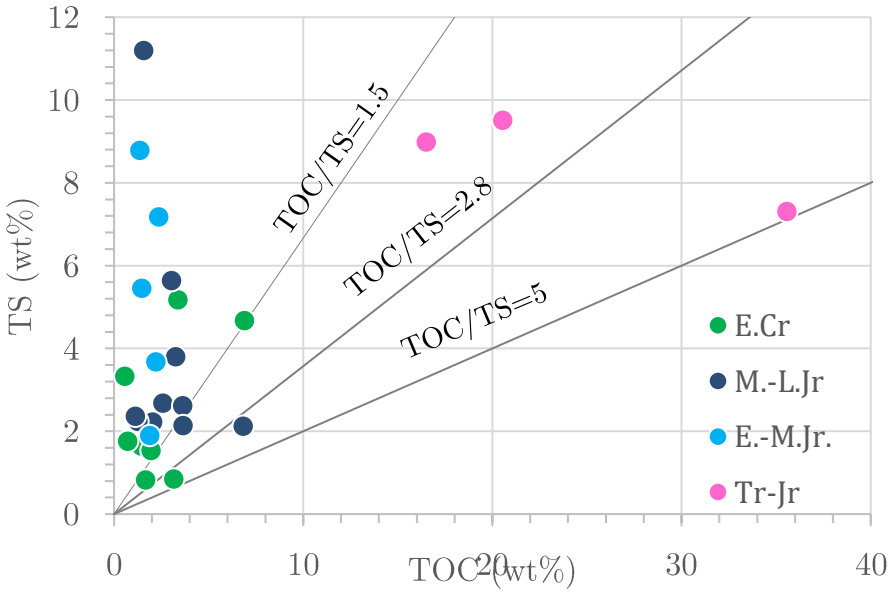

Figure 37. TOC vs. Total Sulfur (TS) plot, with marine condition trendlines. Modified after [183,262]. *"E.Cr." for Early Cretaceous, "M.-L.Jr" for Mid – Late Jurassic, "E.-M.Jr." for Early – Mid Jurassic and "Tr-Jr" for Late Triassic – Early Jurassic.*

The aliphatic content of Late Triassic – Early Jurassic samples shows distinct n-alkane distributions. The northern sample has a bimodal pattern (n-C28, n-C22 peaks), while the central sample exhibits a unimodal peak at n-C28. The middle sample peaks at n-C18, whereas the southern sample shows a shorter-chain alkane focus (n-C19 peak) (Figure 38).

The central sample, rich in long-chain alkanes, has a Paq value of 0.2 (Figure 39), indicating emergent macrophyte contribution. In contrast, northern and southern samples show higher Paq values (0.5–0.8), reflecting input from submerged/floating macrophytes.

Pr/Ph ratios (0.37–0.67) suggest reducing, hypersaline, anoxic conditions, with the central sample having the highest ratio (Figure 40), supported by elevated sulfur content. TAR values increase toward the basin centre (32.84 in the central sample; 3.14, 0.25 in the north; 0.3 in the south), indicating higher terrestrial OM input centrally, while northern/southern samples reflect more aquatic influence [263]. The southern sample, with detectable squalane, shows marine

characteristics, supporting a hypersaline, anoxic setting, further reinforced by the near absence of iC25, in accordance with published research [264].

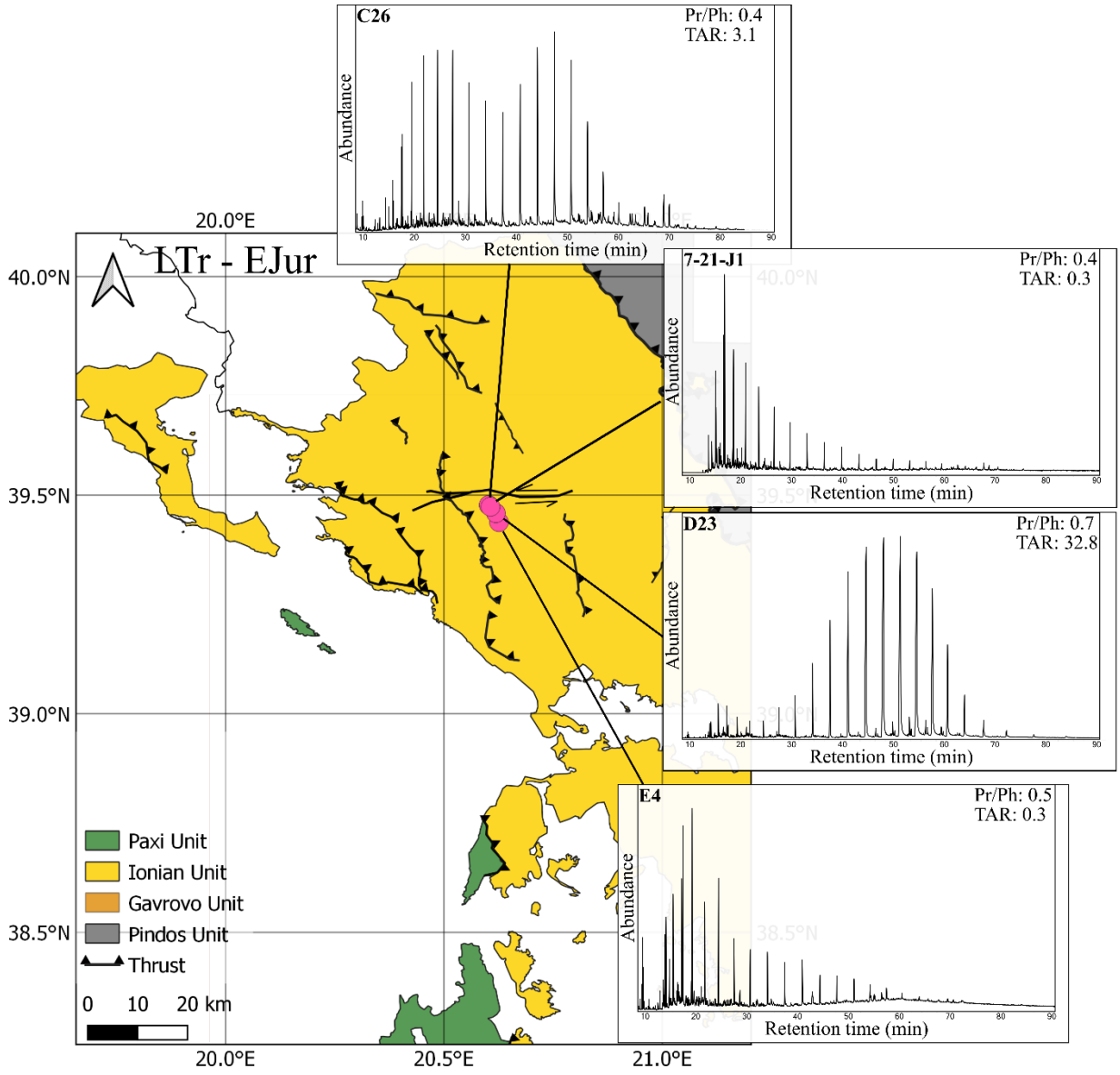

Figure 38. Regional distribution of Late Triassic – Early Jurassic samples. Exemplary m/z 85 gas chromatograms are shown with values for Pr/Ph and TAR.

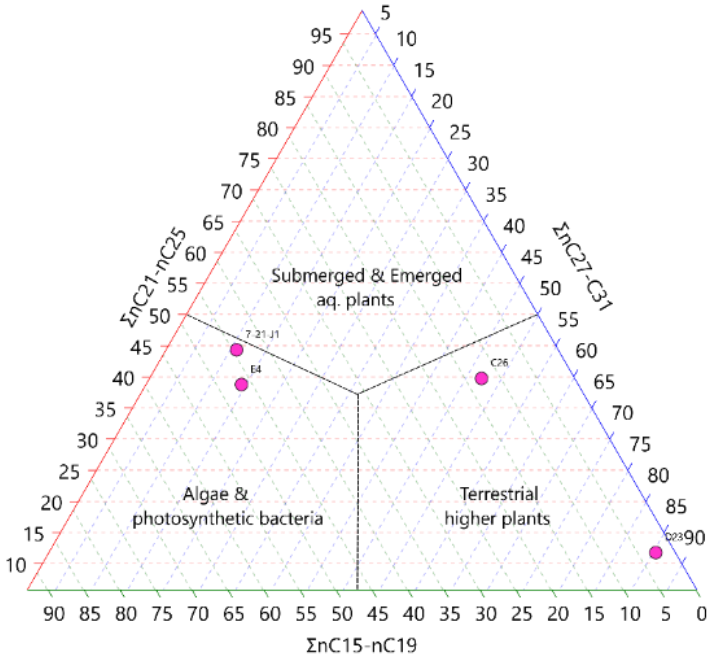

Figure 39. Ternary diagram of short-,mid- and long-chain normal alkanes categorizing OM sources for Late Triassic – Early Jurassic IU samples, modified from the literature [192,193].

The Ea-distribution (40–62 kcal/mol, peak at 50–52 kcal/mol) suggests predominantly marine organic matter [118], aligning with marine Ea-distributions observed by Sundararaman et al. (1992) and Southern European Type IIS kerogen shale reported by Dieckman (2005). Such distributions, consistent with the liptinite-rich interval studied by Alexandridis et al. (2022) coincide with organofacies type A [118,184].

Pregnane and homopregnane steroids, increase towards the geographically central area, indicating a restricted, hypersaline setting [82]. In contrast, the southern sample suggests a sulfur-rich depositional setting [83]. Sterane distributions point to a coastal to shallow marine environment, with higher C29aaaR in the south (Figure 41 and Appendix I, Figure S9). The C30+ steranes in northern and central samples indicate a distal setting [89,216], while their absence in the south indicates a more restricted setting.

The southern sample shows high C34HH and low C30+ steranes, supporting a restricted, evaporitic setting based on published frameworks [217]. Gammacerane presence and Gamm/30H ratio of 0.2 suggest limited freshwater input, and low C35HHI (0.03–0.06) (Figure 41) indicates anoxic conditions where higher homohopanes are not preserved [224]. The absence of tricyclic terpanes further supports this [89].

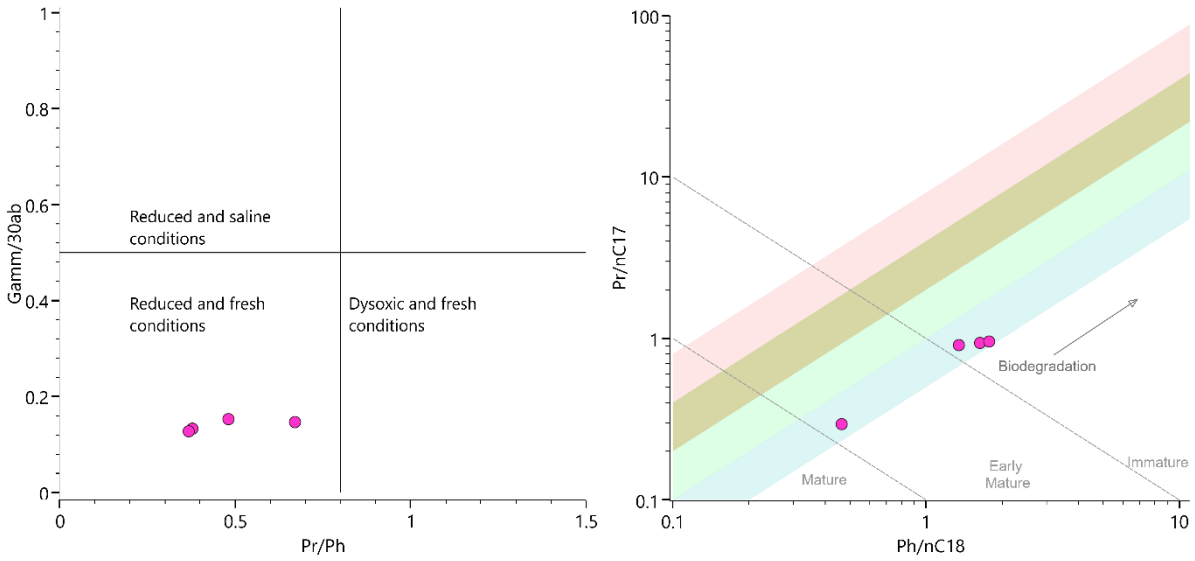

Figure 40. (Left): Pr/Ph vs. Gamm/30H, (Right): Pr/nC17 versus Ph/nC18 for the Late Triassic – Early Jurassic interval. Zonation description in Figure 19.

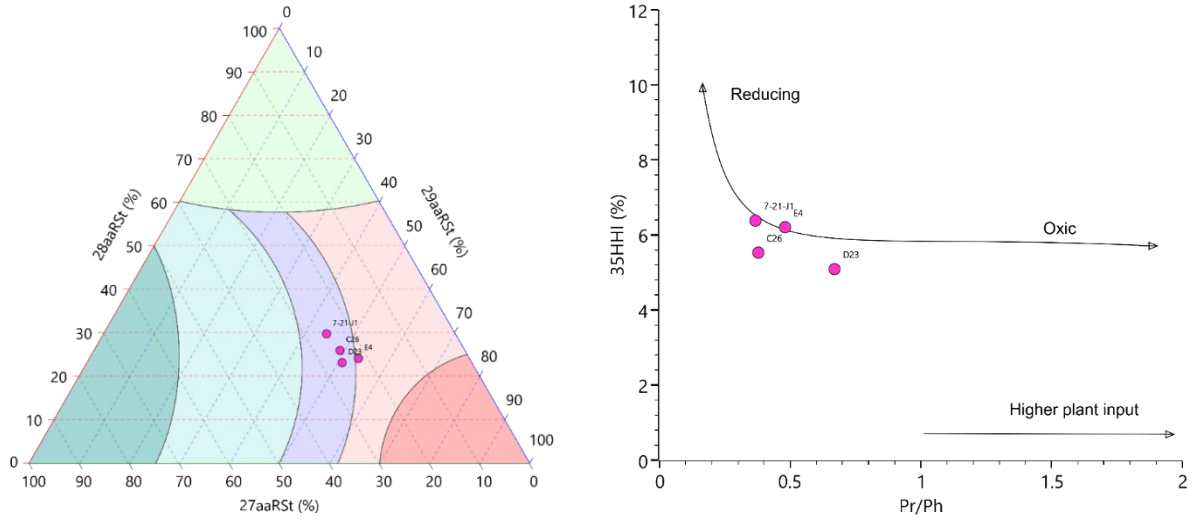

Figure 41. (Left): Ternary diagram of the m/z 218 Steranes of the Late Triassic - Early Jurassic samples. Zonation description in Figure 20. (Right): 35 HHI vs. Pr/Ph for the same interval, based on Peters et al. (2004).

AIP (C15–C22) are present, with C18AIP and C19AIP most abundant (Figure 42 and Appendix I, Figure S11), indicating anoxic/euxinic conditions, likely derived from chlorobactene or isorenieratane (GSB) precursors [230,231,234–236]. AIR values lower than 1 suggest persistent

photic zone euxinia under sulfidic conditions [233]. Such restricted basin environments were common during the Triassic–Jurassic transition [58], supporting the presence of a euxinic photic zone in a coastal setting, intermittently silled, with increased terrigenous input in the central area. The δ^{13}Corg values (–29.6‰ to –29.9‰) align with the Rhaetian negative carbon isotope excursion, linked to CAMP; related carbon cycle disturbances in the Eiberg Basin, western Tethys Ocean [265]. Their narrow range suggests consistent carbon sources and depositional conditions.

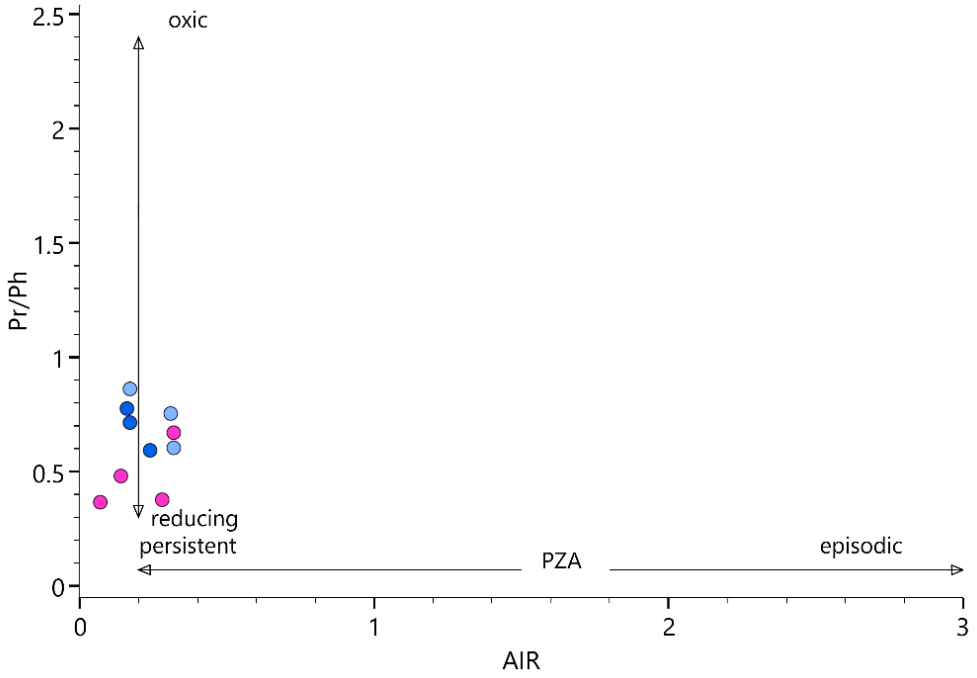

Figure 42. Pr/Ph v. Aryl isoprenoid ratio (C13–C17)/C18–C22) AIR, after literature studies [233,266] *for Late Triassic – Early Jurassic (pink), Early – Mid Jurassic (light blue), and Mid – Late Jurassic (blue). Low AIR values indicate more persistent photic zone anoxia (PZA).*

6.2.2. Early – Mid Jurassic

6.2.2.1. Organic content

Rock-Eval 6 pyrolysis was conducted on 51 samples, including PU (PxGa-1x well), IU outcrop, and IU (AY-3 well) samples.

- PxGa-1x well: S2 = 0.1–21.91 mgHC/grock, TOC up to 4.59 wt%.
- AY-3 well: S2 up to 0.31 mgHC/grock, TOC up to 0.61 wt%.

- IU outcrop: S2 = 0.01–9.28 mgHC/grock, TOC up to 2.55 wt%.

Tmax values indicate higher maturity in PU (418–461 °C) compared to IU (411–439 °C), likely due to deeper burial or less erosion. Kerogen distribution follows the Type II trend in the pseudo-Van Krevelen diagram, consistent with AOM dominance in the Paxi and Ionian Units [51,73,79]. Early–Mid Jurassic intervals in Epirus, Western Greece, contain liptinite macerals (alginite, sporinite) typical of Type I–II kerogens, with minor vitrinite and inertinite, suggesting a marine depositional setting with minimal terrestrial input [51,73,79].

6.2.2.2. Geochemical signatures

A subset of seven organic-rich source rock samples was analyzed, with two samples from the PU and four from IU outcrops. IU outcrop samples (E28, E38, B19, F31) show a balance between carbonates and silicates:

- E28 & E38 (Central IU): Carbonate-rich (calcite ~57 wt%, silicates 40 wt%)
- B19 & F31 (Western IU): Silicate-rich (52–64 wt%, calcite 28–42 wt%)

In the PxGa-1x well, mineralogy is carbonate-dominated with calcite reaching 99 wt%, dolomite lower than 14 wt% and anhydrite reaching 20% (Figure 43), aligning with the literature [28,60].

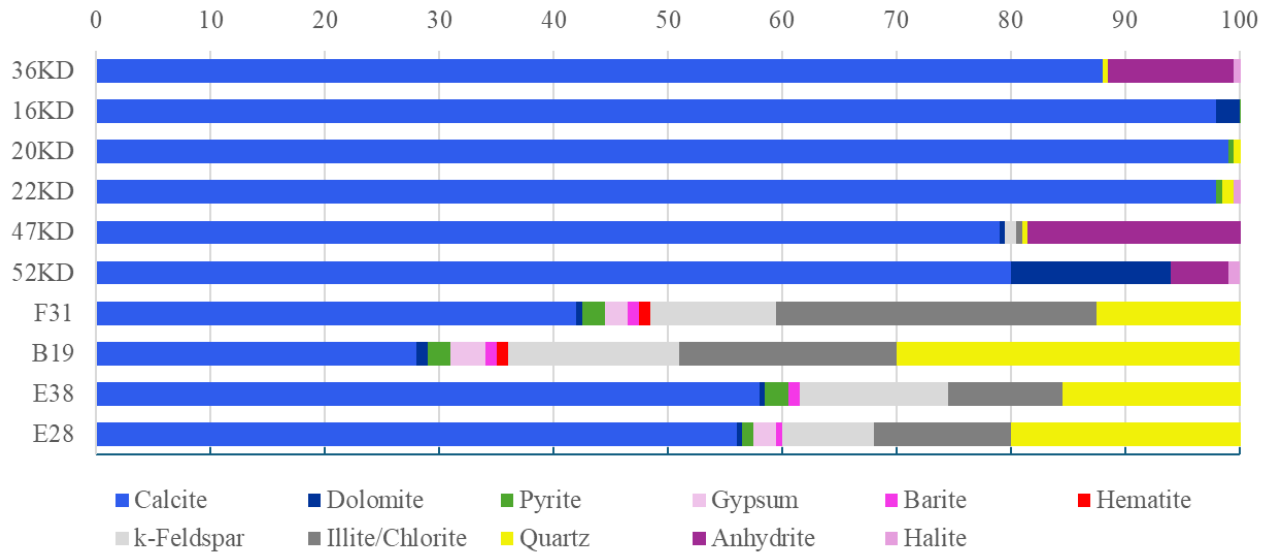

Figure 43. Mineralogy for the Early - Mid Jurassic samples.

Geochemical proxies provide further insight into the depositional environment. The V/(V+Ni) ratio ranges from 0.7 to 0.95, with the highest values observed in the PxGa-1x well. The V/Cr ratio varies between 2.5 and 5.7 in IU outcrop samples but exceeds 30 in PxGa-1x well samples, suggesting dysoxic conditions for samples B19 and F31, and anoxic conditions for E28 and E38. The presence of vanadium and nickel further supports oxygen-deficient to anaerobic conditions, particularly in the deeper PxGa-1x samples with increased anhydrite content. The Sr/Ba ratio, a proxy for paleosalinity [255], is significantly elevated in the PxGa-1x well, ranging from 1.7 to 68, while the outcrop samples indicate moderate salinity, with ratios below 3.8.

Ea-distributions reveal differences in OM composition. PU samples exhibit a narrow Ea range, with two dominant peaks centred around 50 to 54 kcal/mol, accounting for 72 to 93% of their total generation potential. In contrast, IU outcrop samples display broader Ea-distributions, with two principal peaks between 49 and 57 kcal/mol accounting for 46% of their generation potential, suggesting a more diverse organic input.

These samples are classified as Type II kerogen, with abundant liptinite, including alginite and sporinite as discussed by many authors [51,73,79], indicative of dysoxic to anoxic marine conditions. The Ea-distributions, with peaks between 49 and 57 kcal/mol, align with liptinite-rich organofacies described in previous studies and resemble the Ea-distribution of a marine Type II Toarcian source rock [106,108,118,184].

The aliphatic content (m/z 85) further differentiates the PU and IU samples. The IU samples exhibit a unimodal distribution, primarily peaking between n-C16 and n-C18, while the PU samples show a slightly bimodal pattern, with peaks at n-C18 and n-C22 for the 20KD samples and at n-C24 for the 22KD sample (Figure 44). The Paq values are relatively consistent, averaging 0.59 for PU and 0.62 for IU (Figure 45), suggesting input from submerged or floating macrophytes [191].

Pr/Ph ratios average 0.68 for the PU and 1.08 for the outcrop samples (Figure 46 and Figure 47), with the highest values (~1.3) in the central IU samples E28 and E38. TAR values are the lowest in the central IU, increasing three to four times westwards, maximizing in the PU. This pattern suggests reducing conditions in the IU outcrop samples and greater terrestrial influence in the PU. The presence of squalane in the B19 and F31 samples is particularly significant, as these samples exhibit a unimodal alkane distribution and a higher concentration of C30 HBI to the PU, with literature frameworks suggesting lipid-producing organisms adapted to extreme salinity [83,264].

Additionally, these samples contain less carbonate, with gypsum making up 2–3 wt% of their mineral facies.

The nC27/nC17 ratio in the unimodal IU samples remains low, indicating a marine environment, consistent with findings by Karz and Lin (2014). In contrast, this ratio in the PU ranges from 0.99 to 1.82, decreasing with shallower depths, further supporting the interpretation of shallower depositional settings in the PU compared to the IU.

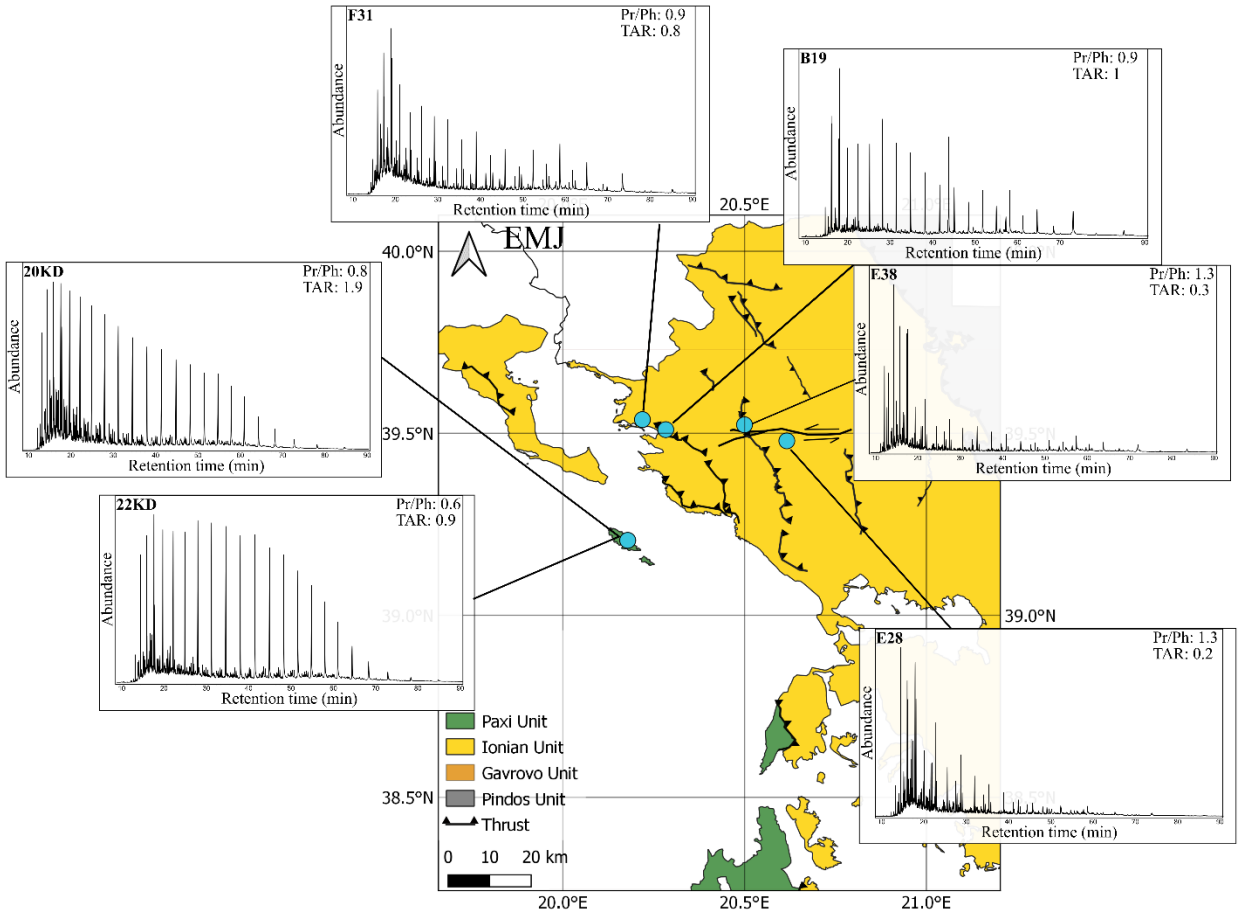

Figure 44. Regional distribution of Early – Mid Jurassic samples. Exemplary m/z 85 gas chromatograms are shown with values for Pr/Ph and TAR.

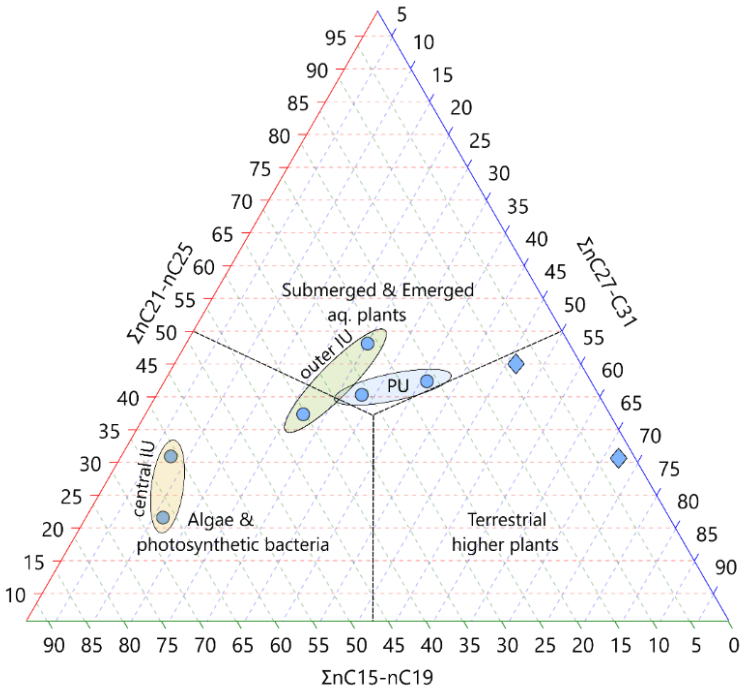

Figure 45.Ternary diagram of short-,mid- and long-chain normal alkanes to essential categories of OM for the Early – Mid Jurassic studied samples, modified from the literature [192,193].

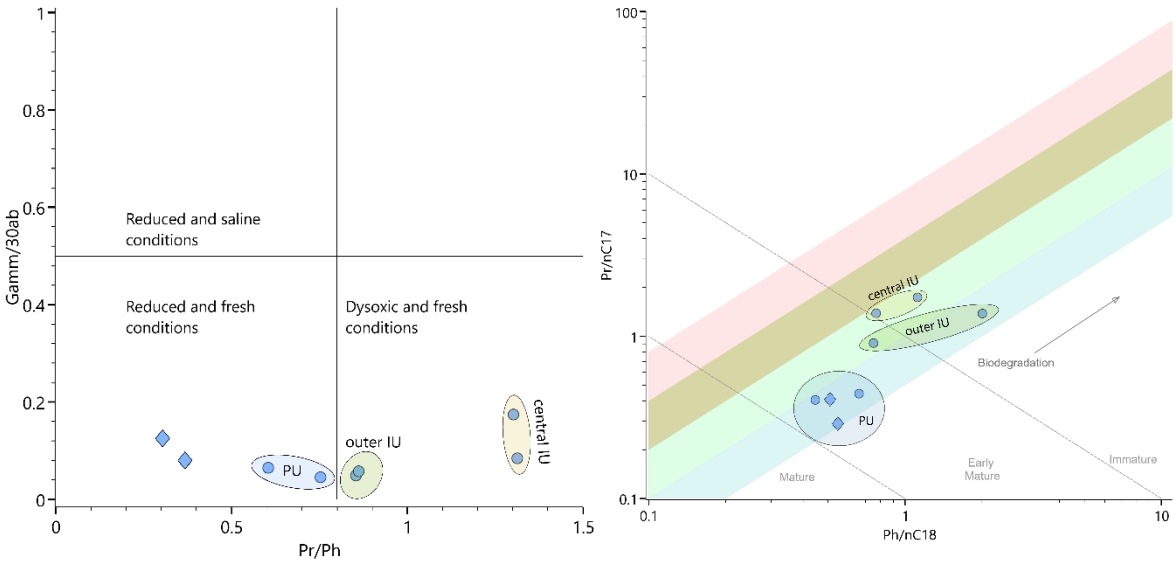

Figure 46.(Left): Gamm/30H vs. Pr/Ph and (Right): Pr/nC17 vs. Ph/nC18 for the Early – Mid Jurassic interval, indicating the depositional conditions. Zonation description in Figure 19.

Pregnane and homopregnane concentrations are lower in the IU than in the PU, suggesting a less restricted basinal setting. The distribution of regular steranes in the IU outcrop samples indicates a stronger terrestrial influence compared to the PU, reflecting a depositional environment closer to the terrestrial OM source. However, potential co-elution of C29aaaR with another biomarker complicates this interpretation.

C30 steranes are less abundant in the IU than in the PU, further supporting a marine depositional setting. Although gammacerane is identified, its low concentration in the B19 sample does not indicate a hypersaline event, an alkaline lake, or a lagoonal environment with strong anoxic conditions [221,224]. Additionally, the absence of elevated C35HHI values [267] suggests a more freshwater-influenced character for the central IU and a less oxidizing environment than the PU based on Peters and Moldowan (1991). However, no other evidence supports a lacustrine freshwater setting, and hopanes remain more abundant than tricyclic terpanes.

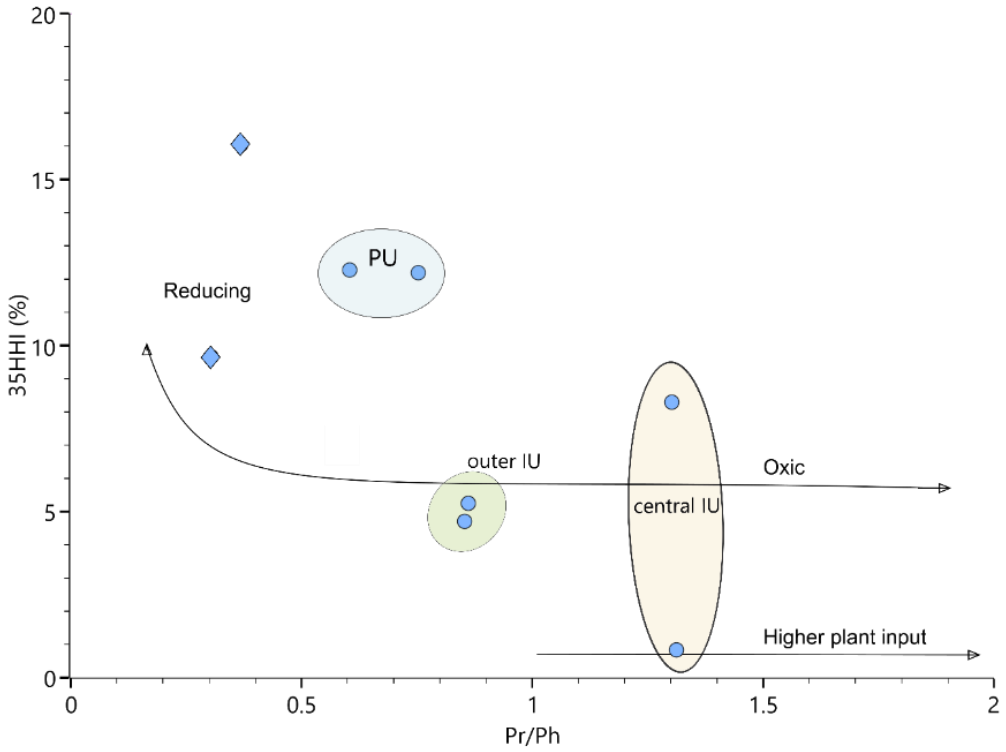

Figure 47. Pr/Ph vs. 35 HHI for the Early - Mid Jurassic interval according to Peters et al. (2004).

Hopenes were not identified in the Early – Mid Jurassic PxGa-1x (PU) samples but are abundant in the onshore organic-rich IU samples from this interval (Appendix I, Figure S12). Unsaturated

and re-arranged hopane derivatives, such as hop-17(21)-ene and neohop-13(18)-ene respectively, typically originate from microbial and plant sources, including anaerobic bacteria [268], ferns [269], and specific bacterial taxa like Alicyclobacillus acidocaldarius, Rhodomicrobium vannielii [270], Frankia sp. [271], and Zymonas mobilis [272].

The origin of neohop-13(18)-ene is debated but often linked to stratified waters and bacteria near or below the chemocline [156]. Hop-17(21)-ene is thought to derive primarily from diploptene, but longer-chain homologs (C31+ homohop-17(21)-enes) may have multiple bacteriohopanepolyol precursors [156,273]. These hopenes are most abundant in thermally immature sediments, where clay-catalysed isomerization occurs [156,274].

Neohop-13(18)-ene has been associated with both terrestrial organic matter and marine bacterial sources [275], supporting the hypothesis that hop-17(21)-enes are synthesized by cyanobacteria and methanotrophs in stratified, reducing environments [276,277]. These compounds have been identified in Toarcian sediments from Germany [278] and Italy [279], Early Cretaceous samples from China [280] and Miocene from Norway [281], often linked to hypersaline or stratified, anoxic conditions [278,280]. However, some studies have detected hopenes in oxic-suboxic settings, sparking debate about their role in marine systems [156,207,276,282,283].

Nytoft et al. (2015) proposed that C30–C35 hop-17(21)-enes likely originate from cyanobacteria and methanotrophs, with C35 hopanoid precursors forming hop-17(21)-enes in the subsurface of reducing, stratified basins [277]. The presence of hopenes in IU samples suggests microbial activity in such stratified, possibly suboxic waters. However, their abundance does not strongly indicate hypersaline conditions, as evidenced by low gammacerane levels, low AIP abundance, and high AIR ratios where present.

The δ^{13}Corg depletion observed in IU samples aligns with global isotopic trends linked to the Toarcian OAE, a period marked by extensive marine anoxia and enhanced organic matter preservation. This depletion suggests a significant influx of isotopically light carbon, likely from large-scale volcanic emissions or methane release, leading to redox changes in the water column [284–286] and enhancing organic matter preservation in sediments.

Central IU samples (–28.26‰ to –28.67‰) suggest marine influence and sustained anoxia. Slightly less depleted outer IU samples (–27.75‰ to –28.33‰) imply episodic oxygenation or increased terrestrial input. PU samples are even less depleted, supporting a restricted setting with periodic anoxia, possibly due to localized euxinia or stratification.

Overall, the geochemical and isotopic data, suggest that during Early – Mid Jurassic, the IU represents a predominantly marine, dysoxic to anoxic setting with Type II kerogen, microbial activity, and periodic stratification. Its δ^{13}Corg depletion of the organic-rich samples aligns with the Toarcian OAE, indicating global carbon cycle disruptions. In contrast, the PU was more restricted, periodically euxinic, with higher salinity and greater terrestrial influence. Mineralogical and biomarker evidence suggests the IU experienced stable anoxic conditions, while the PU underwent fluctuating water levels and localized euxinia.

6.2.3. Mid – Late Jurassic

6.2.3.1. Organic content

Mid to Late Jurassic samples exhibit TOC levels between 1–3.7 wt%, with peak values of 6.85 wt% in Lefkada's Late Jurassic sample. S2 values reach 24.1 mgHC/grock in PxGa-1x and 33.4 mgHC/grock in Lefkada, indicating strong hydrocarbon generation potential. Thermal maturity varies, with PxGa-1x samples showing Tmax values around 419°C, while the 1-19-LE sample is immature (Tmax 409°C).

The HI vs. OI plots the Mid – Late Jurassic samples along the Type I–II kerogen trend and the Late Jurassic samples along the Type II trend. However, there is no indication of a lacustrine depositional environment [22,51,57].

Organic petrography conducted by Oikonomopoulos et al. (2023) confirms gas-prone Type III kerogen with few vitrinite particles, with some Type IV material. Vitrinite has a mean Ro of 0.59%Ro, placing it at the onset of the oil window (~0.60%), indicating early maturity. UV light excitation analysis reveals alginite and hydrocarbon spheres with greenish-yellow fluorescence, and fracture-filling migrabitumen consistent with a marine source [86].

6.2.3.2. Geochemical signatures

The Mid – Late Jurassic samples from the PU are carbonate-dominated (82–99 wt% calcite), with silicate content ranging from 1–17 wt%. In contrast, the Late Jurassic Lefkada sample has a more balanced mineralogy (57 wt% calcite, 36 wt% silicates). Two PU samples contain minor halite, while Lefkada has 6 wt% gypsum (Figure 48).

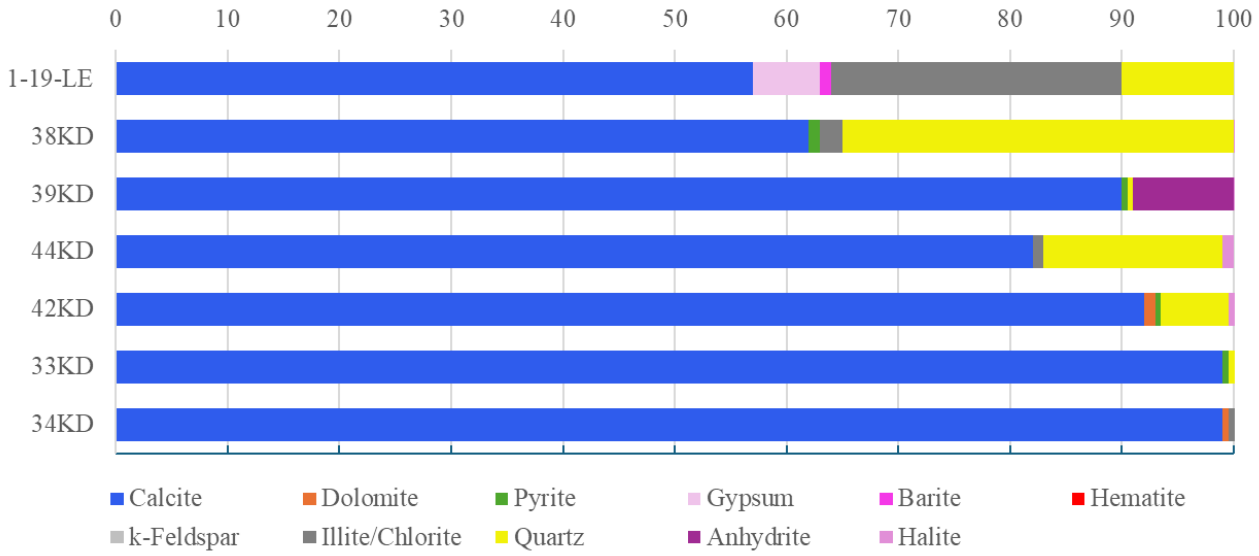

Figure 48. Mineralogical composition of the analyzed Mid – Late Jurassic samples.

Elemental proxies (Ca/(Fe+Ca) averaging 1, V/(V+Ni) averaging 0.8, V/Cr exceeding 5.7, and Sr/Ba ranging between 0.49–6.9) suggest a marine, reducing environment with stratified to strongly stratified waters, according to classifications from several researchers [255,256,287,288]. Alkane distributions highlight differences: PxGa-1x samples contain predominantly short-chain alkanes, while the Late Jurassic Lefkada sample shows a mid-chain alkane dominance with a strong odd-even predominance (Figure 49 and Figure 50). The Paq averages 0.55, and Pr/Ph is lower than in PxGa-1x (Figure 51). The nC27/nC17 ratio is four times higher in Lefkada, and the TAR is three times greater, reflecting a stronger terrestrial influence and the presence of submerged or floating macrophytes [191] in Lefkada compared to the PxGa-1x samples.

Unlike PxGa-1x samples, the Lefkada Late Jurassic sample shows limited C27–C29 steranes, dominated by C29aaaR (Figure 51). The aaaR > aaaS ratio, absence of abb isomers, and RE6 data indicate thermal immaturity. The lack of C30 steranes and C29 dominance suggest a non-marine or marginal marine setting [89].

Tricyclic terpanes, indicative of marine organic matter, are significantly less abundant in Lefkada compared to PxGa-1x. The dominance of C31 moretane and C30 tricyclic terpane further reflects the lower maturity of 1-19-LE. The higher abundance of C30 hopane relative to C29 hopane hints at some marine contribution, while hopenes suggest either an immature setting or bacterial activity.

The absence of abbR homohopanes (> C33) aligns with the overall low maturity of 1-19-LE sample, suggesting a nearshore setting with hopanoid-producing bacteria which did not contribute to longer-chain hopanoids.

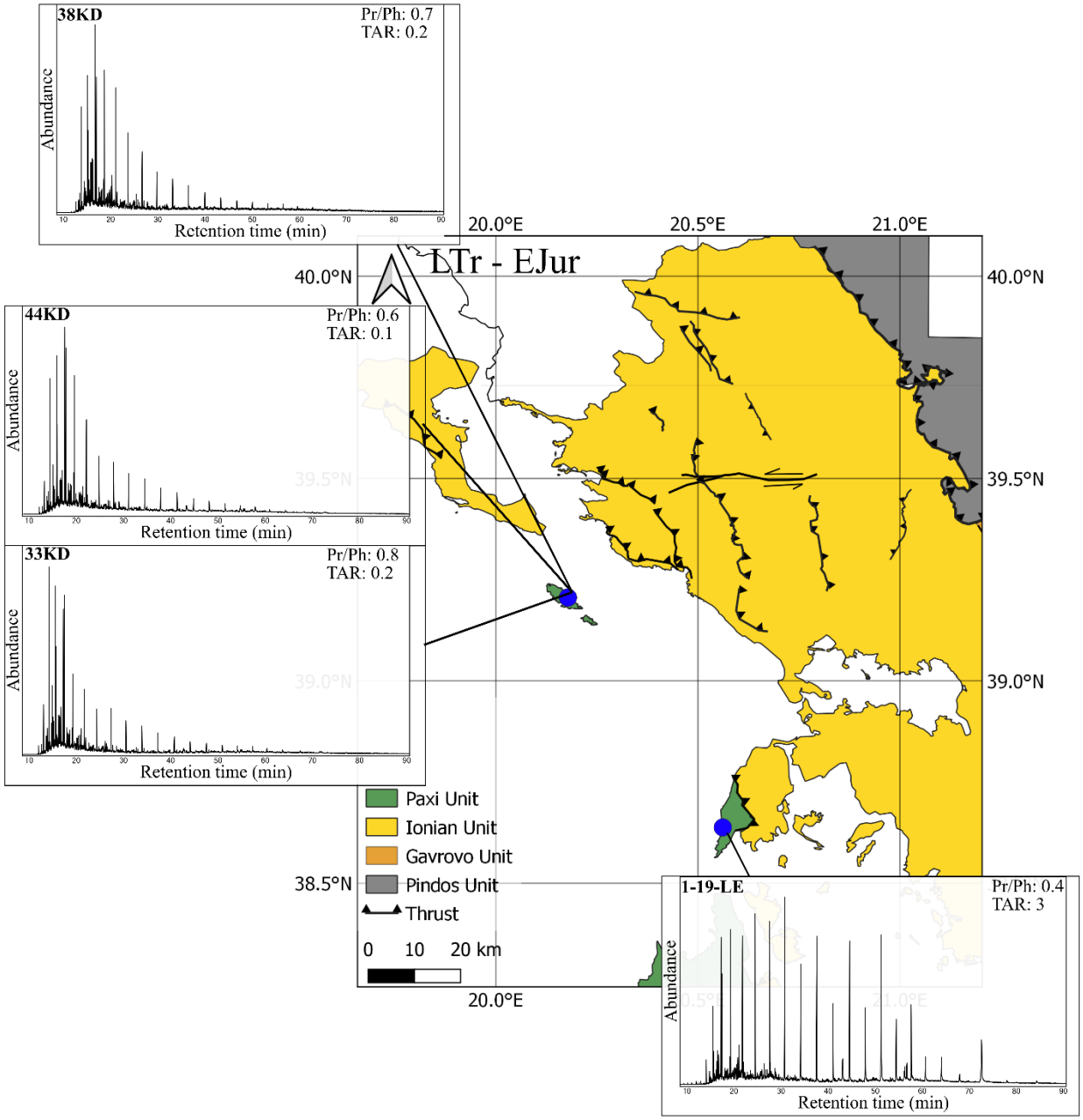

Figure 49. Regional distribution of Mid - Late Jurassic samples. Exemplary m/z 85 gas chromatograms are shown with values for Pr/Ph and TAR.

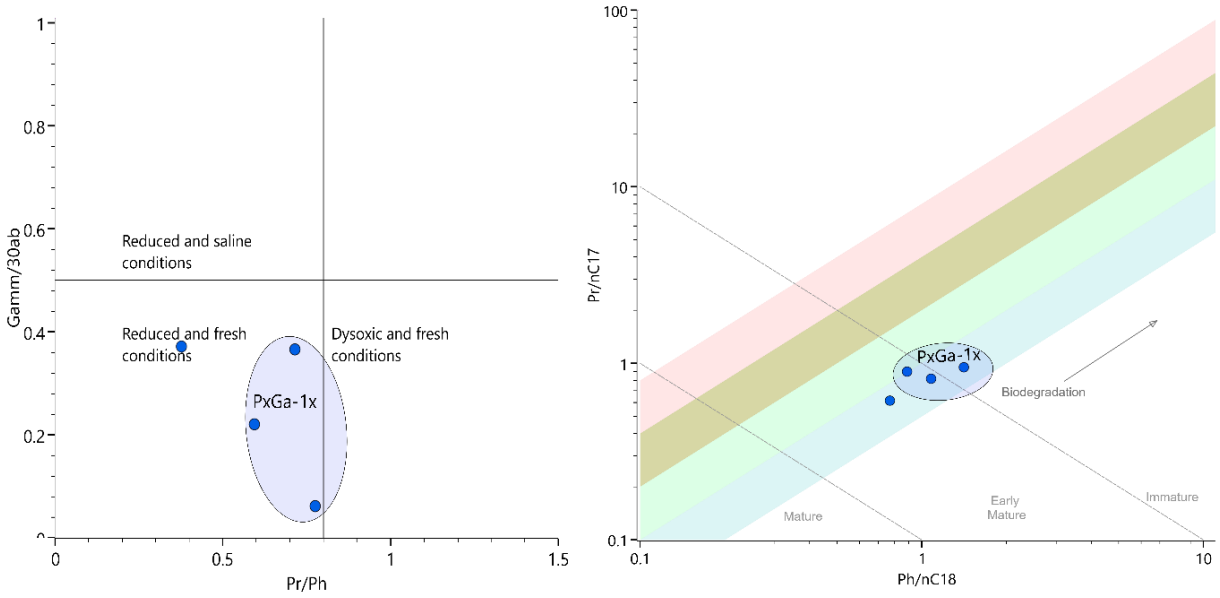

Figure 50.(Left): Gammacerane/C30H vs. Pr/Ph, (Right): Pr/nC17 vs. Ph/nC18 for the Mid – Late Jurassic interval, indicating the depositional condition. Zonation description in Figure 19.

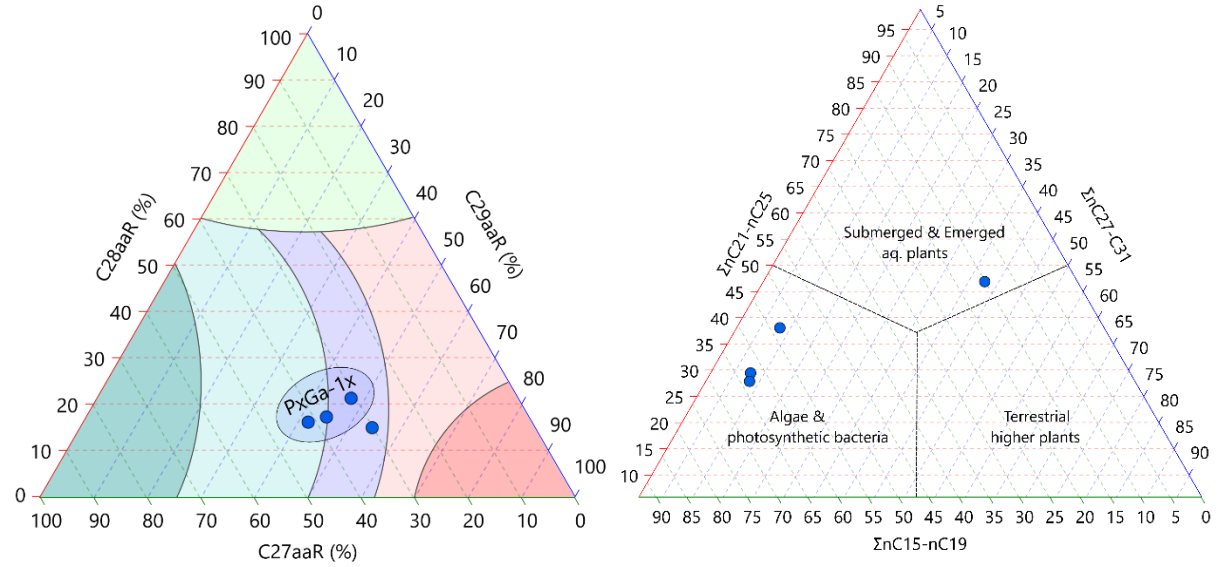

Figure 51. (Left): Ternary diagram of normal sterane distribution of the analyzed Mid – Late Jurassic samples, modified after Huang and Meinschein, Moldowan et al., and Peters et al. [84,222,223]. Zonation description in Figure 20. (Right): Ternary diagram of short-,mid- and long-chain normal alkanes to essential categories of OM for the Mid – Late Jurassic studied samples, modified from the literature [196,197].

The lack of aryl isoprenoids (AIP) (Table 11) further supports a mixed marine-terrestrial setting rather than photic zone euxinia, reinforcing a coastal environment with moderate marine influence and low thermal maturity, in contrast to the marine-dominated Mid – Late Jurassic PxGa-1x samples characterized by algal and bacterial productivity, according to literature classifications [231,232].

The 1-19-LE Late Jurassic sample also exhibits a depleted δ^{13}Corg value of –29.11‰. Elevated CO_2 levels during this period likely enhanced terrestrial vegetation growth, contributing to this isotopic signature [289]. The δ^{13}Corg values are consistent with organic matter derived primarily from C3 plants, reflecting low thermal maturity and limited marine contributions, aligning with broader Late Jurassic carbon cycle trends in Late Jurassic carbon cycle dynamics [289,290].

Kinetic analysis of the Lefkada sample reveals a broad Ea-distribution (49–63 kcal/mol), with focal Ea points between 55–77 kcal/mol comprising 36% of total generation potential. The high frequency factor (7.92e14 s^{-1}) and broad Ea-distribution suggests a chemically diverse kerogen [98,184]. While a broad Ea range often indicates a marine source, the increased magnitude above 55 kcal/mol suggests a stronger terrestrial component [118], similar to vitrinite-rich terrestrial samples analyzed by a recent study [106].

In contrast, Mid – Late Jurassic PxGa-1x samples exhibit a narrower Ea-distribution, ranging primarily between 44–54 kcal/mol, with two major peaks contributing to 55–68% of the total generation potential. This suggests a more homogeneous organic matter composition, with Rigakis (1999) reporting abundant AOM as discussed previously.

These mineralogical and organic geochemical contrasts indicate that the PU developed organic-rich intervals under stratified marine conditions, while 1-19-LE Late Jurassic sample reflects increased terrestrial input, lower maturity, and a marginal marine setting.

6.2.4. Early Cretaceous

6.2.4.1. Organic content

Rock-Eval 6 analysis was conducted on 45 samples from the AY-3 well, 6 from the PxGa-1x well, and 3 outcrop samples.

- TOC values: 1.67–3.16 wt% (outer IU), 0.12–6.89 wt% (inner IU), 0.15–0.72 wt% (PU).
- HI values: reach 516 mgHC/gTOC (outer IU), 544 mgHC/gTOC (inner IU), and 514 mgHC/gTOC (PU).

These values indicate Type II kerogen (Figure 52) and hydrocarbon generation potential ranging from poor to excellent. Less organic-rich samples deviate from this trend, with higher OI values and lower S2, suggesting a predominance of Type III kerogens.

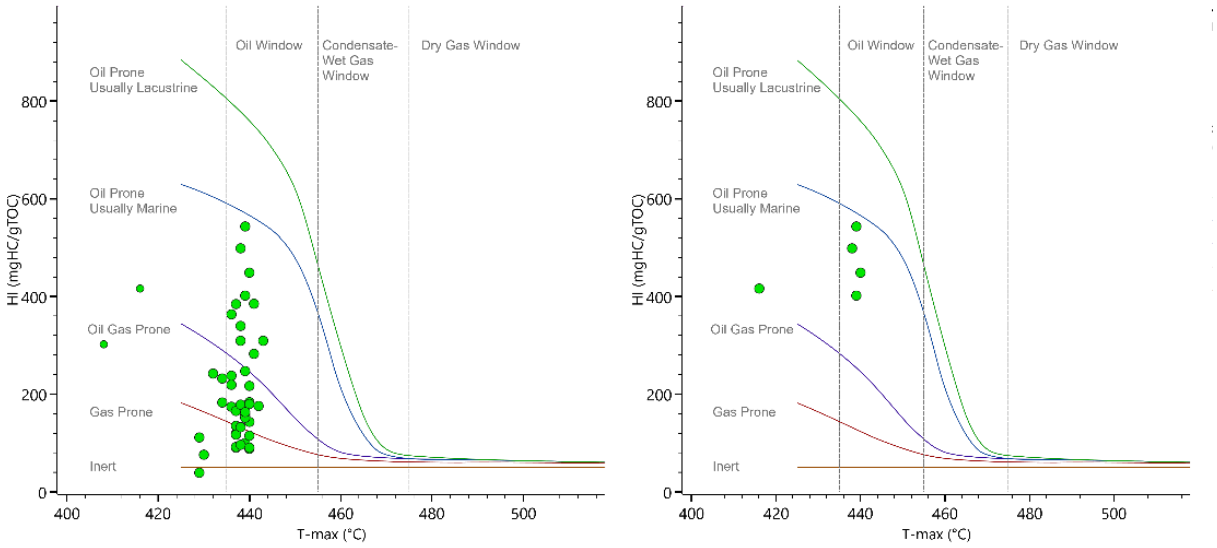

Figure 52. (Left): HI vs. Tmax for the Early Cretaceous analyzed samples, and (Right) for the most organic-rich samples, modified after Hackley and Lünsdorf (2018).

The Early Cretaceous Vigla formation, analyzed by Foscolos (1989) and Rigakis (1999) using samples of corresponding depths to 1KD, 4KD, and 10KD samples, contains abundant liptinite, including Tasmanales marine algae, dinoflagellate cyst traces, and liptodetrinite within an amorphous fluorescing matrix. Vitrinite and inertinite particles are present in smaller quantities.

These studies concluded that the interval represents Type II marine kerogen, deposited under conditions with minimal terrigenous input.

A more recent study [86] identified a mix of primary vitrinite (Type III kerogen), two solid bitumen types, oil-prone liptinite (Type II), and inertinite (Type IV) in the 4KD sample. Vitrinite reflectance (0.68 %Ro) indicates early maturity, supported by Tmax values up to 440 °C. Under UV excitation, highly oil-prone telalginite exhibits golden-yellow fluorescence, while liptodetrinite fluorescence is consistent with VRo values. Bitumen fluorescence varies from greenish to dull yellow within a weakly fluorescing amorphous matrix.

6.2.4.2. Geochemical signatures

Mineralogical differences between the inner and outer IU samples reflect distinct depositional environments. Inner IU samples from the AY-3 well are carbonate-dominated, with calcite reaching 79 wt% and dolomite up to 47 wt% (Figure 53), consistent with pelagic carbonate sedimentation in an open marine setting, aligning with descriptions provided by various authors [28,57,90].

In contrast, outer IU samples from outcrops contain higher silicate content, with quartz (27–61%) and illite/chlorite (24–62%), and significantly lower carbonate content (≤ 14 wt%). One outcrop sample also contains 4 wt% bassanite, further highlighting mineralogical contrasts between the inner and outer IU.

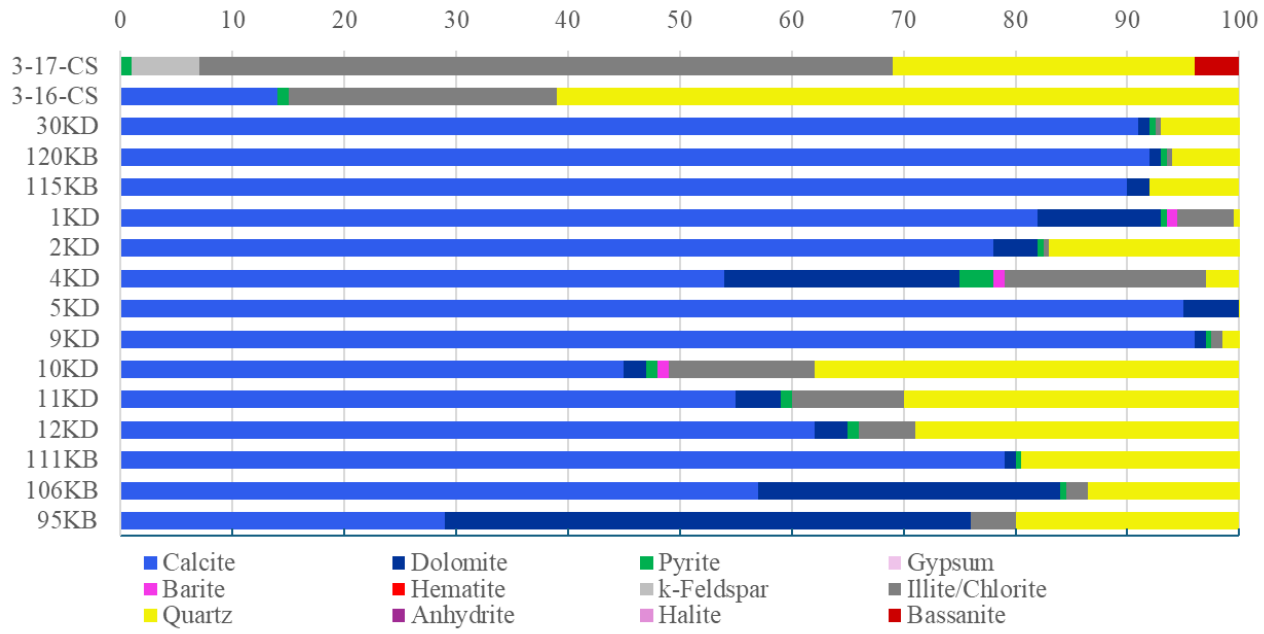

Figure 53. Mineralogical composition of the Early Cretaceous organic-rich samples.

The outer IU samples exhibit Ca/(Fe+Ca) ratios between 0.3 and 0.9, with the lowest recorded value of the 3-17-CS sample, being significantly lower than those of other Early Cretaceous samples. Combined with a very low Sr/Ba ratio, it suggests deposition in a fresh to brackish water setting according to Nelson and Wang [187,288]. The V/(V+Ni) ratio (~0.8) aligns with dysoxic marine conditions, while V/Cr values range from 3.53 to 4.39.

Biomarker analysis of the most organic-rich outer IU sample reveals a unimodal alkane distribution dominated by light and mid-chain alkanes, peaking at Pr and Ph. The Pr/Ph ratio (0.88) suggests suboxic to anoxic conditions, indicative of a reducing environment. The Pr/nC17 and Ph/nC18 ratios further support a mixed depositional setting (Figures 54 and 55).

TAR is relatively low, indicating minimal terrigenous input, while the Paq ratio is moderately high (0.73), pointing to a predominant aquatic source (Figure 55). The nC27/nC17 ratio (0.67) suggests mixed organic inputs, skewed towards aquatic algal sources rather than terrestrial plants.

These biomarker patterns closely resemble those of the inner IU samples, interpreted as representing an aquatic depositional setting with low terrigenous influence, dominated by algae and photosynthetic bacteria, according to widely accepted classifications [89,191,201,202]. However, outer IU samples contain significantly lower pregnane and homopregnane concentrations and reduced diasteranes, suggesting either lower thermal maturity or more

oxidizing depositional conditions. The silicate-rich composition of the outer IU contrasts with the carbonate-rich inner IU, pointing to clastic-dominated open marine conditions.

As noted by Grice (1998) high pregnane and homopregnane concentrations are characteristic of sulfur-rich oils from evaporitic lacustrine source rocks, but the outer IU samples appear more clastic-dominated (Figure 56). The presence of bassanite (4 wt%) in one outer IU sample suggests evaporitic conditions within a clastic-rich, brackish setting, possibly indicative of periodic evaporation.

Biomarker distributions further differentiate the IU subunits. Outer IU samples exhibit an abundance of C29 steranes, contrasting with the more balanced C27–C29 sterane distribution in the inner IU samples (AY-3 well), suggesting a more heterogeneous organic matter source. The inner IU, in contrast, contains a uniform algal-bacterial signature.

Low gammacerane and C30 sterane levels in both outcrop and organic-rich AY-3 samples suggest a lack of strongly stratified water columns during deposition according to published research classifications [221,224], The low C25 HBI index indicates limited anoxia, likely reflecting more oxygenated waters or fluctuating anoxia.

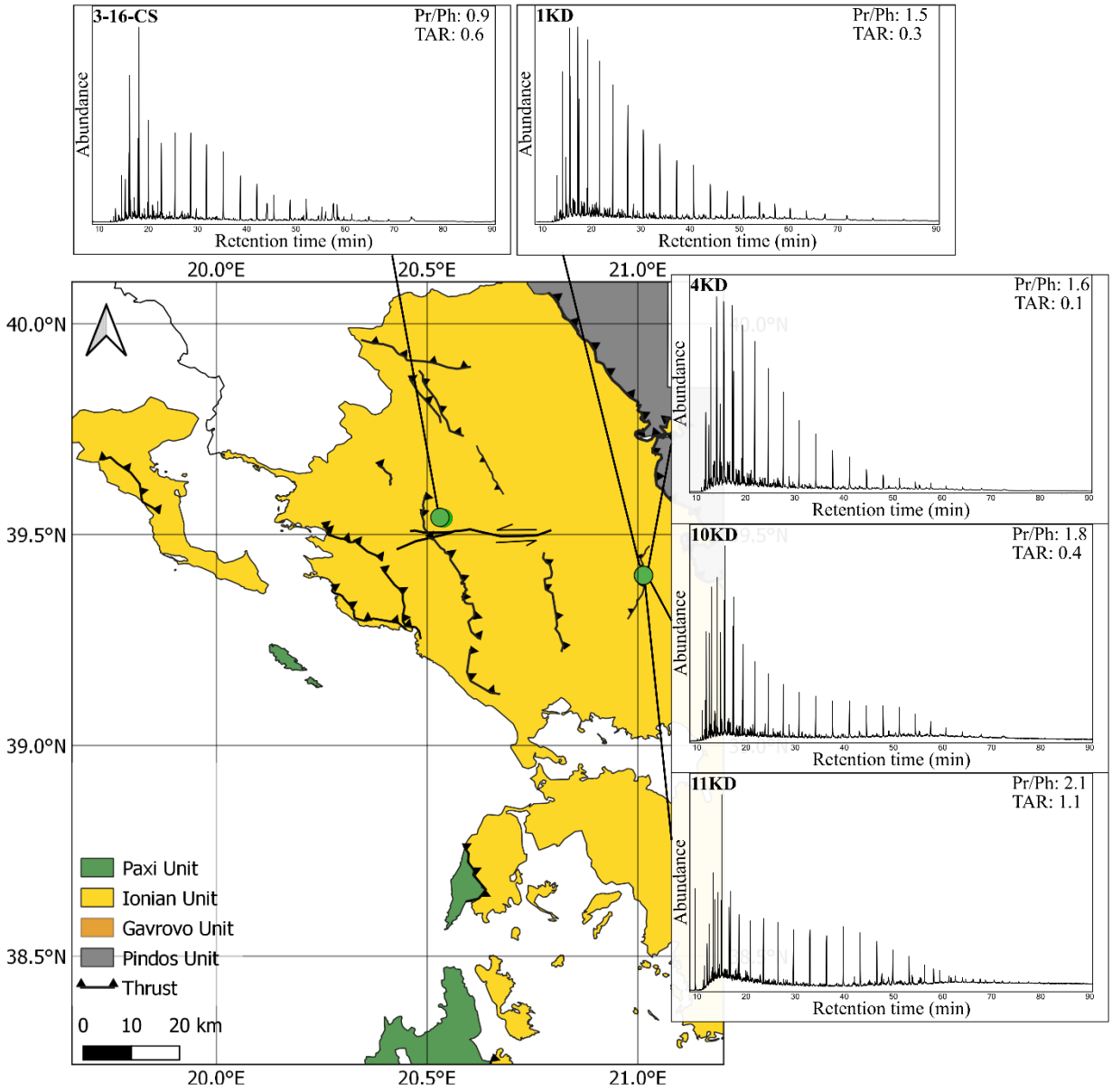

Figure 54. Regional distribution of Early Cretaceous samples. Exemplary m/z 85 gas chromatograms are shown with values for Pr/Ph and TAR.

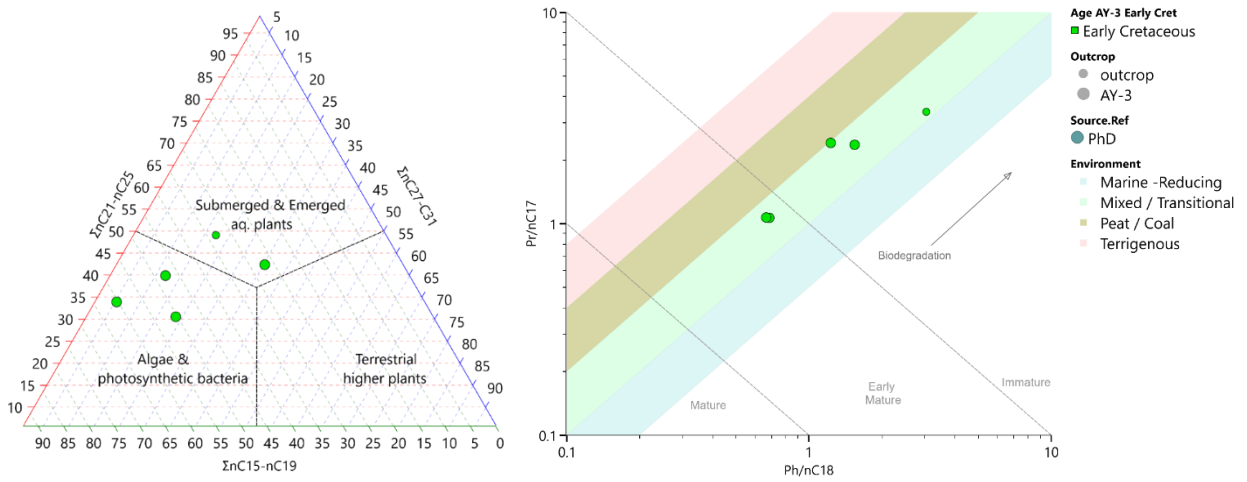

Figure 55. (Left): Triplot of short-,mid- and long-chain normal alkanes to essential categories of OM from the analyzed Early Cretaceous samples, modified after El-Moghazy et al. (2023). (Right): Pr/nC17 vs. Ph/nC18 for the Early Cretaceous samples.

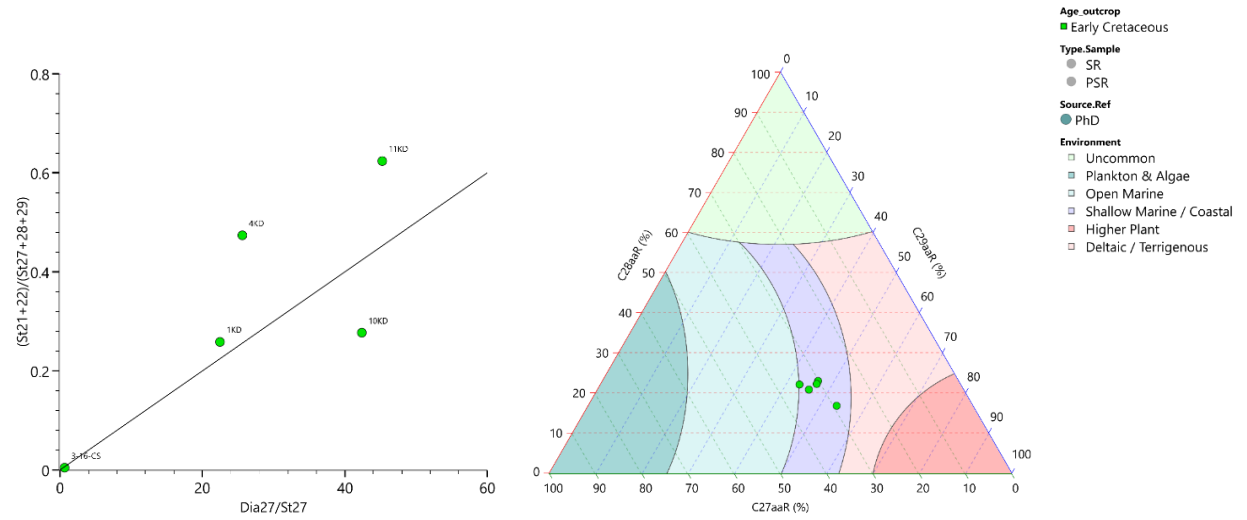

Figure 56. (Left): (C21+C22)/(C27–29) sterane vs. dia/reg C27 sterane. (Right): Triplot of normal sterane distribution. Both plots are used to assess the depositional environments of the Early Cretaceous samples studied.

Aromatic TIC chromatograms (m/z 253) suggest that organic matter in Early Cretaceous outer IU samples derives from freshwater rather than marine environments. The absence of 2,3,6-AIP suggests potentially fluctuating redox conditions. Additionally, the near-absence of C21 and C21 TAS in the m/z 231 chromatogram and the mineralogy of the outer IU samples indicates deposition

under high-salinity conditions, likely brackish environment with periodic evaporation and terrestrial input.

The δ^{13}Corg values range from –27.49‰ to –28.07‰ in the outer IU, consistent with freshwater algae and terrestrial organic matter contributions. In contrast, inner IU samples exhibit moderate δ^{13}Corg values (–26.6‰ to –27‰), indicating a stronger marine influence.

Kinetic analysis highlights differences in the IU subunits. The outer IU samples exhibit a broad Ea range (44–54 kcal/mol), with a principal Ea of 50 kcal/mol and three major peaks accounting for 57% of generation potential, suggesting heterogeneous organic matter inputs and lower maturity due to complex depositional conditions.

In contrast, AY-3 well samples have a narrower Ea-distribution (Figure 13), with 53–95% of generation potential concentrated in just two to three peaks. This suggests more uniform organic matter composition and a higher degree of thermal maturity, reflecting stable, marine conditions [118,251]. Mild maturation effects on inner IU samples may have slightly reduced their generation potential, as noted by Peters et al. (2006).

Biomarker and mineralogical data distinguish the marine, carbonate-rich inner IU from the silicate-dominated, clastic outer IU, which shows lower thermal maturity and more oxidizing conditions. Carbon isotopes and biomarker trends suggest a mixed freshwater-terrestrial influence in the outer IU versus marine dominance in the inner IU. Kinetic analysis reveals heterogeneous, lower-maturity organic matter in the outer IU and more uniform, mature sources in the inner IU, reflecting differences in depositional setting and thermal history.

6.3. Custom generation kinetics – the effect on hydrocarbon generation onset

The thermal behaviour of organic matter in sedimentary basins is critically governed by Ea-distributions, which control the timing and extent of hydrocarbon generation. Although standard kinetic libraries, such as those of Pepper & Corvi (1995a, 1995b), are widely applied in petroleum system modelling, they often fail to capture the variability inherent in region-specific organic matter types. This chapter examines the impact of custom generation kinetics on predicting hydrocarbon generation onset, using organic-rich intervals from Western Greece.

Custom kinetics were derived from RE6 data and discrete modelling using Kinetics2015 and applied to model TR for representative organic-rich samples under a constant heating rate of 3

K/Ma. Resulting TR curves were compared by age interval to those obtained with conventional kinetic models to evaluate differences in predicted generation behaviour. Key variations across four sample groups are discussed. Hydrocarbon generation potential cannot be solely correlated with palynological composition, as organofacies (e.g. AOM) can encompass chemically diverse materials. Type I kerogen, typically derived from algal sources [113,115], exhibits narrow Ea-distributions reflecting its homogeneous composition, leading to steep TR curves over limited temperature ranges. In contrast, Type II kerogen shows broader Ea-distributions [118,128], generating hydrocarbons over wider temperature intervals with gradual TR curves.

As summarised in Table 14, thermally immature Late Triassic – Early Jurassic samples reach TR10 between 106–115 °C. Early – Mid Jurassic samples show a broader TR10 range (106–133 °C), with values higher than 120 °C reflecting early mature stages. Mid – Late Jurassic thermally immature samples reach TR10 at 102–115 °C. Early Cretaceous samples display the widest TR10 variability (104–140 °C), with values above 116 °C generally corresponding to higher maturities.

No clear correlation is observed between TR10 and measured Tmax, indicating that transformation onset is influenced not only by maturity but also by kinetic input. Elevated TR10 values (~130–140 °C) in early mature samples are linked to custom kinetics with narrow Ea-distributions, delaying transformation due to the requirement for higher, more uniform thermal input. Conversely, samples with broader Ea spectra (including low Ea "tails") generate hydrocarbons at lower temperatures, reflecting more reactive, heterogenous kerogen.

Palynofacies analysis (Figure 57) further supports this kinetic behavior. Samples rich in sporomorphs and opaque phytoclasts, typically indicative of more terrestrial, gas-prone Type III kerogen, tend to exhibit slightly lower TR10 values despite similar maturities. This suggests a stronger influence from OM type and preservation than maturity alone. However, no consistent correlation was found between phytoclast percentages and HI values, apart from a general increase in degraded OM (DOM) in more reactive samples. Thermal modelling with constant heating rates and fixed frequency factors illustrates wide TR10 variability among age-defined sample groups (Figures 58 and 59), especially in samples of similar thermal maturity.

Late Triassic – Early Jurassic group: Thermally immature samples reach TR10 at 106–115 °C, aligning closely with the Pepper & Corvi TI(C) model. While the TII-S(A) does not match the TR10 values, it provides a better fit at TR90, suggesting a broader transformation range. Early – Mid Jurassic group: Spanning immature to early mature stages, these samples reach TR10,

between 106–133 °C. Higher TR10 values correlate with more mature and chemically homogeneous kerogen (narrow Ea-distributions). They align best with TI(C), while TII(B) models capture TR10 well but tend to underestimate TR50–TR90.

Mid – Late Jurassic group: Immature samples exhibit TR10 values of 102–115 °C. TII-S(A) and TII(B) kinetics reproduce these transformation onsets well, supporting the presence of Type II to II/III kerogen with reactive, heterogeneous structure.

Early Cretaceous group: Includes Type II to Type III kerogens ranging from immature to early mature. Type II samples show TR10 values of 108–140 °C, with higher values linked to narrow Ea-distributions. Type III samples (104–116 °C) exhibit earlier transformation due to broader Ea-distributions. Pepper & Corvi Type I(C) kinetics replicate the abrupt transformation of narrow Ea-distribution samples (~120 °C TR10), whereas Type IIIH(DE) kinetics do not align well with the lower-reactivity samples.

Across all groups, Ea-distributions (Figure 13) underscore the control of OM composition on transformation behavior. Samples with narrow distributions suggest chemically more uniform and likely sourced from consistent inputs (e.g., algal-rich OM), while broader distributions suggest more mixed OM sources, including terrestrial input. Interestingly, no link was found between Ea peak position and stratigraphic age or total sulfur content.

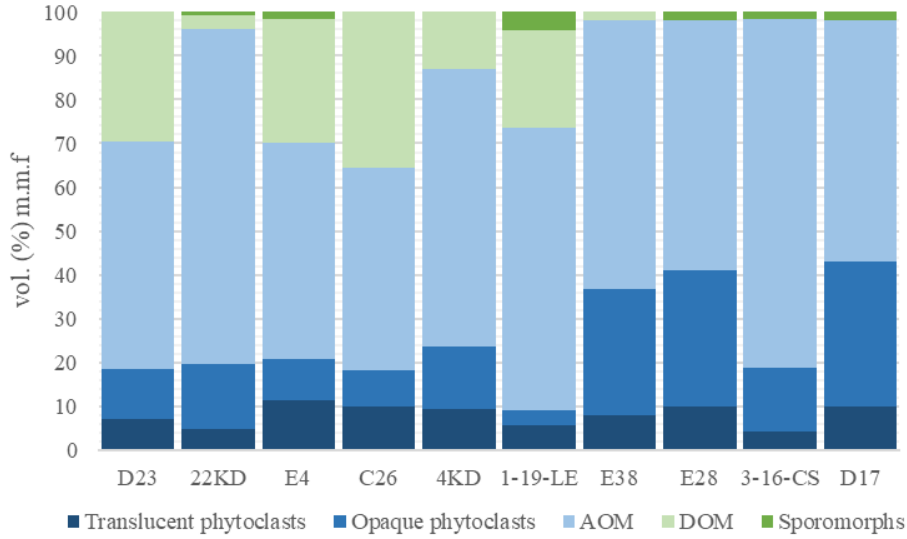

Figure 57. Palynological composition in volume (%) mineral matrix free (m.m.f) of the analyzed kerogens of selected samples, ranked according to increasing HI (from right to left). No correlation between palynomorphs and HI is observed, only the increase in DOM (degraded OM).

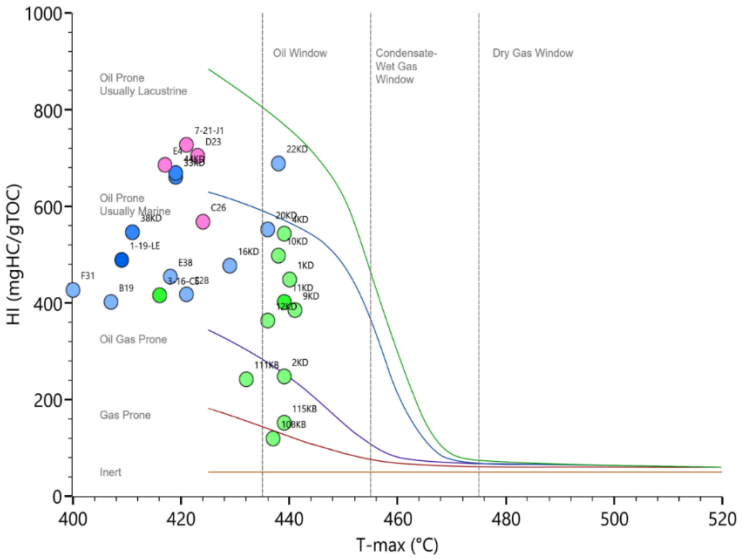

Figure 58. HI vs. Tmax custom kinetic samples, modified after Hackley and Lünsdorf (2018).

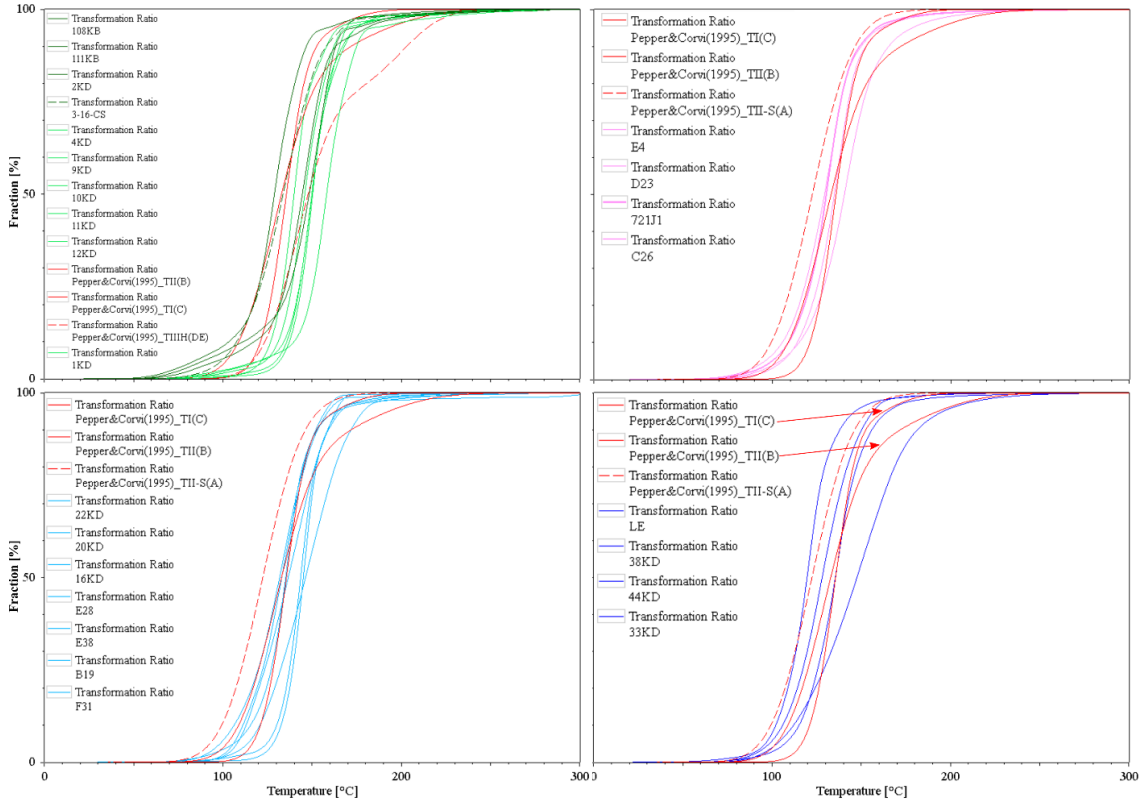

Figure 59. Modelled TR curves for Figure 58 samples using custom Ea-distributions and a fixed frequency factor under a constant heating rate (3 K/Ma). Plots show: (Top left) Early Cretaceous, (Top right) Late Triassic – Early Jurassic, (Bottom left) Early – Mid Jurassic, (Bottom right) Mid

– Late Jurassic. Library kinetics [113] for kerogen types I, II, III, and II-S included for comparison.

Table 14. Transformation ratio (TR) temperatures for all sample-custom multi-ramp kinetics and library kinetics [113] *under a constant heating rate of (3K/Ma).*

Sample	TR10 (°C)	TR50 (°C)	TR90 (°C)
3-16-CS	108	134	158
1KD	126	140	158
2KD	112	148	163
4KD	137	150	166
9KD	131	146	162
10KD	134	149	168
11KD	136	149	165
12KD	140	158	175
111KB	104	129	147
108KB	116	144	164
16KD	116	135	153
20KD	130	143	158
22KD	133	145	159
33KD	102	119	138
44KD	115	136	156
38KD	106	128	150
1-19-LE	112	147	182
E28	111	133	153
E38	106	132	152
F31	120	146	172
B19	113	137	159
C26	115	140	165
D23	114	135	152
E4	106	129	150
7-21-J1	109	130	149
Pepper&Corvi(1995)_TI(C)	120	136	152
Pepper&Corvi(1995)_TII(B)	108	133	173
Pepper&Corvi(1995)_TII-S(A)	99	122	146
Pepper&Corvi(1995)_TIIIH(DE)	123	148	202

6.3.1. Thermal modelling of key wells in Western Greece

To understand the influence of custom generation kinetics on hydrocarbon onset in real geological settings, thermal modelling was performed on two representative wells from the HFTB. For the heat flow simulation, the β factor was selected as 2.5, with two rifting events, one from 235 to 215 Ma and from 190 to 163 Ma, according to literature [43].

Thermal modelling also incorporated variations in erosion thickness, a critical factor in reconstructing the burial history and its influence on hydrocarbon generation onset. These erosion estimates, alongside the heat-flow scenarios, provide a robust framework for understanding the thermal evolution of the basin and its implications for petroleum system development. A detailed procedure of the workflow is presented in Figure 60.

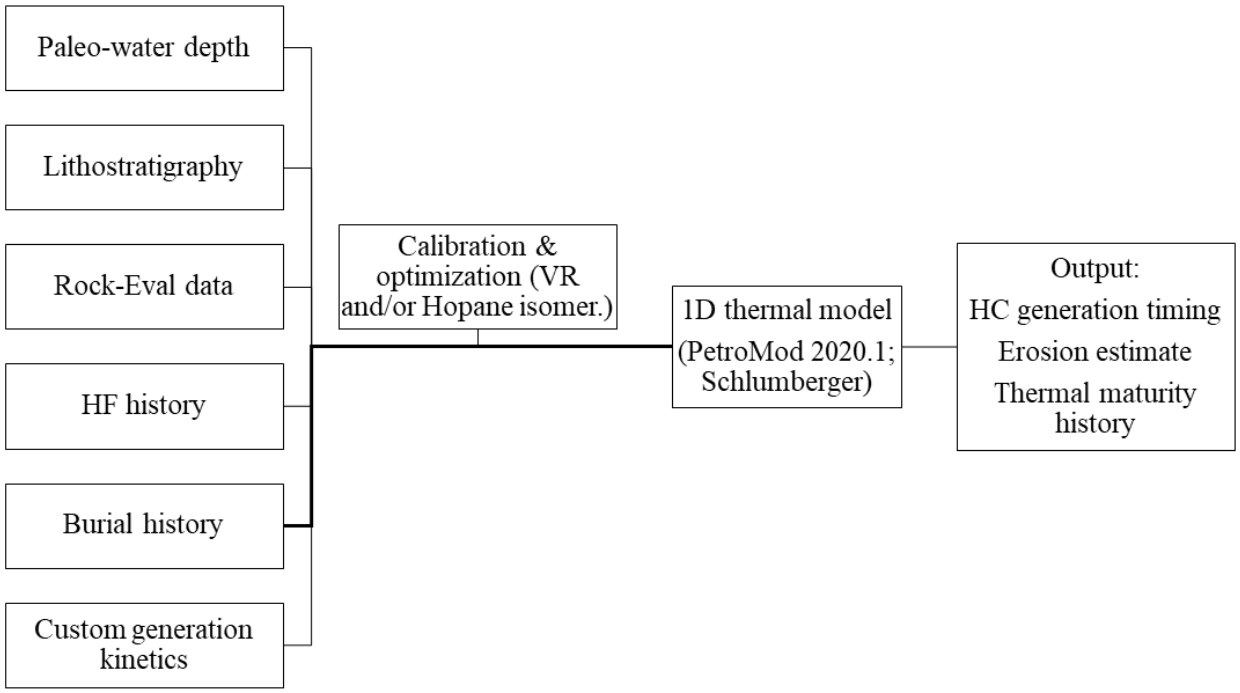

Figure 60. Schematic hierarchical procedure of the workflow and input data for the 1D thermal models. References for the input data are discussed in the following subchapters.

6.3.1.1. AY-3 well

The thermal modelling for the AY-3 well was conducted using lithological profiles derived from cuttings data by Rigakis (1999). Sediment-water interface temperature was estimated from Wygrala (1989) for the location latitude and present-day heat flow was set at 49 mW/m², according to Fytikas and Kollios (1979) and model calibration. Maximum syn-rift heat flow of 61 mW/m² was determined using the McKenzie rift modelling and model calibration. Crustal thickness was set to 30 km and present-day heat flow to 49 mW/m² [294] although it warrants careful consideration due to its impact on thermal gradients and subsidence history.

Two organic-rich intervals were modelled: the shallow Early Cretaceous A (SRA) and the deeper Early Cretaceous B (SRB), represented by samples such as 1KD, 2KD, 4KD, and 9KD (SRA) and 10KD, 11KD (SRB). Calibration of the thermal model relied on vitrinite reflectance (VR) measurements from Rigakis (1999), and hopane isomerization ratios.

The thermal history includes two thrusting phases, one of the bottom flysch sequence between 8.5–7.5 Ma, and one of the bottom Early Cretaceous sequence from 7–6 Ma. Along with a final erosion of 1800 m of the Oligocene turbidite sequence (flysch), provided the best thermal maturity fit of the VR and hopane curves (Figure 61).

Transformation ratios (TRmax) derived from custom kinetics were consistently low, ranging from 8% to 30%, with the hydrocarbon generation onset (TR10) occurring within the last 15 Ma for SRA and 7 Ma for SRB (Table 15). In contrast, library kinetics resulted in significantly higher TRmax values (up to 55% for SRB and 54% for SRA) indicating up to a sixfold difference in modelled transformation due solely to kinetic selection. Generation onset was similarly sensitive: TR10 occurred as early as 104 °C in the SRA (Pepper & Corvi TII(B)) and as late as 145 °C in the SRB with custom kinetics, again highlighting the variability introduced by activation energy structures.

Assuming surface temperature of 15 ºC and a standard geothermal gradient of 30 °C/km, the generation onset in AY-3 spans a modelled depth range from ~3.5 to 4.8 km depending on kinetics and organic-rich layer. For example, sample 1KD (SRA) reaches TR10 at ~4.4 km with custom kinetics (133 °C), whereas the same layer modelled with Pepper & Corvi TI(C) begins generation at ~4.0 km (120–124 °C).

While this approach does not account for the full burial and thermal history, it allows for a direct comparison of the kinetic influence on generation onset, offering insights into potential shifts in

effective source intervals. This variation underscores the importance of kinetic selection not only in predicting the hydrocarbon generation onset and understanding migration, but also in understanding the thermal and geochemical evolution of sedimentary basins.

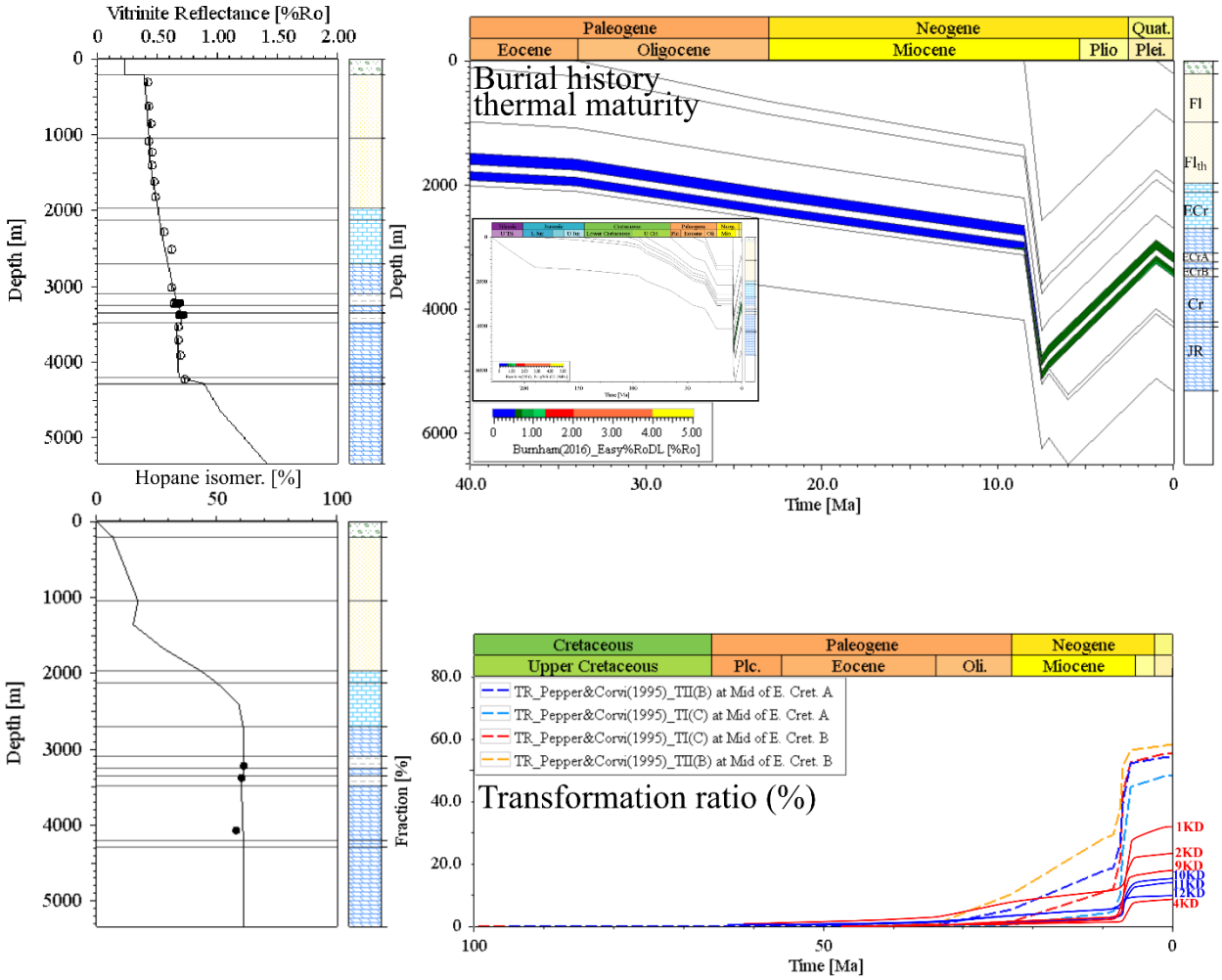

Figure 61. (Top Left): Vitrinite reflectance calibration curve, (top right): Burial history of the PxGa-1x well showing the thermal maturity based on the Easy%RoDL, (bottom left): Hopane isomerization calibration curve, and (bottom right): Modelled transformation ratios (TR) of the Early Cretaceous A and B organic-rich layers, using custom kinetics which are shown on the right, and library kinetics. In the lithostratigraphic column: Jr; Jurassic, Cr; Cretaceous, ECrA, B; Early Cretaceous A and B organic-rich layers, Fl(th); Flysch (thrust).

Table 15. Comparison of transformation ratios (TRmax and TR10%) and associated temperatures for custom and library kinetics across selected organic-rich intervals in models AY-3 and PxGa-1x. ECrA, B; Early Cretaceous A and B, MLJ; Mid – Late Jurassic, EMJ; Early – Mid Jurassic.

Model	OR layer	Sample	Temp TR10 (°C)	Temp max (°C)	TRmax (%)	Library Kinetics	Temp TR10 (°C)	TRmax (%)
AY-3	ECrA	4KD	-	139	8	Pepper&Corvi(1995)_TI(C)	132	48
	ECrA	2KD	103	139	23	Pepper&Corvi(1995)_TII(B)	104	29
	ECrA	1KD	133	139	30			54
	ECrB	10KD	145	145	15	Pepper&Corvi(1995)_TI(C)	110	55
	ECrB	11KD	145	145	12	Pepper&Corvi(1995)_TII(B)	108	33
	ECrB	9KD	138	145	21			58
PxGa-1x	MLJ	38KD	97	108	28	Pepper&Corvi(1995)_TI(C)	-	7
	MLJ	44KD	106	108	14	Pepper&Corvi(1995)_TII(B)	101	22
	MLJ	33KD	90	108	48			
	EMJ	16KD	106	131	76	Pepper&Corvi(1995)_TI(C)	108	72
	EMJ	22KD	121	131	44	Pepper&Corvi(1995)_TII(B)	99	68
	EMJ	20KD	117	131	49			

6.3.1.2. PxGa-1x well

The PxGa-1x model was constructed using lithological input from cuttings data [51] assuming present-day heat flow of 45 mW/m². Maximum syn-rift heat flow (66 mW/m²) was calculated using McKenzie's model and regional tectonic interpretations [295], considering also Lavecchia and Bell (2012), conspiring two rifting periods; one between 230–200 Ma and a second between 190–160 Ma. Calibration was based on VR data. The model includes Triassic to Tertiary deposition, erosion of Eocene-Paleocene and Tertiary units in the last 7 Ma and thrusting of Triassic strata between 6–7 Ma. Crustal thickness was set at 32 km based on regional studies [43,294,297–299].

Source rock intervals of Early – Mid Jurassic and Mid – Late Jurassic were assigned to the organic-rich samples represented by the 20KD, 22KD, 16KD and 38KD, 33KD and 44KD respectively. Best thermal fit was achieved with 1600m of erosion and a Triassic thrusting between 6–7 Ma (Figure 62).

The temperature at TR10 varies significantly across samples and kinetic models, highlighting how different kinetics influence not only the extent of transformation but also the depth or timing at which generation begins. The Early – Mid Jurassic (EMJ) interval shows relatively high temperatures at the onset of hydrocarbon generation (TR10), ranging from 106 °C to 121 °C (Table

15). Maximum transformation ratios (TRmax) reach up to 76% with custom kinetics. When compared to library kinetics, such as Pepper & Corvi, TRmax values are generally similar (e.g., 72%, 68%), but TR10 temperatures differ significantly (e.g., 108 °C vs. 99 °C), indicating that the choice of kinetics strongly affects the modelled depth or timing at which generation begins, even if the final transformation extent converges.

In contrast, the Mid – Late Jurassic (MLJ) interval reaches TR10 at lower temperatures (90 °C to 106 °C) and has lower TRmax values (14% to 48%), suggesting limited hydrocarbon generation. When standard kinetics are applied, TRmax values can drop even further (e.g., down to 7%), emphasizing that library kinetics may underestimate the maturity and generation potential of shallower intervals. The variability in TR10 among samples and kinetics illustrates that even within the same stratigraphic interval, the onset of generation can shift by more than 10 °C, affecting exploration models and depth-to-generation predictions.

Assuming a standard geothermal gradient of 30 °C/km and a surface temperature of 15 °C, the onset of hydrocarbon generation (TR10) in the PxGa-1x model would occur at estimated depths of approximately 3.0–4.0 km. For the Early – Mid Jurassic (EMJ) interval, TR10 using custom kinetics ranges from 106 to 121 °C, translating to ~3.0–3.5 km depth. Library kinetics for the same interval show an earlier onset (e.g., 99–108 °C, or ~2.8–3.1 km), especially for Pepper & Corvi TII(B), highlighting the lower Ea assumptions. In contrast, for the Mid – Late Jurassic (MLJ) interval, custom kinetics yield TR10 temperatures between 90–106 °C, equating to ~2.5–3.0 km depth, while the library model TII(B) shows TR10 at 101 °C, or ~2.9 km.

These differences demonstrate that the choice of kinetic model can shift the predicted onset of hydrocarbon generation (TR10) by up to ~1.2 km in depth, influencing not only maturity assessments and generation timing but also critical factors such as trap integrity. The selection of kinetics thus directly impacts both the extent of transformation (TRmax), the depth and timing of generation, with significant implications for basin modelling accuracy and exploration risk evaluation.

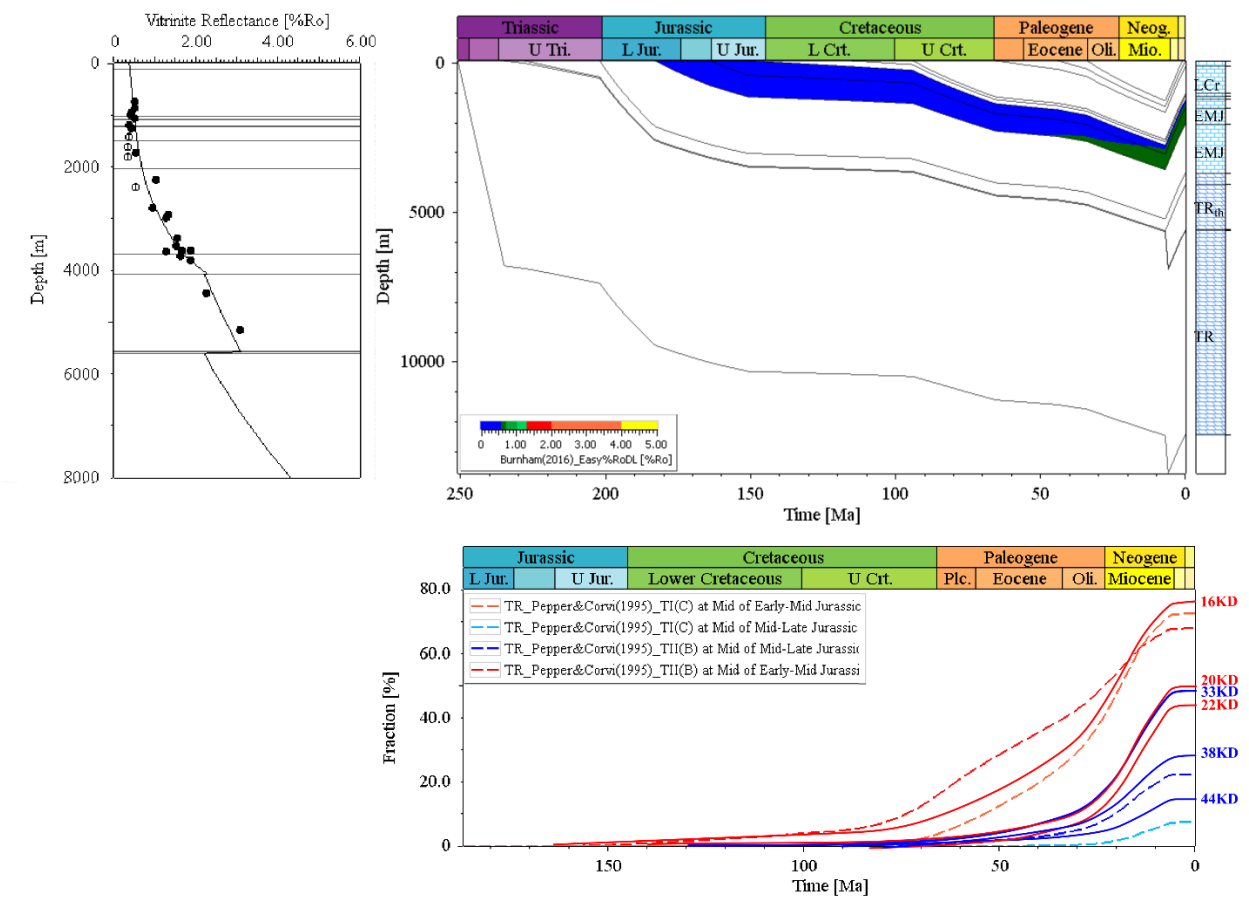

Figure 62. (Top Left): Vitrinite reflectance calibration curve, (top right): Burial history of the PxGa-1x well showing the thermal maturity based on the Easy%RoDL, and (bottom right): Modelled transformation ratios (TR) of the Early – Mid and Mid – Late Jurassic organic-rich layers, using custom kinetics which are shown on the right, and library kinetics. In the lithostratigraphic column: LCr; Early Cretaceous, EMJ; Early – Mid Jurassic, TRth: Triassic thrust, TR; Triassic.

CHAPTER 7.
CONCLUSIONS

This thesis investigates the mineralogical, geochemical, and kinetic characteristics of Mesozoic organic-rich intervals within the fold-and-thrust belt of Western Greece. Through an integrated approach, combining XRD, XRF, biomarker and palynological data with pyrolysis-derived kinetic parameters and 1D thermal modelling, it reveals significant spatial and stratigraphic variations in organic matter quality, depositional conditions, and hydrocarbon generation potential.

7.1. Mineralogical and Geochemical Signatures

Mineralogical analyses show that carbonate phases (dolomite and calcite) dominate the organic-rich sample matrix across the studied intervals.

The Late Triassic – Early Jurassic samples show elevated dolomite and sulfur contents. Elemental proxies and biomarkers, along with abundant aryl isoprenoids (AIP) indicate photic-zone euxinia under sulfate-reducing conditions with increased terrestrial input.

The Early – Mid Jurassic samples of the Ionian Unit display a more balanced mineralogical composition compared to the calcite-dominated PU samples, which also show elevated anhydrite content. Elemental proxies and biomarkers indicate stronger oxygen deficiency in the PU samples relative to the dysoxic conditions inferred for the IU. The abundance of hopenes in the IU suggests microbial activity in stratified, possibly suboxic waters, whereas the PU samples reflect periodically euxinic and anoxic conditions associated with fluctuating water levels and elevated salinity.

The Mid – Late Jurassic samples are carbonate-dominated, whereas the Late Jurassic Lefkada sample shows a more balanced carbonate-silicate composition. Elemental proxies and biomarker data indicate stratified marine conditions for the PU, in contrast to a marginal marine setting with increased terrestrial input for the Lefkada sample.

The Early Cretaceous samples are also carbonate dominated, with outcrop IU samples containing higher silicate contents compared to the inner IU well samples. Elemental proxies and biomarkers distinguish the marine inner IU with enhanced productivity from the more silicate-rich, clastic outer IU, which reflects mixed freshwater to potentially brackish influences.

7.2. Organic Matter Type and Maturity

Palynofacies data show AOM dominance in marine intervals, with sporomorph and phytoclast contributions becoming more prominent in younger, more oxygenated settings.

The Late Triassic – Early Jurassic interval exhibits high TOC values, reaching up to 35.56 wt%, and generally shows good to excellent hydrocarbon generation potential. The samples are rich in AOM and DOM, thermally immature, with kerogen types falling within the Type II trend; however, Type IIS is inferred based on sulfur substitution for oxygen.

The Early – Mid Jurassic interval displays higher TOC values in the PU (PxGa-1x well) compared to the IU samples. In the PU, thermal maturity ranges from immature to mature, whereas the IU samples are predominantly thermally immature. The most organic-rich samples follow a Type I–II kerogen trend rich in AOM and opaque phytoclasts and show poor to excellent hydrocarbon generation potential.

The Mid – Late Jurassic samples exhibit TOC values comparable to those of the Early – Mid Jurassic interval, apart from the Late Jurassic sample from Lefkada, which is notably richer in organic matter. Overall, these samples indicate good to excellent hydrocarbon generation potential and are mainly thermally immature to early mature.

The Early Cretaceous samples show higher TOC values in the inner IU (AY-3 samples) compared to the outer IU outcrop samples and the PU. They are predominantly thermally immature to early mature and rich in AOM. The most organic-rich samples plot along the Type II kerogen trend, while the more immature ones align with Type III, indicating poor to excellent hydrocarbon generation potential.

7.3. Kerogen Reactivity and Kinetic Profiles

Kinetic modelling based on Rock-Eval pyrolysis data reveals substantial variation in Ea-distributions across the studied stratigraphy.

The Late Triassic – Early Jurassic intervals exhibit broad Ea-distributions, typically consisting of two to three principal Ea peaks that account for only 48–70% of the total generation potential. These distributions reflect complex organic inputs and suggest a gradual, extended hydrocarbon generation profile.

The Early – Mid Jurassic samples display similarly broad profiles, consistent with mixed marine and terrestrial sources.

In contrast, the Mid – Late Jurassic and Early Cretaceous intervals exhibit narrower Ea-distributions, often dominated by one or two peaks covering over 77% of the total generation potential. These suggest more chemically uniform kerogens capable of rapid hydrocarbon generation across narrow thermal windows.

The stratigraphic progression from broad to narrow Ea profiles reflects a transition from heterogeneous to more homogeneous organic matter input.

Organic sulfur appears to enhance reactivity, lowering Ea and shifting TR10 to shallower depths, even in samples with comparable HI values.

Mineralogical composition also influences reactivity: high calcite content, when balanced by silicates, appears to inhibit transformation rates, potentially due to mineral matrix effects.

7.4. Thermal Modelling and Burial Histories

One-dimensional thermal modelling of the AY-3 and PxGa-1x wells demonstrates that kinetic model selection significantly influences predictions of hydrocarbon generation timing and extent. Custom kinetic models yield lower transformation ratios (TRmax) and later onset temperatures (TR10) compared to standard library models.

In the AY-3 well, optimal calibration was achieved using 1800 m of final erosion, a present-day heat flow of 49 mW/m^2, and two syn-rift episodes (235–200 Ma and 190–163 Ma), followed by thrusting of the Oligocene flysch (8.5–7.5 Ma) and Early Cretaceous sequences (7–6 Ma).

These models predict TRmax values of 8–30%, whereas standard libraries (e.g., Pepper & Corvi TII(B), TI(C)) yield significantly higher values. Differences in TR10 between kinetic models translate into depth variations exceeding 1 km under a constant geothermal gradient.

For the PxGa-1x well, the best thermal fit was obtained with 1600 m of erosion, a present-day heat flow of 45 mW/m^2, and similar rift phases, with Triassic thrusting between 7–6 Ma.

The Early – Mid Jurassic interval reaches TR10 between 106–121 °C using custom kinetics, corresponding to burial depths of ~3.5–4.1 km. Library models reduce TR10 to 99–108 °C, implying shallower generation depths of ~3.3–3.6 km.

The Mid – Late Jurassic interval shows even lower TR10 values (90–106 °C with custom kinetics), again depending on the kinetic model applied.

These findings underline that kinetic selection influences not only the extent of transformation (TRmax) but also the perceived timing and depth of hydrocarbon generation; parameters critical to accurate maturity modelling, charge prediction, and trap preservation in fold-and-thrust settings.

7.5. Novelty and implications

Beyond petroleum system assessments, this study enhances our understanding of organic matter evolution under shifting redox, mineralogical, and tectonic regimes. It underscores the necessity of source-specific custom kinetics to improve prediction accuracy in complex geological settings. The variability in Ea-distributions and transformation ratio (TR) profiles across different lithofacies and structural domains demonstrates that generic kinetic libraries often fail to reflect true transformation behavior. The observed links between organic sulfur content, kerogen composition, and reactivity point to promising directions for refining kinetic models that are more sensitive to the depositional and diagenetic conditions of source rocks.

These findings have several implications for both applied and theoretical geochemical modelling. First, they reinforce the need to treat source rocks not as geochemically uniform units but as heterogeneous materials shaped by multiple interacting controls, including depositional redox conditions, mineral-organic associations, and structural history. Particularly in fold-and-thrust belt settings like Western Greece, where tectonic overprint interacts with variable thermal regimes, the application of generalized kinetics can lead to significant misinterpretation of maturity, timing, and hydrocarbon generation potential.

The integration of redox-sensitive mineralogical analysis with kinetic modelling provides a framework that may be transferrable to other carbonate-dominated basins. While this study does not provide a complete kinetic solution, it highlights the benefits of tailoring activation energy distributions to geologically and geochemically distinct intervals. The implications extend to exploration risk assessment and resource evaluation, where models grounded in generic assumptions can lead to over- or under-estimation of system behavior.

Additionally, by identifying the potential influence of sulfur-rich organic matter on thermal reactivity, the study opens space for re-evaluating the kinetic treatment of Type IIS kerogens in

complex stratigraphic packages. Although not fully explored here, these relationships present an opportunity for further refinement of kinetic models that account for sulfur content as an active control, rather than a passive geochemical indicator.

7.6. Broader Applicability

Although this study focuses on Western Greece, the methodological framework and insights developed here are applicable to other carbonate-dominated, structurally complex petroleum systems. The integration of source-specific kinetic modelling with redox-sensitive mineralogical and geochemical characterization provides a transferable approach for evaluating source rock evolution in fold-and-thrust belts and foreland basins. Analogous regions such as the Albanides, Zagros, Sub-Andean basins, and the Apennines may lend themselves to the application of these techniques, particularly where complex burial histories and heterogeneous organic matter inputs complicate thermal modelling. As exploration increasingly targets frontier and tectonically active settings, the approaches refined in this research can support more accurate predictions of hydrocarbon generation timing and extent in comparable geological contexts. Moreover, aspects of this framework may contribute to broader basin analysis, including the reconstruction of thermal histories, paleoenvironmental conditions, and geochemical pathways of organic matter preservation and transformation.

7.7. Future Work

To deepen and extend the insights gained from this study, future research should begin with additional pyrolysis experiments designed to capture the kinetic behavior of diverse source rock types under varying redox and thermal conditions. This is particularly important because the current study reveals significant variability in Ea-distributions and transformation behavior, suggesting that standard kinetic libraries do not adequately capture the diversity of kerogen reactivity in complex geological settings. Developing a larger suite of custom kinetic models based on such experiments would help to reduce the uncertainty inherent in generalized kinetic assumptions and improve the predictive resolution of basin models.

Additional experiments could include maceral-specific analyses to isolate the influence of organic matter type, as well as systematic variation in mineralogy and organic sulfur content to better

constrain their effects on thermal reactivity. This would allow for the construction of compositionally and mineralogically informed kinetic parameters, particularly in sulfur-rich or redox-variant environments.

In parallel, applying compound-specific isotope analysis (CSIA) could provide more refined insights into the provenance and alteration of organic matter, especially in settings where early diagenetic sulfurization and mixed marine-terrestrial inputs may obscure traditional biomarker interpretations.

Finally, the modelling and interpretive framework established in this work could be applied to analogous carbonate-dominated fold-and-thrust belts in other regions. Such comparative studies will help evaluate the transferability of the kinetic modeling approach, identify region-specific constraints, and support the broader development of geochemically grounded kinetic models for structurally complex basins worldwide.

About the author

Vagia Ioanna Makri received her diploma from the Department of Geology and Geoenvironment at the National and Kapodistrian University of Athens (NKUA) in 2017. She holds two Master's degrees: one in Petroleum Engineering from the School of Mineral Resources Engineering at the Technical University of Crete (TUC), Greece, and another in Integrated Petroleum Geoscience from the University of Aberdeen (UoA), Scotland.

In 2019, she completed a traineeship at ARCEx (Research Centre for Arctic Petroleum Exploration) in Tromsø, Norway. She began her PhD in 2021 supported by Helleniq Energy S.A., within a sponsorship to the Institute of GeoEnergy (FORTH/IG), Foundation for Research and Technology – Hellas. That same year, she worked as a Geoscientist Intern with the G&G team at Capricorn Energy (formerly Cairn Energy) in Edinburgh, Scotland. In 2023, she joined Equinor in Oslo, Norway, as a Geoscientist intern, and since 2024 she has been working as a Senior Geologist at Equinor.

Journal Publications

Makri, V.I.; Oikonomopoulos, I.; Muirhead, D.; Pasadakis, N. Kerogen Kinetics and the Effect of Rock Matrix: Insights from Western Greece. *Int. J. Coal Geol.* 2024, *292*, 104585, doi:10.1016/j.coal.2024.104585.

Makri, V.I.; Bellas, S.; Moschou, G.; Pasadakis, N. An Integrated Approach for the Thermal Maturity Modeling Re-Assessment of an Exploration Well in the Hellenides Fold-and-thrust Belt. *Geosci.* 2023, *13*, doi:10.3390/geosciences13030076.

Telemenis, D.; **Makri, V.I.**; Manoutsoglou, E.; Bellas, S. Exploring Neogene Marine Diatomites in Western Crete: A New Source-Rock Candidate with Hydrocarbon Generation Potential? Eng 2023, *4*, 285–300, doi:10.3390/eng4010017.

International and National Conference presentations

Makri, V.I.; Pasadakis, D. The Clustering of Source Rocks: A Spectral Approach. In: Çiner, A., et al. Recent Research on Sedimentology, Stratigraphy, Paleontology, Geochemistry, Volcanology, Tectonics, and Petroleum Geology. *MedGU 2022*. Advances in Science, Technology & Innovation. Springer, Cham. *https://doi.org/10.1007/978-3-031-48758-3_72*.

Makri, V. I.; Schito, A.; Muirhead, D.; Oikonomopoulos, I.; Bellas, S. Preliminary results of a thermal maturity modelling study as a tool for understanding a structural setting – the case of the Fold-and-thrust Belt of Western Greece. *EGU General Assembly 2023*, Vienna, Austria, 24–28 Apr 2023, EGU23-712, *https://doi.org/10.5194/egusphere-egu23-712*.

Telemenis, D.; **Makri, V.I.**; Manoutsoglou, E.; Pasadakis, N.; Bellas, S. A geochemical analysis of the Neogene diatomites in Western Crete for their hydrocarbon potential. *16th International Congress, Geological Society of Greece.*

Moschou, G.; **Makri, V.I.**; Bellas, S.; Pasadakis, N. An Integrated Approach for the Thermal Maturity Modelling Re-Assessment of the AY-3 Well, Arta-Preveza Exploration Block, Western Greece. *Bull. Geol. Soc. Greece, Special Publication* 2022, 10, 738–739.

Makri, V.I.; Bellas, S.; Gaganis, V. Assessing Natural Gas Versus CO2 Potential Underground Storage Sites in Greece: A Pragmatic Approach. *Mater. Proc.* 2021, 5, 98. *https://doi.org/10.3390/materproc2021005098*.

Makri, V.I.; Panagopoulos, G.; Nikolaou, K.; Bellas, S.; Pasadakis, N. Evaluation of Gas Generation Potential Using Thermal Maturity Modelling—The Katakolo Case: A Probable Pathway to Energy Transition. *Mater. Proc.* 2021, 5, 70. *https://doi.org/10.3390/materproc2021005070*.

Makri, V.I.; Brackenridge, R.E.; Diamantakis, N.; Bramwell, N. Re-Evaluation of the Forth Approaches Basin: The Debatable Hydrocarbon Prospectivity and the Storage Potential. European *Association of Geoscientists & Engineers*, 2021, 1–5. *https://doi.org/10.3997/2214-4609.202113233*.

REFERENCES

1. Magoon, L.B.; Beaumont, E.A. Petroleum Systems. In *Exploring for Oil and Gas Traps*; Beaumont, E.A., Foster, N.H., Eds.; AAPG: Tulsa, OK, 1999; pp. 3–24.
2. Demaison, G.J.; Moore, G.T. Anoxic Environments and Oil Source Bed Genesis. *Org. Geochem.* **1980**, *2*, 9–31, doi:10.1016/0146-6380(80)90017-0.
3. Cacosian, R.B.; Lee, C. Chapter 5 Processes Controlling the Distribution of Biogenic Organic Compounds in Seawater. In *Marine Organic Chemistry*; Duursma, E.K., Dawson, R., Eds.; Elsevier, 1981; pp. 91–123 ISBN 9780444418920.
4. Gagosian, R.B.; Peltzer, E.T. The Importance of Atmospheric Input of Terrestrial Organic Material to Deep Sea Sediments. *Org. Geochem.* **1986**, *10*, 661–669, doi:10.1016/S0146-6380(86)80002-X.
5. Calvert, S.E. Oceanographic Controls on the Accumulation of Organic Matter in Marine Sediments. *Geol. Soc. London, Spec. Publ.* **1987**, *26*, 137–151, doi:10.1144/GSL.SP.1987.026.01.08.
6. Didyk, B.M.; Simoneit, B.R.T.; Brassell, S.C.; Eglinton, G. Organic Geochemical Indicators of Palaeoenvironmental Conditions of Sedimentation. *Nature* **1978**, *272*, 216–222, doi:10.1038/272216a0.
7. Tissot, B.P.; Welte, D.H. The Fate of Organic Matter in Sedimentary Basins: Generation of Oil and Gas. In *Petroleum Formation and Occurrence*; Springer-Verlag: Berlin, 1984; pp. 67–266.
8. Johnson Ibach, L.E. Relationship between Sedimentation Rate and Total Organic Carbon Content in Ancient Marine Sediments. *Am. Assoc. Pet. Geol. Bull.* **1982**, *66*, 170–188, doi:10.1306/03b59a5d-16d1-11d7-8645000102c1865d.
9. Bohacs, K.M.; Grabowski, G.J.; Carroll, A.R.; Mankiewicz, P.J.; Miskell-Gerhardt, K.J.; Schwalbach, J.R.; Wegner, M.B.; Simo, J.A. Production, Destruction, and Dilution—The Many Paths to Source-Rock Development. In *Deposition of Organic-Carbon-Rich Sediments: Models*; Harris, N.B., Ed.; SEPM (Society for Sedimentary Geology), 2011; pp. 61–101.
10. Kandiyoti, R.; Herod, A.A.; Bartle, K.D. Solid Fuels: Origins and Characterization. In *Solid*

Fuels and Heavy Hydrocarbon Liquids; Shapiro, A., Ed.; Elsevier, 2006; pp. 13–35 ISBN 978-0-08-100784-6.

11. Jørgensen, B.B. Mineralization of Organic Matter in the Sea Bed—the Role of Sulphate Reduction. *Nature* **1982**, *296*, 643–645, doi:10.1038/296643a0.
12. Horsfield, B.; Rullkötter, J. Diagenesis, Catagenesis, and Metagenesis of Organic Matter. In *The Petroleum System—From Source to Trap*; Magoon, L.B., Dow, W.G., Eds.; AAPG, 1994; pp. 189–200.
13. Tissot, B.; Espitalié, J. L'evolution Thermique de La Matière Organique Des Sédiments : Applications d'une Simulation Mathématique. Potentiel Pétrolier Des Bassins Sédimentaires de Reconstitution de l'histoire Thermique Des Sédiments. *Rev. l'Institut Français du Pétrole* **1975**, *30*, 743–778, doi:10.2516/ogst:1975026.
14. Tissot, B.P.; Welte, D.H. From Kerogen to Petroleum. In *Petroleum Formation and Occurrence*; Springer Berlin Heidelberg: Berlin, Heidelberg, 1984; pp. 160–198.
15. Peters, K.E.; Cassa, M.R. Applied Source Rock Geochemistry. In *The Petroleum System—From Source to Trap*; Magoon, L.B., Dow, W.G., Eds.; American Association of Petroleum Geologists (AAPG), 1994; pp. 93–120 ISBN 0891813381.
16. Tissot, B.P.; Welte, D.H. *Petroleum Formation and Occurrence*; Springer Berlin Heidelberg: Berlin, Heidelberg, 1978; ISBN 978-3-642-96448-0.
17. Karakitsios, V. Western Greece and Ionian Sea Petroleum Systems. *Am. Assoc. Pet. Geol. Bull.* **2013**, *97*, 1567–1595, doi:10.1306/02221312113.
18. Soto, J.I.; Tranos, M.D.; Bega, Z.; Dooley, T.P.; Hernández, P.; Hudec, M.R.; Konstantopoulos, P.A.; Lula, E.; Nikolaou, K.; Pérez, R.; et al. Contrasting Styles of Salt-Tectonic Processes in the Ionian Zone (Greece and Albania): Integrating Surface Geology, Subsurface Data, and Experimental Models. *Tectonics* **2024**, *43*, doi:10.1029/2023TC008104.
19. Aubouin, J. Contribution à l' Étude Géologique de La Grèce Septentrionale: Le Confins de l' Epire et de La Thessalie. *Ann. Géologiques des Pays Helléniques* **1959**, *9*, 1–483.
20. Papanikolaou, D. Greece within the Alpine Orogenic System. In *Geology of Greece*; 2015; pp. 15–24.

21. Handy, M.R.; M. Schmid, S.; Bousquet, R.; Kissling, E.; Bernoulli, D. Reconciling Plate-Tectonic Reconstructions of Alpine Tethys with the Geological–Geophysical Record of Spreading and Subduction in the Alps. *Earth-Science Rev.* **2010**, *102*, 121–158, doi:10.1016/J.EARSCIREV.2010.06.002.

22. IGRS–IFP Etude Géologique de l' Epire (Grèce Nord – Occidentale). *Inst. Geol. Subsurf. Res. Inst. Français du Pétrole* 1966, 1–306.

23. Papanikolaou, M.; Papanikolaou, D.; Triantaphyllou, M. Post-Alpine Late Pliocene - Middle Pleistocene Uplifted Marine Sequences in Zakynthos Island. *Bull. Geol. Soc. Greece* **2017**, *43*, doi:10.12681/bgsg.11198.

24. Karakitsios, V. The Influence of Preexisting Structure and Halokinesis on Organic Matter Preservation and Thrust System Evolution in the Ionian Basin, Northwest Greece. *Am. Assoc. Pet. Geol. Bull.* **1995**, *79*, 960–980, doi:10.1306/8D2B2191-171E-11D7-8645000102C1865D.

25. Kamberis, E.; Kokinou, E.; Koci, F.; Lioni, K.; Alves, T.M.; Velaj, T. Triassic Evaporites and the Structural Architecture of the External Hellenides and Albanides (SE Europe): Controls on the Petroleum and Geoenergy Systems of Greece and Albania. *Int. J. Earth Sci.* **2022**, *111*, 789–821, doi:10.1007/s00531-021-02151-4.

26. Karakitsios, V. Evolution and Petroleum Potential of the Ionian Basin (Northwest Greece). In Proceedings of the AAPG International Conference; 2003.

27. Karakitsios, V.; Rigakis, N. Evolution and Petroleum Potential of Western Greece. *J. Pet. Geol.* **2007**, *30*, 197–218, doi:10.1111/j.1747-5457.2007.00197.x.

28. Alexandridis, I.; Oikonomopoulos, I.K.; Carvajal-Ortiz, H.; Gentzis, T.; Kalaitzidis, S.; Georgakopoulos, A.N.; Christanis, K. Discovery of a New Source-Rock Interval within the Pantokrator Formation, Ionian Zone, Western Greece: Insights from Sulfur Speciation and Kinetics Analyses. *Mar. Pet. Geol.* **2022**, *145*, 105918, doi:10.1016/j.marpetgeo.2022.105918.

29. Rigakis, N.; Karakitsios, V. The Source Rock Horizons of the Ionian Basin (NW Greece). *Mar. Pet. Geol.* **1998**, *15*, 593–617, doi:10.1016/S0264-8172(98)00032-4.

30. Bourli, N.; Pantopoulos, G.; Maravelis, A.G.; Zoumpoulis, E.; Iliopoulos, G.; Pomoni-Papaioannou, F.; Kostopoulou, S.; Zelilidis, A. Late Cretaceous to Early Eocene Geological

History of the Eastern Ionian Basin, Southwestern Greece: A Sedimentological Approach. *Cretac. Res.* **2019**, *98*, 47–71, doi:10.1016/j.cretres.2019.01.026.

31. de Graciansky, P.C.; Dardeau, G.; Lemoine, M.; Tricart, P. The Inverted Margin of the French Alps and Foreland Basin Inversion. *Geol. Soc. London, Spec. Publ.* **1989**, *44*, 87–104, doi:10.1144/GSL.SP.1989.044.01.06.
32. BP (British Petroleum) Co. Ltd. *The Geological Results of Petroleum Exploration in Western Greece*; Institute of Geological Subsurface Research, 1971; Vol. 10;.
33. Underhill, J.R. Late Cenozoic Deformation of the Hellenide Foreland, Western Greece. *Geol. Soc. Am. Bull.* **1989**, *101*, 613–634, doi:10.1130/0016-7606(1989)101<0613:LCDOTH>2.3.CO;2.
34. Sotiropoulos, S.; Lykakis, N.; Oikonomopoulos, I.; Spanos, D.; Stathopoulou, A.; Gagala, L.; Pagoulatos, A. Hydrocarbon Plays in Western Greece: An Overview. In Proceedings of the 83rd EAGE Annual Conference & Exhibition; European Association of Geoscientists & Engineers, June 6 2022; Vol. 2022, pp. 1–5.
35. Kamberis, E.; Sotiropoulos, S.; Aximniotou, O.; Tsaila-Monopoli, S.; Cryssanthi, I. Late Cenozoic Deformation of the Gavrovo and Ionian Zones in NW Peloponnesos (Western Greece). *Ann. di Geofis.* **2000**, *43*, 905–919, doi:10.4401/ag-3679.
36. Zoumpouli, E.; Maravelis, A.G.; Iliopoulos, G.; Botziolis, C.; Zygouri, V.; Zelilidis, A. Re-Evaluation of the Ionian Basin Evolution during the Late Cretaceous to Eocene (Aetoloakarnania Area, Western Greece). *Geosciences* **2022**, *12*, 106, doi:10.3390/geosciences12030106.
37. Bourli, N.; Pasadakis, N.; Chamilaki, E.; Sianni, M.; Zelilidis, A. The Lower Cretaceous "Vigla" Shales Potentiality to Be Source Rocks in the Ionian Basin, Greece. *Geosciences* **2023**, *13*, 44, doi:10.3390/geosciences13020044.
38. Zelilidis, A.; Bourli, N.; Andriopoulos, K.; Georgoulas, E.; Peridis, S.; Asimakopoulos, D.; Maravelis, A.G. Unraveling the Origin of the Messinian? Evaporites in Zakynthos Island, Ionian Sea: Implications for the Sealing Capacity in the Mediterranean Sea. *J. Mar. Sci. Eng.* **2023**, *11*, 271, doi:10.3390/jmse11020271.
39. Bellas, S. International Tender for Hydrocarbons' E&P, Onshore Western Greece 2014; Technical Report "Arta-Preveza Contract Area (Block 1). *Minist. Environ. Energy Clim.*

Chang. 2014, 1–139.

40. Makri, V.I.; Schito, A.; Muirhead, D.; Oikonomopoulos, I.; Bellas, S. Preliminary Results of a Thermal Maturity Modelling Study as a Tool for Understanding a Structural Setting – the Case of the Fold and Thrust Belt of Western Greece. In Proceedings of the EGU General Assembly 2023; Vienna, Austria, 2023.
41. Telemenis, D.; Makri, V.-I.; Manoutsoglou, E.; Bellas, S. Exploring Neogene Marine Diatomites in Western Crete: A New Source-Rock Candidate with Hydrocarbon Generation Potential? *Eng* **2023**, *4*, 285–300, doi:10.3390/eng4010017.
42. Kontakiotis, G.; Moforis, L.; Karakitsios, V.; Antonarakou, A. Sedimentary Facies Analysis, Reservoir Characteristics and Paleogeography Significance of the Early Jurassic to Eocene Carbonates in Epirus (Ionian Zone, Western Greece). *J. Mar. Sci. Eng.* **2020**, *8*, 1–25, doi:10.3390/jmse8090706.
43. van Hinsbergen, D.J.J.; Torsvik, T.H.; Schmid, S.M.; Maţenco, L.C.; Maffione, M.; Vissers, R.L.M.; Gürer, D.; Spakman, W. Orogenic Architecture of the Mediterranean Region and Kinematic Reconstruction of Its Tectonic Evolution since the Triassic. *Gondwana Res.* **2020**, *81*, 79–229, doi:10.1016/j.gr.2019.07.009.
44. Avramidis, P.; Zelilidis, A. The Nature of Deep-Marine Sedimentation and Palaeocurrent Trends as Evidence of Pindos Foreland Basin Fill Conditions. *Episodes* **2001**, *24*, 252–256.
45. Avramidis, P.; Zelilidis, A.; Vakalas, I.; Kontopoulos, N. Interactions between Tectonic Activity and Eustatic Sea-Level Changes in the Pindos and Mesohellenic Basins, NW Greece: Basin Evolution and Hydrocarbon Potential. *J. Pet. Geol.* **2002**, *25*, 53–82, doi:10.1111/j.1747-5457.2002.tb00099.x.
46. Pantopoulos, G.; Vakalas, I.; Maravelis, A.; Zelilidis, A. Statistical Analysis of Turbidite Bed Thickness Patterns from the Alpine Fold and Thrust Belt of Western and Southeastern Greece. *Sediment. Geol.* **2013**, *294*, 37–57, doi:10.1016/j.sedgeo.2013.05.007.
47. Karakitsios, V.; Roveri, M.; Lugli, S.; Manzi, V.; Gennari, R.; Antonarakou, A.; Triantaphyllou, M.; Agiadi, K.; Kontakiotis, G.; Kafousia, N.; et al. A Record of the Messinian Salinity Crisis in the Eastern Ionian Tectonically Active Domain (Greece, Eastern Mediterranean). *Basin Res.* **2017**, *29*, 203–233, doi:10.1111/bre.12173.
48. Velaj, T. The Structural Style and Hydrocarbon Exploration of the Subthrust in the Berati

Anticlinal Belt, Albania. *J. Pet. Explor. Prod. Technol.* **2015**, *5*, 123–145, doi:10.1007/s13202-015-0162-1.

49. Nikolaou, K. Contribution to the Knowledge of the Neogene, the Geology and the Ionian and Pre-Apulian Limits in Relation to the Petroleum Geology Observations in Strophades, Zakynthos, and Kephalynia Islands, National & Kapodistrian University of Athens: Athens, 1986.
50. Alexandridis, I. Contribution to the Understanding of the Geological Structure and Petroleum Systems of Epirus with Integration of Field Geology and Organic Geochemistry Methods, Aristotle University of Thessaloniki, 2023.
51. Rigakis, N. Contribution to Stratigraphic Research on Wells and Outcrops of the Alpine Formations in Western Greece, in Relation to the Petroleum Generation Efficiency of Their Organic Matter, National and Kapodistrian University of Athens: Athens, 1999.
52. Prifti, I.; Muska, K. Hydrocarbon Occurrences and Petroleum Geochemistry of Albanian Oils. *Ital. J. Geosci.* **2013**, *132*, 228–235, doi:10.3301/ijg.2012.29.
53. Doutsos, T.; Pe-Piper, G.; Boronkay, K.; Koukouvelas, I. Kinematics of the Central Hellenides. *Tectonics* **1993**, *12*, 936–953, doi:10.1029/93TC00108.
54. Curi, F. Oil Generation and Accumulation in the Albanide Ionian Basin. In *Generation, Accumulation and Production of Europe's Hydrocarbons III*; Springer Berlin Heidelberg: Berlin, Heidelberg, 1993; pp. 281–293.
55. Robertson, A.; Shallo, M. Mesozoic–Tertiary Tectonic Evolution of Albania in Its Regional Eastern Mediterranean Context. *Tectonophysics* **2000**, *316*, 197–254, doi:10.1016/S0040-1951(99)00262-0.
56. Neumeister, S.; Gawlick, H.-J.; Bechtel, A.; Hoxha, L.; Missoni, S.; Gratzer, R.; Dumitrica, P. Source Rock Investigations of a Middle Jurassic Posidonia Marl of the Ionian Zone of Albania. *J. Alp. Geol.* **2010**, *52*, 192–192.
57. Bernoulli, D.; Renz, O. Jurassic Carbonate Facies and New Ammonite Faunas from Western Greece. *Eclogae Geol. Helv.* **1970**, *63*, 573–607, doi:10.5169/seals-163861.
58. Zappaterra, E. Source-Rock Distribution Model of the Periadriatic Region. *Am. Assoc. Pet. Geol. Bull.* **1994**, *78*, 333–354.

59. Gupta, S.; Cowie, P.A.; Dawers, N.H.; Underhill, J.R. A Mechanism to Explain Rift-Basin Subsidence and Stratigraphic Patterns through Fault-Array Evolution. *Geology* **1998**, *26*, 595–598, doi:10.1130/0091-7613(1998)026<0595:AMTERB>2.3.CO;2.

60. Kafousia, N.; Karakitsios, V.; Mattioli, E.; Kenjo, S.; Jenkyns, H.C. The Toarcian Oceanic Anoxic Event in the Ionian Zone, Greece. *Palaeogeogr. Palaeoclimatol. Palaeoecol.* **2014**, *393*, 135–145, doi:10.1016/j.palaeo.2013.11.013.

61. Kafousia, N.; Karakitsios, V.; Jenkyns, H. Indications for the Global Character of the Early Toarcian Oceanic Anoxic Event: Evidence from the Pindos Zone, Western Greece. In Proceedings of the Geochimica et Cosmochimica Acta Supplement; June 1 2009; Vol. 73, p. A612.

62. Karakitsios, V.; Tsikos, H.; van Breugel, Y.; Bakopoulos, I.; Koletti, L. Cretaceous Oceanic Anoxic Events in Western Continental Greece. *Bull. Geol. Soc. Greece* **2004**, *36*, 846–855, doi:10.12681/bgsg.16832.

63. Tzortzaki, E.; Karakitsios, V.; Tsikos, H. Biomarker Evidence for Intermittent Photic Zone Euxinia in the Aptian–Albian Organic Sedimentary Record from the Ionian Zone (Epirus, Greece). *Org. Geochem.* **2013**, *64*, 84–93, doi:10.1016/j.orggeochem.2013.08.013.

64. Nikolaou, K. Origin and Migration Mechanism of the Main Hydrocarbon Seeps in Western Greece. *Bull. Geol. Soc. Greece* **2001**, 1213–1219, doi:10.12681/bgsg.17185.

65. Makri, V.I.; Oikonomopoulos, I.; Muirhead, D.; Pasadakis, N. Kerogen Kinetics and the Effect of Rock Matrix: Insights from Western Greece. *Int. J. Coal Geol.* **2024**, *292*, 104585, doi:10.1016/j.coal.2024.104585.

66. Monopolis, D.; Bruneton, A. Ionian Sea (Western Greece): Its Structural Outline Deduced from Drilling and Geophysical Data. *Tectonophysics* **1982**, *83*, 227–242.

67. Roussos, N.; Marnelis, F. Greece Licensing Round to Focus on Western Sedimentary Basins. *Oil Gas J.* 1995, *93*, 58–62.

68. Zelilidis, A.; Tserolas, P.; Chamilaki, E.; Pasadakis, N.; Kostopoulou, S.; Maravelis, A.G. Hydrocarbon Prospectivity in the Hellenic Trench System: Organic Geochemistry and Source Rock Potential of Upper Miocene–Lower Pliocene Successions in the Eastern Crete Island, Greece. *Int. J. Earth Sci.* **2016**, *105*, 1859–1878, doi:10.1007/s00531-015-1278-8.

69. Maravelis, A.G.; Koukounya, A.; Tserolas, P.; Pasadakis, N.; Zelilidis, A. Geochemistry of Upper Miocene-Lower Pliocene Source Rocks in the Hellenic Fold and Thrust Belt, Zakynthos Island, Ionian Sea, Western Greece. *Mar. Pet. Geol.* **2015**, *66*, 217–230, doi:10.1016/j.marpetgeo.2014.09.014.

70. Maravelis, A.; Makrodimitras, G.; Pasadakis, N.; Zelilidis, A. Stratigraphic Evolution and Source Rock Potential of a Lower Oligocene to Lower–Middle Miocene Continental Slope System, Hellenic Fold and Thrust Belt, Ionian Sea, Northwest Greece. *Geol. Mag.* **2014**, *151*, 394–413, doi:10.1017/S0016756813000289.

71. Zelilidis, A.; Maravelis, A.G.; Tserolas, P.; Konstantopoulos, P.A. An Overview of the Petroleum Systems in the Ionian Zone, Onshore NW Greece and Albania. *J. Pet. Geol.* **2015**, *38*, 331–348, doi:10.1111/jpg.12614.

72. Maravelis, A.; Panagopoulos, G.; Piliotis, I.; Pasadakis, N.; Manoutsoglou, E.; Zelilidis, A. Pre-Messinian (Sub-Salt) Source-Rock Potential on Back-Stop Basins of the Hellenic Trench System (Messara Basin, Central Crete, Greece). *Oil Gas Sci. Technol. – Rev. d'IFP Energies Nouv.* **2013**, *71*, 6, doi:10.2516/ogst/2013130.

73. Rallakis, D.; Siavalas, G.; Oskay, G.; Tsimiklis, D.; Christanis, K. Maturity of Dispersed Organic Matter in Bituminous Formations of the Ionian Zone (Epirus Region, NW Greece). *Bull. Geol. Soc. Greece* **2013**, *47*, 880–889, doi:10.12681/bgsg.11127.

74. Bourli, N. Stratigraphic Processes and Ionian Basin Evolution in Kastos Island from Triassic to Eocene , for Hydrocarbon Fields Development . Correlation with NW Peloponnesus (Araxos Peninsula) Outcrops. **2021**, 1–168.

75. Plakogiannakis, E. Geochemical Evaluation of Petroleum Oil Formation from Corfu Island., University of Patras, 2020.

76. Klokotini, V. Organic Geochemical Study of Bituminous Formation of Epirus, Technical University of Crete, 2015.

77. Bourli, N.; Iliopoulos, G.; Makrodimitras, G.; Nikitas, A.; Stefatos, A.; Zelilidis, A. Upper Triassic to Lower Jurassic Plattenkalk Series, South Peloponnesus and Crete Island, Could Represent Source Rocks. In Proceedings of the 83rd EAGE Annual Conference & Exhibition; European Association of Geoscientists & Engineers, 2022; pp. 1–5.

78. Hackley, P.C.; Lünsdorf, N.K. Application of Raman Spectroscopy as Thermal Maturity

Probe in Shale Petroleum Systems: Insights from Natural and Artificial Maturation Series. *Energy & Fuels* **2018**, *32*, 11190–11202, doi:10.1021/acs.energyfuels.8b02171.

79. Rallakis, D. Study of the Maturity of Dispersed Organic Matter in Bituminous Formations of the Ionian Zone (Epirus Region, NW Greece), University of Patras, 2013.

80. Bellanca, A.; Masetti, D.; Neri, R.; Venezia, F. Geochemical and Sedimentological Evidence of Productivity Cycles Recorded in Toarcian Black Shales from the Belluno Basin, Southern Alps, Northern Italy. *J. Sediment. Res.* **1999**, *69*, 466–476, doi:10.2110/jsr.69.466.

81. Sabatino, N.; Neri, R.; Bellanca, A.; Jenkyns, H.C.; Masetti, D.; Scopelliti, G. Petrography and High-Resolution Geochemical Records of Lower Jurassic Manganese-Rich Deposits from Monte Mangart, Julian Alps. *Palaeogeogr. Palaeoclimatol. Palaeoecol.* **2011**, *299*, 97–109, doi:10.1016/j.palaeo.2010.10.039.

82. ten Haven, H.L.; de Leeuw, J.W.; Schenck, P.A. Organic Geochemical Studies of a Messinian Evaporitic Basin, Northern Apennines (Italy) I: Hydrocarbon Biological Markers for a Hypersaline Environment. *Geochim. Cosmochim. Acta* **1985**, *49*, 2181–2191, doi:10.1016/0016-7037(85)90075-4.

83. Grice, K.; Schouten, S.; Nissenbaum, A.; Charrach, J.; Sinninghe Damsté, J.S. Isotopically Heavy Carbon in the C21 to C25 Regular Isoprenoids in Halite-Rich Deposits from the Sdom Formation, Dead Sea Basin, Israel. *Org. Geochem.* **1998**, *28*, 349–359, doi:10.1016/S0146-6380(98)00006-0.

84. Jiang, J.-H.; Liang, Y.; Ozaki, Y. Principles and Methodologies in Self-Modeling Curve Resolution. *Chemom. Intell. Lab. Syst.* **2004**, *71*, 1–12.

85. Peters, K.E.; Walters, C.; Moldowan, J.M. Maturity-Related Biomarker Parameters. In *The Biomarker Guide*; Cambridge University Press: Cambridge, 2004; Vol. 2, pp. 608–640.

86. Oikonomopoulos, I.; Gentzis, T.; Carvajal-Ortiz, H.; Tripsanas, E. New Insights into Oil-to-Source Rock Correlation of Oils and Asphalt Seeps from Zakynthos Island and the West Coast of Peloponnese, Western Greece. In Proceedings of the Joint 74th ICCP and 39th TSOP Meeting “Organic Petrology in the Energy Transition Era: Challenges ahead”; Geological Society of Greece: Patras, 2023; Vol. 12, p. 29.

87. Foscolos, A. Organic Petrology and Maturity of the Sedimentary Succession of the Agios

Georgios-3 Drillhole, Syncline of Arta, Western Greece, Technical University of Crete, 1989.

88. Karakitsios, V. Studying the Carbonates from Triassic to Eocene in the Ionian Zone. In Proceedings of the 25th IAS Meeting of Sedimentology; 2007; pp. 123–142.

89. Peters, K.E.; Walters, C.C.; Moldowan, J.M. Source- and Age-Related Biomarker Parameters. In *The Biomarker Guide*; Cambridge University Press, 2004; pp. 483–607.

90. Tsikos, H.; Karakitsios, V.; van Breugel, Y.; Walsworth-Bell, B.; Bombardiere, L.; Petrizzo, M.R.; Sinninghe Damsté, J.S.; Schouten, S.; Erba, E.; Premoli Silva, I.; et al. Organic-Carbon Deposition in the Cretaceous of the Ionian Basin, NW Greece: The Paquier Event (OAE 1b) Revisited. *Geol. Mag.* **2004**, *141*, 401–416, doi:10.1017/S0016756804009409.

91. Kuypers, M.M.M.; Blokker, P.; Erbacher, J.; Kinkel, H.; Pancost, R.D.; Schouten, S.; Sinninghe Damsté, J.S. Massive Expansion of Marine Archaea during a Mid-Cretaceous Oceanic Anoxic Event. *Science (80-.).* **2001**, *293*, 92–94, doi:10.1126/science.1058424.

92. Kuypers, M.M.M.; Pancost, R.D.; Nijenhuis, I.A.; Sinninghe Damsté, J.S. Enhanced Productivity Led to Increased Organic Carbon Burial in the Euxinic North Atlantic Basin during the Late Cenomanian Oceanic Anoxic Event. *Paleoceanography* **2002**, *17*, doi:10.1029/2000PA000569.

93. Dembicki, H. The Effects of the Mineral Matrix on the Determination of Kinetic Parameters Using Modified Rock Eval Pyrolysis. *Org. Geochem.* **1992**, *18*, 531–539, doi:10.1016/0146-6380(92)90116-F.

94. Burnham, A.K. Principles of Kinetic Analysis for Condensed-Phase Thermal Decomposition. *Presentation* 2014, 62.

95. Burnham, A.K. Introduction to Chemical Kinetics. In *Global Chemical Kinetics of Fossil Fuels*; Springer International Publishing: Cham, 2017; pp. 25–74.

96. Petersen, H.I.; Bojesen-Koefoed, J.A.; Nytoft, H.P. Source Rock Evaluation of Middle Jurassic Coals, Northeast Greenland, by Artificial Maturation: Aspects of Petroleum Generation from Coal. *Am. Assoc. Pet. Geol. Bull.* **2002**, *86*, 233–256, doi:10.1306/61EEDA9E-173E-11D7-8645000102C1865D.

97. Bojesen-Koefoed, J.A.; Dam, G.; Nytoft, H.P.; Pedersen, G.K.; Petersen, H.I. Drowning of a Nearshore Peat-Forming Environment, Atane Formation (Cretaceous) at Asuk, West Greenland: Sedimentology, Organic Petrography and Geochemistry. *Org. Geochem.* **2001**, *32*, 967–980, doi:10.1016/S0146-6380(01)00072-9.

98. Petersen, H.I.; Bojesen-Koefoed, J.A.; Mathiesen, A. Variations in Composition, Petroleum Potential and Kinetics of Ordovician - Miocene Type I and Type II Source Rocks (Oil Shales): Implications for Hydrocarbon Generation Characteristics. *J. Pet. Geol.* **2010**, *33*, 19–41, doi:10.1111/j.1747-5457.2010.00462.x.

99. Burnham, A.K.; Braun, R.L.; Gregg, H.R.; Samoun, A.M. Comparison of Methods for Measuring Kerogen Pyrolysis Rates and Fitting Kinetic Parameters. *Energy Fuels* **1987**, *1*, 452–458.

100. Peters, K.E.; Burnham, A.K.; Walters, C.C. Petroleum Generation Kinetics: Single versus Multiple Heating-Ramp Open-System Pyrolysis. *Am. Assoc. Pet. Geol. Bull.* **2015**, *99*, 591–616, doi:10.1306/11141414080.

101. Ungerer, P. State of the Art of Research in Kinetic Modelling of Oil Formation and Expulsion. *Org. Geochem.* **1990**, *16*, 1–25, doi:10.1016/0146-6380(90)90022-R.

102. Burnham, A.K. Pyrolysis in Open Systems. In *Global Chemical Kinetics of Fossil Fuels*; Springer International Publishing: Cham, 2017; pp. 107–169.

103. Behar, F.; Kressmann, S.; Rudkiewicz, J.L.; Vandenbroucke, M. Experimental Simulation in a Confined System and Kinetic Modelling of Kerogen and Oil Cracking. *Org. Geochem.* **1992**, *19*, 173–189, doi:10.1016/0146-6380(92)90035-V.

104. Romero-Sarmiento, M.F.; Euzen, T.; Rohais, S.; Jiang, C.; Littke, R. Artificial Thermal Maturation of Source Rocks at Different Thermal Maturity Levels: Application to the Triassic Montney and Doig Formations in the Western Canada Sedimentary Basin. *Org. Geochem.* **2016**, *97*, 148–162, doi:10.1016/J.ORGGEOCHEM.2016.05.002.

105. Liang, H.; Xu, F.; Grice, K.; Xu, G.; Holman, A.; Hopper, P.; Fu, D.; Yu, Q.; Liang, J.; Wang, D. Kinetics of Oil Generation from Brackish-Lacustrine Source Rocks in the Southern Bohai Sea, East China. *Org. Geochem.* **2020**, *139*, 103945, doi:10.1016/J.ORGGEOCHEM.2019.103945.

106. Cedeño, A.; Ohm, S.; Escalona, A.; Marín, D.; Olaussen, S.; Demchuk, T. Upper Jurassic

to Lower Cretaceous Source Rocks in the Norwegian Barents Sea, Part II: Insights from Open- and Closed-System Pyrolysis Experiments. *Mar. Pet. Geol.* **2021**, *134*, 105343, doi:10.1016/j.marpetgeo.2021.105343.

107. Juntgen, H.; Klein, J. Entstehung von Erdgas Aus Kohligen Sedimenten. **1975**.

108. Dieckmann, V. Modelling Petroleum Formation from Heterogeneous Source Rocks: The Influence of Frequency Factors on Activation Energy Distribution and Geological Prediction. *Mar. Pet. Geol.* **2005**, *22*, 375–390, doi:10.1016/j,marpetgeo.2004.11.002.

109. Pepper, A.S.; Dodd, T.A. Simple Kinetic Models of Petroleum Formation. Part II: Oil-Gas Cracking. *Mar. Pet. Geol.* **1995**, *12*, 321–340, doi:10.1016/0264-8172(95)98382-F.

110. Schaefer, R.G.; Schenk, H.J.; Hardelauf, H.; Harms, R. Determination of Gross Kinetic Parameters for Petroleum Formation from Jurassic Source Rocks of Different Maturity Levels by Means of Laboratory Experiments. *Org. Geochem.* **1990**, *16*, 115–120, doi:10.1016/0146-6380(90)90031-T.

111. Arrhenius, S. Über Die Reaktionsgeschwindigkeit Bei Der Inversion von Rohrzucker Durch Säuren. *Zeitschrift für Phys. Chemie* **1889**, *4*, 226–248, doi:10.1515/zpch-1889-0416.

112. Schenk, H.J.; Di Primio, R.; Horsfield, B. The Conversion of Oil into Gas in Petroleum Reservoirs. Part 1: Comparative Kinetic Investigation of Gas Generation from Crude Oils of Lacustrine, Marine and Fluviodeltaic Origin by Programmed-Temperature Closed-System Pyrolysis. *Org. Geochem.* **1997**, *26*, 467–481, doi:10.1016/S0146-6380(97)00024-7.

113. Pepper, A.S.; Corvi, P.J. Simple Kinetic Models of Petroleum Formation. Part I: Oil and Gas Generation from Kerogen. *Mar. Pet. Geol.* **1995**, *12*, 291–319, doi:10.1016/0264-8172(95)98381-E.

114. Juntgen, H.; Heek, K. Gas Release from Coal as a Function of Rate of Heating. *Fuel* **1968**, *47*, 103–117.

115. Tissot, B.P.; Pelet, R.; Ungerer, P. Thermal History of Sedimentary Basins, Maturation Indices, and Kinetics of Oil and Gas Generation. *Am. Assoc. Pet. Geol. Bull.* **1987**, *71*, 1445–1466, doi:10.1306/703c80e7-1707-11d7-8645000102c1865d.

116. Stainforth, J.G. Practical Kinetic Modeling of Petroleum Generation and Expulsion. *Mar.*

Pet. Geol. **2009**, *26*, 552–572, doi:10.1016/j.marpetgeo.2009.01.006.

117. Rullkötter, J.; Leythaeuser, D.; Horsfield, B.; Littke, R.; Mann, U.; Müller, P..; Radke, M.; Schaefer, R..; Schenk, H.-J.; Schwochau, K.; et al. Organic Matter Maturation under the Influence of a Deep Intrusive Heat Source: A Natural Experiment for Quantitation of Hydrocarbon Generation and Expulsion from a Petroleum Source Rock (Toarcian Shale, Northern Germany). *Org. Geochem.* **1988**, *13*, 847–856, doi:10.1016/0146-6380(88)90237-9.

118. Sundararaman, P.; Merz, P.H.; Mann, R.G. Determination of Kerogen Activation Energy Distribution. *Energy & Fuels* **1992**, *6*, 793–803.

119. Waples, D. *Organic Geochemistry for Exploration Geologists*; Springer, 1981; ISBN 0934634254.

120. Waples, D.W.; Nowaczewski, V.S. *Source-Rock Kinetics*; 2013;

121. Chen, Z.; Liu, X.; Jiang, C. Quick Evaluation of Source Rock Kerogen Kinetics Using Hydrocarbon Pyrograms from Regular Rock-Eval Analysis. *Energy & Fuels* **2017**, *31*, 1832–1841, doi:10.1021/acs.energyfuels.6b01569.

122. Froidl, F.; Zieger, L.; Mahlstedt, N.; Littke, R. Comparison of Single- and Multi-Ramp Bulk Kinetics for a Natural Maturity Series of Westphalian Coals: Implications for Modelling Petroleum Generation. *Int. J. Coal Geol.* **2020**, *219*, 103378, doi:10.1016/j.coal.2019.103378.

123. Chen, Z.; Guo, Q.; Jiang, C.; Liu, X.; Reyes, J.; Mort, A.; Jia, Z. Source Rock Characteristics and Rock-Eval-Based Hydrocarbon Generation Kinetic Models of the Lacustrine Chang-7 Shale of Triassic Yanchang Formation, Ordos Basin, China. *Int. J. Coal Geol.* **2017**, *182*, 52–65, doi:10.1016/j.coal.2017.08.017.

124. Orr, W.L. Kerogen/Asphaltene/Sulfur Relationships in Sulfur-Rich Monterey Oils. *Org. Geochem.* **1986**, *10*, 499–516, doi:10.1016/0146-6380(86)90049-5.

125. Baskin, D.K.; Peters, K.E. Early Generation Characteristics of a Sulfur-Rich Monterey Kerogen. *Am. Assoc. Pet. Geol. Bull.* **1992**, *76*, 1–13.

126. Lewan, M.D.; Kotarba, M.J.; Curtis, J.B.; Więcław, D.; Kosakowski, P. Oil-Generation Kinetics for Organic Facies with Type-II and -IIS Kerogen in the Menilite Shales of the

Polish Carpathians. *Geochim. Cosmochim. Acta* **2006**, *70*, 3351–3368, doi:10.1016/j.gca.2006.04.024.

127. Espitalié, J.; Madec, M.; Tissot, B.P. Role of Mineral Matrix in Kerogen Pyrolysis: Influence on Petroleum Generation and Migration. *Am. Assoc. Pet. Geol. Bull.* **1980**, *64*, 59–66, doi:10.1306/2F918928-16CE-11D7-8645000102C1865D.

128. Tegelaar, E.W.; Noble, R.A. Kinetics of Hydrocarbon Generation as a Function of the Molecular Structure of Kerogen as Revealed by Pyrolysis-Gas Chromatography. *Org. Geochem.* **1994**, *22*, 543–574, doi:10.1016/0146-6380(94)90125-2.

129. Garner, L. Sulfur-Rich (Type II-S) Source Rocks and Associated Hydrocarbons Available online: https://igiltd.com/news/sulfur-rich-type-ii-s-source-rocks-and-associated-hydrocarbons (accessed on 10 January 2024).

130. Jarvie, D.M.; Claxton, B.L.; Henk, F.; Breyer, J.T. Oil and Shale Gas from the Barnett Shale, Ft. Worth Basin, Texas. In Proceedings of the AAPG National Convention; AAPG National Convention: Denver, Colorado, 2001.

131. Lewan, M.D.; Ruble, T.E. Comparison of Petroleum Generation Kinetics by Isothermal Hydrous and Nonisothermal Open-System Pyrolysis. *Org. Geochem.* **2002**, *33*, 1457–1475, doi:10.1016/S0146-6380(02)00182-1.

132. Dembicki, H. Three Common Source Rock Evaluation Errors Made by Geologists during Prospect or Play Appraisals. *Am. Assoc. Pet. Geol. Bull.* **2009**, *93*, 341–356, doi:10.1306/10230808076.

133. Jarvie, D.M.; Lundell, L.L. Kerogen Type and Thermal Transformation of Organic Matter in the Miocene Monterey Formation. In *The Monterey Formation: from rocks to molecules*; Isaacs, C.M., Rullkőtter, J., Eds.; Columbia University Press: New York, 2001; pp. 268–295.

134. Espitalié, J.; Senga Makadi, K.; Trichet, J. Role of the Mineral Matrix during Kerogen Pyrolysis. *Org. Geochem.* **1984**, *6*, 365–382, doi:10.1016/0146-6380(84)90059-7.

135. Tannenbaum, E.; Kaplan, I.R. Role of Minerals in the Thermal Alteration of Organic Matter—I: Generation of Gases and Condensates under Dry Condition. *Geochim. Cosmochim. Acta* **1985**, *49*, 2589–2604, doi:10.1016/0016-7037(85)90128-0.

136. Rahman, H.M.; Kennedy, M.; Löhr, S.; Dewhurst, D.N.; Sherwood, N.; Yang, S.; Horsfield, B. The Influence of Shale Depositional Fabric on the Kinetics of Hydrocarbon Generation through Control of Mineral Surface Contact Area on Clay Catalysis. *Geochim. Cosmochim. Acta* **2018**, *220*, 429–448, doi:10.1016/j.gca.2017.10.012.

137. Al-Harahsheh, M.; Al-Ayed, O.; Robinson, J.; Kingman, S.; Al-Harahsheh, A.; Tarawneh, K.; Saeid, A.; Barranco, R. Effect of Demineralization and Heating Rate on the Pyrolysis Kinetics of Jordanian Oil Shales. *Fuel Process. Technol.* **2011**, *92*, 1805–1811, doi:10.1016/j.fuproc.2011.04.037.

138. Pan, C.; Jiang, L.; Liu, J.; Zhang, S.; Zhu, G. The Effects of Calcite and Montmorillonite on Oil Cracking in Confined Pyrolysis Experiments. *Org. Geochem.* **2010**, *41*, 611–626, doi:10.1016/j.orggeochem.2010.04.011.

139. Thompson, K.F.M. Compositional Regularities Common to Petroleum Reservoir Fluids and Pyrolysates of Asphaltenes and Kerogens. *Org. Geochem.* **2002**, *33*, 829–841, doi:10.1016/S0146-6380(02)00030-X.

140. Jasper, K.; Krooss, B.M.; Flajs, G.; Hartkopf-Fröder, C.; Littke, R. Characteristics of Type III Kerogen in Coal-Bearing Strata from the Pennsylvanian (Upper Carboniferous) in the Ruhr Basin, Western Germany: Comparison of Coals, Dispersed Organic Matter, Kerogen Concentrates and Coal–Mineral Mixtures. *Int. J. Coal Geol.* **2009**, *80*, 1–19, doi:10.1016/j.coal.2009.07.003.

141. Yan, J.; Jiang, X.; Han, X.; Liu, J. A TG–FTIR Investigation to the Catalytic Effect of Mineral Matrix in Oil Shale on the Pyrolysis and Combustion of Kerogen. *Fuel* **2013**, *104*, 307–317, doi:10.1016/j.fuel.2012.10.024.

142. Labus, M.; Matyasik, I.; Ziemianin, K. Thermal Decomposition Processes in Relation to the Type of Organic Matter, Mineral and Maceral Composition of Menilite Shales. *Energies* **2023**, *16*, 4500, doi:10.3390/en16114500.

143. Yang, S.; Horsfield, B. Some Predicted Effects of Minerals on the Generation of Petroleum in Nature. *Energy & Fuels* **2016**, *30*, 6677–6687, doi:10.1021/acs.energyfuels.6b00934.

144. Pelet, R. Comments on the Paper “The Effects of the Mineral Matrix on the Determination of Kinetic Parameters Using Modified Rock-Eval Pyrolysis” by H. Dembicki Jr, Org. Geochem., 18, 531-539 (1992). *Org. Geochem.* **1994**, *21*, 979–981, doi:10.1016/0146-

6380(94)90056-6.

145. Burnham, A.K. Comments on “The Effects of the Mineral Matrix on the Determination of Kinetic Parameters Using Modified Rock-Eval Pyrolysis” by H. Dembicki Jr, and the Resulting Comment by R. Pelet. *Org. Geochem.* **1994**, *21*, 985–986, doi:10.1016/0146-6380(94)90058-2.

146. Lehne, E.; Dieckmann, V. Bulk Kinetic Parameters and Structural Moieties of Asphaltenes and Kerogens from a Sulphur-Rich Source Rock Sequence and Related Petroleums. *Org. Geochem.* **2007**, *38*, 1657–1679, doi:10.1016/j.orggeochem.2007.06.006.

147. Di Primio, R.; Horsfield, B. Predicting the Generation of Heavy Oils in Carbonate/Evaporitic Environments Using Pyrolysis Methods. *Org. Geochem.* **1996**, *24*, 999–1016, doi:10.1016/S0146-6380(96)00116-7.

148. Hatzistavros, V.S.; Kallithrakas-Kontos, N.G. X-Ray Fluorescence Mercury Determination Using Cation Selective Membranes at Sub-Ppb Levels. *Anal. Chim. Acta* **2014**, *809*, 25–29, doi:10.1016/j.aca.2013.11.045.

149. Lafargue, E.; Marquis, F.; Pillot, D. Rock-Eval 6 Applications in Hydrocarbon Exploration, Production, and Soil Contamination Studies. *Oil Gas Sci. Technol.* **1998**, *53*, 421–437, doi:10.2516/ogst:1998036.

150. Espitalié, J.; Marquis, F.; Barsony, I. Geochemical Logging. In *Analytical Pyrolysis-Technics and Applications*; Voorhees, K.J., Ed.; Elsevier: Boston, 1984; pp. 276–304 ISBN 0408014172.

151. Behar, F.; Beaumont, V.; De B. Penteado, H.L. Rock-Eval 6 Technology: Performances and Developments. *Oil Gas Sci. Technol.* **2001**, *56*, 111–134, doi:10.2516/ogst:2001013.

152. Espitalié, J. Use of Tmax as a Maturation Index for Different Types of Organic Matter. Comparison with Vitrinite Reflectance. In *Thermal Modelling in Sedimentary Basins*; Burrus, J., Ed.; Institut Français du Pétrole: Paris, 1986; pp. 475–496.

153. Espitalié, J.; Laporte, J.L.; Madec, M.; Marquis, F.; Leplat, P.; Paulet, J.; Boutefeu, A. Méthode Rapide de Caractérisation Des Roches Mères, de Leur Potentiel Pétrolier et de Leur Degré d’évolution. *Rev. l’Institut Français du Pétrole* **1977**, *32*, 23–42, doi:10.2516/ogst:1977002.

154. Hackley, P.C.; Ryder, R.T.; Trippi, M.H.; Alimi, H. Thermal Maturity of Northern Appalachian Basin Devonian Shales: Insights from Sterane and Terpane Biomarkers. *Fuel* **2013**, *106*, 455–462, doi:10.1016/j.fuel.2012.12.032.

155. Peakman, T.M.; Maxwell, J.R. Early Diagenetic Pathways of Steroid Alkenes. *Org. Geochem.* **1988**, *13*, 583–592, doi:10.1016/0146-6380(88)90078-2.

156. Sinninghe Damsté, J.S.; Schouten, S.; Volkman, J.K. C27–C30 Neohop-13(18)-Enes and Their Saturated and Aromatic Derivatives in Sediments: Indicators for Diagenesis and Water Column Stratification. *Geochim. Cosmochim. Acta* **2014**, *133*, 402–421, doi:10.1016/j.gca.2014.03.008.

157. Volkman, J.K.; Barrett, S.M.; Dunstan, G.A. C25 and C30 Highly Branched Isoprenoid Alkenes in Laboratory Cultures of Two Marine Diatoms. *Org. Geochem.* **1994**, *21*, 407–414, doi:10.1016/0146-6380(94)90202-X.

158. Burnham, A.K.; Braun, R.L. Global Kinetic Analysis of Complex Materials. *Energy & Fuels* **1999**, *13*, 1–22, doi:10.1021/ef9800765.

159. Spangenberg, J.E.; Frimmel, H.E. Basin-Internal Derivation of Hydrocarbons in the Witwatersrand Basin, South Africa: Evidence from Bulk and Molecular Δ13C Data. *Chem. Geol.* **2001**, *173*, 339–355, doi:10.1016/S0009-2541(00)00283-7.

160. Stukins, S.; Jolley, D.W.; McIlroy, D.; Hartley, A.J. Middle Jurassic Vegetation Dynamics from Allochthonous Palynological Assemblages: An Example from a Marginal Marine Depositional Setting; Lajas Formation, Neuquén Basin, Argentina. *Palaeogeogr. Palaeoclimatol. Palaeoecol.* **2013**, *392*, 117–127, doi:10.1016/j.palaeo.2013.09.002.

161. Riding, J.B. A Guide to Preparation Protocols in Palynology. *Palynology* **2021**, *45*, 1–110, doi:10.1080/01916122.2021.1878305.

162. Tyson, R. V. *Sedimentary Organic Matter*; Springer Netherlands: Dordrecht, 1995; ISBN 978-94-010-4318-2.

163. He, C.; Ji, L.; Su, A.; Wu, Y.; Zhang, M.; Zhou, S.; Li, J.; Hao, L.; Ma, Y. Source-Rock Evaluation and Depositional Environment of Black Shales in the Triassic Yanchang Formation, Southern Ordos Basin, North-Central China. *J. Pet. Sci. Eng.* **2019**, *173*, 899–911, doi:10.1016/j.petrol.2018.10.089.

164. López, L. Study of the Biodegradation Levels of Oils from the Orinoco Oil Belt (Junin Area) Using Different Biodegradation Scales. *Org. Geochem.* **2014**, *66*, 60–69, doi:10.1016/j.orggeochem.2013.10.014.

165. Peters, K.E.; Burnham, A.K.; Walters, C.C.; Schenk, O. Guidelines for Kinetic Input to Petroleum System Models from Open-System Pyrolysis. *Mar. Pet. Geol.* **2018**, *92*, 979–986, doi:10.1016/J.MARPETGEO.2017.11.024.

166. Bornovas, J. *Geological Study of Leukas Island*; Institute of Geology and Subsurface Research: Athens, 1964;

167. Aljahdali, M.H.; Deaf, A.S.; Gentzis, T.; Bantan, R.A.; Abu-Zied, R.H.; Carvajal-Ortiz, H.; Khalaf, M.M. Organic Petrographic, Geochemical, and Sequence Stratigraphic Analyses for Evaluating the Hydrocarbon Potential of Middle Jurassic–Lower Cretaceous Rocks in Shushan Basin, Northwestern Egypt. *Front. Earth Sci.* **2023**, *11*, 1–25, doi:10.3389/feart.2023.1129379.

168. Jones, R.W. Organic Facies. In *Advances in Petroleum Geochemistry*; Brooks, J., Welte, D.H., Eds.; Academic Press: London, 1987; pp. 1–90 ISBN 0-12-6320020-9.

169. Vandenbroucke, M.; Largeau, C. Kerogen Origin, Evolution and Structure. *Org. Geochem.* **2007**, *38*, 719–833, doi:10.1016/j.orggeochem.2007.01.001.

170. Brennecka, G.A.; Herrmann, A.D.; Algeo, T.J.; Anbar, A.D. Rapid Expansion of Oceanic Anoxia Immediately before the End-Permian Mass Extinction. *Proc. Natl. Acad. Sci.* **2011**, *108*, 17631–17634, doi:10.1073/pnas.1106039108.

171. Marenco, P.J.; Martin, K.R.; Marenco, K.N.; Barber, D.C. Increasing Global Ocean Oxygenation and the Ordovician Radiation: Insights from Th/U of Carbonates from the Ordovician of Western Utah. *Palaeogeogr. Palaeoclimatol. Palaeoecol.* **2016**, *458*, 77–84, doi:10.1016/j.palaeo.2016.05.014.

172. Ronov, A.B. Organic Carbon in Sedimentary Rocks in Relation to the Presence of Petroleum. *Geochemistry* **1958**, *5*, 497–509.

173. Hunt, J.M. *Petroleum Geochemistry and Geology (Textbook)*; 2nd ed.; WH Freeman Company, 1995;

174. Palacas, J.G. Preliminary Assessment of Organic Carbon Content and Petroleum Source

Rock Potential of Cretaceous and Lower Tertiary Carbonates, South Florida Basin. *Am. Assoc. Pet. Geol. Bull.* **1978**, *28*, 357–381.

175. Zhang, S.C.; Liang, D.G.; Zhang, B.M.; Wang, F.Y.; Bian, L.Z.; Zhao, M.J. Generation of Marine Oil and Gas in Tarim Basin. *Pet. Ind. Press* **2004**, 1–433.

176. Liang, D.G.; Zhang, S.C.; Zhang, B.M.; Wang, F.Y. Understanding on Marine Oil Generation in China Based on Tarim Basin. *Earth Sci. Front.* **2000**, *7*, 534–547.

177. Huo, Z.; Pang, X.; Chen, J.; Zhang, J.; Song, M.; Guo, K.; Li, P.; Li, W.; Liang, Y. Carbonate Source Rock with Low Total Organic Carbon Content and High Maturity as Effective Source Rock in China: A Review. *J. Asian Earth Sci.* **2019**, *176*, 8–26, doi:10.1016/j.jseaes.2019.01.038.

178. Hunt, J.M. The Origin of Petroleum in Carbonate Rocks. In *Developments in Sedimentology*; Chilingar, G. V., Bissell, H.J., Fairbridge, R.W., Eds.; Elsevier, 1967; pp. 225–251.

179. Langford, F.F.; Blanc-Valleron, M.M. Interpreting Rock-Eval Pyrolysis Data Using Graphs of Pyrolizable Hydrocarbons vs. Total Organic Carbon. *Am. Assoc. Pet. Geol. Bull.* **1990**, *74*, 799–804, doi:10.1306/0C9B238F-1710-11D7-8645000102C1865D.

180. Walters, C.C. The Origin of Petroleum. In *Practical Advances in Petroleum Processing*; Springer New York: New York, NY, 2006; pp. 79–101.

181. Moldoveanu, S.C. Analytical Pyrolysis of Several Organic Geopolymers. In *Analytical Pyrolysis of Natural Organic Polymers*; Elsevier, 2021; pp. 403–425.

182. Dow, W.G.; O'Connor, D.I. Kerogen Maturity and Type by Reflected Light Microscopy Applied to Petroleum Exploration. In *How To Assess Maturation and Paleotemperatures*; SEPM (Society for Sedimentary Geology), 1982; pp. 133–157.

183. Berner, R.A.; Raiswell, R. Burial of Organic Carbon and Pyrite Sulfur in Sediments over Phanerozoic Time: A New Theory. *Geochim. Cosmochim. Acta* **1983**, *47*, 855–862, doi:10.1016/0016-7037(83)90151-5.

184. Braun, R.L.; Burnham, A.K.; Reynolds, J.G.; Clarkson, J.E. Pyrolysis Kinetics for Lacustrine and Marine Source Rocks by Programmed Micropyrolysis. *Energy & Fuels* **1991**, *5*, 192–204, doi:10.1021/ef00025a033.

185. Miao, H.; Guo, J.; Wang, Y.; Jiang, Z.; Zhang, C.; Li, C. Mineralogical and Elemental Geochemical Characteristics of Taodonggou Group Mudstone in the Taibei Sag, Turpan–Hami Basin: Implication for Its Formation Mechanism. *Solid Earth* **2023**, *14*, 1031–1052, doi:10.5194/se-14-1031-2023.

186. Thorpe, C.L.; Law, G.T.W.; Boothman, C.; Lloyd, J.R.; Burke, I.T.; Morris, K. The Synergistic Effects of High Nitrate Concentrations on Sediment Bioreduction. *Geomicrobiol. J.* **2012**, *29*, 484–493, doi:10.1080/01490451.2011.581332.

187. Wang, Z.; Yu, F.; Wang, J.; Fu, X.; Chen, W.; Zeng, S.; Song, C. Palaeoenvironment Evolution and Organic Matter Accumulation of the Upper Triassic Mudstones from the Eastern Qiangtang Basin (Tibet), Eastern Tethys. *Mar. Pet. Geol.* **2021**, *130*, 105113, doi:10.1016/j.marpetgeo.2021.105113.

188. Shi, J.; Zou, Y.R.; Cai, Y.L.; Zhan, Z.W.; Sun, J.N.; Liang, T.; Peng, P. Organic Matter Enrichment of the Chang 7 Member in the Ordos Basin: Insights from Chemometrics and Element Geochemistry. *Mar. Pet. Geol.* **2022**, *135*, 105404, doi:10.1016/j.marpetgeo.2021.105404.

189. Kidder, D.L.; Erwin, D.H. Secular Distribution of Biogenic Silica through the Phanerozoic: Comparison of Silica-Replaced Fossils and Bedded Cherts at the Series Level. *J. Geol.* **2001**, *109*, 509–522, doi:10.1086/320794.

190. Schoepfer, S.D.; Shen, J.; Wei, H.; Tyson, R. V.; Ingall, E.; Algeo, T.J. Total Organic Carbon, Organic Phosphorus, and Biogenic Barium Fluxes as Proxies for Paleomarine Productivity. *Earth-Science Rev.* **2015**, *149*, 23–52, doi:10.1016/j.earscirev.2014.08.017.

191. Ficken, K.J.; Li, B.; Swain, D.L.; Eglinton, G. An N-Alkane Proxy for the Sedimentary Input of Submerged/Floating Freshwater Aquatic Macrophytes. *Org. Geochem.* **2000**, *31*, 745–749, doi:10.1016/S0146-6380(00)00081-4.

192. Basu, S.; Anoop, A.; Sanyal, P.; Singh, P. Lipid Distribution in the Lake Ennamangalam, South India: Indicators of Organic Matter Sources and Paleoclimatic History. *Quat. Int.* **2017**, *443*, 238–247, doi:10.1016/j.quaint.2016.08.045.

193. El-Moghazy, A.F.; Deaf, A.S.; Edress, N.A.A. Integrated Organic, Inorganic Geochemical and Palynofacies Analyses to Characterize the Paleoenvironment of the Tortonian (Late Miocene) Wakar Formation, Offshore Nile Delta, Egypt. *Mar. Pet. Geol.* **2023**, *156*,

106456, doi:10.1016/j.marpetgeo.2023.106456.

194. Tomás, S.; Frijia, G.; Bömelburg, E.; Zamagni, J.; Perrin, C.; Mutti, M. Evidence for Seagrass Meadows and Their Response to Paleoenvironmental Changes in the Early Eocene (Jafnayn Formation, Wadi Bani Khalid, N Oman). *Sediment. Geol.* **2016**, *341*, 189–202, doi:10.1016/j.sedgeo.2016.05.016.

195. Eglinton, G.; Hamilton, R.J. Leaf Epicuticular Waxes. *Science (80-.).* **1967**, *156*, 1322–1335, doi:10.1126/science.156.3780.1322.

196. Cranwell, P.A.; Eglinton, G.; Robinson, N. Lipids of Aquatic Organisms as Potential Contributors to Lacustrine Sediments-II. *Org. Geochem.* **1987**, *11*, 513–527, doi:10.1016/0146-6380(87)90007-6.

197. Pomoni-Papaioannou, F.; Kostopoulou, V. Microfacies and Cycle Stacking Pattern in Liassic Peritidal Carbonate Platform Strata, Gavrovo-Tripolitza Platform, Peloponnesus, Greece. *Facies* **2008**, *54*, 417–431, doi:10.1007/s10347-008-0142-8.

198. Brooks, J.D.; Gould, K.; Smith, J.W. Isoprenoid Hydrocarbons in Coal and Petroleum. *Nature* **1969**, *222*, 257–259, doi:10.1038/222257a0.

199. Powell, T.G.; McKirdy, D.M. Relationship between Ratio of Pristane to Phytane, Crude Oil Composition and Geological Environment in Australia. *Nat. Phys. Sci.* **1973**, *243*, 37–39, doi:10.1038/physci243037a0.

200. ten Haven, H.L.; de Leeuw, J.W.; Rullkötter, J.; Damsté, J.S.S. Restricted Utility of the Pristane/Phytane Ratio as a Palaeoenvironmental Indicator. *Nature* **1987**, *330*, 641–643, doi:10.1038/330641a0.

201. Bourbonniere, R.A.; Meyers, P.A. Sedimentary Geolipid Records of Historical Changes in the Watersheds and Productivities of Lakes Ontario and Erie. *Limnol. Oceanogr.* **1996**, *41*, 352–359, doi:10.4319/lo.1996.41.2.0352.

202. Katz, B.; Lin, F. Lacustrine Basin Unconventional Resource Plays: Key Differences. *Mar. Pet. Geol.* **2014**, *56*, 255–265, doi:10.1016/j.marpetgeo.2014.02.013.

203. Petersen, H.I.; Hertle, M.; Sulsbrück, H. Upper Jurassic–Lowermost Cretaceous Marine Shale Source Rocks (Farsund Formation), North Sea: Kerogen Composition and Quality and the Adverse Effect of Oil-Based Mud Contamination on Organic Geochemical

Analyses. *Int. J. Coal Geol.* **2017**, *173*, 26–39, doi:10.1016/j.coal.2017.02.006.

204. Shanmugam, G. Significance of Coniferous Rain Forests and Related Organic Matter in Generating Commercial Quantities of Oil, Gippsland Basin, Australia. *Am. Assoc. Pet. Geol. Bull.* **1985**, *69*, 1241–1254, doi:10.1306/AD462BC3-16F7-11D7-8645000102C1865D.

205. Peters, K.E.; Fraser, T.H.; Amris, W.; Rustanto, B.; Hermanto, E. Geochemistry of Crude Oils from Eastern Indonesia. *Am. Assoc. Pet. Geol. Bull.* **1999**, *83*, 1927–1942, doi:10.1306/E4FD4643-1732-11D7-8645000102C1865D.

206. Wang, G.; Chang, X.; Wang, T.-G.; Simoneit, B.R.T. Pregnanes as Molecular Indicators for Depositional Environments of Sediments and Petroleum Source Rocks. *Org. Geochem.* **2015**, *78*, 110–120, doi:10.1016/j.orggeochem.2014.11.004.

207. ten Haven, H.L.; de Leeuw, J.W.; Peakman, T.M.; Maxwell, J.R. Anomalies in Steroid and Hopanoid Maturity Indices. *Geochim. Cosmochim. Acta* **1986**, *50*, 853–855, doi:10.1016/0016-7037(86)90361-3.

208. Requejo, A.G.; Hieshima, G.B.; Hsu, C.S.; McDonald, T.J.; Sassen, R. Short-Chain (C21 and C22) Diasteranes in Petroleum and Source Rocks as Indicators of Maturity and Depositional Environment. *Geochim. Cosmochim. Acta* **1997**, *61*, 2653–2667, doi:10.1016/S0016-7037(97)00106-3.

209. Moldowan, J.M.; Sundararaman, P.; Schoell, M. Sensitivity of Biomarker Properties to Depositional Environment and/or Source Input in the Lower Toarcian of SW-Germany. *Org. Geochem.* **1986**, *10*, 915–926, doi:10.1016/S0146-6380(86)80029-8.

210. Huang, W.-Y.; Meinschein, W.G. Sterols as Ecological Indicators. *Geochim. Cosmochim. Acta* **1979**, *43*, 739–745, doi:10.1016/0016-7037(79)90257-6.

211. El Nady, M.M. Biomarkers Assessment of Crude Oils and Extracts from Jurassic-Cretaceous Rocks, North Qattara Depression, North Western Desert, Egypt. *Pet. Sci. Technol.* **2008**, *26*, 1063–1082, doi:10.1080/10916460701208496.

212. Amoako, K.; Osei-Boakye, N.P.; Zhong, N.; De Sales Konan, N.F.; Foli, G.; Appau, P.O.; Fenyi, C.; Apesegah, E. Geochemical Fingerprints and Hydrocarbon Potential of Paleocene Mudrocks in the Tano Basin, Ghana: Insights from Biomarkers and Stable Carbon Isotopes. *Acta Geochim.* **2024**, *43*, 255–279, doi:10.1007/s11631-023-00652-4.

213. Tao, S.; Wang, C.; Du, J.; Liu, L.; Chen, Z. Geochemical Application of Tricyclic and Tetracyclic Terpanes Biomarkers in Crude Oils of NW China. *Mar. Pet. Geol.* **2015**, *67*, 460–467, doi:10.1016/j.marpetgeo.2015.05.030.

214. Moldowan, J.M.; Fago, F.J.; Lee, C.Y.; Jacobson, S.R.; Watt, D.S.; Slougui, N.-E.; Jeganathan, A.; Young, D.C. Sedimentary 12-n-Propylcholestanes, Molecular Fossils Diagnostic of Marine Algae. *Science (80-.).* **1990**, *247*, 309–312, doi:10.1126/science.247.4940.309.

215. Djerassi, C. Recent Studies in the Marine Sterol Field. *Pure Appl. Chem.* **1981**, *53*, 873–890, doi:10.1351/pac198153040873.

216. De Grande, S.M.B.; Aquino Neto, F.R.; Mello, M.R. Extended Tricyclic Terpanes in Sediments and Petroleums. *Org. Geochem.* **1993**, *20*, 1039–1047, doi:10.1016/0146-6380(93)90112-O.

217. Moldowan, J.M.; Lee, C.; Sundararaman, P. Source Correlation and Maturity Assessment of Select Oils and Rocks from the Central Adriatic Basin (Italy and Yugoslavia). In Proceedings of the Biological Markers in Sediments and Petroleum; Moldowan, J.M., Albrecht, P., Philp, R.P., Eds.; American Chemical Society: Englewood Cliffs, New Jersey, 1992; Vol. 34, pp. 370–401.

218. Moldowan, J.M.; Wolfgang, S.K.; Gallegos, E.J. Relationship Between Petroleum Composition and Depositional Environment of Petroleum Source Rocks. *Am. Assoc. Pet. Geol. Bull.* **1985**, *69*, 1255–1268, doi:10.1306/AD462BC8-16F7-11D7-8645000102C1865D.

219. ten Haven, H.L.; Rohmer, M.; Rullkötter, J.; Bisseret, P. Tetrahymanol, the Most Likely Precursor of Gammacerane, Occurs Ubiquitously in Marine Sediments. *Geochim. Cosmochim. Acta* **1989**, *53*, 3073–3079, doi:10.1016/0016-7037(89)90186-5.

220. Blumenberg, M.; Zink, K.G.; Scheeder, G.; Ostertag-Henning, C.; Erbacher, J. Biomarker Paleo-Reconstruction of the German Wealden (Berriasian, Early Cretaceous) in the Lower Saxony Basin (LSB). *Int. J. Earth Sci.* **2019**, *108*, 229–244, doi:10.1007/s00531-018-1651-5.

221. Henderson, W.; Steel, G. Isolation and Characterization of a Triterpenoid Alcohol from the Green River Shale. *J. Chem. Soc., Chem. Commun.* **1971**, 1331–1332,

doi:10.1039/c29710001331.

222. Damsté, J.S.S.; Schouten, S.; de Leeuw, J.W. The Occurrence and Distribution of Low-Molecular-Weight Sulfoxides in Polar Fractions of Sediment Extracts and Petroleum. *Org. Geochem.* **1995**, *23*, 129–138.

223. Hills, I.R.; Whitehead, E. V.; Anders, D.E.; Cummins, J.J.; Robinson, W.E. An Optically Active Triterpane, Gammacerane in Green River, Colorado, Oil Shale Bitumen. *Chem. Commun.* **1966**, 752–752, doi:10.1039/c1966000752b.

224. Peters, K.E.; Moldowan, J.M. Effects of Source, Thermal Maturity, and Biodegradation on the Distribution and Isomerization of Homohopanes in Petroleum. *Org. Geochem.* **1991**, *17*, 47–61, doi:10.1016/0146-6380(91)90039-M.

225. Damsté, J.S.S.; van Duin, A.C.; Hollander, D.; Kohnen, M.E.; de Leeuw, J.W. Early Diagenesis of Bacteriohopanepolyolderivatives: Formation of Fossil Homohopanoids. *Geochim. Cosmochim. Acta* **1995**, *59*, 5141–5157.

226. Volkman, J.K.; Zhang, Z.; Xie, X.; Qin, J.; Borjigin, T. Biomarker Evidence for Botryococcus and a Methane Cycle in the Eocene Huadian Oil Shale, NE China. *Org. Geochem.* **2015**, *78*, 121–134, doi:10.1016/j.orggeochem.2014.11.002.

227. Brassell, S.C. Aliphatic Hydrocarbons of a Cretaceous Black Shale and Its Adjacent Green Claystone from the Southern Angola Basin, Deep Sea Drilling Project Leg 75. In *Initial Reports of the Deep Sea Drilling Project, 75*; U.S. Government Printing Office: Washington, D.C, 1984; pp. 1019–1030.

228. van Dongen, B.E.; Schouten, S.; Sinninghe Damsté, J.S. Preservation of Carbohydrates through Sulfurization in a Jurassic Euxinic Shelf Sea: Examination of the Blackstone Band TOC Cycle in the Kimmeridge Clay Formation, UK. *Org. Geochem.* **2006**, *37*, 1052–1073, doi:10.1016/j.orggeochem.2006.05.007.

229. Moldowan, J.M.; Peters, K.E.; Carlson, R.M.K.; Schoell, M.; Abu-Ali, M.A. Diverse Applications of Petroleum Biomarker Maturity Parameters. *Arab. J. Sci. Eng.* **1994**, *19*, 273–298.

230. Lu, H.; Shen, C.; Zhang, Z.; Liu, M.; Sheng, G.; Peng, P.; Hsu, C.S. 2,3,6-/2,3,4-Aryl Isoprenoids in Paleocene Crude Oils from Chinese Jianghan Basin: Constrained by Water Column Stratification. *Energy & Fuels* **2015**, *29*, 4690–4700,

doi:10.1021/acs.energyfuels.5b00110.

231. Summons, R.E.; Powell, T.G. Identification of Aryl Isoprenoids in Source Rocks and Crude Oils: Biological Markers for the Green Sulphur Bacteria. *Geochim. Cosmochim. Acta* **1987**, *51*, 557–566, doi:10.1016/0016-7037(87)90069-X.

232. Sousa Júnior, G.R.; Santos, A.L.S.; de Lima, S.G.; Lopes, J.A.D.; Reis, F.A.M.; Santos Neto, E. V.; Chang, H.K. Evidence for Euphotic Zone Anoxia during the Deposition of Aptian Source Rocks Based on Aryl Isoprenoids in Petroleum, Sergipe–Alagoas Basin, Northeastern Brazil. *Org. Geochem.* **2013**, *63*, 94–104, doi:10.1016/j.orggeochem.2013.07.009.

233. Schwark, L.; Frimmel, A. Chemostratigraphy of the Posidonia Black Shale, SW-Germany. *Chem. Geol.* **2004**, *206*, 231–248, doi:10.1016/j.chemgeo.2003.12.008.

234. Schwark, L.; Püttmann, W. Aromatic Hydrocarbon Composition of the Permian Kupferschiefer in the Lower Rhine Basin, NW Germany. *Org. Geochem.* **1990**, *16*, 749–761, doi:10.1016/0146-6380(90)90114-F.

235. Koopmans, M.P.; Köster, J.; van Kaam-Peters, H.M.E.; Kenig, F.; Schouten, S.; Hartgers, W.A.; de Leeuw, J.W.; Sinninghe Damsté, J.S. Diagenetic and Catagenetic Products of Isorenieratene: Molecular Indicators for Photic Zone Anoxia. *Geochim. Cosmochim. Acta* **1996**, *60*, 4467–4496, doi:10.1016/S0016-7037(96)00238-4.

236. Hartgers, W.A.; Sinninghe Damsté, J.S.; Requejo, A.G.; Allan, J.; Hayes, J.M.; Ling, Y.; Xie, T.-M.; Primack, J.; de Leeuw, J.W. A Molecular and Carbon Isotopic Study towards the Origin and Diagenetic Fate of Diaromatic Carotenoids. *Org. Geochem.* **1994**, *22*, 703–725, doi:10.1016/0146-6380(94)90134-1.

237. van Breugel, Y.; Baas, M.; Schouten, S.; Mattioli, E.; Sinninghe Damsté, J.S. Isorenieratane Record in Black Shales from the Paris Basin, France: Constraints on Recycling of Respired CO2 as a Mechanism for Negative Carbon Isotope Shifts during the Toarcian Oceanic Anoxic Event. *Paleoceanography* **2006**, *21*, doi:10.1029/2006PA001305.

238. Le Tran, K.; Philippe, B. Oil and Rock Extract Analysis. In *Applied Petroleum Geochemistry*; Bordenave, M.L., Ed.; 1993; pp. 373–394.

239. Wesenlund, F.; Grundvåg, S.-A.; Engelschiøn, V.S.; Thießen, O.; Pedersen, J.H. Linking Facies Variations, Organic Carbon Richness and Bulk Bitumen Content – A Case Study of

the Organic-Rich Middle Triassic Shales from Eastern Svalbard. *Mar. Pet. Geol.* **2021**, *132*, 105168, doi:10.1016/j.marpetgeo.2021.105168.

240. Wang, A.; Wang, Z.; Liu, J.; Xu, N.; Li, H. The Sr/Ba Ratio Response to Salinity in Clastic Sediments of the Yangtze River Delta. *Chem. Geol.* **2021**, *559*, 119923, doi:10.1016/j.chemgeo.2020.119923.

241. Gelpi, E.; Schneider, H.; Mann, J.; Oró, J. Hydrocarbons of Geochemical Significance in Microscopic Algae. *Phytochemistry* **1970**, *9*, 603–612, doi:10.1016/S0031-9422(00)85700-3.

242. Mille, G.; Asia, L.; Guiliano, M.; Malleret, L.; Doumenq, P. Hydrocarbons in Coastal Sediments from the Mediterranean Sea (Gulf of Fos Area, France). *Mar. Pollut. Bull.* **2007**, *54*, 566–575, doi:10.1016/j.marpolbul.2006.12.009.

243. Arthur, M.A.; Dean, W.E.; Claypool, G.E. Anomalous 13C Enrichment in Modern Marine Organic Carbon. *Nature* **1985**, *315*, 216–218, doi:10.1038/315216a0.

244. Makri, V.I.; Bellas, S.; Moschou, G.; Pasadakis, N. An Integrated Approach for the Thermal Maturity Modeling Re-Assessment of an Exploration Well in the Hellenides Fold and Thrust Belt. *Geosci.* **2023**, *13*, doi:10.3390/geosciences13030076.

245. Tissot, B.; Pelet, R.; Roucoche, J.; Combaz, J. Alkanes as Geochemical Fossil Indicators of Geological Environments. In *Advances in Organic Geochemistry*; Campos, R., Goni, J., Ed.; Madrid, 1975; pp. 117–154.

246. Gatt, P. Facies, Depositional Environments and Drowning of Tethyan Isolated Carbonate Platforms: The Paleogene Carbonates of Malta. *Facies* **2022**, *68*, 9, doi:10.1007/s10347-022-00648-1.

247. Beigi, M.; Jafarian, A.; Javanbakht, M.; Wanas, H.A.; Mattern, F.; Tabatabaei, A. Facies Analysis, Diagenesis and Sequence Stratigraphy of the Carbonate-Evaporite Succession of the Upper Jurassic Surmeh Formation: Impacts on Reservoir Quality (Salman Oil Field, Persian Gulf, Iran). *J. African Earth Sci.* **2017**, *129*, 179–194, doi:10.1016/j.jafrearsci.2017.01.005.

248. van Breugel, Y.; Schouten, S.; Tsikos, H.; Erba, E.; Price, G.D.; Sinninghe Damsté, J.S. Synchronous Negative Carbon Isotope Shifts in Marine and Terrestrial Biomarkers at the Onset of the Early Aptian Oceanic Anoxic Event 1a: Evidence for the Release of 13C-

depleted Carbon into the Atmosphere. *Paleoceanography* **2007**, *22*, doi:10.1029/2006PA001341.

249. Berner, R.A. Biogeochemical Cycles of Carbon and Sulfur and Their Effect on Atmospheric Oxygen over Phanerozoic Time. *Glob. Planet. Change* **1989**, *1*, 97–122, doi:10.1016/0921-8181(89)90018-0.

250. Sundararaman, P.; Biggs, W.R.; Reynolds, J.G.; Fetzer, J.C. Vanadylporphyrins, Indicators of Kerogen Breakdown and Generation of Petroleum. *Geochim. Cosmochim. Acta* **1988**, *52*, 2337–2341, doi:10.1016/0016-7037(88)90136-6.

251. Peters, K.E.; Walters, C.C.; Mankiewicz, P.J. Evaluation of Kinetic Uncertainty in Numerical Models of Petroleum Generation. *Am. Assoc. Pet. Geol. Bull.* **2006**, *90*, 387–403, doi:10.1306/10140505122.

252. Pu, F.; Philip, R.P.; Zhenxi, L.; Guangguo, Y. Geochemical Characteristics of Aromatic Hydrocarbons of Crude Oils and Source Rocks from Different Sedimentary Environments. *Org. Geochem.* **1990**, *16*, 427–435, doi:10.1016/0146-6380(90)90059-9.

253. Volkman, J.K.; Alexander, R.; Kagi, R.I.; Rowland, S.J.; Sheppard, P.N. Biodegradation of Aromatic Hydrocarbons in Crude Oils from the Barrow Sub-Basin of Western Australia. *Org. Geochem.* **1984**, *6*, 619–632, doi:10.1016/0146-6380(84)90084-6.

254. Williams, L.A. Subtidal Stromatolites in Monterey Formation and Other Organic-Rich Rocks as Suggested Source Contributors to Petroleum Formation. *Am. Assoc. Pet. Geol. Bull.* **1984**, *68*, 1879–1893.

255. Wang, J.; Guo, S. Comparison of Geochemical Characteristics of Marine Facies, Marine-Continental Transitional Facies and Continental Facies Shale in Typical Areas of China and Their Control over Organic-Rich Shale. *Energy Sources, Part A Recover. Util. Environ. Eff.* **2020**, 1–13, doi:10.1080/15567036.2020.1796855.

256. Pech, S.; Eng, C.; Or, C.; Rahim, A.B.; Heng, R.; Buth, C.; Sio, S. Depositional Environment of Sediments in Tonle Sap Sedimentary Basin, Western Part of Cambodia: Insights from Field and Geochemical Studies. *Open J. Geol.* **2023**, *13*, 651–666, doi:10.4236/ojg.2023.137028.

257. Jones, B.; Manning, D.A.C. Comparison of Geochemical Indices Used for the Interpretation of Palaeoredox Conditions in Ancient Mudstones. *Chem. Geol.* **1994**, *111*, 111–129,

doi:10.1016/0009-2541(94)90085-X.

258. Tyson, R. V.; Pearson, T.H. Modern and Ancient Continental Shelf Anoxia: An Overview. *Geol. Soc. London, Spec. Publ.* **1991**, *58*, 1–24, doi:10.1144/GSL.SP.1991.058.01.01.

259. Tribovillard, N.; Algeo, T.J.; Lyons, T.; Riboulleau, A. Trace Metals as Paleoredox and Paleoproductivity Proxies: An Update. *Chem. Geol.* **2006**, *232*, 12–32, doi:10.1016/j.chemgeo.2006.02.012.

260. Alexandridis, I.; Schwark, L. Preliminary Results of a Biomarker Study of the Upper Triassic -Lower Jurassic Source Rocks in Ionian Zone, Epirus, NW Greece. Basin and Depositional Setting Implications. In Proceedings of the 16th International Congress, Geological Society of Greece; Bulletin of the Geological Society of Greece: Patras, 2022; pp. 728–729.

261. Huang, H.; Pearson, M.J. Source Rock Palaeoenvironments and Controls on the Distribution of Dibenzothiophenes in Lacustrine Crude Oils, Bohai Bay Basin, Eastern China. *Org. Geochem.* **1999**, *30*, 1455–1470, doi:10.1016/S0146-6380(99)00126-6.

262. Burnaz, L.; Littke, R.; Grohmann, S.; Erbacher, J.; Strauss, H.; Amann, F. Lower Jurassic (Pliensbachian–Toarcian) Marine Paleoenvironment in Western Europe: Sedimentology, Geochemistry and Organic Petrology of the Wells Mainzholzen and Wickensen, Hils Syncline, Lower Saxony Basin. *Int. J. Earth Sci.* **2024**, doi:10.1007/s00531-023-02381-8.

263. Derenne, S.; Largeau, C.; Casadevall, E.; Connan, J. Comparison of Torbanites of Various Origins and Evolutionary Stages. Bacterial Contribution to Their Formation. Causes of the Lack of Botryococcane in Bitumens. *Org. Geochem.* **1988**, *12*, 43–59, doi:10.1016/0146-6380(88)90114-3.

264. Šajnović, A.; Stojanović, K.; Jovančićević, B.; Golovko, A. Geochemical Investigation and Characterisation of Neogene Sediments from Valjevo-Mionica Basin (Serbia). *Environ. Geol.* **2008**, *56*, 1629–1641, doi:10.1007/s00254-008-1260-x.

265. Ruhl, M.; Bonis, N.R.; Reichart, G.-J.; Damsté, J.S.S.; Kürschner, W.M. Atmospheric Carbon Injection Linked to End-Triassic Mass Extinction. *Science (80-.).* **2011**, *333*, 430–434, doi:10.1126/science.1204255.

266. Haddad, E.E.; Tuite, M.L.; Martinez, A.M.; Williford, K.; Boyer, D.L.; Droser, M.L.; Love, G.D. Lipid Biomarker Stratigraphic Records through the Late Devonian

Frasnian/Famennian Boundary: Comparison of High- and Low-Latitude Epicontinental Marine Settings. *Org. Geochem.* **2016**, *98*, 38–53, doi:10.1016/j.orggeochem.2016.05.007.

267. Ando, T.; Sawada, K.; Nakamura, H.; Omatsu, K.; Takashima, R.; Nishi, H. Depositional Environments and Maturity Evaluated by Biomarker Analyses of Sediments Deposited across the Cenomanian–Turonian Boundary in the Yezo Group, Tomamae Area, Hokkaido, Japan. *Isl. Arc* **2017**, *26*, doi:10.1111/iar.12178.

268. Howard, D. POLYCYCLIC TRITERPENES OF THE ANAEROBIC PHOTOSYNTHETIC BACTERIUM RHODOMICROBIUM VANNIELII, University of California, 1981.

269. Bottari, F.; Marsili, A.; Morelli, I.; Pacchiani, M. Aliphatic and Triterpenoid Hydrocarbons from Ferns. *Phytochemistry* **1972**, *11*, 2519–2523, doi:10.1016/S0031-9422(00)88528-3.

270. Ageta, H.; Shiojima, K.; Arai, Y.; Suzuki, H.; Kiyotani, T. NMR Spectra of Triterpenoids. II. Hopenes and Migrated Hopenes. *Chem. Pharm. Bull.* **1994**, *42*, 39–44, doi:10.1248/cpb.42.39.

271. Rosa Putra, S. Role Du 1-Desoxy-d-Xylulose Dans La Biosynthese Des Isoprenoides, Université Louis Pasteur, 1998.

272. Douka, E.; Koukkou, A.-I.; Drainas, C.; Grosdemange-Billiard, C.; Rohmer, M. Structural Diversity of the Triterpenic Hydrocarbons from the Bacterium Zymomonas Mobilis: The Signature of Defective Squalene Cyclization by the Squalene/Hopene Cyclase. *FEMS Microbiol. Lett.* **2001**, *199*, 247–251, doi:10.1111/j.1574-6968.2001.tb10682.x.

273. Méjanelle, L.; Rivière, B.; Pinturier, L.; Khripounoff, A.; Baudin, F.; Dachs, J. Aliphatic Hydrocarbons and Triterpenes of the Congo Deep-Sea Fan. *Deep Sea Res. Part II Top. Stud. Oceanogr.* **2017**, *142*, 109–124, doi:10.1016/j.dsr2.2017.06.003.

274. Moldowan, J.M.; Fago, F.J.; Carlson, R.M.K.; Young, D.C.; Van Duvne, G.; Clardy, J.; Schoell, M.; Pillinger, C.T.; Watt, D.S. Rearranged Hopanes in Sediments and Petroleum. *Geochim. Cosmochim. Acta* **1991**, *55*, 3333–3353, doi:10.1016/0016-7037(91)90492-N.

275. Garel, S.; Quesnel, F.; Jacob, J.; Roche, E.; Le Milbeau, C.; Dupuis, C.; Boussafir, M.; Baudin, F.; Schnyder, J. High Frequency Floral Changes at the Paleocene–Eocene Boundary Revealed by Comparative Biomarker and Palynological Studies. *Org. Geochem.* **2014**, *77*, 43–58, doi:10.1016/j.orggeochem.2014.09.005.

276. Nytoft, H.P.; Ingermann Petersen, H.; Bryld Wessel Fyhn, M.; Nielsen, L.H.; Hovikoski, J.; Abatzis, I. Novel Saturated Hexacyclic C34 and C35 Hopanes in Lacustrine Oils and Source Rocks. *Org. Geochem.* **2015**, *87*, 107–118, doi:10.1016/j.orggeochem.2015.07.013.

277. Niu, C.; Hou, D.; Cheng, X.; Han, X.; Li, Y.; Li, Y. Origin and Geochemical Implications of Hopanoids in Saline Lacustrine Crude Oils from Huanghekou East Sag and Laizhouwan Northeastern Sag, Bohai Bay Basin. *ACS Omega* **2021**, *6*, 30298–30314, doi:10.1021/acsomega.1c02762.

278. Farrimond, P.; Eglinton, G.; Brassell, S.C.; Jenkyns, H.C. Toarcian Anoxic Event in Europe: An Organic Geochemical Study. *Mar. Pet. Geol.* **1989**, *6*, 136–147, doi:10.1016/0264-8172(89)90017-2.

279. Farrimond, P.; Telnæs, N. Three Series of Rearranged Hopanes in Toarcian Sediments (Northern Italy). *Org. Geochem.* **1996**, *25*, 165–177, doi:10.1016/S0146-6380(96)00127-1.

280. Luo, Q.; Yu, S.; Liu, Y.; Zhang, Y.; Han, H.; Qi, L.; Zhong, N. Existence and Implications of Hop-17(21)-Enes in the Lower Cretaceous of the Saihantala Sag, Erlian Basin, China. *Pet. Sci.* **2012**, *9*, 154–160, doi:10.1007/s12182-012-0195-8.

281. Ikehara, M.; Kawamura, K.; Ohkouchi, N.; Taira, A. Organic Geochemistry of Greenish Clay and Organic-Rich Sediments since the Early Miocene from Hole 985A, Norway Basin. In Proceedings of the Ocean Drilling Program, 162 Scientific Results; Raymo, M.E., Jansen, E., Blum, P., Herbert, T.D., Eds.; Ocean Drilling Program, June 1999; pp. 209–216.

282. Nytoft, H.P. Novel Side Chain Methylated and Hexacyclic Hopanes: Identification by Synthesis, Distribution in a Worldwide Set of Coals and Crude Oils and Use as Markers for Oxic Depositional Environments. *Org. Geochem.* **2011**, *42*, 520–539, doi:10.1016/j.orggeochem.2011.03.006.

283. Nytoft, H.P.; Fyhn, M.B.W.; Hovikoski, J.; Rizzi, M.; Abatzis, I.; Tuan, H.A.; Tung, N.T.; Huyen, N.T.; Cuong, T.X.; Nielsen, L.H. Biomarkers of Oligocene Lacustrine Source Rocks, Beibuwan-Song Hong Basin Junction, Offshore Northern Vietnam. *Mar. Pet. Geol.* **2020**, *114*, 104196, doi:10.1016/j.marpetgeo.2019.104196.

284. Schouten, S.; van Kaam-Peters, H.M.E.; Rijpstra, W.I.C.; Schoell, M.; Sinninghe Damsté, J.S. Effects of an Oceanic Anoxic Event on the Stable Carbon Isotopic Composition of Early Toarcian Carbon. *Am. J. Sci.* **2000**, *300*, 1–22, doi:10.2475/ajs.300.1.1.

285. Kemp, D.B.; Izumi, K. Multiproxy Geochemical Analysis of a Panthalassic Margin Record of the Early Toarcian Oceanic Anoxic Event (Toyora Area, Japan). *Palaeogeogr. Palaeoclimatol. Palaeoecol.* **2014**, *414*, 332–341, doi:10.1016/j.palaeo.2014.09.019.

286. Al-Suwaidi, A.H.; Hesselbo, S.P.; Damborenea, S.E.; Manceñido, M.O.; Jenkyns, H.C.; Riccardi, A.C.; Angelozzi, G.N.; Baudin, F. The Toarcian Oceanic Anoxic Event (Early Jurassic) in the Neuquén Basin, Argentina: A Reassessment of Age and Carbon Isotope Stratigraphy. *J. Geol.* **2016**, *124*, 171–193, doi:10.1086/684831.

287. Martinez-Ruiz, F.; Kastner, M.; Gallego-Torres, D.; Rodrigo-Gámiz, M.; Nieto-Moreno, V.; Ortega-Huertas, M. Paleoclimate and Paleoceanography over the Past 20,000 Yr in the Mediterranean Sea Basins as Indicated by Sediment Elemental Proxies. *Quat. Sci. Rev.* **2015**, *107*, 25–46, doi:10.1016/j.quascirev.2014.09.018.

288. Nelson, B.W. Sedimentary Phosphate Method for Estimating Paleosalinities. *Science (80-.).* **1967**, *158*, 917-920.

289. Langrock, U.; Stein, R.; Lipinski, M.; Brumsack, H. Late Jurassic to Early Cretaceous Black Shale Formation and Paleoenvironment in High Northern Latitudes: Examples from the Norwegian-Greenland Seaway. *Paleoceanography* **2003**, *18*, doi:10.1029/2002PA000867.

290. Katz, M.E.; Wright, J.D.; Miller, K.G.; Cramer, B.S.; Fennel, K.; Falkowski, P.G. Biological Overprint of the Geological Carbon Cycle. *Mar. Geol.* **2005**, *217*, 323–338, doi:10.1016/j.margeo.2004.08.005.

291. Pepper, A.S.; Corvi, P.J. Simple Kinetic Models of Petroleum Formation. Part III: Modelling an Open System. *Mar. Pet. Geol.* **1995**, *12*, 417–452, doi:10.1016/0264-8172(95)96904-5.

292. Wygrala, B.P. Integrated Study of an Oil Field in the Southern Po Basin, Northern Italy, University of Cologne, 1989.

293. Fytikas, M.D.; Kolios, N.P. Preliminary Heat Flow Map of Greece. In *Terrestrial heat flow in Europe*; Cermak, V., Rybach, L., Eds.; Springer-Verlag Berlin Heidelberg: Berlin-Heidelberg-New York, 1979; pp. 197–205 ISBN 978-3-642-95359-0.

294. Kokinou, E.; Kamberis, E. Deep Seismic Reflection Data from Offshore Western Greece: A New Crustal Model for the Ionian Sea. *J. Pet. Geol.* **2005**, *28*, 185–201, doi:10.1111/j.1747-5457.2005.tb00079.x.

295. McKenzie, D. The Plate Tectonics of the Mediterranean Region. *Nature* **1970**, *226*, 239–243, doi:10.1038/226239a0.

296. Lavecchia, G.; Bell, K. Magmatectonic Zonation of Italy: A Tool to Understanding Mediterranean Geodynamics. In *Updates in Volcanology - A Comprehensive Approach to Volcanological Problems*; Stoppa, F., Ed.; InTech: Rijeka, 2012; pp. 153–178 ISBN 978-953-307-434-4.

297. Tsokas, G.N.; Hansen, R.O. Study of the Crustal Thickness and the Subducting Lithosphere in Greece from Gravity Data. *J. Geophys. Res. Solid Earth* **1997**, *102*, 20585–20597, doi:10.1029/97JB00730.

298. Papoulia, J.; Makris, J. Tectonic Processes and Crustal Evolution on Offshore Western Peloponnese Derived from Active and Passive Seismics. *Bull. Geol. Soc. Greece* **2017**, *43*, 357–367, doi:10.12681/bgsg.11187.

299. Bravo-Gutiérrez, E.; Vergés, J.; Torne, M.; García-Castellanos, D.; Negredo, A.M.; Zhang, W.; Cruset, D.; Viaplana-Muzas, M.; Jiménez-Munt, I. Pre-Shortening Reconstruction of the Adria Microplate: Balanced and Restored Cross-Sections through the Southern Apennines–Dinarides (Central Mediterranean Sea). *Mar. Pet. Geol.* **2024**, *169*, 107055, doi:10.1016/j.marpetgeo.2024.107055.

APPENDIX I – Supplementary Figures

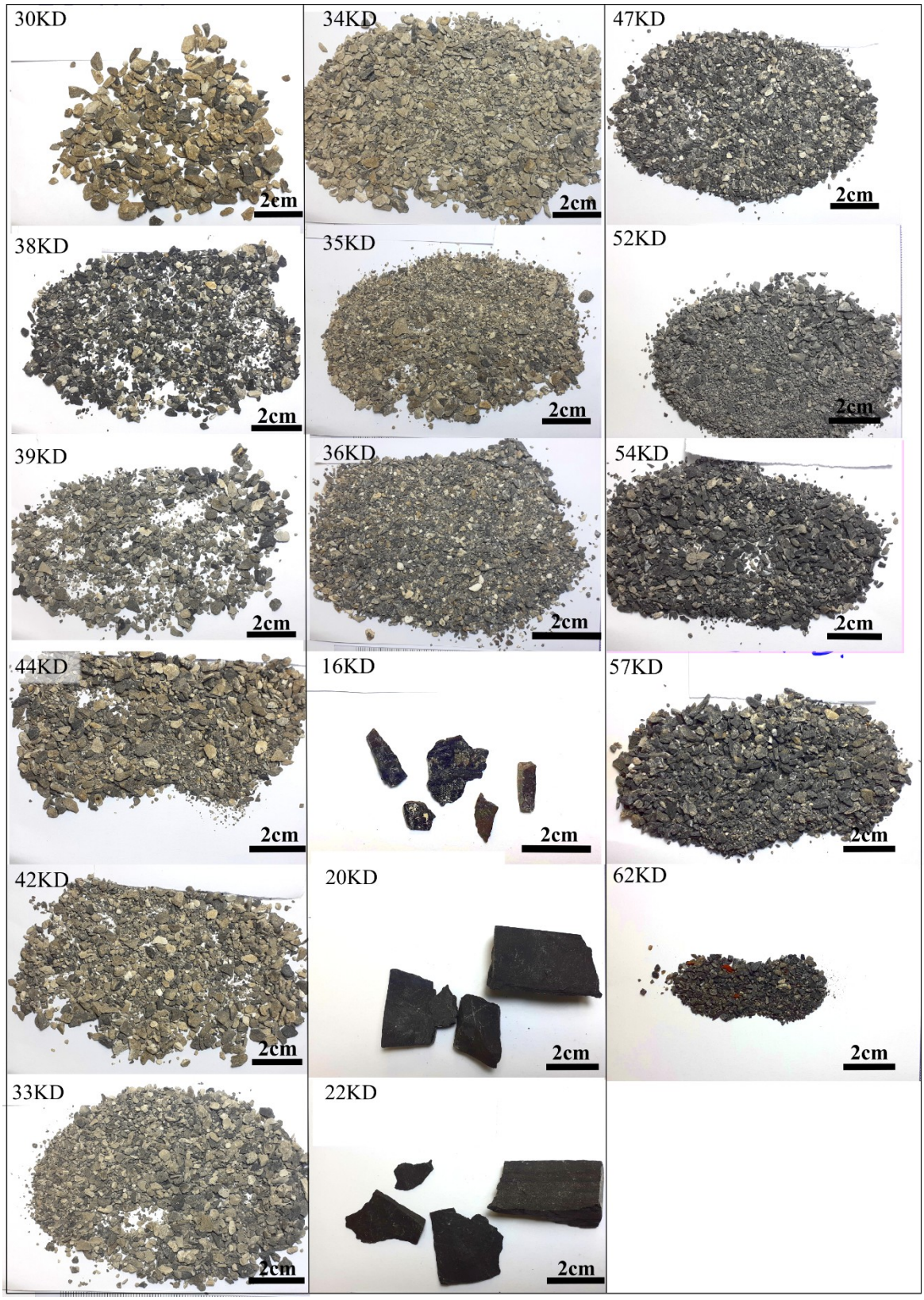

Figure S1. PxGa-1x well samples from the shallowest (top left) to the deepest (bottom right).

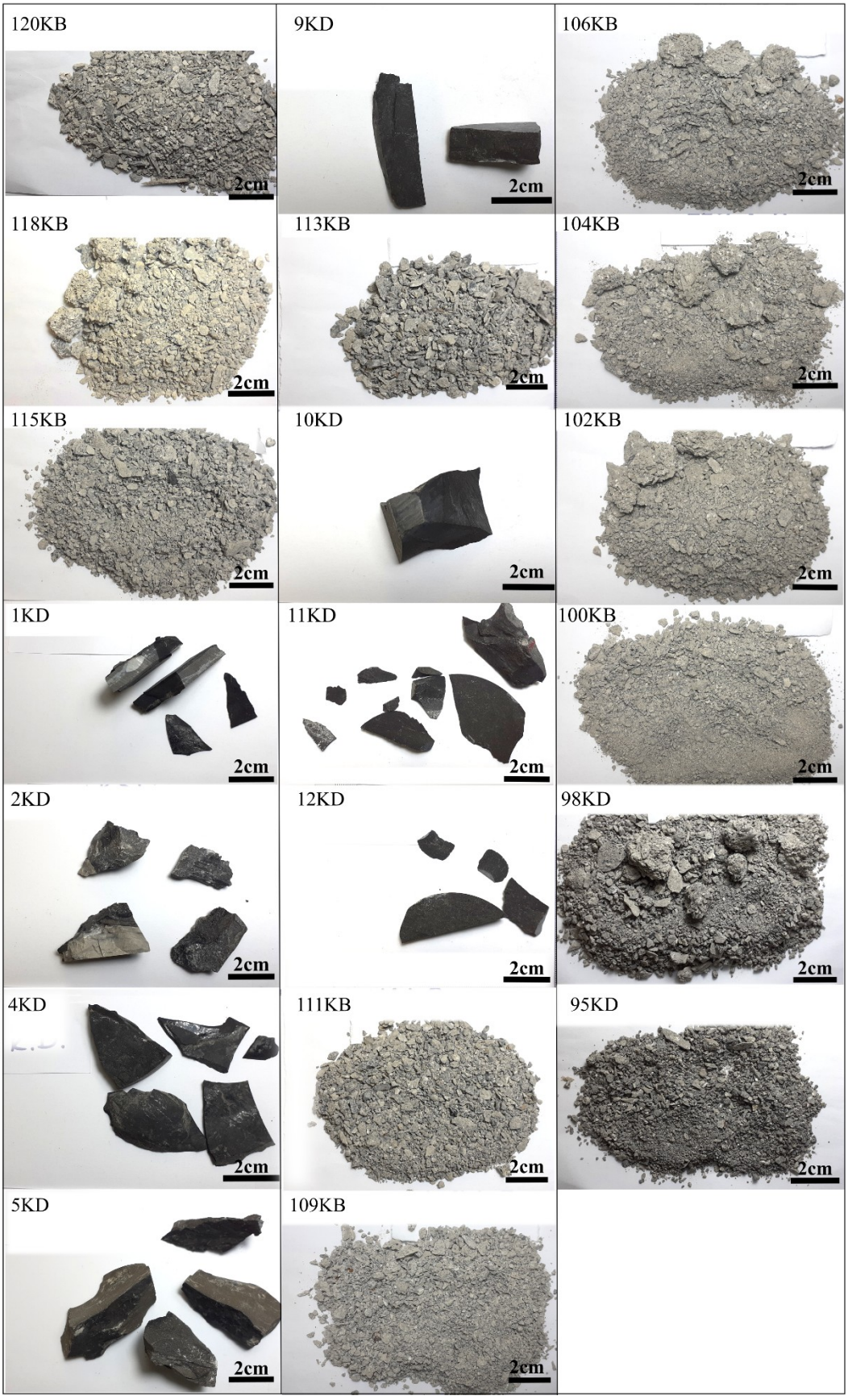

Figure S2. AY-3 well samples from the shallowest (top left) to the deepest (bottom right).

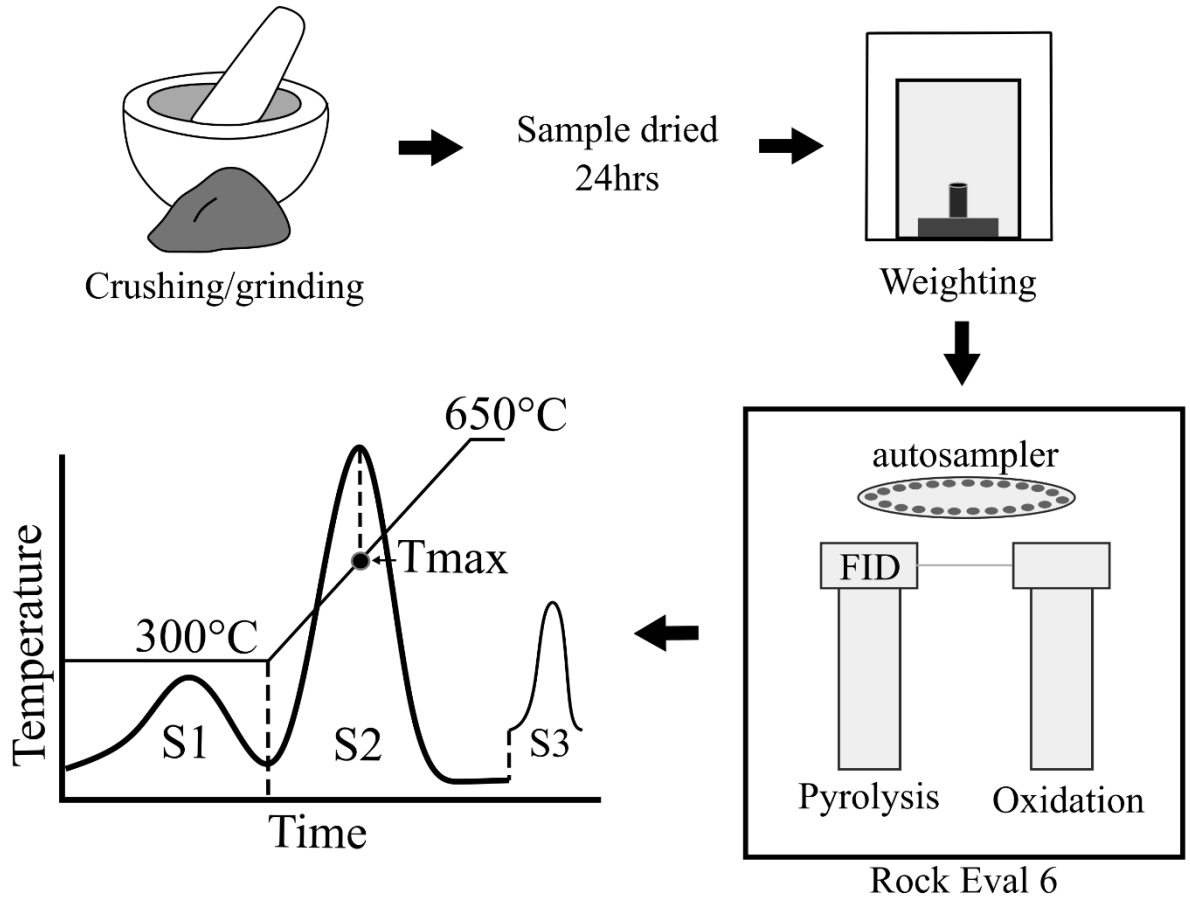

Figure S3. Rock-Eval 6 analysis workflow. Schematic illustration of sample preparation, pyrolysis, and data acquisition for Rock-Eval 6 analysis, including the generation of S1, S2, Tmax, and S3 parameters.

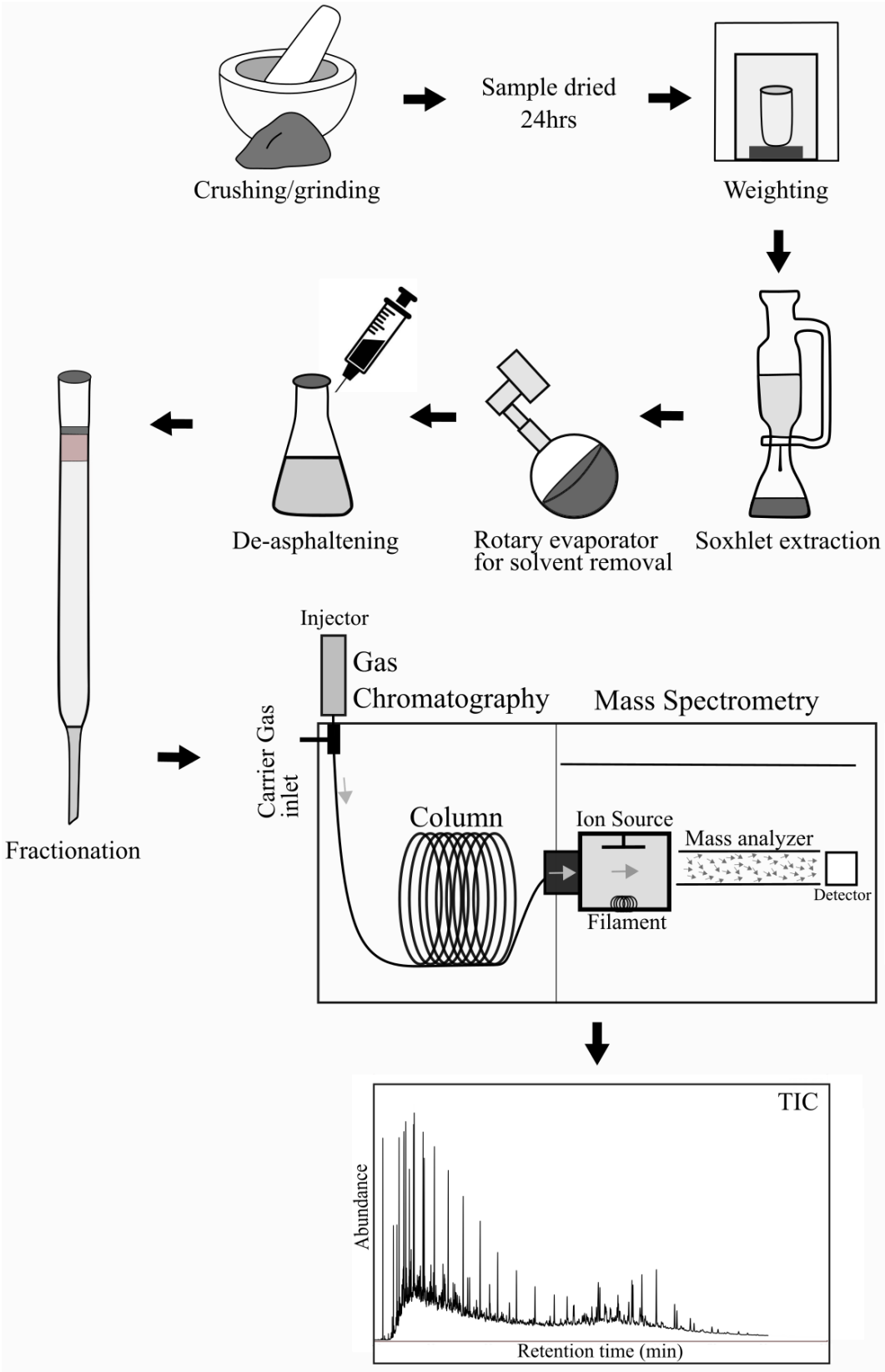

Figure S4. GC-MS analytical workflow. Stepwise process of sample extraction, de-asphalting, fractionation, and GC-MS analysis of saturated and aromatic fractions for biomarker characterization.

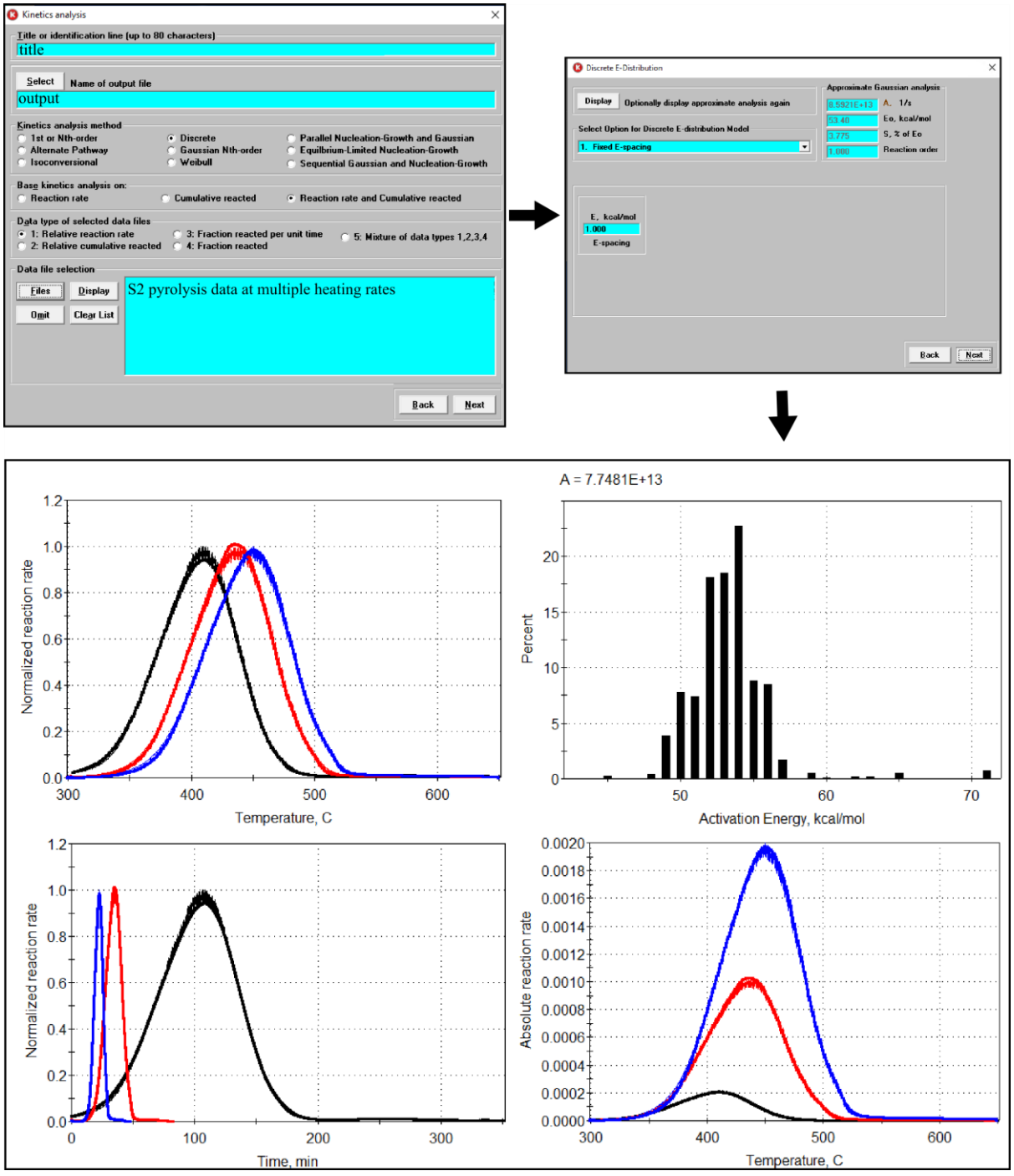

Figure S5. Kerogen kinetic modelling workflow using S2 pyrolysis data at multiple heating rates. The discrete E-distribution model was applied with 1kcal/mol spacing, with resulting reaction rates, activation energy distribution, and absolute reaction rates shown

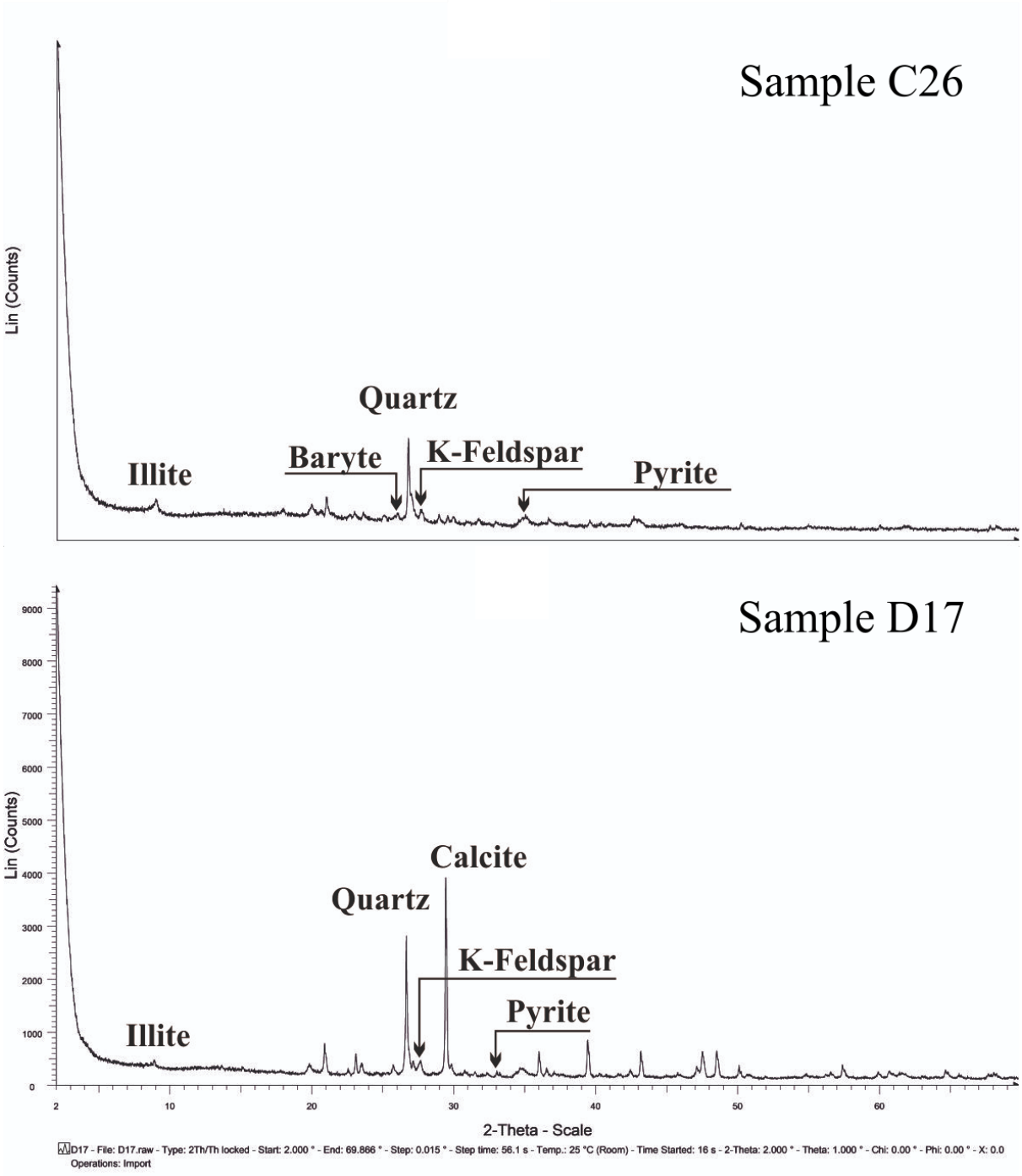

Figure S6. *Representative X-ray diffractograms showing the mineralogical composition of two analyzed samples, including quartz, illite, K-feldspar, pyrite, baryte, and calcite.*

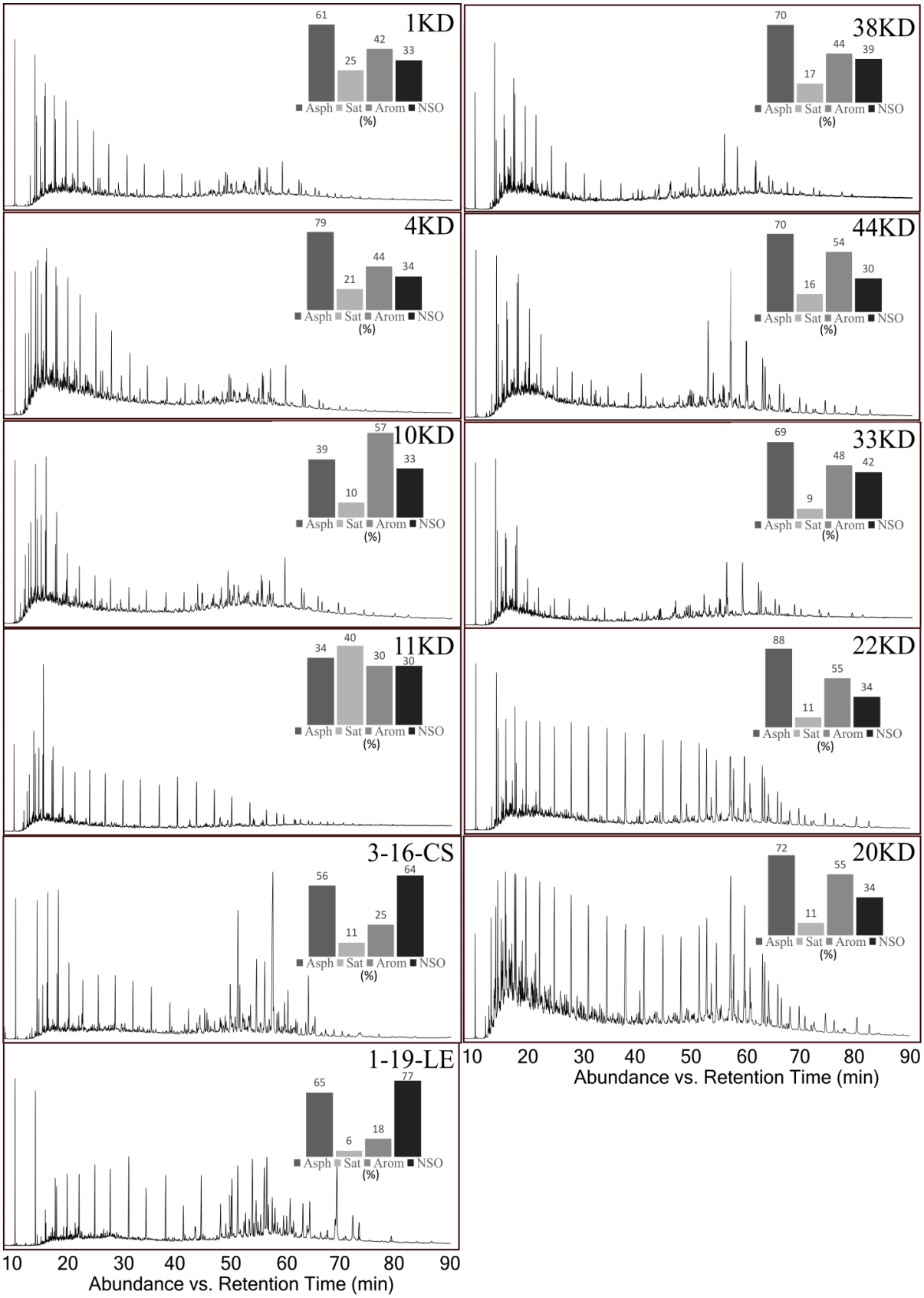

Figure S7. TIC chromatograms with overlaid histograms showing the bulk composition: asphaltenes, saturates, aromatics, and NSO compounds in percentage.

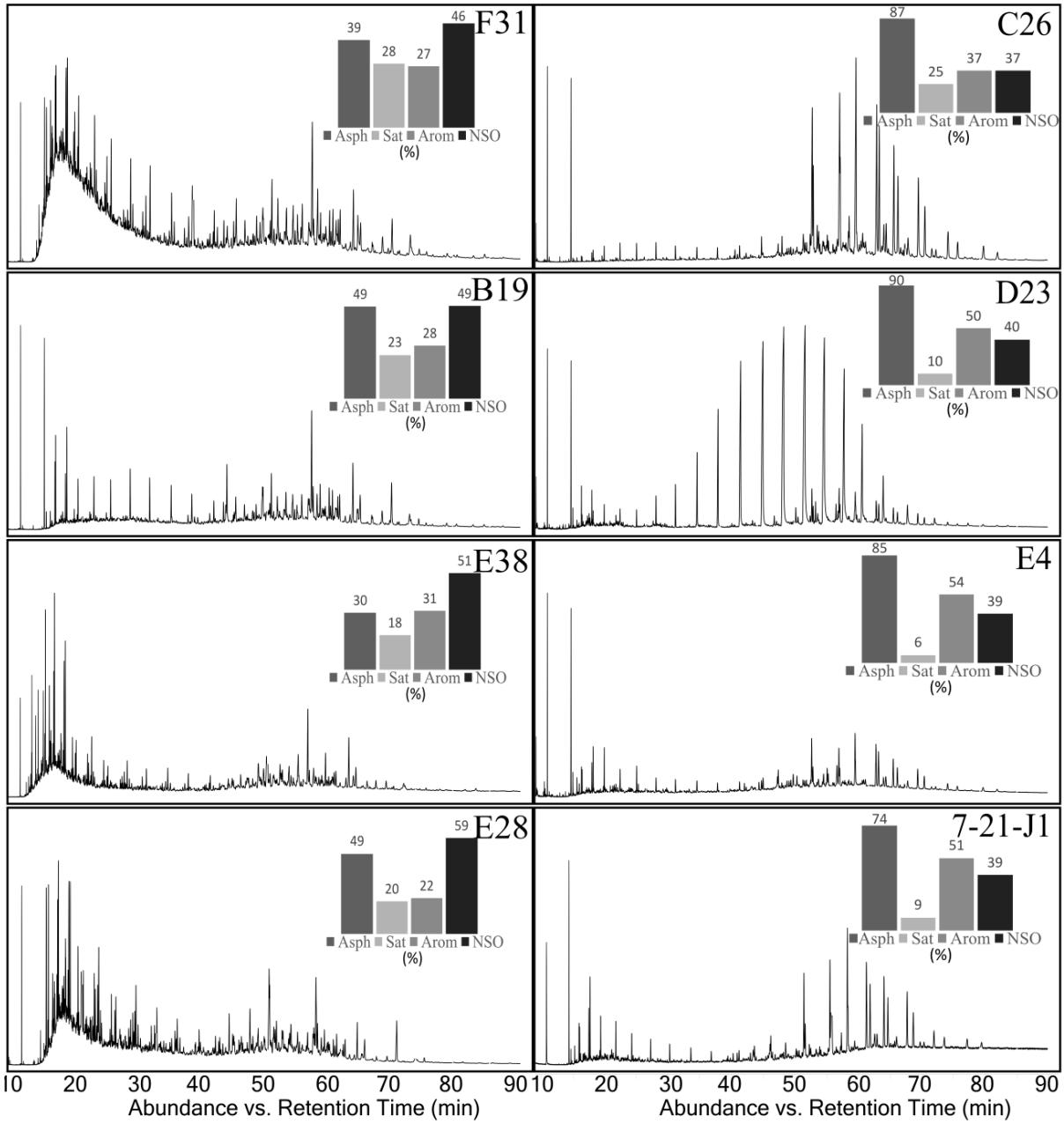

Figure S7. Continued.

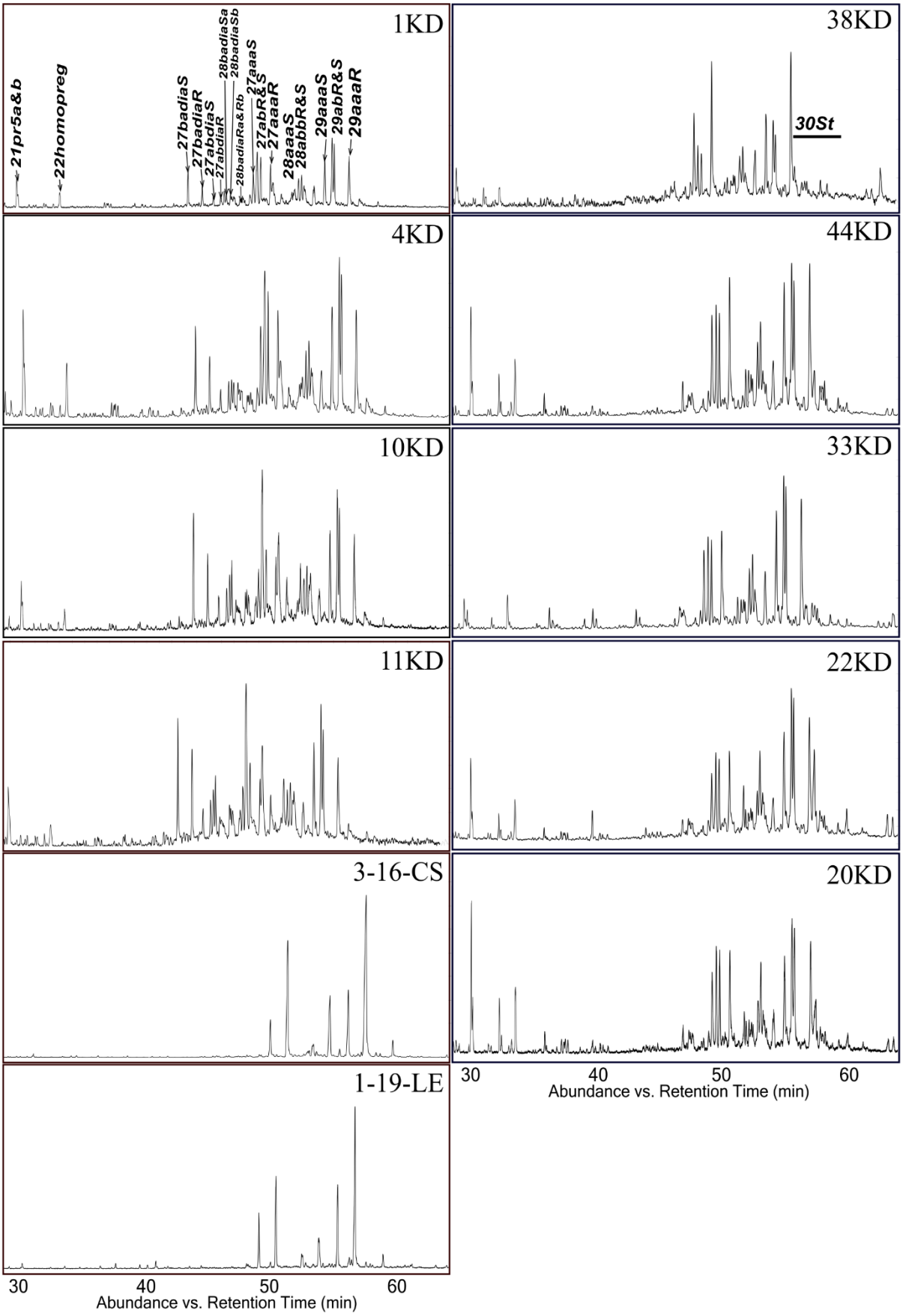

Figure S8. GC-MS mass chromatograms (ion m/z 191) of the saturated fraction.

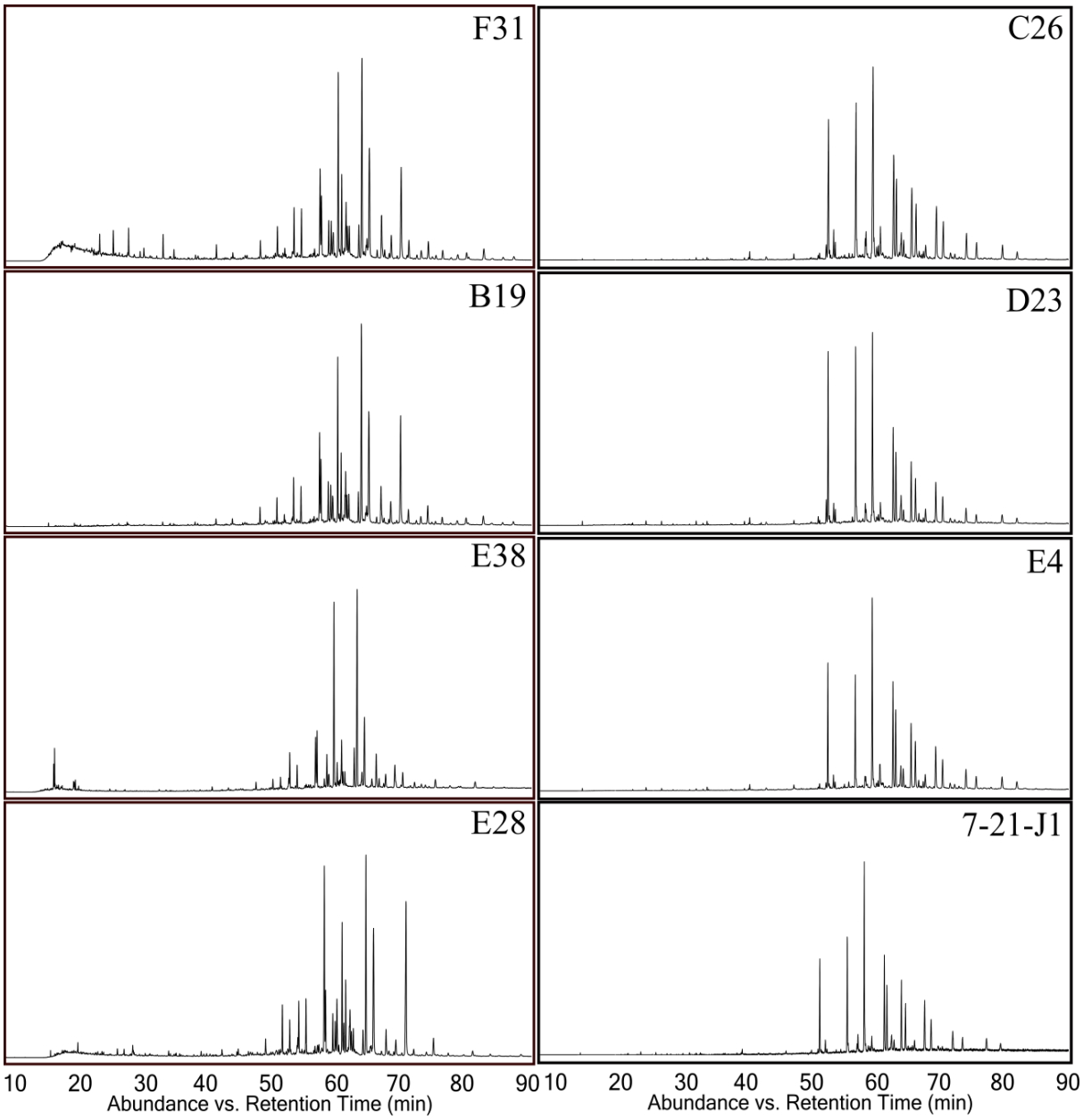

Figure S8 Continued.

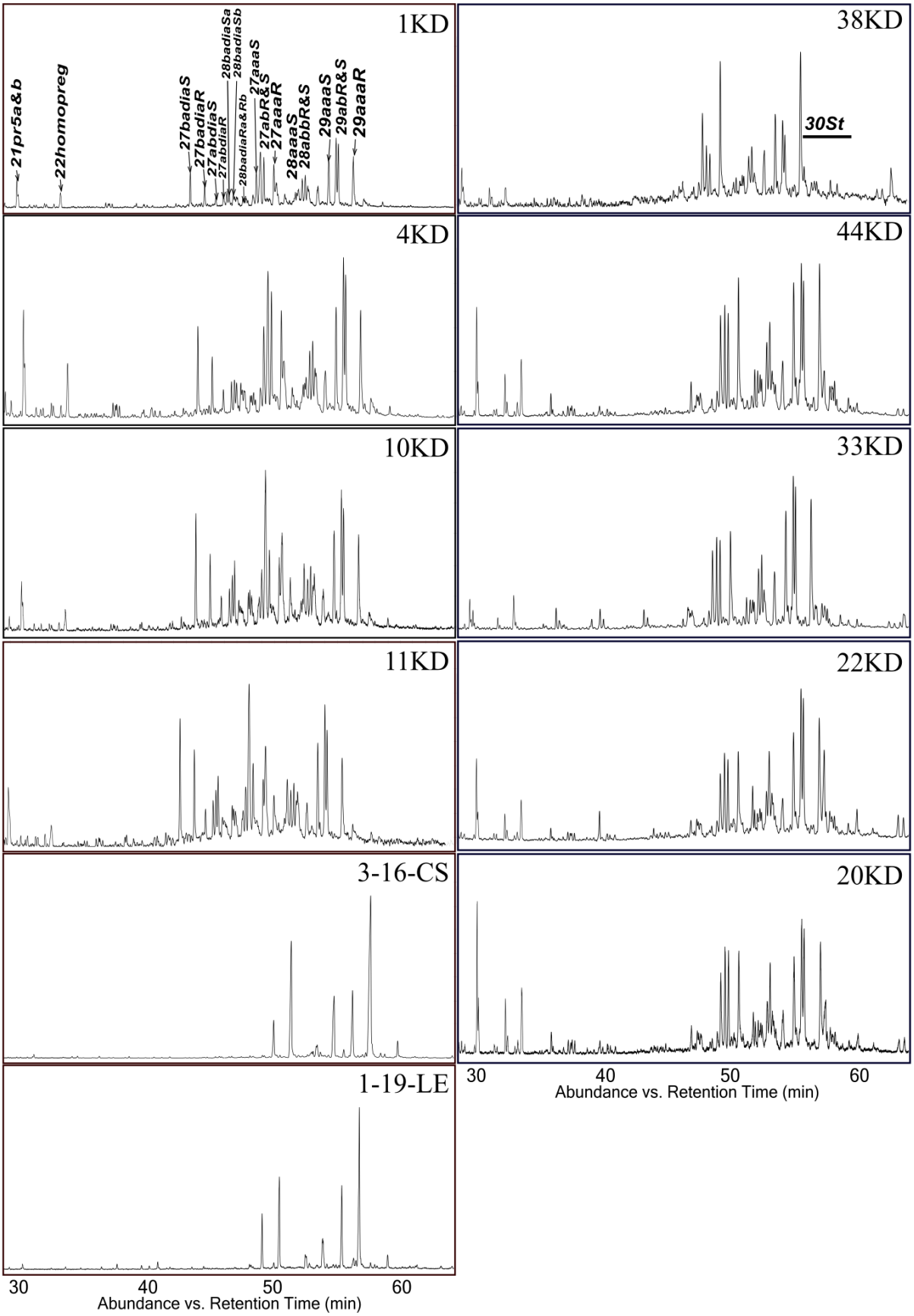

Figure S9. GC-MS mass chromatograms (ion m/z 217) of the saturated fraction. 30St underlines the area of C30 steranes.

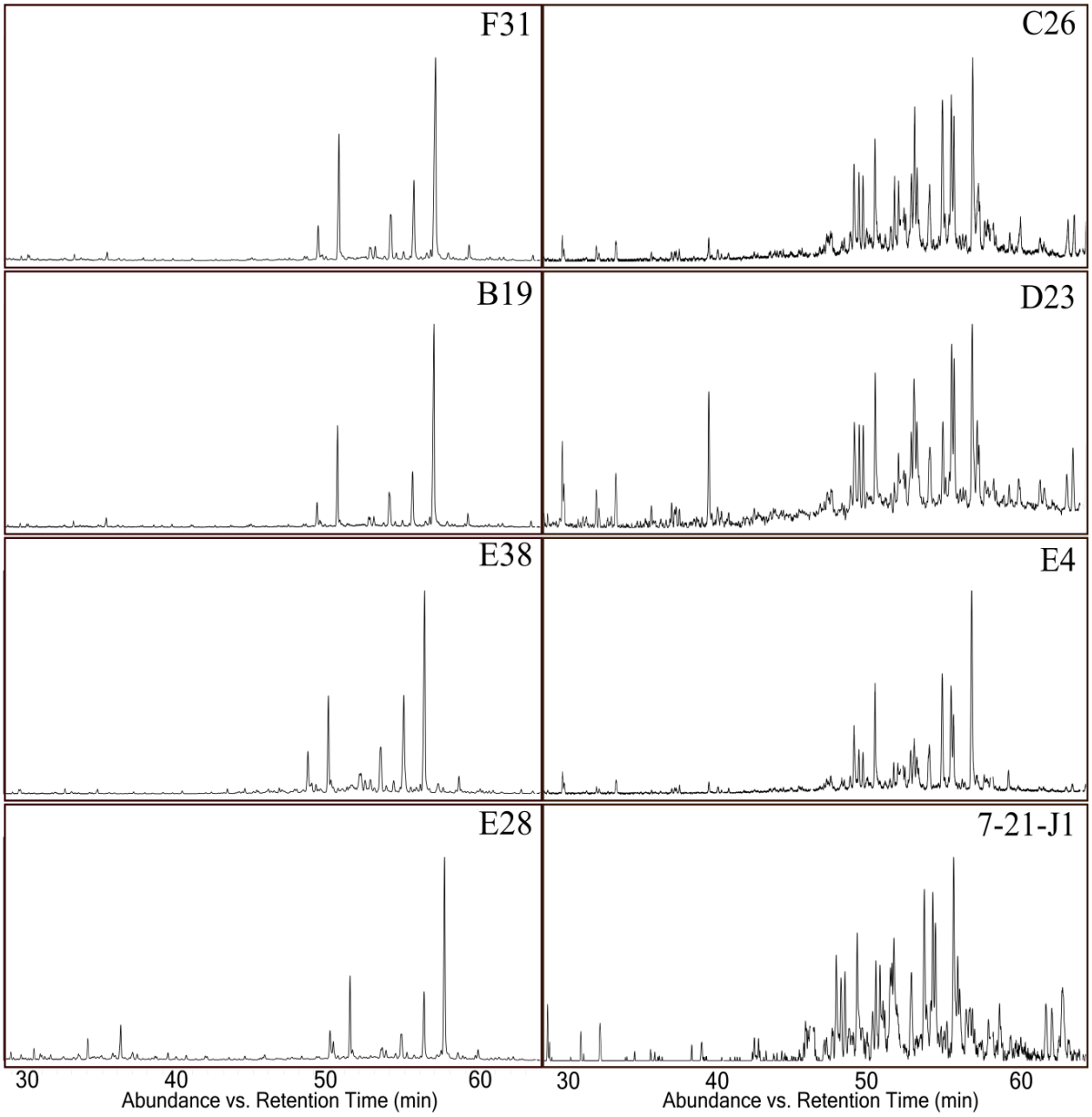

Figure S9 Continued.

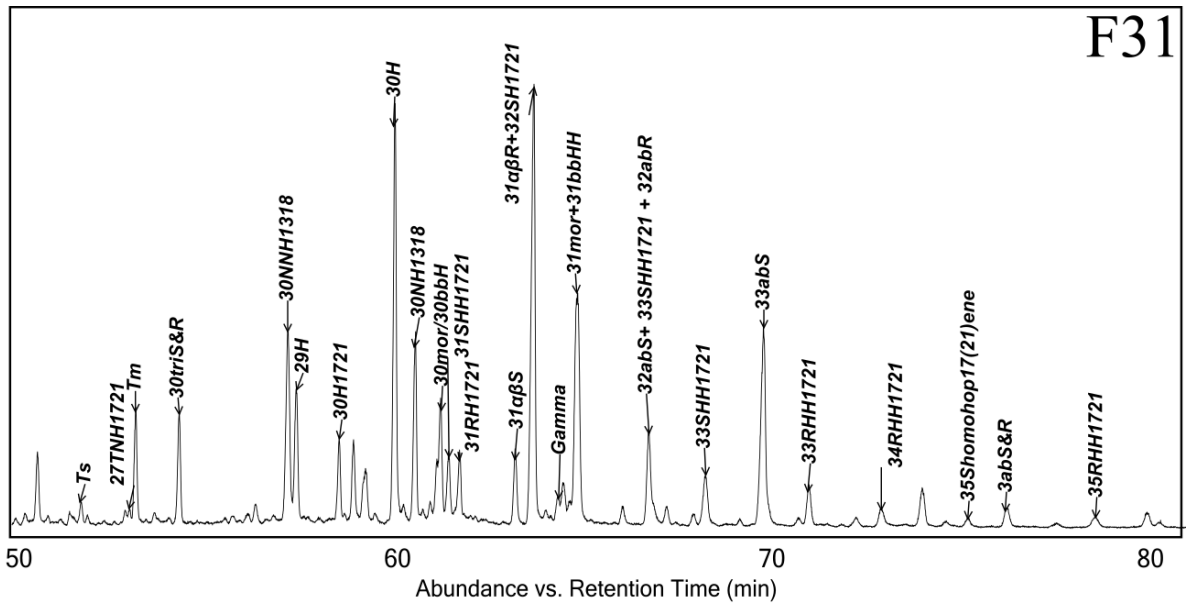

Figure S10. Exemplary zoomed-in m/z 191 mass chromatogram highlighting the hopene region within the sample.

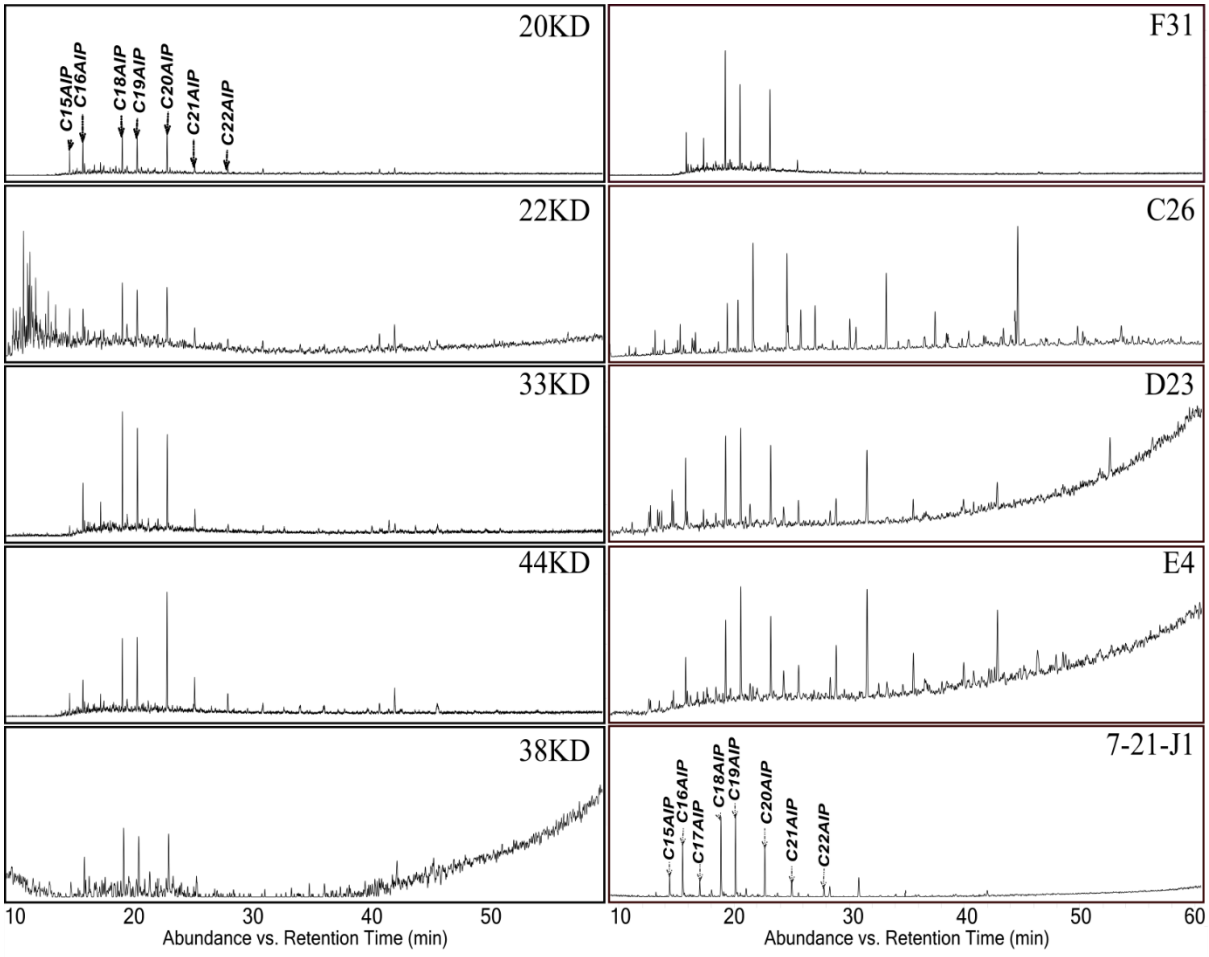

Figure S11. GC-MS mass chromatograms (ion m/z 133+134) showing aryl isoprenoid (AIP) distributions.

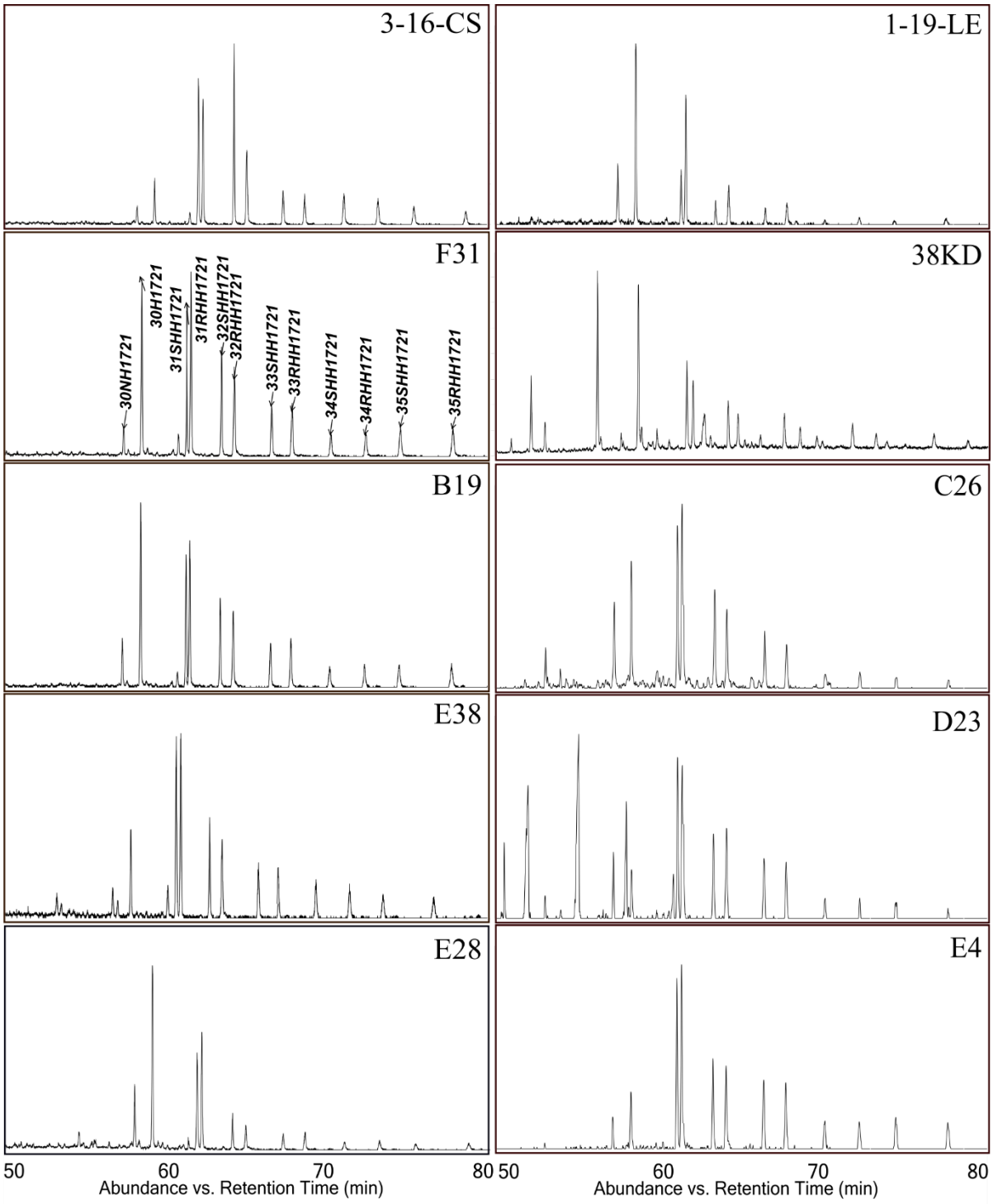

Figure S12. GC-MS mass chromatograms (ion m/z 367) showing hopene distributions.

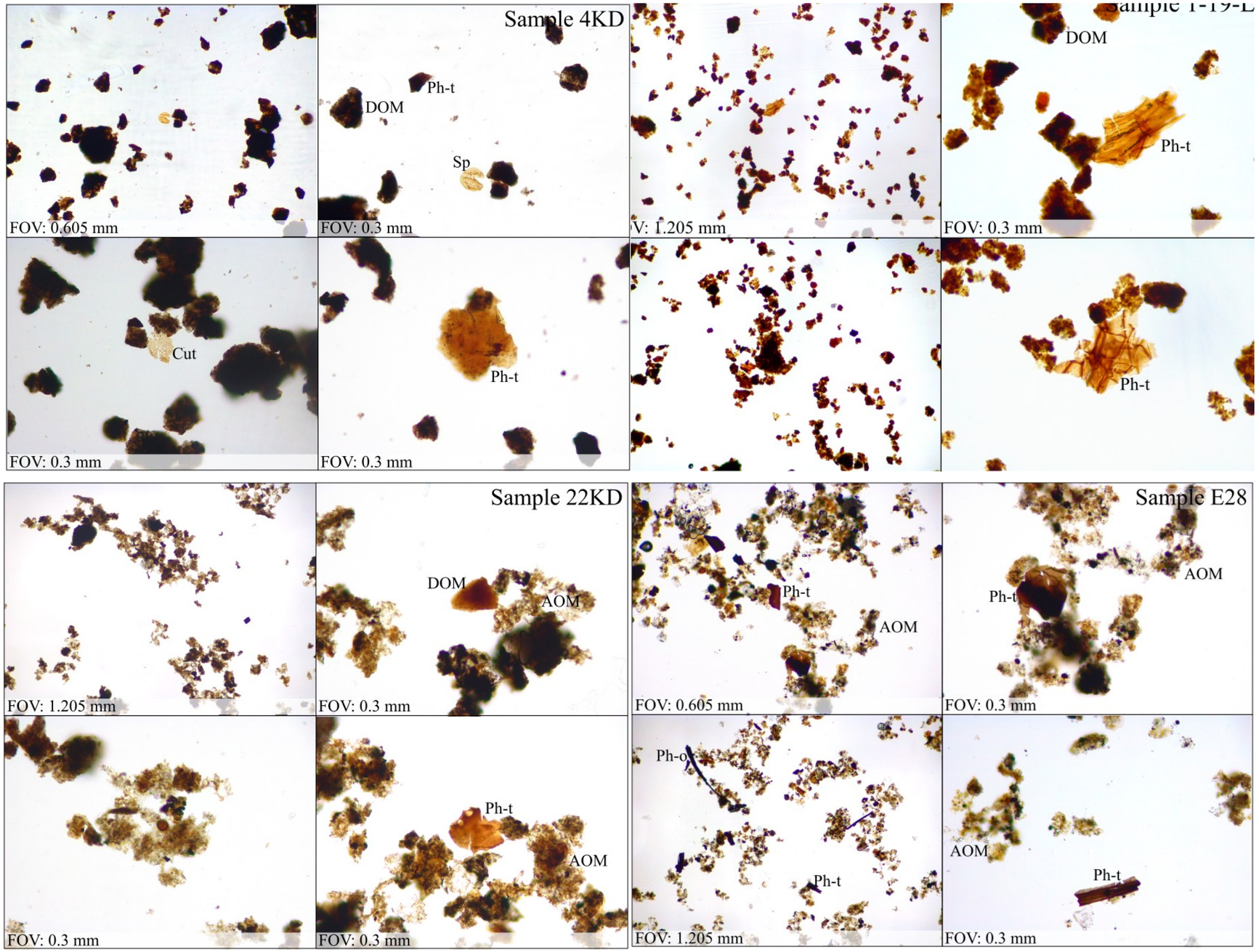

Figure S13. Representative transmitted light photomicrographs of organic palynofacies for samples 4KD, 22KD, 1-19-LE, E28, E3, C26, D17, D23, and E4. Each group of four images represents one sample, showing different field-of-view magnifications and particle distributions. The main categories of particulate organic matter are annotated, including translucent and phytoclasts (Ph-t and Ph-o), cuticles (Cut), amorphous organic matter (AOM), degraded organic matter (DOM), and sporomorphs (Sp). Field of view (FOV) varies between 0.3 and 1.205 mm.

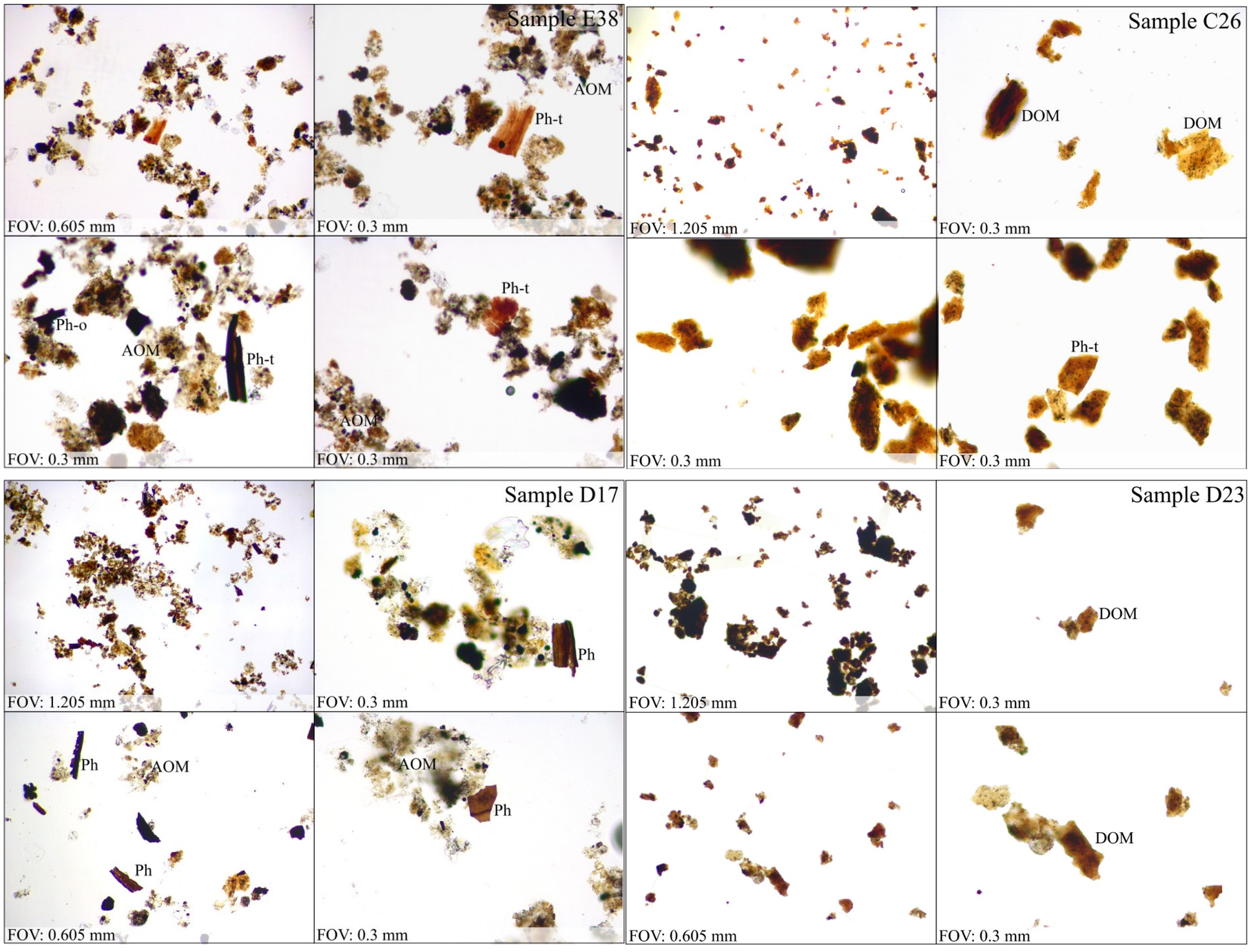

Figure S13 continued.

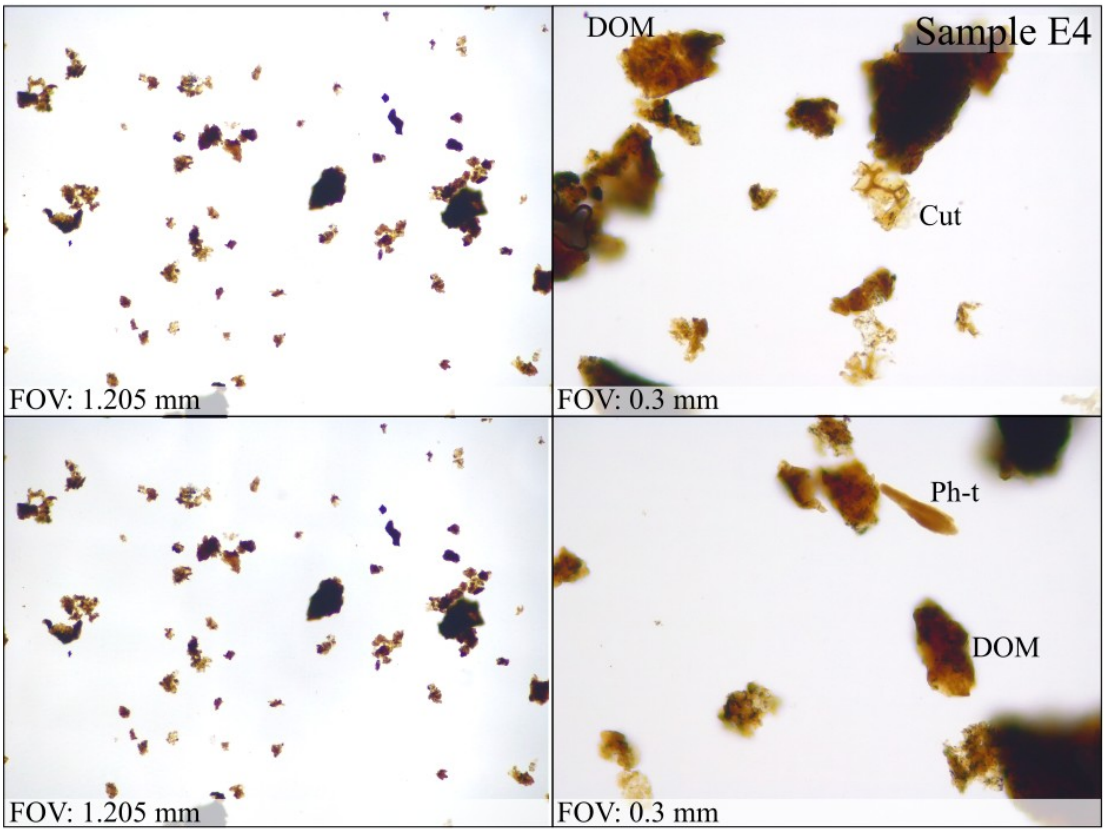

Figure S13 continued.

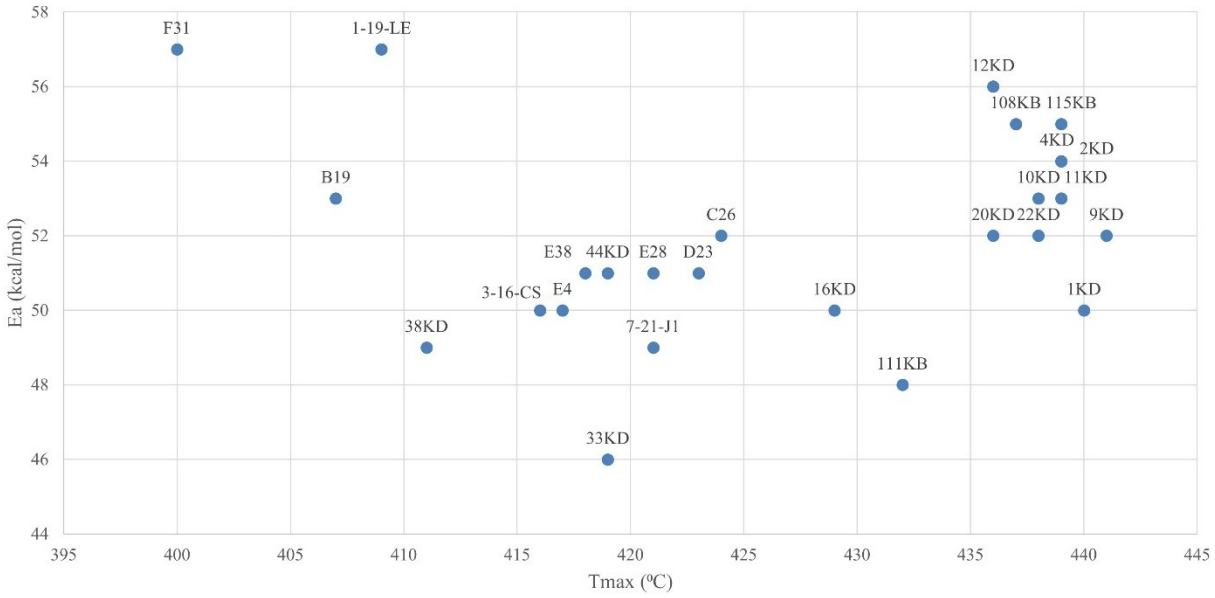

Figure S14. Principal Ea (kcal/mol) vs. Tmax (ºC).

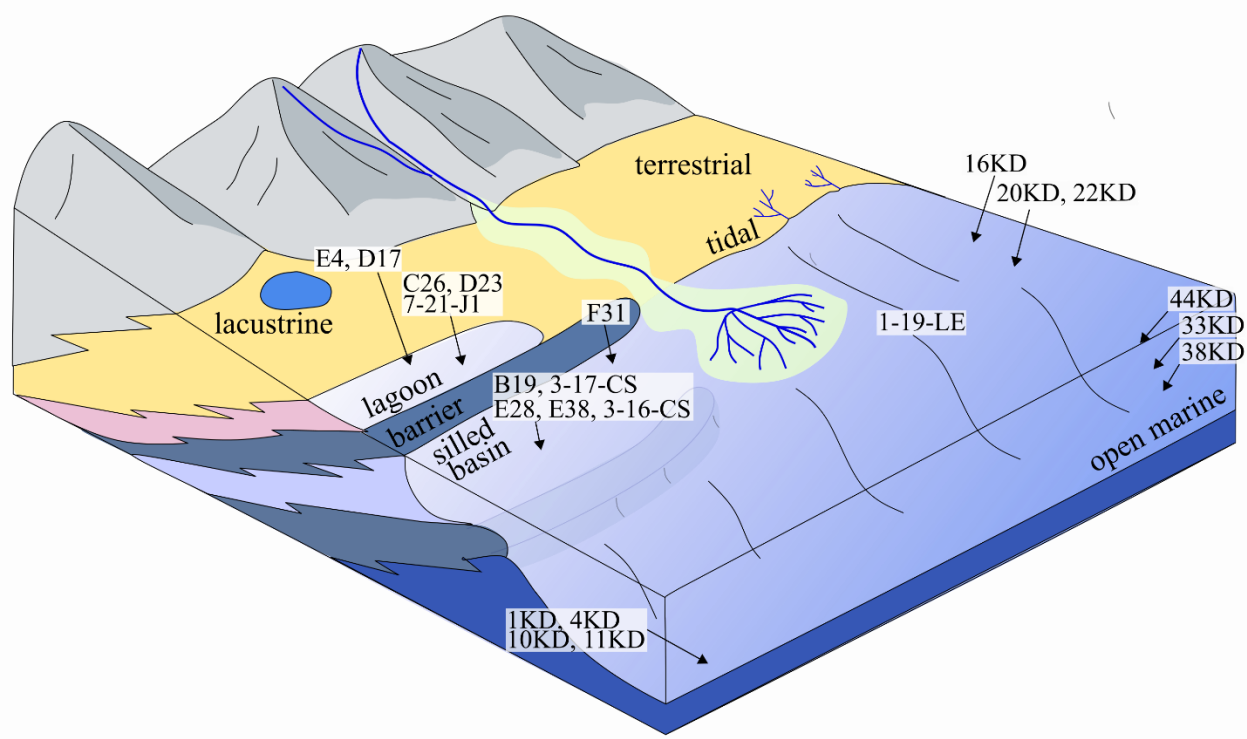

Figure S15. Conceptual model illustrating paleodepositional environments and the relative positions of the organic-rich samples based on geochemical and biomarker criteria. This model is schematic and does not represent a specific paleogeographic reconstruction.

APPENDIX II – Supplementary Tables

Table S1. Distribution of the main elements in wt% and ppm from XRF analysis for the studied samples, categorized by geological age. Na; Sodium, Mg; Magnesium, Al; Aluminum, Si; Silicon, P; Phosphorus, S; Sulfur, Cl; Chlorine, K; Potassium, Ca; Calcium, Ti; Titanium , V; Vanadium, Cr; Chromium, Mn; Manganese Fe; Iron, Co; Cobalt, Ni; Nickel, Cu; Copper, Sr; Strontium, Mo; Molybdenum, Ba; Barium, Pb; Lead, Th; Thorium, U; Uranium, V; Vanadium, Cr; Chromium, Mn; Manganese, Fe; Iron, Co; Cobalt, Ni; Nickel ,Cu; Copper, Sr; Strontium, Mo; Molybdenum, Ba; Barium, Pb; Lead, Th; Thorium, and U; Uranium.

Symbol	Location	Na	Mg	Al	Si	P	S	Cl	K	Ca	Ti	V	Cr	Mn	Fe	Co	Ni	Cu	Sr	Mo	Ba	Pb	Th	U
		wt%										ppm												
3-17-CS	outcrop	0.39	1.11	4.91	24.47	0.12	1.59	0.01	2.12	1.35	0.41	457	104	138	27259	31	90	123	101	7	1187	21	11	7
3-16-CS	outcrop	0.18	0.30	1.64	24.34	0.10	0.59	0.00	0.59	6.62	0.10	160	45	96	8463	28	50	36	108	2	529	8	4	2
120KB	AY-3	0.33	0.32	0.24	2.10	0.08	0.05	0.01	0.12	29.20	0.01	28	1	114	1677	2	2	7	460	2	323	6	2	1
118KB	AY-3	0.29	0.35	0.30	1.91	0.04	0.04	0.01	0.13	29.06	0.01	36	1	110	1721	2	0	5	409	2	298	4	2	1
115KB	AY-3	0.28	0.36	0.29	2.30	0.03	0.09	0.01	0.18	28.72	0.01	99	4	170	1949	2	9	18	440	3	840	7	2	3
1KD	AY-3	0.51	1.04	0.96	2.20	0.21	0.37	0.01	0.68	25.81	0.07	808	53	120	4925	2	93	106	511	30	2120	13	4	17
2KD	AY-3	0.24	0.57	0.21	4.01	0.03	0.15	0.01	0.13	27.47	0.01	137	1	135	1825	2	17	20	444	8	1491	25	7	29
4KD	AY-3	0.72	1.86	2.41	5.50	0.35	0.79	0.01	1.64	20.68	0.16	2145	215	118	10909	2	172	275	404	68	1283	6	2	1
5KD	AY-3	0.28	0.88	0.22	1.13	0.03	0.09	0.01	0.16	30.07	0.01	72	1	188	1051	2	6	15	507	4	1396	12	3	1
9KD	AY-3	0.31	0.38	0.50	1.65	0.03	0.12	0.00	0.36	30.40	0.03	97	1	187	2643	2	12	15	413	4	784	8	5	1
113KB	AY-3	0.25	0.54	0.45	4.41	0.04	0.10	0.01	0.26	25.72	0.02	57	1	335	3169	2	12	16	338	2	940	11	6	2
10KD	AY-3	0.28	0.49	1.45	15.07	0.05	0.40	0.00	0.74	16.94	0.09	106	8	144	7947	7	42	36	207	13	1137	9	3	1
11KD	AY-3	0.27	0.69	1.67	12.06	0.05	0.35	0.00	0.92	19.37	0.10	79	10	208	9086	7	36	38	217	3	993	7	1	1
12KD	AY-3	0.24	0.55	1.06	11.01	0.04	0.21	0.01	0.57	22.19	0.06	55	1	223	5730	2	21	26	219	2	855	8	3	1
111KB	AY-3	0.36	0.37	0.42	4.89	0.02	0.13	0.01	0.20	25.24	0.02	92	9	170	3351	2	15	23	231	5	333	6	3	1
109KB	AY-3	0.28	0.98	0.47	3.95	0.03	0.10	0.01	0.23	26.35	0.02	38	7	273	3572	2	13	18	250	3	451	6	3	1
106KB	AY-3	0.29	2.76	0.54	4.15	0.03	0.11	0.01	0.25	25.33	0.03	55	5	230	3507	2	11	18	237	3	483	9	3	1
104KB	AY-3	0.27	2.43	0.58	4.54	0.03	0.14	0.01	0.33	25.67	0.03	49	8	246	4428	9	12	16	240	3	422	9	3	2
102KB	AY-3	0.23	3.86	0.62	3.89	0.03	0.13	0.01	0.30	24.03	0.03	63	9	216	4216	2	13	18	219	4	378	26	1	2
100KD	AY-3	0.24	3.83	0.69	3.99	0.02	0.13	0.01	0.32	23.56	0.04	55	12	214	4565	2	12	21	213	4	328	6	3	3
98KD	AY-3	0.21	2.82	0.51	6.85	0.03	0.14	0.00	0.26	21.79	0.03	60	1	174	3145	8	13	17	193	5	263	4	3	1
95KD	AY-3	0.21	4.23	0.57	5.97	0.03	0.16	0.01	0.25	19.98	0.03	86	9	137	3412	2	16	25	178	11	198	8	5	0
30KD	PxGa-1x	0.28	0.26	0.06	2.10	0.01	0.18	0.07	0.01	29.93	0.00	45	1	13	538	2	5	1	368	3	2	3	3	1
1-19-LE	outcrop	0.61	0.84	2.49	8.23	0.21	1.13	0.05	1.01	17.49	0.16	691	121	74	11664	7	99	58	232	29	194	13	7	12
38KD	PxGa-1x	0.46	0.36	0.78	11.31	0.02	0.96	0.15	0.41	20.24	0.05	200	14	50	5940	361	93	150	139	16	281	5	3	4
39KD	PxGa-1x	0.40	0.24	0.17	6.38	0.02	0.58	0.09	0.09	27.55	0.01	115	3	25	1463	2	47	23	142	10	89	5	1	2
44KD	PxGa-1x	0.47	0.28	0.20	4.57	0.01	0.64	0.14	0.09	26.75	0.02	153	1	20	1335	2	35	13	171	11	37	5	2	1
42KD	PxGa-1x	0.51	0.36	0.15	1.79	0.01	0.57	0.15	0.08	28.78	0.01	169	1	23	1120	2	31	10	180	13	62	4	3	1
33KD	PxGa-1x	0.58	0.38	0.20	0.81	0.01	0.67	0.15	0.13	29.10	0.02	271	4	28	1718	2	51	16	200	15	29	7	2	2
34KD	PxGa-1x	0.40	0.32	0.08	0.30	0.01	0.32	0.09	0.03	31.63	0.00	95	1	25	694	2	13	0	171	9	68	4	2	1
35KD	PxGa-1x	0.46	0.34	0.05	0.20	0.01	0.25	0.14	0.01	32.18	0.00	50	1	9	469	2	2	0	184	12	105	4	2	1
36KD	PxGa-1x	0.93	0.63	0.05	0.26	0.00	2.02	0.18	0.04	31.08	0.00	65	1	6	826	2	11	0	372	17	65	2	3	3
16KD	PxGa-1x	0.45	0.50	0.32	0.65	0.06	0.59	0.02	0.19	30.49	0.03	440	1	10	2609	2	179	12	224	112	3	5	3	42
20KD	PxGa-1x	0.31	0.43	0.34	0.84	0.01	0.28	0.01	0.19	30.42	0.02	45	1	10	1575	2	18	3	352	5	35	4	1	1
22KD	PxGa-1x	0.36	0.42	0.16	0.42	0.02	0.37	0.01	0.08	30.69	0.01	60	1	8	836	2	16	0	326	23	41	3	3	1

47KD	PxGa-1x	1.07	0.90	0.07	0.32	0.00	3.50	0.09	0.05	29.61	0.01	25	1	8	1024	2	2	2	2405	2	192	5	0	5
52KD	PxGa-1x	0.56	1.44	0.00	0.06	0.00	0.87	0.09	0.00	30.38	0.00	41	1	7	93	2	2	0	505	12	64	3	2	2
54KD	PxGa-1x	0.34	1.45	0.03	0.68	0.01	0.21	0.08	0.00	28.94	0.00	46	1	8	260	2	3	1	1696	7	171	4	1	4
F31	outcrop	0.27	0.96	3.31	12.07	0.03	0.92	0.00	1.87	16.34	0.27	69	28	127	19897	7	28	25	164	7	157	12	8	5
B19	outcrop	0.21	0.97	2.61	16.65	0.02	0.90	0.00	1.84	12.12	0.21	48	19	113	15768	6	20	21	203	2	1231	10	7	1
E28	outcrop	0.28	0.56	2.10	11.54	0.02	0.53	0.00	1.32	19.66	0.15	79	9	171	12361	2	28	21	307	5	83	10	6	3
E38	outcrop	0.28	0.58	2.38	10.07	0.02	0.80	0.00	1.80	19.71	0.18	64	11	153	15604	8	29	29	349	7	92	11	7	2
D23	outcrop	0.80	4.08	1.03	2.55	0.00	2.44	0.00	0.62	11.55	0.06	1116	4	30	7634	19	247	23	136	321	1829	4	2	18
D17	outcrop	0.18	0.73	3.99	14.57	0.02	0.64	0.00	2.91	12.30	0.31	148	38	130	17557	22	39	46	338	4	180	16	9	6
E4	outcrop	0.85	3.71	1.56	3.73	0.00	3.38	0.01	0.85	8.49	0.08	765	20	20	8249	16	191	14	43	157	48	4	3	18
C29	outcrop	0.64	5.09	0.85	2.07	0.01	1.86	0.01	0.46	13.41	0.04	489	1	32	6839	27	191	23	196	162	5082	5	2	14
C26	outcrop	0.76	0.74	2.58	6.12	0.02	4.13	0.00	1.39	1.71	0.16	1948	38	56	11508	25	344	67	227	106	11970	10	43	12
7-21-J1	outcrop	0.42	5.50	0.83	2.02	0.00	1.15	0.00	0.47	15.81	0.04	790	1	29	5458	50	130	15	182	120	3284	4	3	13
57KD	PxGa-1x	0.33	9.26	0.08	0.24	0.00	0.46	0.07	0.01	19.63	0.00	74	1	5	385	2	18	4	4330	48	107	10	1	23
62KD	PxGa-1x	0.20	9.30	0.05	0.24	0.01	0.24	0.03	0.00	18.98	0.00	42	4	22	2210	10	20	18	5225	31	381	15	1	24

Table S1 Continued.

Table S2. Rock-Eval 6 parameters for the main well and outcrop samples of this study.

Sample	Well	Depth (m MD)	S1 (mg/g)	S2 (mg/g)	S3 (mg/g)	PI	Tmax (°C)	HI (mgHC/gTOC)	OI (mgHC/gTOC)	TOC (%)	MINC (%)	Age
27KD	PxGa-1x	835	0.01	0.48	0.16	0.03	414	320	107	0.15	10.74	Early Cretaceous
28KD	PxGa-1x		0.06	0.75	0.13	0.07	410	469	81	0.16	9.6	Early Cretaceous
29KD	PxGa-1x		0.24	2.87	0.51	0.08	410	495	88	0.58	10.36	Early Cretaceous
30KD	PxGa-1x		0.26	3.65	0.55	0.07	413	514	77	0.71	9.94	Early Cretaceous
31KD	PxGa-1x		0.19	2.7	0.61	0.07	415	375	85	0.72	10.5	Early Cretaceous
32KD	PxGa-1x		0.08	2.26	0.34	0.03	404	377	57	0.6	9.56	Early Cretaceous
38KD	PxGa-1x		0.53	19.84	1.46	0.03	411	547	40	3.63	6.53	Mid - Late Jurassic
39KD	PxGa-1x		0.56	14.94	0.82	0.04	409	579	32	2.58	9.11	Mid - Late Jurassic
40KD	PxGa-1x		0.14	5.07	0.48	0.03	411	502	48	1.01	11.17	Mid - Late Jurassic
43KD	PxGa-1x		0.66	21.86	0.47	0.03	419	734	16	2.98	9.61	Mid - Late Jurassic
44KD	PxGa-1x		0.59	21.74	0.56	0.03	419	669	17	3.25	9.37	Mid - Late Jurassic
41KD	PxGa-1x		0.22	6.93	0.37	0.03	413	648	35	1.07	11.36	Mid - Late Jurassic
42KD	PxGa-1x		0.76	21.56	0.55	0.03	419	709	18	3.04	10.59	Mid - Late Jurassic
33KD	PxGa-1x		0.76	24.13	1.44	0.03	419	661	39	3.65	10.85	Mid - Late Jurassic
34KD	PxGa-1x		0.49	10.67	0.58	0.04	419	680	37	1.57	10.22	Mid - Late Jurassic
35KD	PxGa-1x		0.66	7.44	0.25	0.08	418	689	23	1.08	11.88	Early - Mid Jurassic
36KD	PxGa-1x		0.44	9.59	0.35	0.04	426	705	26	1.36	10.31	Early - Mid Jurassic
37KD	PxGa-1x		0.7	9	0.21	0.07	423	698	16	1.29	10.8	Early - Mid Jurassic
45KD	PxGa-1x		0.06	1.71	0.31	0.04	420	428	78	0.4	8.2	Early - Mid Jurassic
16KD	PxGa-1x		1.1	21.91	0.18	0.05	429	477	4	4.59	10.28	Early - Mid Jurassic
20KD	PxGa-1x		0.25	8.06	0.27	0.03	436	552	18	1.46	11.12	Early - Mid Jurassic
22KD	PxGa-1x		0.09	16.26	0.12	0.01	438	689	5	2.36	9.95	Early - Mid Jurassic

46KD	PxGa-1x		0.11	1.17	0.7	0.08	433	249	149	0.47	10.09	Early - Mid Jurassic
47KD	PxGa-1x		0.05	0.3	0.57	0.15	432	167	317	0.18	9.14	Early - Mid Jurassic
48KD	PxGa-1x		0.06	0.17	0.18	0.26	438	100	106	0.17	10.09	Early - Mid Jurassic
49KD	PxGa-1x		0.06	0.17	0.28	0.24	444	71	117	0.24	10.31	Early - Mid Jurassic
50KD	PxGa-1x		0.26	0.5	0.21	0.34	464	98	41	0.51	10.88	Early - Mid Jurassic
51KD	PxGa-1x		0.3	0.59	0.35	0.33	453	81	48	0.73	11.87	Early - Mid Jurassic
52KD	PxGa-1x		0.22	0.65	0.34	0.25	456	92	48	0.71	11.5	Early - Mid Jurassic
53KD	PxGa-1x		0.18	0.38	0.46	0.32	455	70	85	0.54	11.42	Early - Mid Jurassic
54KD	PxGa-1x		0.19	0.26	0.33	0.43	461	54	69	0.48	10.92	Early - Mid Jurassic
55KD	PxGa-1x		0.07	0.1	0.28	0.4	445	38	108	0.26	11.03	Early - Mid Jurassic
56KD	PxGa-1x		0.1	0.18	0.37	0.36	452	41	84	0.44	11.69	Early - Mid Jurassic
57KD	PxGa-1x		0.07	0.1	0.34	0.41	584	23	79	0.43	12.88	Triassic
58KD	PxGa-1x		0.09	0.08	0.76	0.53	421	10	90	0.84	12.38	Triassic
59KD	PxGa-1x		0.09	0.09	0.47	0.48	417	14	75	0.63	12.29	Triassic
60KD	PxGa-1x		0.06	0.09	0.52	0.38	413	15	87	0.6	12.66	Triassic
61KD	PxGa-1x		0.03	0.04	0.3	0.4	503	8	62	0.48	12.51	Triassic
62KD	PxGa-1x		0.03	0.1	1.16	0.2	414	24	283	0.41	12.88	Triassic
63KD	PxGa-1x		0.09	0.25	1.37	0.26	418	36	196	0.7	12.54	Triassic
25KD	PxGa-1x		0.01	0.03	0.74	0.27	404	6	157	0.47	12.53	Triassic
26KD	PxGa-1x	5242	0	0.02	0.58	0.14	415	6	187	0.31	12.38	Triassic
124KB	AY-3		0.03	0.16	0.93	0.14	430	76	443	0.21	11.48	Early Cretaceous
123KB	AY-3		0.05	0.36	1.06	0.12	439	164	482	0.22	9.53	Early Cretaceous
121KB	AY-3		0.05	0.39	0.76	0.11	440	115	224	0.34	8.84	Early Cretaceous
122KB	AY-3		0.05	0.45	0.9	0.09	440	180	360	0.25	10.24	Early Cretaceous
120KB	AY-3		0.13	0.9	2.19	0.13	438	132	322	0.68	10.12	Early Cretaceous
119KB	AY-3		0.04	0.34	0.91	0.09	437	117	314	0.29	10.49	Early Cretaceous
118KB	AY-3		0.02	0.26	0.39	0.07	440	217	325	0.12	9.32	Early Cretaceous
117KB	AY-3		0.03	0.25	0.92	0.12	438	96	354	0.26	10.62	Early Cretaceous
116KB	AY-3		0.08	0.68	0.79	0.11	438	179	208	0.38	10.18	Early Cretaceous
115KB	AY-3		0.08	0.82	1.29	0.09	439	152	239	0.54	10.08	Early Cretaceous
1KD	AY-3	3224.5	0.57	15.16	0.52	0.04	440	449	15	3.38	10	Early Cretaceous
2KD	AY-3		0.35	1.51	0.53	0.19	439	248	87	0.61	9.66	Early Cretaceous
3KD	AY-3		0.36	1.5	0.36	0.19	441	283	68	0.53	10.43	Early Cretaceous
4KD	AY-3		0.74	37.45	0.52	0.02	439	544	8	6.89	7.53	Early Cretaceous
5KD	AY-3		1.39	2.19	0.08	0.39	437	384	14	0.57	11.66	Early Cretaceous
6KD	AY-3		0.1	0.65	0.08	0.13	443	310	38	0.21	10.5	Early Cretaceous
7KD	AY-3		0.06	0.85	0.14	0.07	438	340	56	0.25	10.57	Early Cretaceous
8KD	AY-3		0.09	1.36	0.4	0.06	438	309	91	0.44	10.53	Early Cretaceous
9KD	AY-3		0.15	1.81	0.2	0.08	441	385	43	0.47	9.77	Early Cretaceous
114KB	AY-3		0.12	0.62	1.19	0.16	439	159	305	0.39	10.68	Early Cretaceous
113KB	AY-3		0.08	0.68	1.19	0.11	438	133	233	0.51	9.05	Early Cretaceous
112KB	AY-3		0.05	0.29	0.81	0.14	440	91	253	0.32	8.13	Early Cretaceous
10KD	AY-3	3377	0.71	9.72	0.12	0.07	438	498	6	1.95	5.77	Early Cretaceous
11KD	AY-3		0.54	5.79	0.41	0.08	439	402	28	1.44	6.66	Early Cretaceous

12KD	AY-3		0.26	2.29	0.22	0.1	436	363	35	0.63	7.67	Early Cretaceous
111KB	AY-3		0.24	1.89	1.04	0.11	432	242	133	0.78	9.12	Early Cretaceous
110KB	AY-3	3392	0.06	0.72	0.75	0.07	434	232	242	0.31	9.6	Early Cretaceous
109KB	AY-3		0.04	0.54	0.72	0.08	437	135	180	0.4	9.84	Early Cretaceous
108KB	AY-3		0.05	0.61	0.7	0.08	437	120	137	0.51	9.36	Early Cretaceous
107KB	AY-3		0.03	0.44	0.96	0.07	437	92	200	0.48	9.44	Early Cretaceous
106KB	AY-3		0.04	0.5	0.61	0.08	437	119	145	0.42	9.73	Early Cretaceous
105KB	AY-3		0.05	0.46	0.83	0.1	439	100	180	0.46	10.32	Early Cretaceous
104KB	AY-3		0.04	0.46	0.91	0.09	437	90	178	0.51	9.25	Early Cretaceous
103KB	AY-3		0.03	0.46	0.8	0.06	440	88	154	0.52	9.11	Early Cretaceous
102KB	AY-3		0.05	0.48	0.66	0.1	439	155	213	0.31	10.16	Early Cretaceous
101KB	AY-3		0.05	0.69	0.29	0.07	436	238	100	0.29	8.12	Early Cretaceous
100KB	AY-3		0.07	0.48	0.7	0.12	437	166	241	0.29	10.13	Early Cretaceous
99KB	AY-3		0.37	1.27	1.32	0.22	436	219	228	0.58	10.48	Early Cretaceous
98KB	AY-3		0.08	0.55	0.55	0.13	440	183	183	0.3	8.64	Early Cretaceous
97KB	AY-3		0.11	0.68	1	0.14	436	174	256	0.39	9.55	Early Cretaceous
96KB	AY-3		0.02	0.3	0.41	0.07	440	143	195	0.21	8.95	Early Cretaceous
95KB	AY-3		0.17	1.32	1.85	0.12	442	176	247	0.75	9.39	Early Cretaceous
94KB	AY-3		0.58	1.5	1.28	0.28	434	183	156	0.82	10.27	Early Cretaceous
93KB	AY-3		0.13	0.48	1.13	0.21	429	112	263	0.43	10.57	Early Cretaceous
92KB	AY-3		0.05	0.14	0.76	0.28	429	39	211	0.36	8.82	Early Cretaceous
91KD	AY-3		3.1	3.91	3.63	0.44	292	266	247	1.47	6.59	Jurassic
90KD	AY-3		0.11	0.31	0.89	0.27	436	51	146	0.61	6.26	Jurassic
89KD	AY-3		0.07	0.21	1.01	0.25	427	39	187	0.54	7.96	Jurassic
88KD	AY-3	4228	0.03	0.14	1.4	0.2	416	26	264	0.53	11.46	Jurassic
3-16-CS	outcrop	-	0.03	6.95	0.27	0	416	416	16	1.67	1.95	Early Cretaceous
3-17-CS	outcrop	-	0.03	9.53	0.54	0	408	302	17	3.16	0.12	Early Cretaceous
1-19-LE	outcrop	-	0.23	33.39	3.78	0.01	409	489	55	6.83	5.16	Late Jurassic
D17	outcrop	-	8.23	0.20	0.20	0.00	409	403	10.00	2.04	4.03	Mid - Late Jurassic
B19	outcrop	-	0.01	4.5	0.29	0	407	402	26	1.12	4.83	Early - Mid Jurassic
F31	outcrop	-	0	5.34	0.24	0	400	427	19	1.25	4.95	Early - Mid Jurassic
E28	outcrop	-	0.01	7.85	0.39	0	421	418	21	1.88	3.71	Early - Mid Jurassic
E38	outcrop	-	0.03	10	0.43	0	418	455	20	2.2	4.92	Early - Mid Jurassic
E4	outcrop	-	3.01	140.79	2.29	0.02	417	685	11	20.54	5.89	Late Triassic - Early Jurassic
D23	outcrop	-	0.76	116.15	1.47	0.01	423	704	9	16.49	6.49	Late Triassic - Early Jurassic
D22	outcrop	-	0.60	34.28	0.84	0.02	415	679	17	5.05	4.50	Late Triassic - Early Jurassic
C26	outcrop	-	2.23	202.04	8.78	0.01	424	568	25	35.56	0.65	Late Triassic - Early Jurassic
C29	outcrop	-	0.74	91.36	2.61	0.01	421	652.00	19	14.01	6.26	Late Triassic - Early Jurassic
7-21-J1	outcrop	-	0.67	57.55	1.35	0.01	421	728	17	7.91	10.93	Late Triassic - Early Jurassic

Table S3. Quantity of normal alkanes for the samples analyzed, shown in ppm.

Compounds	C10	C11	C12	C13	C14	C15	C16	C17	Pr	C18	Ph	C19	C20	C21	C22	C23	C24	C25	C26	C27	C28	C29	C30	C31	C32	C33	C34	C35
1KD	0.00	0.00	0.00	0.00	0.12	4.57	15.97	21.20	22.15	22.84	15.38	21.96	22.01	20.23	17.62	14.34	13.37	11.31	10.60	8.54	6.95	6.49	6.12	5.03	4.32	4.54	3.61	2.55
4KD	0.02	0.01	0.02	0.62	12.71	25.89	32.16	31.58	30.90	32.35	21.87	31.59	30.85	27.41	21.94	16.22	13.73	10.73	10.15	6.58	4.80	5.75	3.79	3.62	4.43	2.96	2.25	1.73
10KD	0.01	0.01	0.20	2.42	8.84	11.87	14.40	13.68	29.56	11.60	18.16	10.61	10.15	8.92	8.07	7.00	7.19	8.08	8.04	6.47	8.38	10.04	6.48	6.18	5.31	3.15	2.57	0.00
11KD	0.00	0.00	0.00	0.29	5.32	11.87	17.92	20.04	44.24	18.98	23.64	19.45	22.72	26.89	28.13	27.82	31.59	32.59	39.17	36.68	33.14	29.63	24.01	19.75	11.09	8.34	5.19	0.00
91KD	0.01	0.05	0.13	0.23	0.54	0.51	0.86	0.67	0.58	0.77	1.10	0.74	0.88	1.02	0.80	0.66	1.60	7.88	0.00	2.25	2.08	4.89	2.99	2.86	0.00	0.00	10.97	5.81
3-16-CS	0.00	0.00	0.03	0.03	0.19	1.73	5.27	7.89	24.41	9.84	30.41	13.12	11.36	13.41	12.81	12.71	11.19	8.12	7.20	7.27	6.13	6.88	5.52	6.55	3.62	3.80	2.65	2.92
1-19-LE	0.08	0.07	0.09	0.10	0.18	0.20	1.67	5.69	3.20	11.89	9.29	14.39	15.88	20.57	19.94	28.74	17.46	24.97	13.28	30.12	15.84	39.56	15.99	23.36	8.75	10.54	4.42	40.84
38KD	0.00	0.00	0.00	0.00	0.00	0.80	9.25	13.54	11.13	18.91	17.02	16.19	16.94	13.16	10.00	7.40	6.98	6.11	4.66	3.82	3.25	3.41	3.62	2.07	2.68	2.34	0.00	0.00
33KD	0.00	0.00	0.00	0.00	0.92	4.05	15.30	15.25	13.42	13.18	18.90	8.05	7.35	5.72	6.07	4.88	4.48	3.78	3.51	2.89	2.78	3.09	3.08	1.98	2.24	2.56	1.98	0.00
44KD	0.01	0.01	0.01	0.01	0.59	2.83	12.35	17.24	12.90	21.73	23.77	16.91	13.79	8.84	7.83	6.63	6.20	5.22	4.23	3.66	3.21	4.65	3.39	2.92	3.85	2.55	1.76	0.00
B19	0.04	0.01	0.02	0.02	0.02	0.11	1.94	8.42	10.65	6.72	13.66	6.34	7.14	8.04	10.83	9.50	9.00	7.28	6.25	7.13	4.91	8.83	6.30	10.35	6.31	7.99	3.78	7.97
F31	0.04	0.02	0.02	0.03	0.41	7.02	22.28	30.77	25.58	42.56	32.47	24.23	21.05	27.92	24.68	27.08	20.28	24.14	14.48	20.44	13.76	23.64	16.48	30.39	13.49	24.68	7.91	13.55
E38	0.00	0.00	0.00	3.99	37.12	30.04	73.12	44.30	76.68	54.32	63.06	19.26	27.11	14.35	18.23	14.75	17.03	13.85	14.06	8.79	8.81	11.57	10.72	18.83	8.59	15.25	7.00	8.68
E28	0.03	0.00	0.08	0.07	0.53	4.10	26.58	19.00	24.11	25.73	20.10	9.21	16.38	9.91	12.59	8.57	7.32	5.77	4.43	3.91	3.31	4.40	2.92	5.15	1.71	3.28	1.92	2.61
22KD	0.04	0.03	0.02	0.03	0.16	3.14	14.56	17.29	6.42	20.61	9.32	19.25	21.49	25.30	29.68	32.76	35.30	33.13	37.19	40.11	38.03	37.79	33.27	29.20	21.57	18.52	11.78	4.51
20KD	0.04	0.02	0.04	0.06	5.29	30.01	47.47	54.25	21.99	59.38	39.77	58.76	67.17	73.36	73.18	69.32	66.41	61.02	61.51	68.11	66.47	62.36	64.70	62.96	37.33	34.60	25.39	8.36
C26	0.00	0.12	0.10	0.02	0.05	0.17	0.42	0.63	0.52	1.10	1.51	2.15	2.59	2.91	2.98	2.82	2.54	2.85	4.06	6.03	6.75	6.37	5.07	3.27	1.68	0.00	0.00	0.00
E4	0.00	0.28	0.00	0.02	0.05	0.55	2.60	3.30	2.84	3.90	6.46	6.37	3.75	4.82	2.41	2.31	2.25	2.16	2.84	2.57	2.20	2.38	2.36	2.06	1.64	0.00	0.00	0.00
D23	0.43	0.19	0.10	0.04	0.23	0.53	2.48	5.38	1.44	5.00	2.36	3.59	2.53	3.19	6.04	10.23	21.64	43.70	90.32	142.25	179.11	187.84	176.74	119.15	58.21	29.14	14.18	9.32
7-21-J1	0.00	0.00	0.00	0.00	0.00	0.10	1.74	4.93	4.31	7.14	12.85	7.33	7.03	6.00	4.79	4.23	3.62	3.05	2.86	2.04	2.00	2.37	2.80	1.55	2.00	2.46	0.00	0.00

Table S4. Bulk organic carbon isotope composition ($\delta^{13}C$, ‰ VPDB) of selected organic-rich samples.

Samples	1KD	4KD	10KD	3-16-CS	3-17-CS	1-19-LE	30KD	38KD	44KD	42KD	33KD	16KD	20KD	22KD	F31	B19	E38	E28	D17	C26	D23	E4
$\delta^{13}C$ (‰)	-27.1	-26.9	-26.7	-27.5	-28.1	-29.1	-26.4	-28.7	-28.6	-26.7	-28.8	-26.0	-27.4	-27.7	-28.3	-27.8	-28.7	-28.3	-29.3	-29.8	-29.5	-29.6

Table S5. Raw kinetic data for all analyzed bulk-rock samples, including residual error (rR), cumulative residual error (cR), frequency factor (A, s^{-1}), and activation energy distributions (Ea, kcal/mol) expressed as percentage of total reactions.

	3-16-CS	115KB	1KD	2KD	4KD	9KD	10KD	11KD	12KD	111KB	108KB	1-19-LE	38KD	44KD	33KD	16KD	20KD	22KD	E38	E28	B19	F31	7-21-J1	D23	E4	C26
rR	1.0E+00	2.0E+00	1.6E+00	8.8E-01	4.9E-01	2.0E+00	5.5E-01	5.9E+00	1.2E+00	8.2E-01	1.1E+00	7.6E-01	1.3E+00	1.3E+00	8.7E-01	7.2E-01	1.7E+00	1.6E+00	2.9E-01	4.5E-01	4.2E-01	1.5E+00	1.9E+00	1.2E+00	2.4E+00	9.0E-01
cR	2.0E-01	1.5E-01	1.7E-01	2.4E-01	3.7E-02	4.1E-01	6.2E-02	1.9E+00	2.6E-01	1.4E-01	3.0E-01	7.1E-02	1.5E-01	1.6E-01	1.5E-01	9.8E-02	3.8E-01	2.3E-01	5.3E-03	5.2E-02	4.7E-03	2.3E-01	5.2E-01	9.8E-02	2.9E-01	3.6E-02
A (s^{-1})	1.3E+13	1.0E+14	4.5E+12	3.8E+13	1.2E+14	3.3E+13	4.2E+13	5.1E+13	5.1E+14	2.8E+12	1.0E+14	7.9E+14	1.6E+13	2.6E+13	5.5E+11	8.5E+12	3.0E+13	2.1E+13	1.2E+13	4.0E+12	7.5E+13	1.0E+15	6.1E+12	1.5E+13	9.0E+12	4.9E+13
Ea (kcal/mol)	Percentage (%)																									
40	0.00	0.00	0.06	0.00	0.00	0.00	0.00	0.00	0.00	0.49	0.00	0.00	0.00	0.00	0.40	0.00	0.00	0.00	0.00	0.00	0.00	0.00	0.08	0.00	0.00	0.00
41	0.00	0.00	0.09	0.00	0.00	0.00	0.00	0.00	0.00	1.36	0.00	0.00	0.00	0.00	0.52	0.05	0.00	0.00	0.15	0.00	0.00	0.00	0.14	0.00	0.17	0.00
42	0.14	0.00	0.00	0.54	0.00	0.02	0.00	0.00	0.00	1.19	0.00	0.00	0.04	0.10	0.00	0.09	0.00	0.00	0.00	0.00	0.00	0.00	0.38	0.05	0.34	0.00
43	0.22	0.20	0.58	0.90	0.00	0.10	0.21	0.00	0.00	2.42	0.00	0.00	0.39	0.28	0.00	0.60	0.07	0.02	0.01	0.00	0.21	0.00	0.63	0.13	0.75	0.15
44	0.78	0.45	0.00	1.44	0.04	0.07	0.43	0.00	0.00	0.70	0.54	0.00	0.39	0.17	9.31	0.25	0.22	0.00	0.60	0.00	0.00	0.00	0.57	0.62	1.08	0.25
45	0.90	0.90	0.00	1.71	0.00	0.61	0.43	0.19	0.00	3.56	0.35	0.01	1.34	0.93	3.21	1.78	0.25	0.22	1.67	0.00	0.38	0.00	2.05	0.00	1.90	0.68
46	2.58	1.15	0.00	1.22	0.19	0.00	0.95	0.14	0.51	0.49	1.49	0.06	1.77	0.01	55.11	0.39	0.00	0.11	3.63	10.80	0.00	0.04	1.38	2.35	2.49	1.28
47	5.79	1.59	0.00	2.50	0.03	1.45	0.00	0.00	0.34	0.00	1.29	0.62	6.26	2.49	13.33	3.19	1.21	0.00	5.89	4.47	0.00	0.18	8.64	0.29	5.63	1.13
48	7.15	1.70	0.00	0.80	0.49	0.23	1.95	1.04	0.50	39.30	1.26	0.91	8.45	0.08	10.38	4.55	0.01	0.00	6.70	21.51	0.07	0.42	1.05	7.87	13.20	2.83
49	12.10	1.64	0.00	3.37	0.00	0.00	0.32	0.33	1.37	20.67	1.02	2.37	21.35	12.08	2.58	0.00	0.00	0.00	16.76	26.86	12.84	0.66	40.49	5.20	14.46	2.79
50	21.21	2.32	73.54	1.57	0.00	0.00	0.00	0.00	0.09	23.25	3.11	3.05	22.25	7.05	2.69	56.72	0.00	0.00	20.19	18.67	7.29	0.88	28.42	21.46	39.70	7.93
51	16.54	1.65	0.00	0.00	0.49	0.00	0.00	0.00	1.76	0.00	0.71	5.77	17.72	39.86	0.00	15.03	0.00	0.00	23.86	10.98	17.47	1.46	4.23	44.68	5.92	9.73
52	19.01	2.98	20.48	16.98	0.00	45.69	0.00	0.00	1.80	1.17	0.00	5.54	8.66	15.16	1.12	9.83	68.79	80.13	8.99	5.70	11.29	6.60	7.58	3.92	7.89	26.48
53	2.20	7.57	0.56	17.84	0.00	18.36	60.00	54.23	0.00	2.56	11.58	9.10	9.04	11.92	0.04	1.56	10.19	3.46	11.02	0.00	25.77	10.41	0.00	8.67	1.14	22.17
54	8.43	22.25	1.25	45.44	68.58	28.21	9.89	14.18	0.00	0.00	25.15	8.24	0.74	3.44	0.36	2.54	15.04	12.77	0.00	0.00	5.26	11.04	2.35	0.00	2.48	9.05
55	0.00	31.17	0.00	0.00	9.73	0.00	16.85	26.61	0.00	0.82	35.30	12.49	0.00	3.63	0.02	0.05	0.00	0.00	0.00	0.00	18.90	15.42	0.00	2.56	0.26	6.34
56	0.59	11.10	0.93	0.00	13.38	0.39	5.20	1.23	47.79	0.54	8.96	10.68	0.91	0.28	0.35	1.18	1.64	0.47	0.00	0.28	0.00	13.96	0.85	0.07	1.17	2.81
57	0.69	4.50	0.17	1.71	1.40	2.14	0.47	0.00	13.31	0.00	0.00	12.90	0.00	1.05	0.00	0.10	0.29	1.28	0.15	0.12	0.00	17.19	0.06	0.94	0.00	2.01
58	0.00	2.44	0.94	1.81	3.74	0.00	0.37	0.24	27.27	0.59	2.55	9.89	0.33	0.00	0.00	0.48	0.56	0.00	0.00	0.00	0.00	7.54	0.40	0.00	0.57	1.32
59	0.42	2.12	0.00	0.00	0.00	0.48	0.88	0.00	0.00	0.13	3.20	6.45	0.11	0.65	0.00	0.50	0.28	0.36	0.01	0.27	0.23	8.92	0.00	0.46	0.08	0.94
60	0.17	1.24	0.00	0.48	0.00	0.49	0.00	0.00	0.00	0.00	0.00	3.48	0.00	0.05	0.22	0.00	0.33	0.25	0.09	0.00	0.04	3.22	0.32	0.11	0.13	0.51
61	0.00	1.12	0.71	0.66	0.65	0.32	0.42	0.00	1.07	0.00	1.08	2.69	0.16	0.00	0.00	0.57	0.00	0.00	0.00	0.17	0.00	0.00	0.10	0.11	0.31	0.39
62	0.17	0.00	0.00	0.13	0.10	0.00	0.18	0.00	1.20	0.54	0.33	1.38	0.00	0.25	0.00	0.10	0.39	0.48	0.13	0.18	0.00	0.00	0.00	0.27	0.00	0.42
63	0.31	0.60	0.00	0.29	0.33	0.52	0.26	0.46	0.00	0.00	0.64	1.44	0.00	0.15	0.00	0.00	0.21	0.00	0.00	0.00	0.08	0.17	0.00	0.00	0.00	0.00
64	0.00	0.00	0.00	0.00	0.05	0.29	0.22	0.62	0.42	0.00	0.33	0.57	0.00	0.00	0.00	0.00	0.00	0.00	0.00	0.00	0.02	0.20	0.00	0.00	0.00	0.32
65	0.00	0.33	0.00	0.00	0.31	0.00	0.34	0.00	0.78	0.00	0.01	0.95	0.09	0.07	0.00	0.43	0.00	0.00	0.15	0.00	0.00	0.10	0.27	0.00	0.00	0.19
66	0.00	0.08	0.68	0.00	0.20	0.00	0.00	0.12	0.34	0.00	0.00	0.04	0.00	0.00	0.00	0.00	0.00	0.00	0.00	0.00	0.00	0.00	0.00	0.25	0.34	0.00
67	0.00	0.00	0.00	0.62	0.00	0.63	0.00	0.61	0.00	0.00	0.00	0.74	0.00	0.00	0.00	0.00	0.00	0.00	0.00	0.00	0.13	0.08	0.00	0.00	0.00	0.00
68	0.58	0.00	0.00	0.00	0.00	0.00	0.00	0.00	0.61	0.00	1.12	0.00	0.00	0.00	0.00	0.00	0.00	0.46	0.00	0.00	0.00	0.07	0.00	0.00	0.00	0.00
69	0.00	0.89	0.00	0.00	0.00	0.00	0.00	1.54	0.27	0.00	0.00	0.16	0.00	0.31	0.00	0.00	0.00	0.00	0.00	0.00	0.00	0.20	0.00	0.00	0.00	0.28
70	0.00	0.00	0.00	0.00	0.28	0.00	0.62	0.00	0.00	0.00	0.00	0.20	0.00	0.00	0.00	0.00	0.00	0.00	0.00	0.00	0.00	0.00	0.00	0.00	0.00	0.00